The University Of Sheffield.

Alternative Processing Methods for the Thermal Treatment of Radioactive Wastes

THESIS

Submitted for the degree of Doctor of Philosophy

Paul George Heath

Immobilisation Science Laboratory

Department of Materials Science and Engineering

The University of Sheffield

Sponsored by EPSRC as part of the Nuclear First DTC program

August 2015

Abstract

The UK has large volumes of radioactive materials which are classified as Intermediate Level Waste (ILW). The baseline treatment for these wastes is encapsulation via cementation, however, this method is not ideally suited for numerous wastes, both in the UK and globally. Alternative thermal processing methods for these materials may be capable of producing wasteforms with improved properties. This thesis presents a series of scoping studies on the thermal treatment of a diverse range of ILWs in order to identify the potential benefits and pits falls of such processes. The wastes selected were Tri-Structural Isotropic (TRISO) Fuel Particles, Prototype Fast Reactor (PFR) raffinate, SIXEP sand/clinoptilolite ion exchange materials and SrTreat® Ion exchange material.

The scoping studies performed showed promise for the thermal treatment of all selected waste streams. A summary of the main results for each waste stream are provided below;

TRISO Fuel Particles: Immobilisation focused on encapsulation of the particles in highly durable glass matrices. Alumino-borosilicates were determined to be the most effective glass composition for the production of composites, in terms of both their physical and chemical properties. The ability of Hot Isostatic Pressing (HIPing) to improve composites was investigated. Unfortunately, this was shown to result in severe fracturing within the composite. This was hypothesised to occur as a result of excessive pressurisation during the cooling cycle. The HIP process did show some benefits in terms of particle coating properties and with small alterations to the HIP cycle utilised it should also be possible to eliminate the detrimental fracturing features.

PFR Raffinate: The vitrification of PFR raffinate was investigated using the G73 glass composition, a glass which has been previously proposed for the immobilisation of other ILWs. This glass was proven to be capable of accommodating a waste loading of up to 20 wt% PFR raffinate. The glass produced was homogeneous with good waste retention, had no noted crystal formation, an aqueous durability comparable to currently employed HLW glasses and the thermal characteristics necessary for industrial scale up. Further study should be performed on the ability of this waste to retain Cs during processing and in aqueous solution.

SIXEP Sand/Clinoptilolite Waste: SIXEP sand/clinoptilolite was processed at 95 wt% with a 50 % volume reduction by HIPing. The waste produced was a phase separated glass-ceramic. The wasteform was deemed to be suitable for ILW immobilisation and had an exceptional Cs

retention in aqueous solutions. However, the presence of an alkali earth sulphate phase increased the Sr release to solution. Attempts to qualify the suitability of this wasteform for disposal, developed methodologies to investigate the properties of phase separated materials. A combination of vertical scanning interferometry (VSI), dissolution experiments and SEM imaging was shown to be capable of elucidating the dissolution behaviour based upon compositional variation.

SrTreat®: SrTreat® was processed at 100% waste loading via HIPing. This aim was to investigate the potential for developing ion exchange columns which could subsequently be HIPed, as such, providing a complete waste treatment solution. The HIP process produced a monolithic, mixed phase sodium titanate ceramic. This ceramic was formed by the sintering of individual grain structures and retained the compositional variations seen in the granular waste stream. The wasteform was porous around the grain edges, determined to occur as a result of carbonate formation prior to HIPing. The carbonation of this material is likely to limit the potential to utilise HIPing as a disposal methodology for these wastes. However the aqueous dissolution behaviour of these wastes was still favourable and the process was shown to create a significant reduction in waste volume.

The work performed in this thesis has shown that various methods for thermal treatment can be rapidly investigated to determine the potential benefits and pit falls. The application of thermal treatments was shown to be capable of producing significant improvements in wasteform quality by comparison with the cementitious alternatives.

Acknowledgements

To exaggerate how much the completion of this thesis is owed to those around me would be a difficult task. I have been extremely lucky to be surrounded by fantastic people during my PhD and I count myself blessed for this. To name everyone who has had a part in the competition would likely double my word count, therefore, if you feel you have been unjustly omitted, please come to see me and I'll buy you a beer.

I should start by thanking Professor Neil Hyatt and Professor Russell Hand for their outstanding academic supervision. Their help, support and encouragement; both academic and pastoral, has been extremely beneficial. I am grateful for all that they have brought to both this body of work and my development as a person, scientist and engineer. Neil, I look forward to hearing 'the story' soon.

Along with my primary supervisors I have been lucky to receive substantial academic support from other sources. I would like to thank Dr. Claire Corkhill and Dr. Martin 'Stendog' Stennett who have faced a great deal of pestering. I appreciate how supportive you have both been and that you never throttled me during the course of this research. Dr. Ewan Maddrell from NNL has been equally helpful in providing advice, samples and materials, which have proven invaluable. I would also like to thank Dr. Felix 'Papa' Brandt at Jülich Forshungszentrum for helping to arrange my secondment, being so accommodating of a cheeky Englishman and for teaching me the joy of beschäftigung.

I would like to thank EPSRC for their financial support through the Nuclear First DTC programme. I would also like to thank the University of Sheffield for financial support in the form of a KTA grant, which helped advance the work on TRISO particle encapsulation and the Worshipful Society of Armourers and Brasiers for supporting the dissemination of my work on the immobilisation of clinoptilolite.

Being part of the Nuclear First DTC course allowed me to be part of a talented group of scientists from whose association and friendship I have benefited. I would like to thank all those from both the University of Sheffield and the University of Manchester who took the time to provide lecture courses and administrative support during my studies. My fellow students from both the Nuclear First DTC and ISL groups have helped to make this a most enjoyable period and are all deserving of my thanks here. I won't try to thank you all individually here (see paragraph 1) but I would like to single out Sam Walling for his helpful, yet worryingly complete, knowledge of both the cement and NDA literature.

The skill and knowledge of the technical staff within the Department of Materials Science and Engineering at the University of Sheffield has been the bed rock upon which this research has been built. A special thank you should go to the foundry cabal; 'Uncle' Ian Watts, Kyle Armhold, Dr. Amit Khan, Dr. Lisa Holland and Dr. Fatos Derfugi. Not only have you helped me almost daily, but you also made that lab one of my favourite places to be. Another special thanks should go to Andrew 'Fatman' Mould for helping with the initial set up of the University's HIP facility and generally helping to fix things….the viscometer will get there in the end. I can safely say there is not a single technician in this department who hasn't been subjected to my fluttering eyelashes at some point. Therefore in no particular order I would like to thank Ben Palmer, Dean Haylock, Dr. Nik Reeves, Dr. Oday Hussein, Michael Bell, Richard Kangley, Paul Hawksworth and Beverly Lane. The amount of help you have provided couldn't possibly be listed but is well remembered.

On the same theme I would like to thank Paul Lythgoe and Alastair Bewsher at School of Earth, Atmospheric and Environmental Sciences, the University of Manchester for providing the majority of XRF and ICP-AES/MS data used in this study. I would like to thank John Charnock of the same department for his help in performing the EPMA measurements presented in Chapter 6 and Tristan Lowe at the Henry Mosley Facility for the XCT measurements presented in Chapter 4.

One of the highlights of my PhD has been the opportunity afforded to me to travel, especially for the duration of my work in Germany. Thank you to everyone at Forschungszentrum Jülich for being so welcoming and giving me the best placement I could have hoped for. I would like to highlight the help of Martina Klinkenberg and her 200 Mega Pixel eyes on the SEM, Fabi Sadowski who ran almost 1000 ICP-MS samples without a single complaint, Dr Cornelius Fischer of Univeristät Bremen for his help in performing the VSI measurements and Andrey Bukaemskiy for accompanying me to Bremen for these experiments. I would like to thank the following people for all their help and for being so welcoming during this time; 'Onkel' Philip Kegler, Stefan Neumeirer, Julia Arinacheva, Sarah Finkeldei, Julianna Webber, Giuseppe Modolo, Jakob Dellen, Christian Fischer and Andreas Fichtner. The dubious joy of Mickey Krauser is still with me...

Thanks to all those who accompanied me on my research and conference trips for such adventures as; '£40 pound cafeteria card', 'The Boston Taxi Party', 'drei Milano bitte', 'The Villigen Spesh - featuring Carly Rae Jepson', 'Yakult science day' and the infamous 'CIGGARETTU!!!'.

Naturally an acknowledgements section would not be complete without a mention of family and friends. Thanks to all of you for your support and love. Mother you're probably the funniest person I know. Thanks for all your strange and misguided advice. Nan and Granddad thanks for putting me up for 'a couple of weeks', I won't ever forgot it. I'd like to welcome Charlie to the family. If you're ever too bad I might force you to read this thesis. To my friends, thanks. I hope you haven't changed your phone numbers during the last 6 months.

I would like to thank my current employers at GeoRoc Ltd for helping me develop a greater understanding of the implications for the commercial application of this work and the numerous collaborators who have shown great patience whilst I have worked to complete this tome.

I would like to dedicate this thesis to my much missed friend Gary Cunliffe. You had the greatest effect on shaping my life. I couldn't have hoped to be who or where I am if it hadn't been for the years of support, guidance and friendship you provided. More than anything else I wish you could have been here now.

My final thanks should go to Steph Thornber. It turns out writing a PhD thesis is quite taxing. Both my hair and sanity are still intact thanks to your love, advice and support. If I turn out to be any less accommodating during your write up, please feel free to ram this page down my throat…

Publications

The author has contributed to the following publications during the production of this thesis;

1. P.G. Heath, C.L. Corkhill, M.C. Stennett, R.J. Hand, W.C.H.M. Meyer, N.C. Hyatt, Encapsulation of TRISO particle fuel in durable soda-lime-silicate glasses, *Journal of Nuclear Materials*, **436** (2013) p.139-149.
2. P.G. Heath, M.C. Stennett, O. J. McGann, R.J. Hand, N.C. Hyatt, The Use of High Durability Alumino-Borosilicate Glass for the Encapsulation of High Temperature Reactor (HTR) Fuel, *MRS Proceedings* **1518,** (2013), p.3-8.
3. N.C. Hyatt, R.R. Schwarz, P.A. Bingham, M.C. Stennett, C.L. Corkhill, P.G. Heath, R.J. Hand, M. James, A. Pearson, S. Morgan, Thermal treatment of simulant plutonium contaminated materials from the Sellafield site by vitrification in a blast-furnace slag, *Journal of Nuclear Materials*, *Journal of Nuclear Materials*, **444,** (2014), p.186-199.
4. C.L. Corkhill, N.J. Cassingham, P.G. Heath, N.C. Hyatt, Dissolution of UK high level waste glass under simulated hyper-alkaline conditions of a co-located geological disposal facility" *Journal of Applied Glass Science*, **4**, 4 (2013), p. 341-356
5. M. C. Stennett, L. D. Casey, C. L. Corkhill, C. L. Freeman, A. S. Gandy, P. G. Heath, I. J. Pinnock, D. P. Reid, N.C. Hyatt, Advanced Ceramic Wasteforms for the Immobilisation of Radwastes *Ceramic Transactions,* **241**, (2013), p.11-22.
6. M.Z.H. Mayzan, P.G. Heath, J.W. Lloyd, M.C. Stennett, N.C. Hyatt & R.J. Hand, Glass-Graphite Composite Materials, Co-ordinated Research Project on Treatment of Irradiated Graphite to Meet Waste Acceptance Criteria for Disposal - Technical Report, International Atomic Energy Agency.
7. H. Zhang, C.L. Corkhill, P.G. Heath, R.J. Hand, M.C. Stennett, N.C Hyatt, Effect of Zn- and Ca-oxides on the Structure and Chemical Durability of Simulant Alkali Borosilicate Glasses for Immobilisation of UK High Level Wastes, *Journal of Nuclear Materials,* In Press, Accepted Manuscript, 17 April 2015

The work included in this thesis has also been disseminated at a number of conferences and meetings during this time which are listed below;

Oral Presentations;

- Meeting of the Materials Research Society - Boston, November 2012
- International Congress on Glass - Prague, July 2013
- Royal Society of Chemistry/AWE, Young Researchers Meeting - Aldermaston, September 2013
- Institut de minéralogie et de physique des milieux condenses - Guest Presentation - Université Pierre et Marie Curie - Paris, November 2013
- IEK6 – Guest Presentation - Jülich Forschungszentrum - September 2014

Poster Presentations;

- REDDUP, Environmental Mineralogy Research in Progress - University of Sheffield, May 2013
- Research Frontiers in Radioactive Waste Management - University of Sheffield, October 2012
- Thermal Treatment of Radioactive Wastes I & II - University of Sheffield/Sellafield, December 2013 and January 2014
- SET for Britain – The Parliamentary and Scientific Committee – Westminster - March 2015

Note to Reader

Due to the nature of the investigations presented in this thesis, the liberty has been taken to deviate slightly from the classical thesis structure. This has been done in order to aid the readers understanding of the work and it is hoped that the reasoning behind this decision will be appreciated.

The introduction, literature review and experimental sections have been produced to support and provide information which relates to the thesis as a single body of work. However, based upon the identity of the waste stream under investigation, the results and any discussion of these results has been compartmentalised into experimental chapters. These chapters are therefore presented as four individual studies, partitioned into sub-sections as follows; Introduction, Materials and Experimental, Results, Discussion and Conclusions. It should be remembered that, although compartmentalised, the overall aim was to investigate the applicability of thermal treatments across a breadth of ILW wastes, through the completion of experimental and scooping studies. To draw the work into a coherent body a short summary chapter has been included.

Contents

Chapter 3 - Experimental

Chapter 4 - Encapsulation of TRISO Fuel Particles in Sintered Glass Composites

Chapter 5 - Prototype Fast Reactor (PFR) Raffinate

Chapter 6 - Clinoptilolite Ion Exchange Material

List of Abbreviations

AIP	American Isostatic Presses
ASTM	American Society for Testing and Materials
BISO	Bi-Structural Isotropic
BPEO	Best Practicable Environmental Option
CPS	Cold Press and Sinter
DSRP	Dounreay Site Restoration Plan
DTA	Differential Thermal Analysis
DSC	Differential Scanning Calorimetry
EPMA	Electron Probe Micro-Analysis
HIP	Hot Isostatic Press
HIPed	Hot Isostatically Pressed
HIPing	Hot Isostatic Pressing
HTR	High Temperature Reactor
ICP-AES	Inductively Coupled Plasma Atomic Emission Spectroscopy
ICP-MS	Inductively Coupled Plasma Mass Spectroscopy
JHCM	Joule Heated Ceramic Melter
MCC-1	Materials Characterisation Centre - 1 (Protocol)
NBO(s)	Non Bonding Oxygen(s)
NL_i	Normalised Elemental loss of element i
NR_i	Normalised Elemental Loss Rate of Element i
PC	Portland Cement
PCT	Product Consistency Test
PFA	Per-Fluoroalkoxy alkane
PFR	Prototype Fast Reactor
POI	Point of Interest
PSA	Particle Size Analysis
RSD	Relative Standard Deviation
SA/V	Surface Area to Volume Ratio
SEM	Scanning Electron Microscopy
SEM-BSE	Scanning Electron Microscopy - Back Scattered Electron
SEM-EDX	Scanning Electron Microscopy - Energy Dispersive X-ray Analysis
SEM-WDX	Scanning Electron Microscopy - Wavelength Dispersive X-ray Analysis
SIXEP	Site Ion Exchange Plant
SPFT	Single Pass Flow Through (protocol)
TEC	Thermal Expansion Coefficient
T_g	Glass Transition Temperature
TGA	Thermal Gravimetric Analysis
TRISO	Tri-Structural Isotropic
UKAEA	United Kingdom Atomic Energy Agency
VSI	Vertical Scanning Interferometry
XCT	X-ray Computed Tomography
XRD	X-ray Diffraction

XRF	X-ray Fluorescence Spectroscopy

Sample Identification Notation

ABS-1	Alumino-borosilicate 1
CSXC	Caesium/Strontium exchanged clinoptilolite
CSXC-BORAX	HIPed caesium/strontium exchanged clinoptilolite with 5 wt% $Na_2B_4O_7$
CSXC-$NaAlO_2$	HIPed caesium/strontium exchanged clinoptilolite with 5 wt% $NaAlO_2$
G73-(10/15/20)	G73 barium silicate base glass loaded with 10 wt%, 15 wt% and 20 wt% PFR calcine
HIP-SrT	HIPed Sr exchanged SrTreat®
MW25	UK magnox waste HLW glass with 25 % calcine waste loading
SLS(A/B/C)	Various compositions of soda-lime silicate glass
SON68	French base HLW Glass

Chapter 1 - Introduction

This chapter will provide the reader with the background information necessary to understand and contextualise the aims of this PhD thesis. It is split into three sections, firstly a brief history of the role which nuclear power has played in the UK, secondly an introduction to the radioactive wastes created during the nuclear power generation (this section includes background on the current disposal policy for radioactive wastes) and finally the aims of this PhD thesis are presented.

1.1 - Nuclear Power in the UK

The UK was the first country in the world to generate electricity on a commercial scale using nuclear power [1]. The Calder Hall plant went online in 1956 and ever since nuclear energy has provided a significant contribution to the nation's energy mix. This peaked in 1998 at 28.9% of total electricity generation and the statistics from 2013 show electricity generation from nuclear power is still substantial, providing 19.8% of the UK's total electricity [2, 3]. This is in spite of the closure of seven reactors since 1998.

An overview of nuclear power generation, in which the fuel cycle is separated into three phases, is provided below [4].

Front End: Uranium ore is mined and purified. The natural uranium is processed to enrich the concentration of its fissile ^{235}U isotope. This is then fabricated into fuel pellets, usually in the form of UO_2.

Electricity Generation: When a ^{235}U nucleus captures a neutron, an unstable ^{236}U nucleus is formed. This unstable nucleus will then split into two smaller fragments, as well as 2-3 neutrons and a large amount of energy. This process is known as nuclear fission. The amount of energy produced by the fission of ^{235}U is enormous; each ^{235}U atom which undergoes fission releases approximately 2.07×10^8 eV [5]. This can be put into perspective by comparison with a typical chemical reaction used for electricity production. The complete combustion of one molecule of natural methane gas releases just 8.31 eV of energy [6]. Nuclear power generation utilises the heat produced during this reaction in the same way which a coal fired power station utilises chemical energy. The heat evolved is used to produce steam, this steam is used to rotate a turbine, which in turn generates electricity. As each

fission event produces an excess of neutrons, the nuclear fission reaction and the subsequent generation of heat can be made self-sustaining.

Back End: Once spent fuel is removed from the reactor it can either be stored or reprocessed to recover the reusable fuel fraction. The majority of the UK's fuel is currently reprocessed. Reprocessing in the UK utilises the PUREX process, which separates the spent fuel into three major components; uranium, plutonium and fission products (plus minor actinides) [1]. The uranium and plutonium are currently stored, awaiting a decision on whether they should be disposed of or fabricated into MOX fuel assemblies. The separated fission products and minor actinides are treated to produce a High Level Waste (HLW) glass.

Nuclear power is capable of producing large amounts of energy reliably, with little fluctuation in fuel pricing and with a small carbon footprint [7]. These characteristics are increasingly desirable due to international concerns over global warming, uncertainties in the price of fossil fuels and ever increasing energy demands. Despite this, use of nuclear power has been a controversial subject in the past for a number of reasons. These include long held fears over the proliferation of weapons grade materials and media attention on a small number of nuclear accidents, which have helped to shape the public perception of nuclear power. One of the most frequent arguments against the utilisation of nuclear power focuses on the unavoidable production of radioactive wastes as a by-product. To dispose of legacy wastes and provide confidence in the safety of the UKs next generation of nuclear reactors, it is important to address these concerns in the near future.

1.2 - Radioactive Wastes

Radioactive wastes are materials which contain radioisotopes which are not deemed to serve a useful function. Radioactive wastes are produced during every stage of the nuclear fuel cycle, whether as a result of the concentration of naturally occurring radiation, contamination of materials or directly from the burning of nuclear fuels [1, 4].

1.2.1 - The Potential Dangers of Radioactive Wastes

Radioactive wastes pose a danger to human health due to the radioisotopes which they contain [8, 9]. As the unstable nucleus of a radioisotope decays, emission of ionising radiation occurs. The type and energy of the radiation emitted is dependent on the identity of the radioisotope undergoing nuclear decay [10]. The radioactive emissions from nuclear decay include α-particles, β-particles, γ-rays and neutrons. The health risks posed by radioactive

waste are a result of the destructive interactions of ionising radiation with biological systems [9].

The damage to biological systems from the interaction with radioactivity depends upon the dose received and is commonly separated into two categories; acute and chronic radiation damage. Acute damage results from exposure to high level doses of radiation; these incidents are rare and result in the severe damage or complete destruction of bodily systems such as the bone marrow, the gastro-intestinal tract or central nervous system. In turn, this often leads to the death of the individual exposed. Chronic radiation damage refers to lower levels of exposure over time. The effects on health, if any, are more contentious. Although there is limited evidence which correlates an increased incidence of cancers with increased exposure to low level radiation, the sampling methodologies used have always rendered this assertion inconclusive [9, 11-13]. However, due to the weight of public opinion and the potential health risks posed by radioactive wastes they should always be treated in a manner which minimises any potential danger to the human population.

1.2.2 - UK Classification of Radioactive Wastes

Radioactive wastes in the UK are separated into five categories; three major categories which are described below, as well as spent fuel and very low level waste (VLLW). These categories have been developed primarily on considerations of operational efficiency [14, 15];

1. **High Level Waste (HLW)**: HLW is classified as waste which has a radioactive content >4 GBq/t of alpha or >12 GBq/t of beta/gamma activity and which may also cause a significant rise in temperature due to its radioactive decay. HLW usually comes from the reprocessing of spent fuel and consists of the fission products which are removed from fuel elements in an acidic liquor. HLW in the UK is processed into a vitrified wasteform and is currently stored above ground awaiting final disposal in a Geological Disposal Facility (GDF). Spent fuel elements also fit the above description; however, these wastes have their own set of considerations, and as noted above, are commonly categorised with their own classification.
2. **Intermediate Level Waste (ILW):** ILW wastes have a radioactive content >4 GBq/t of alpha or >12 GBq/t of beta/gamma activity where heat generation does not have to be taken into account. Typically ILW comes from reprocessing operations or the decommissioning of nuclear facilities. ILW wastes include fuel cladding, sludges,

effluents and building materials. ILW is most commonly treated by encapsulation in cement and is stored above ground awaiting final disposal in a GDF.

3. **Low Level Waste (LLW)**: LLWs are radioactive wastes with a low level of contamination. To be classified as LLW a waste must have a total radioactive content <4 GBq/t of alpha or <12 GBq/t of beta/gamma activity. These wastes are typically lightly contaminated materials such as lab equipment and hospital refuse. The majority of LLW is super compacted, cemented into steel containers and disposed of in the LLW repository near Drigg, Cumbria. Waste materials with lower levels of activity can also be also be classified as VLLW and are suitable for controlled disposal by conventional means.

1.2.3 - The Safe Disposal of Radioactive Waste and the GDF Concept

In deciding how to treat radioactive wastes it should be noted that they are inherently different to chemically hazardous elemental wastes. Chemically hazardous wastes such as the heavy metals will remain chemically hazardous, however, radioactive wastes do not need to be considered dangerous in-perpetuity. The time taken for radiological effects to be considered inconsequential is generally accepted to be ten half-lives ($t_{1/2}$). Alternatively, this can be described as the time taken for < 0.1 % of the original number of radioactive atoms to remain. The half-life is an inherent physical property of a radioisotope and may vary by several orders of magnitude for the variety of radioactive elements produced during nuclear fission [10]. Some have short half-lives, such as ^{135}I ($t_{1/2}$ = 6.7 h) and as such will decay beyond the point of significance in a number of days [16]. However the contribution from others with longer half-lives, such as ^{242}Pu ($t_{1/2}$ = 0.38 My), will be of concern over geological time frames [16]. Due to the longevity of the risk posed by some isotopes, especially the transuranic elements, the most effective disposal options have been thoroughly debated [17]. The UK has determined that its reference scenario for disposal of HLW and ILW should involve the use of a Geological Disposal Facility (GDF) [18, 19].

A GDF is one of the most ambitious engineering projects ever conceived, aiming to isolate radioactive wastes from the human population for periods varying from tens to hundreds of thousands of years [19]. This will be accomplished by utilising a series of engineered barriers as listed below and illustrated in Figure 1.1 c).

1. **Wasteform** - The radioactive wastes will be conditioned to produce a physically and chemically stable solid, able to prevent (or significantly retard) the release of radioisotopes into the surrounding environment.
2. **Canister** - The wasteform will be contained in a corrosion resistant canister, made from a material such as stainless steel or copper. This canister and associated overpacks will facilitate transport to the GDF and once in the GDF it will isolate the wasteform from the environment until at least the time the GDF is closed.
3. **Vault Backfill** - The canisters will be placed in underground vaults and surrounded by an appropriate backfill or 'buffer' material. This will act as a barrier delaying the transport of any radioisotopes released into the immediate vicinity of the vault.
4. **Host Geology** - The vaults will be located between 100 m and 1000 m underground. GDF sites will have a geology suitable to prevent any released radioisotopes reaching the surface prior to sufficient decay occurring.

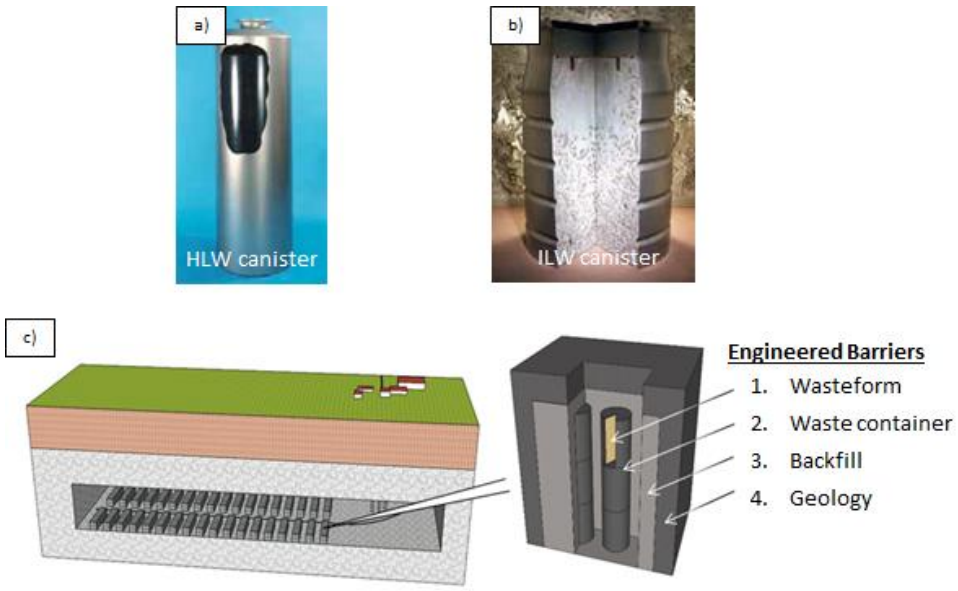

Figure 1.1 - Images of a) a simulated vitreous HLW canister b) a simulated cementitious ILW canister and c) a schematic of the UK GDF concept. (Images *a) and b) adapted from [20]*)

1.2.4 - The Requirements of Radioactive Wasteforms

The focus of this PhD is to develop processing methods capable of producing wasteforms suitable for geological disposal by the thermal treatment of ILW. As such only the first of these barriers, the wasteform, will be discussed in further detail here. It can be argued that the wasteform is the most reliable barrier preventing the migration of radioactivity into the

environment. As the radioisotopes are all initially contained within the wasteform, only radioisotopes which are released from the wasteform can enter the biosphere. As such, the wasteform's stability provides the source term for any repository. In principle, an effective wasteform, able to retain its radioisotope inventory over geological timeframes, provides the most effective barrier to radioactive releases. Furthermore, the wasteform is the barrier whose properties can be most readily optimised to the identity of an individual waste stream. This optimisation ensures maximum chemical and physical stability is obtained, limiting the release of harmful species in a manner that transport retarding barriers cannot.

A high quality wasteform for radioactive wastes should possess a number of essential properties [21, 22].

a) **Solid monolith** - Wasteforms should be both solid and monolithic in structure. This serves three purposes. Firstly fluids and powders pose an inherent dispersion hazard; secondly higher surface areas increase the area from which chemical dissolution can occur, potentially increasing the rate at which radioisotopes are released; and finally the solids should be physically robust facilitating both transport and stacking during storage.
b) **Chemical stability** - Wasteforms must be able to incorporate all the radioisotopes of a waste stream and be chemically durable. This is particularly important of the ability to retain the radioactive inventory in aqueous solutions during GDF storage.
c) **Radiation stability** - The physical and chemical properties should not be significantly degraded by radiation induced damage mechanisms.
d) **Criticality control** - Actinide bearing wastes must be unable to reach criticality, even when waste packages are fully moderated by water.
e) **Remotely processed** - It should be possible to produce wasteforms using remotely operated technologies to minimise the associated operational risks.

Other favourable properties include high waste loadings, a high waste volume reduction, thermal stability of the product, the ability of the processing methodology to accept variations in waste stream composition and use of readily available starting materials, at acceptable costs.

These objectives are commonly achieved using one of two methodologies.

1. **Encapsulation:** The waste is encapsulated into a surrounding matrix, which physically binds the waste into a monolithic structure. Chemical barriers may also be present in the matrix; such as the high pH in cementitious waste products which

promotes the precipitation of actinide elements. The most common example of encapsulation in the UK is found in the cementation of ILW waste.

2. **Chemical incorporation:** Radionuclides are bound directly into the chemical structure of the material. This is the reference method for highly active wastes as it renders the radioisotopes passively safe. The most common example in the UK is the vitrification of HLW into a glass wasteform.

1.2.5 - The UK Radioactive Waste Inventory and Orphan Wastes

In terms of radioactive content, HLW accounts for ~95% of the UK's waste radioactive waste inventory. This waste exists as a vitreous glass product, formed from wastes produced during the reprocessing operations on the Sellafield site [23]. As ILW waste streams are non-heat generating and are generally believed to be compatible with cementation, the accepted UK methodology for their disposal is via direct encapsulation. It has previously been noted that LLW is super compacted, cemented and disposed of in a sub-surface repository.

ILW only accounts for 5% of the UKs volume by waste activity, however, it provides a much greater percentage of the waste inventory by volume. This volume accounts for >99.5 % of the waste volume which is designated for GDF disposal. The relative contributions of each waste classification to the UK waste inventory in terms of both volume and activity are shown in Table 1.1. Plans already exist for the transformation of almost all the UK's radioactive waste inventory into suitable wasteforms.

Waste Classification	Contribution to Total Waste Inventory by Volume	Contribution to Total Waste Inventory by Activity
LLW	93.9 %	0.00005 %
ILW	6.1 %	5 %
HLW	0.02 %	95 %
Total Inventory	4,720,000 m^3	84,000,000 TBq

Table 1.1 - UK radioactive waste inventory volumes and activity, classified by category, as of April 2010 [23].

Due to the large diversity in the materials which contain or have been contaminated with radioactive isotopes, it comes as no surprise that some wastes are not compatible with these reference processing methodologies [24-28]. Such wastes are often referred to as 'orphan wastes'. The term orphan refers to the lack of an agreed waste treatment methodology, or

transfer strategy for these wastes. Orphan wastes exist on almost all UK nuclear sites. They tend to have a low priority for the Nuclear Decommissioning Authority (NDA) as typically there is only a low volume of each waste type, they do not hinder ongoing decommissioning operations and do not pose an immediate barrier to site hazard reduction. Some examples of materials categorised as orphan wastes include; oils, solvents, silts, sludges, lead, asbestos, mercury, resins, ion exchangers, graphite, encapsulated wastes unfit for purpose, exotic fuels, plutonium contaminated materials (PCMs) and laboratory chemicals. Except in the situation where appropriate incineration methodologies are deemed acceptable, these wastes require treatment and conditioning to produce wasteforms suitable for interim storage and future disposal in a GDF.

1.3 - Project Aims

This thesis will present a series of studies to demonstrate how thermal treatments may be applied across a diverse range of ILW wastes. Thermal treatment methodologies for the production of wasteforms from the four waste streams listed below have been investigated:

1. TRISO Fuel Particles (e.g. Dragon high temperature reactor fuels)
2. Prototype Fast Reactor (PFR) Raffinate (produced during the reprocessing of PFR fuel at Dounreay)
3. Clinoptilolite Ion-Exchange Material (*produced during SIXEP operations*)
4. SrTreat® Ion Exchange Material (Fortum Nuclear Services, multiple sites globally)

The physical form, chemistry, radioisotope inventory and designated disposal volume for these wastes differs significantly. However, the above wastes can all be classified as ILW and are currently destined for immobilisation via cementation. The individual properties of these waste streams means cementation may provide a sub-optimal processing route. The problems associated with cementation technology for radioactive waste immobilisation, in general and with respect to each of these selected waste streams, are discussed further in Chapter 2.1.2.

The studies presented in this thesis were performed using the following common methodology;

1. Characterisation of waste stream/simulant.
2. Processing of waste stream.
3. Characterisation of wasteform properties.

4. Evaluation of wasteform properties and suggestions for further optimisation of processing techniques.

Characterisation of the wasteform properties, where appropriate, includes the compatibility of the waste stream with the process and analysis of the wasteform's phase assemblage, aqueous durability and mechanical properties. It was hoped this work should provide a basis for future investigations into improvements to the baseline operational and disposal options of these waste streams. The potential pit falls of such methodologies have also been discussed and suggestions made as to where future research may best be focused in order to optimise these processes.

Chapter 2 - Literature Review

This chapter will present background information to facilitate the understanding and critical analysis of this PhD Thesis. The chapter is split into four sections which complement the work package. First a brief overview of the cementitious encapsulation of radioactive wastes is provided to allow comparison with the thermal treatments developed in this thesis. As the focus of this thesis primarily concerns vitreous materials the background of glass science and technology is then provided. Hot Isostatic Pressing (HIPing) has been utilised in numerous chapters therefore the technical background and its application to nuclear wastes is briefly reviewed. Finally the properties of the waste streams being investigated are outlined, with reference to work performed previously on their immobilisation. Where deemed appropriate, further discussion of the literature is provided within each results chapter.

2.1 - Existing Technology for ILW immobilisation - Cementation

Hydraulic cements are widely accepted as the reference solution to the immobilisation of ILW in the UK. This situation is a result of the wide range of advantageous properties they offer for the disposal of radioactive wastes, which are listed below [22, 29-35];

- ILW wastes are often liquid and therefore compatible with cementitious systems.
- Cementitious wastes provide their own radiation shielding.
- Tailoring of cement composition can improve properties for a given waste stream.
- Some active elements can be incorporated directly into the cement structure.
- The high pH of cement pastes limits the aqueous solubility of many radionuclides, especially for the transuranic elements.
- The cementation process is relatively simple and can be performed remotely in a shielded environment.
- Cement products are readily available on an industrial scale.
- The high surface area of cement provides many sorption sites which can limit the diffusive transfer of radionuclides.
- Cements generally have a high stability in radiation fields.

2.1.1 - Cement Formulation

Cements used in the nuclear industry are usually based on Portland Cement (PC) [4]. PC is formed as the result of heating clay silicate minerals with lime and then pulverising the products with calcium sulphate (gypsum). This produces a variety of calcium rich mineral phases, primarily $3CaO.SiO_2$, $2CaO.SiO_2$, $3CaO.Al_2O_3$ and $4CaO.Al_2O_3.Fe_2O_3$. These phases react with water, resulting in a slurry which hardens over time, producing a variety of hydrated mineral and amorphous phases. These include ettringite ($3CaO.Al_2O_3.3CaSO_4.32H_2O$), hydrogarnet ($Ca_3Al_2(SiO_4)_{3-x}(OH)_{4x}$), portlandite ($Ca(OH)_2$) and calcium silicate hydrate (CSH) gel. These reactions are progressive and the phase assemblages alter over time.

Radioactive waste immobilisation commonly utilises the addition of pozzolans such as pulverised fly ash (PFA) or blast furnace slag (BFS). Pozzolans are materials which do not undergo cementitious reaction on their own but will react with $Ca(OH)_2$ to form cementitious materials. PFA and BFS are widely available materials, produced as by-products from coal fired power stations and in the manufacture of steel respectively. These pozzolans are utilised primarily to reduce the rate of the exothermic reaction which occurs during PC hydration, lowering the maximum heat generated during processing. Lowering this heat generation decreases the likelihood of detrimental wasteform fracturing occurring [4]. The addition of these pozzolans also improves the microstructure of the cement decreasing the size of pores and improving the diffusive barrier to the release of radionuclides.

2.1.2 - Issues with Cement for the Immobilisation of Radioactive Wastes

As noted in section 1.3 not all waste streams are suitable for immobilisation in cement [24, 36-42]. The key issues precluding the use of cementation are outlined below.

High Concentrations of Soluble Radionuclides

Cement is a poor host phase for a number of radioactive species [33]. Key cationic species to note are the alkali cations $^{135/137}Cs$, ^{87}Rb and ^{40}K. These cations are highly soluble at the alkaline pH levels existing in cementitious pore waters and do not form stable solid structures within the cement assemblages [33, 43]. Small levels of these species are acceptable for disposal in cement matrices, as some weak sorption to the C-S-H phase may hinder rapid release. However, wastes with higher levels of these species should be avoided because of the potentially rapid release through the porous cement structure [34]. Other radionuclides of concern for cementitious immobilisation include the anionic species $^{99}TcO_4^-$ and $^{129}I^-$ [31].

The most frequent radio-chemical barrier precluding the use of cementation is due to high concentrations of ^{137}Cs. This is not only due to the high mobility of ^{137}Cs in cementitious systems, but also because of the high yield of this isotope (~ 6.2 %) produced during the fission of ^{235}U [44]. This means many waste streams from reprocessing or irradiated exotic fuels are not ideally suited to immobilisation within cement.

Heat loading

Cements are unsuitable for wastes with a high thermal output. Dehydration of the cement at elevated temperatures leads to cracking and a degradation of its physical properties [4]. This precludes the use of cements for HLW and wastes with high levels of fission products which will dominate heat output of wastes during the first 75 years [45].

Corrosive Metals and Gas Generation

The UK ILW inventory contains a large volume of reactive metals such as aluminium and uranium. Cementation of these materials is not ideal as in the high pH of the cement pore water they will react. The general process for Al and U reaction is outlined in Equations 2.1 and 2.2 respectively [38, 39].

$$2Al + 6H_2O \rightarrow 2Al(OH)_3 + 3H_2$$ **Equation 2.1**

$$U + 2H_2O \rightarrow UO_2 + 2H_2$$ **Equation 2.2**

These reactions are of concern in the disposal of ILW due to the potential for the generation of flammable gases and the formation of expansive alteration phases. Both of these factors can lead to cracking and a potential loss of the physical integrity of the wasteform. This effect is especially prominent in ILW canisters containing cladding swarf from magnox fuel elements [46].

Pozzolans

Pozzolanic materials can also be detrimental to the production of certain wasteforms. Clinoptilolite, as used at SIXEP, Sellafield (see Section 2.4.3 and Chapter 6 for further details), is a pozzolanic material which is selective for the removal of Cs and Sr from aqueous solutions. However, in the high pH and $Ca(OH)_2$ rich solutions of cements, the zeolitic structure responsible for the sorption of Cs in the clinoptilolite is destroyed and is therefore no longer able to retain its Cs inventory [38, 47]. The Cs is subsequently poorly immobilised

in the cement matrix and thus release rates to aqueous solution are increased, even by comparison with the pre-treated material.

Graphite

Cementitious wasteforms pose a number of problems for graphitic waste streams. Issues include the potential for the release of Wigner energy in un-annealed waste packages. This energy release could increase the temperature and cause dehydration of the cement phase. Other difficulties include the poor wetting characteristics of cement with graphite and the floatation of the graphite during encapsulation, especially prevalent for associated dusts [48, 49]. The key radionuclides in graphitic wastes are ^{3}H, ^{14}C, ^{36}Cl and ^{137}Cs. All of these isotopes are poorly immobilised by cementitious phases.

Economic considerations also cause concern for the cementation of graphitic wastes due to the large volume of graphite requiring disposal and the low levels of graphitic incorporation typical for cementitious wasteforms. These large volumes present a significant economic liability for the final disposal in a GDF facility using cementation encapsulation [50].

Further Problems and Alternatives

Further issues precluding the cementation of radioactive waste streams includes the immobilisation of organic materials, poor waste stream characterisation and the control of fissile material content [24]. To provide the optimum waste disposal safety case these issues necessitate the study of alternative methodologies for the immobilisation of certain waste streams. Heat treatment of materials potentially provides a promising processing route for a number of these waste streams and forms the basis for the work performed in the course of this thesis [50]. The background to the key aspects of glass science are reviewed below.

2.2 - Glass

Shelby defines a glass as “an amorphous solid completely lacking in long range order, periodic atomic structure and exhibiting a region of glass transformation behaviour” [51]. Most common glasses are based on silicate materials, these include vitreous silica, soda-lime silicates, alumino-borosilicates and borosilicates. Although these common silicate glasses are readily formed, in theory a wide range of other materials can be turned into glasses when quenched sufficiently rapidly. Many other classes of glass exist including metallic glasses, halide glasses, chalcogenide glasses and phosphates [51, 52].

As stated in the above description a glass must show a region of glass transformation. This refers to the behaviour of a glass during the transition from the solid to liquid state. During this transition a number of properties show a gradual change in behaviour, unlike the abrupt change of properties which occur in their crystalline analogues [51]. The properties in question include the specific volume, electrical conductivity, heat capacity and enthalpy [53]. Figure 2.1 provides a schematic highlighting this behaviour for specific volume changes with temperature.

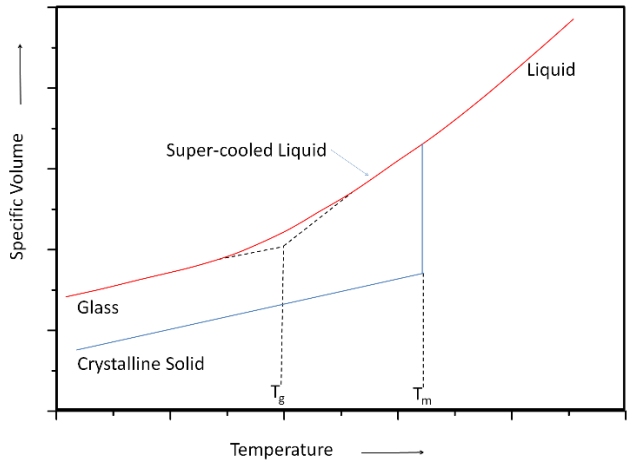

Figure 2.1 – Schematic illustrating the changes to specific volume whilst cooling from a melt with a rate sufficient to result in the formation of either an amorphous or a crystalline solid (Figure adapted from [51])

The abrupt property change seen in crystalline materials is a result of the conversion of the disordered liquid state to that of a periodically ordered crystalline solid. Vitreous materials are formed when the cooling rate is sufficiently fast to prevent structural reorganisation into an ordered crystal occurring. Instead, a super-cooled liquid is formed. In this state the liquid continues to rearrange its atomic structure with decreasing temperature until the viscosity of the liquid becomes too high to allow for significant atomic rearrangements. At this point the structure is frozen into the solid state, resulting in a vitreous solid. This transformation happens over a range of temperatures, but a value is often presented to identify this transformation. This point is known as the glass transition temperature (T_g) and corresponds to a viscosity in the liquid of $10^{11.3}$ Pa s [51].

The immobilisation of radioactive waste in vitreous materials has historically focused on the use of borosilicate based glasses [4]. As the vitreous materials examined during the course

of this thesis are all silicate based, further discussion of the properties and structure of silicate glasses are presented below.

2.2.1 - Glass Structure

Structural Order

To understand the properties of vitreous nuclear wasteforms, it is important to appreciate the structure of vitreous materials. As mentioned above, vitreous materials are defined by their lack of discernible long range structure; however, glasses are not devoid of structure at a more localised scale. Four length scales can be identified at which glasses show different degrees of ordering [54]. The degree of order observed decreases with increased length scales, which ultimately results in the lack of long range periodic ordering which characterises amorphous materials.

Scale I: The basic building blocks of vitreous material are the structural units which form the glass network. These are cationic sites surrounded by anions. In the case of silicate glasses the structural units are silicon atoms, tetrahedrally coordinated to four oxygen atoms. The bond angles and lengths observed at this scale are similar to those observed in their crystalline analogues [55].

Scale II: The manner in which these structural units arrange themselves provides the second level of structural ordering. In silicate glass these silicon tetrahedra take a corner sharing arrangement. As each corner sharing unit allows variation in one bond angle and two torsion angles, a degree of disorder is introduced at this scale, which propagates throughout the system.

Scale III: This relates to how the interconnected structural units arrange themselves into larger structures, such as rings and channels, which may be statistically averaged [56].

Scale IV: Although not characterised by true periodic ordering, phase separations can lead to segregated areas in the glasses on a larger scale, with measurable alterations in both density and composition.

Structural Categories

The structure of a glass depends not only on the basic structural units, but also on any other components which enter the glass structure. Different components play varying roles in the

structure depending on charge, their atomic size and co-ordination number. The roles played by various components can be broadly separated into three categories [51, 57-59]:

***Network Former**:* Network formers create the primary glass structure. These network formers bind with bond angles which deviate from their equilibrium values as described above, thus producing the interconnected network structure. Examples of network forming components include SiO_2, P_2O_5, B_2O_3 and GeO_2.

***Network Modifier**:* Network modifiers break up the primary network creating non-bonding oxygens (NBOs) in the network structure. The network modifiers are ionically bonded to these NBOs compensating their inherent negative charge. Network modifying components include Li_2O, Na_2O, K_2O, Cs_2O, MgO, CaO, SrO, BaO and PbO.

Intermediate: Intermediates are components which can form part of the glass network structure, but which are unfavourable for glass formation on their own. They can behave as either the network former or modifier depending on the circumstances. The classic example is Al_2O_3 in silicate glasses. The negative charge associated with each AlO_4^- tetrahedron, is compensated for by a network modifying cation. However, in the absence of sufficient charge compensation Al can also behave as a network modifier.

Sun proposed that for a glass to form on cooling from the melt, the networking components must have strong bonds with oxygen [60]. The strength of the bonds in turn allows the formation of long chains in the melt, and therefore, hinders restructuring into a crystalline form during cooling. It was proposed that the role a given component has in the formation of a silicate glass is a result of its oxygen bond dissociation energy. When using this theory a component is classified as a network former if it has a bond dissociation energy $\geq$ -335 kJ mol^{-1}, a modifier if it has a bond dissociation energy $\leq$ -250 kJ mol^{-1} and an intermediate if it has a bond energy in-between these two values.

2.2.2 - Structural Models

Most discussion of glass structure is based upon the idea of a random network, as proposed by Zachariasen [55]. This theory sets the rules for the formation of a three-dimensional network of oxides. The basic rules as set out by Zachariasen are given below;

1. The co-ordination number of each cation with oxygen should be small (< 5).
2. Oxygen atoms should never be bound to more than two cations.
3. Each cationic polyhedron should share a minimum of three corners in order to produce a three-dimensional network.

4. Cationic polyhedra should only ever link by sharing corners.

Zachariasen also stipulates that in order to form an amorphous structure some deformation from equilibrium conditions must occur. This deformation of the network, as created by alterations in network bond angles, is necessary to maintain short range order and eliminate long range periodicity.

Zachariasen's theory was supported by Warren's work on the X-ray diffraction (XRD) of glasses. This work attributed the peak broadening seen in vitreous XRD patterns to random network connections of structural units, as shown in Figure 2.2 a) [59]. The network model was further developed by Greaves in X-ray Absorption Spectroscopy (XAS) studies, identifying the location of modifier cations in the structure. He proposed the modified random network model, as illustrated in Figure 2.2 b) [55-57]. In this model the NBOs form channels between islands of network structure. The NBO channels are charge compensated by the modifier ions in the glass structure.

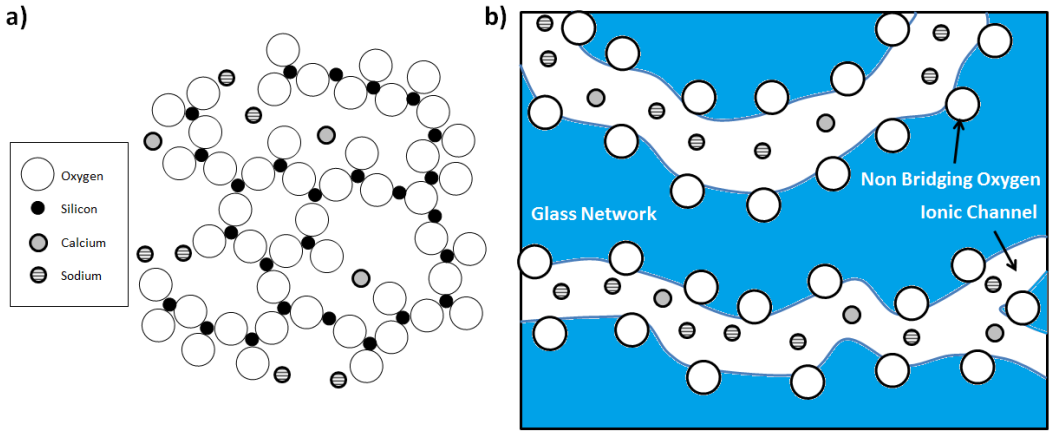

Figure 2.2 - a) Schematic of the silicate glass network structure represented in 2D, showing the structural units with disordered bonding, non-bonding oxygen atoms and network modifiers and b) a schematic of the channels which form in the network structure to accommodate network modifiers associated with non-bonding oxygen atoms.

Several of the glasses used in this study contain the components Al_2O_3 and B_2O_3, as such a brief description of their role in the glass structure is provided below.

The Structural Role of B_2O_3 and the Boron Anomaly

The addition of B_2O_3 to silicate melts has a pronounced effect on the properties of the glass formed and results in a phase separation within the final vitreous product. As a result, what appears to be a homogeneous glass, is in reality two compositionally distinct glasses phase

separated at the nanometre scale. The first of these glasses can be considered to be silica rich and the second similar to an alkali-borate glass [61]. This small scale separation and the ability for the boron to exist in different coordination states leads to what has been termed "the boron anomaly" [62].

The boron anomaly relates to the trend in T_g and thermal expansion coefficients (TEC) with increasing modifier content for borosilicate glass compositions [63, 64]. In silicate glasses, the addition of modifier cations promotes the presence of NBOs in the structure. As a result of this disruption in the structure, T_g decreases and the TEC increases. In boron containing glasses, additions of modifier components at first increase the T_g and decrease the TEC, with maximum effect observed at approximately 16 mol% modifier addition [64]. With further increases in modifier concentrations T_g is then lowered and TEC rises.

This is attributed to the two coordination states in which boron can reside in its vitreous form [65]. The first is as trigonal planar BO_3 units, which preferentially form boroxyl rings. The second form of coordination state is as BO_4^- tetrahedral units. The presence these tetrahedral structures results from the addition of modifier cations to the glass structure, which in turn increases the connectivity of the network units. However, further increases in the modifier content will eventually result in the formation of excess of NBOs as described previously for silicate glasses. At this point the T_g and TEC will start to decrease accordingly.

The Structural Role of Al_2O_3

Silicate melts containing additions of Al_2O_3 form $[AlO_4]^-$ tetrahedral units by utilising what would otherwise exist as a non-bridging oxygen [66]. This is shown schematically in Figure 2.3 b).

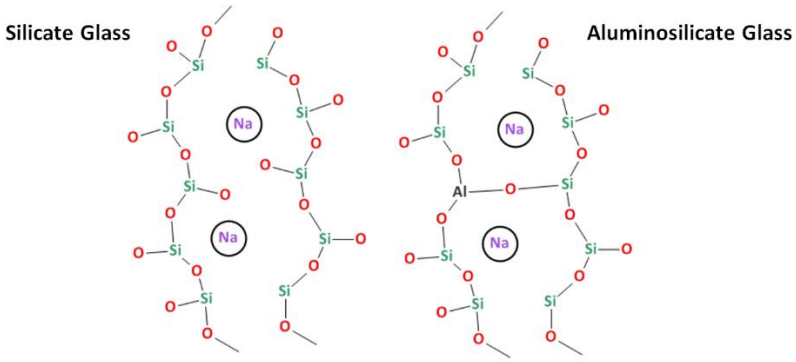

Figure 2.3 – Schematic of the coordination states of Al in the network structure of silicate melts (Figure adapted from [67]).

As is the case for borate units, the negative charge associated with this structural unit is charge compensated by a modifier cation. The addition of alumina to silicate glasses in the presence of suitable modifiers increases glass structural connectivity in two ways. First is by acting as a network former, consuming NBO sites and second by closing the ionic channels in the glass, binding modifier ions more into a localised area.

2.2.3 - Aqueous Dissolution of Silicate Glasses

The original Encyclopaedia Britannica description of glass made in 1786, which remains unchanged to this day, states that '[glass is a material] impervious to the natural elements' [68, 69]. However, it is well documented that this is not the case and that the dissolution of silicate glasses has been under investigation from as early as 1666 [70]. The need to understand the dissolution behaviour of glass in water is important in a number of applications such as optical fibre failure, bio-medical glass production, preserving ancient glasses and in medical vial production [71].

However, for the last 60 years the driving force behind the investigation of the glass dissolution mechanisms has been the necessity to underpin the safety case for the disposal case for vitreous radioactive HLW. Modern glass compositions used in the nuclear industry have an excellent durability in aqueous solution [72]. This was fundamental to the selection of vitrification as the reference disposal methodology for processing HLW in countries such as the UK, Russia, Germany, Japan and France. The most effective way a wasteform can provide protection against environmental release is to be inert under disposal conditions. As such, an effective knowledge of the aqueous corrosion mechanism is key to understanding the risks involved in waste disposal.

A wide array of literature is available on the topic of glass dissolution and a number of reviews on the subject have been carried out over the last century [71, 73-82]. These reviews not only provide the reader with a greater depth of understanding regarding the dissolution of glass than will be provided here, but also detail how the understanding and methodologies used in these studies have developed during this time period. The movement away from simple 'hazing' experiments to the more advanced modern experiments, involving analysis of both the solution and the glass sample, are highlighted in these reviews, which provide the basis for understanding the mechanism of dissolution [83-86]. The short review provided below will set out the basic corrosion mechanisms, define the molecular scale reactions

deemed responsible for the temporal dependence of the dissolution rate regime and highlight the variables known to have the greatest influence on the corrosion of glasses.

Mechanisms of Aqueous Dissolution

There are two mechanisms which are commonly identified to be the cause of silicate glass dissolution. These are the inter-diffusion of ions between the glass and solution (ion exchange) and hydrolysis of network forming units, resulting in the breakdown of the glass structure [87, 88].

Ion Exchange: This is the dominant process during the initial stages of aqueous corrosion. As described earlier, network modifiers are ionically bound to NBOs within the glass structure. This mechanism alters the glass structure by exchanging these modifier ions for a proton or hydronium ion according to Equation 2.3. This results in the release of alkali to solution and the formation of silanol groups in the glass structure.

$$\equiv Si\text{-}O^- M^+_{(s)} + H^+_{(aq)} \rightarrow \equiv Si\text{-}OH + M^+_{(aq)} \qquad \textbf{Equation 2.3}$$

There is an ongoing debate, based upon discrepancies in the hydrogen ratio measured within the leached layers, whether this mechanism is based on a direct proton exchange or hydronium ion exchange [89-94]. Regardless, this exchange reaction results in the outer glass surface becoming depleted in alkali and alkali-earth cations and enriched with respect to H^+/H_3O^+. This exchange and the ingress of water into the glass structure increases the pH in the surrounding solution, by release of alkali and alkali-earth cations. As the ion exchange mechanism proceeds via diffusion it has a rate dependant on the square root of time, as shown in Equation 2.4 [80].

$$C_i = \sqrt[2]{\frac{Dt}{\pi}\ \rho\chi_0 \frac{SA}{V}} \qquad \textbf{Equation 2.4}$$

Where C_i is the amount of alkali released to solution (g m^{-3}), D is the diffusion coefficient ($m^2\ s^{-1}$), t is time (s), ρ is the glass density (g m^{-3}), χ_0 is the initial mass fraction of alkali in the glass (g g^{-1}), SA is glass surface area (m^2) and V is volume of leachate (m^3).

Hydrolysis of Glass Network: This involves the direct reaction of the silicate glass network with water. Two mechanisms for this hydration are possible. The first is for nucleophilic

attack on water from one of the glass network's NBOs, resulting in the dissociation of a water molecule to a silanol group and an OH^- anion, this is shown in Equation 2.5. The second is for an OH^- anion to attack a siloxane bond forming a silanol bond and a NBO in the glass structure, as shown in Equation 2.6 [78, 82].

$$\equiv Si\text{-}O^-_{(s)} + H_2O_{(aq)} \rightarrow \equiv Si\text{-}OH_{(S)} + OH^-_{(aq)} \quad \textbf{Equation 2.5}$$

$$\equiv Si\text{-}O\text{-}Si\equiv_{(S)} + OH^- \rightarrow \equiv Si\text{-}OH_{(S)} + \equiv Si\text{-}O^-_{(s)} \quad \textbf{Equation 2.6}$$

Both of these mechanisms provide positive feedback to the system, creating new nucleophiles which can continue the reaction. This mechanism is what leads to the formation of the amorphous silica and water rich alteration layer on the surface of the glass, which will be described later in this chapter.

There is also the potential for the condensation of these silanol groups to reform siloxane bonds, resulting in the reordering of the altered structure forming an amorphous gel layer as described in Equation 2.7.

$$2 \equiv Si\text{-}OH_{(s)} \rightarrow \equiv Si\text{-}O\text{-}Si\equiv_{(s)} + H_2O_{(aq)} \quad \textbf{Equation 2.7}$$

The final stage of hydrolysis involves the removal of silicon from the glass to solution. This proceeds according to the mechanism shown in Equation 2.8, by the culmination of four hydrolysis reactions around a silica tetrahedron, resulting in the release of a silicic acid molecule.

$$=Si=_{(s)} + 2\ H_2O_{(aq)} \rightarrow H_4SiO_{4\,(aq)} \quad \textbf{Equation 2.8}$$

The rate of this reaction can be expressed empirically through Equation 2.9 as described by Aagard and Helgeson's law and transition state theory [78, 95].

$$r_{0(T,pH)} = k_0 v_i e^{\frac{-E_a}{RT}} a_{H^+}^{\eta} \left[1 - \left(\frac{Q}{K}\right)^{\sigma}\right] \quad \textbf{Equation 2.9}$$

Where $r_{0(T, pH)}$ is the rate at a set temperature and pH, k_0 is the intrinsic rate constant, v_i is the intrinsic rate constatnt, E_a is the activation energy, R is the gas constant, T is the temperature, a_{H+} is the hydronium ion activity, η is the reactive order with respect to a_{H+}, Q is the activity product of the rate limiting reaction, K is the equilibrium constant and σ is the overall reaction order. Equation 2.9 highlights the factors which determine the forward dissolution rate of a given glass, as will be discussed below; mainly pH, composition (from E_a) and temperature.

Stages of Glass Dissolution

The current understanding of silicate glass dissolution comes from a culmination of 60 years of research, primarily investigating the dissolution of borosilicate glass formulations from both the US and France. This understanding is based, amongst other things, on the rate changes for glass components entering solution observed during static solution experiments. These conditions are likely to be indicative of disposal conditions in a GDF.

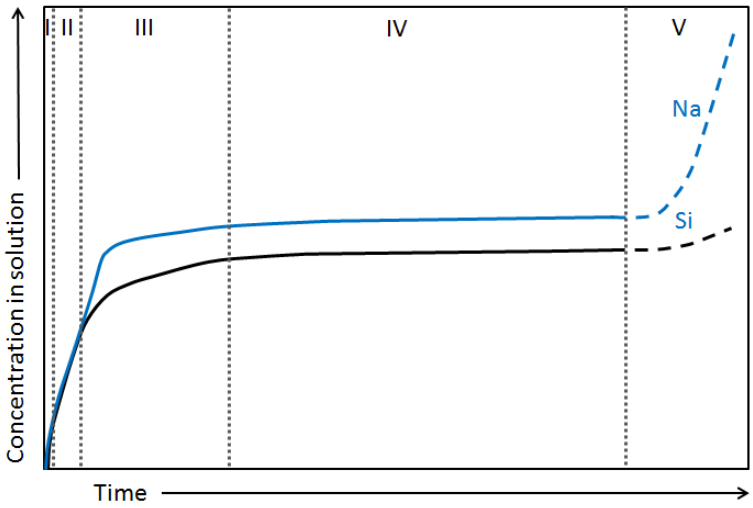

Figure 2.4 - Stages of aqueous dissolution during static testing of glass (figure adapted from [80]).

When a glass is altered in static aqueous solutions up to five rate regimes can be identified as illustrated in Figure 2.4. The processes responsible for each of these stages (I-V) are summarised below [80].

I - Initial Ion Exchange: The first stage of dissolution shows a rapid release of mobile alkali ions into solution. This is a behaviour common to a number of mineral phases, especially in

acidic media [96]. This high initial rate of alkali release, corresponds to the diffusive nature of the ion exchange mechanism and its rate dependence on the inverse square of time.

It has recently been shown that not only does this initial diffusion mechanism apply to network modifying alkalis but also similarly affects the boron in the glass structure [97]. This is hypothesised to result from the structural rearrangement of tetrahedrally coordinated boron atoms after the removal of alkali modifiers. It is suggested that once the alkali is removed, the proton containing replacement is unable to effectively charge compensate the tetrahedral boron arrangement, and thus, these boron atoms are subsequently released into solution. As time progresses this rate decreases rapidly and the rate limiting step becomes dependent upon the hydrolysis of the glass network.

II – Forward Rate: The second stage of glass dissolution shows a congruent, steady release rate of glass elements. This stage is dominated by the hydration of the glass network, described by Equations 2.5 and 2.6, through the nucleophilic attack on structural unit bridging bonds (Si-O-Si, Si-O-Al, Si-O-B). This process produces silicic acid as the final product and determines the forward rate of reaction. The forward rate may be obtained using dynamic solution experimental conditions where no contribution from solution saturation or the passivating effects of a leached layer (discussed below) comes into effect. This forward rate of reaction can be expressed using Equation 2.9.

III - Rate Drop: The drop observed in the rate of dissolution for silicate glasses has been a source of contention until the recent GLAMOR project. Two opposing schools debated the reasoning behind the drop in the rate of dissolution which occurs when silicon levels in solution reach approximately 1 ppm at 90 °C [80].

Aagard and Helgeson's law and transition state theory describe the first effect based on the chemical affinity of a solution [78, 95]. In its simplest terms, this theory states that the dissolution rate will drop as silica concentration in solution increases. This is a result of the solution affinity decreasing for the reaction limiting step; in this case the hydration of silanol groups to produce H_4SiO_4. The rate drop in this model is therefore assumed to be a result of approaching silica saturation in solution.

The second explanation was based around the idea that the dense gel layer, which forms as a result of silanol condensation at solution 'saturation' levels, provides a protective barrier. It is suggested that this gel layer provides a kinetic barrier to the diffusion of reactive species into the glass network [98]. The gel layer has been suggested to form two distinct layers over time [99]. The first to form is a porous gel layer on top of the alkali-depleted diffusion layer.

This forms as a homogeneous, porous gel, which eventually develops a concentration gradient with increasing gel thickness. Due to the higher concentration of dissolved species near the glass surface, a denser protective gel layer forms at the interface of the diffusion zone. The final result of these processes are shown schematically in Figure 2.5. An alternative mechanism for gel formation has been offered by Geisler et al who propose a dissolution-reprecipitation mechanism at the glass/solution boundary. This is proposed to occur as colloidal precipitates aggregate to form the amorphous gel layer [85].

It is now accepted that the rate drop is likely to be a result of a combination of both the increase of silica levels in solution and the alteration layer formation, as shown from detailed studies of solution saturation effects, modelling and study of the gel layer properties [80, 84, 85, 100-102]. Once the dense gel layer has formed and 'quasi equilibrium' in the solution is reached the reaction proceeds according to regime IV.

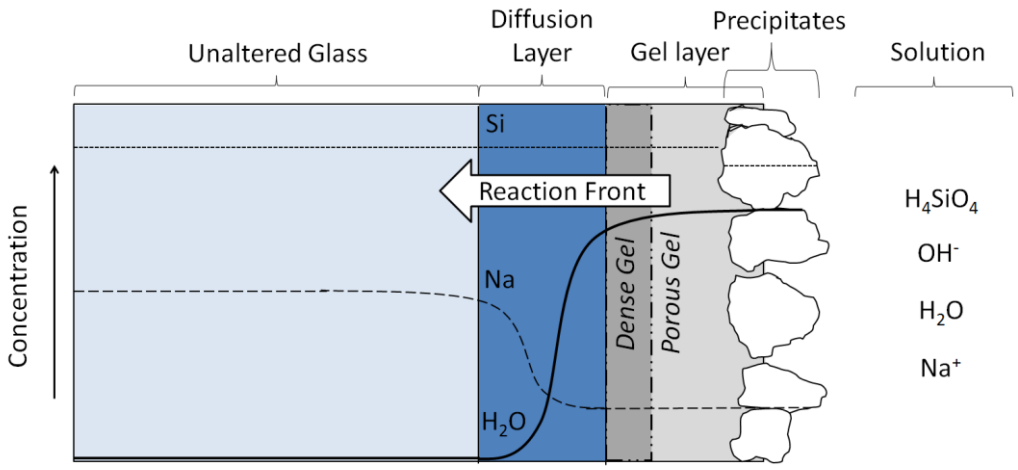

Figure 2.5 - Schematic of the alteration products which form on the surface of silicate glasses during aqueous dissolution, with concentration gradients of key species (illustration adapted from [99])

IV- Residual Rate Regime: During this stage of alteration in closed systems the glass maintains a low rate of dissolution. The glass will continue to be leached into solution despite the 'quasi-equilibrium' solution conditions encountered and the formation of the dense protective gel layer. This is because glass is inherently, thermodynamically unstable by comparison to a collection of crystalline alteration products. As such it can be expected that glass will continue to undergo some form of reaction in perpetuity [78].

V - Resumption of alteration: This stage is not seen in all compositions of glass or under all test scenarios. This resumption is proposed to occur due to a precipitation of crystalline

phases which break up the passivating gel layer. As a result, the concentration of dissolved species in the surrounding solution is reduced, the affinity for reaction is increased and the diffusive barrier is destroyed. This is usually due to a precipitation of zeolites at a given pH or solution concentration level. There is the possibility of eventually returning to stable conditions where a steady residual state and dense gel layer are reformed, as such cycling between regime IV and regime V would occur [80, 103].

Variables Affecting the Aqueous Dissolution Behaviour of Glasses

The dissolution behaviour of glass in aqueous solution depends on a wide range of factors. A number of these factors and their effects on dissolution are summarised below. The terms in Equation 2.9 highlight the importance of composition (E_a), pH and temperature for the aqueous dissolution of glasses which will be discussed below.

***Chemical Composition**:* While the glasses used in the nuclear industry have been developed to be resistant to aqueous dissolution, this is not true for all glasses. Sodium silicate glasses for example will dissolve readily in aqueous solution. The composition of a glass is extremely important in determining the dissolution rate of the material. Various ideas have been utilised to explain how composition affects aqueous durability.

The thermodynamic approach to dissolution of glasses is based on the ΔG_{hyd} of glass components to their fully hydrated equivalent [104, 105]. This approach attempts to qualify which glass constituents have a positive effect on aqueous durability and which will be deleterious. It does this by comparing the free energy of hydration of their individual crystalline counterparts [79]. The summation of the components in a glass is weighted to provide a free energy of hydration for the entire glass. A good correlation has been found for a wide range of glass compositions between the free energy of hydration with experimental results for normalised elemental mass of silica, providing evidence supporting this approach. It can therefore be considered a useful guide to which components will increase or decrease the aqueous durability of a glass. However, the effects of compositional change are not truly additive, therefore, a thermodynamic approach can only provide an estimate of glass stability in solution.

***Effect of Modifier Cation Ratios**:* While sodium silicate glasses are readily soluble, soda-lime-silicate glasses form the basis for most modern glass production due to their superior performance in aqueous solutions [106]. The diffusion coefficients are lowered in glasses with more than one type of modifier, compared to a glass containing an individual modifier in the same molar proportions [107]. The effect is usually attributed to the blockage of ionic

diffusion channels in the glass structure, created by the need to accommodate cations of varying charge density. Equi-molar concentrations of numerous modifier cations tends to have a positive effect on aqueous durability and are favoured in the formulations of glasses for HLW immobilisation.

Precipitating Phases: Glass composition can also play a leading factor in the initiation of large scale crystalline precipitation. This can be detrimental to aqueous durability due to the breakdown of the dense passivating gel layer. This has been shown to occur in glasses containing high proportions of Al and Zr. Due to the high free energies of hydration for these components, they are often favoured in compositions due to the improved durability seen in the short term [86]. However, due to the low solubility of these elements in solution they are more liable to precipitate en-masse resulting in a stage V re-initiation of corrosion.

pH: The pH of aqueous solutions has a pronounced effect on the dissolution of glasses [82, 108]. It affects the dominant mechanism of corrosion as well as the rate. Between pH 5 - 9 silicate glasses typically show a rapid decrease in their rate of corrosion, when compared to more acidic or alkaline conditions, as shown in Figure 2.6 a). At low pHs the role of ion exchange within solution is dominant and a high rate of corrosion is observed.

At high pH values the dominant mechanism is hydrolysis. The effects are shown in Figure 2.6 b), where the equilibrium pH of SON68 glass has been shown to have a minimal dissolution rate between pH 9.5-10, this is suggested to relate to the formation of a more stable dense gel layer at the equilibrium pH of the glass [86].

Temperature: Higher temperatures provide the activation energy required for the dissolution mechanism to proceed. As such, an increased dissolution rate is seen at higher temperatures. This is useful for accelerating leaching experiments but consideration of potential changes in the mechanism of dissolution are required, especially when testing above 100 °C [78].

Surface Area to Volume Ratio (SA/V): The surface area to volume ratio affects the dissolution of silicate glasses significantly [109]. Higher SA/V ratios result in earlier formation of the passivating gel layer, pH equilibrium conditions and solution saturation. As such the alteration mechanism is accelerated to stage IV behaviour more rapidly with higher SA/V ratios. Therefore, methods for accelerated testing of glass durability, such as in the PCT method utilise a high SA/V ratio [110]. However lower SA/V ratios allow for a more in-depth study of the initial diffusion rate and the rate of hydrolysis in stage II. Agglomeration of powders are however known to cause issues in high SA/V test conditions.

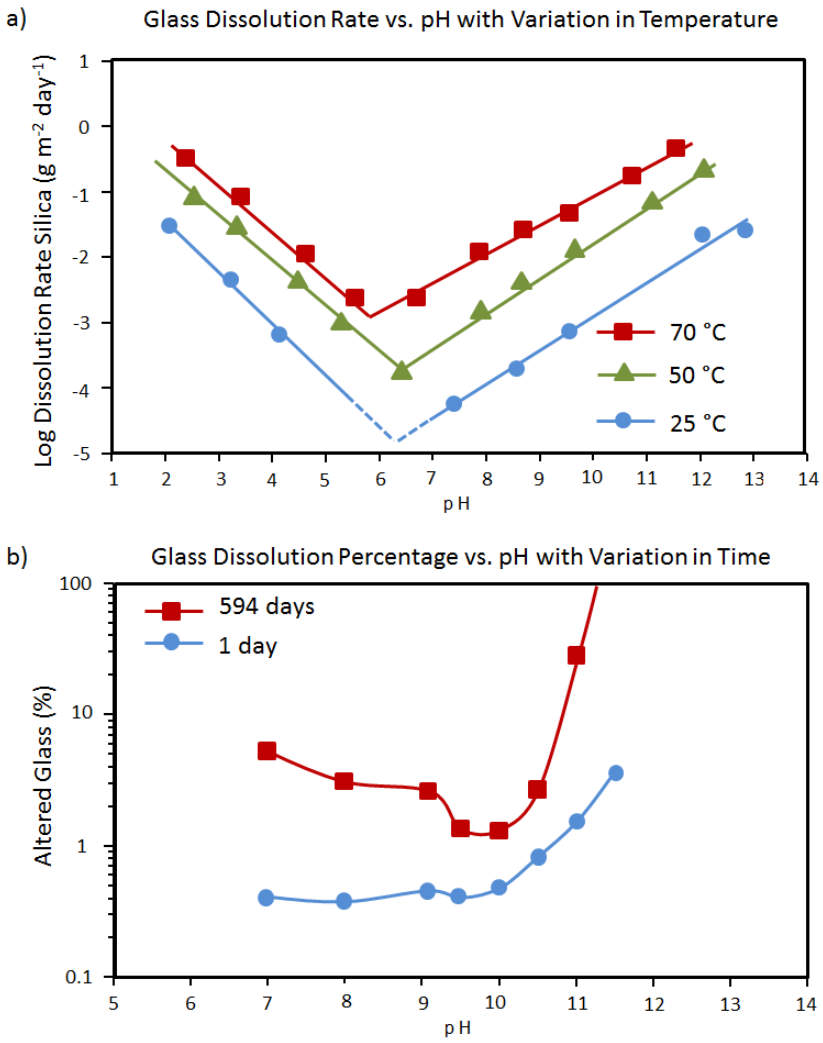

Figure 2.6 – Plots illustrating a) the dissolution rate dependence of borosilicate glass on temperature and pH (Figure adapted from [108]) and b) the dependence of degree of borosilicate glass dissolution on pH over time (Figure adapted from [86]).

2.3 - Hot Isostatic Pressing

HIPing is a methodology where elevated temperatures and isostatic pressures are applied simultaneously to achieve densification and remove of porosity from materials [111]. The process was developed as a nuclear technology by the Battelle Institute in the 1950s for the diffusion bonding of nuclear submarine fuels. This process is widely used on an industrial scale to process high value work pieces, such as turbine blades and biomedical implants [112, 113].

A HIP is essentially a furnace contained within a pressure vessel. Pressure is applied to work pieces at elevated temperatures using an inert gas, most commonly argon, as the pressurising medium [114]. HIPs are used in numerous applications such as in the cladding of materials, work piece rejuvenation and in the consolidation and densification of powders. However, the most common practice is in the homogenisation and pore removal of castings.

HIPs are capable of operating within a wide processing window; units can produce pressures up to 300 MPa and with maximum temperatures ranging from 1450 °C (molybdenum furnace elements) to 2200 °C (graphite furnace elements). The temperatures and pressures used during materials processing are dependent on the material being HIPed. The temperature used is usually somewhere between 70 % and 85 % of its melting temperature [111]. The high pressures essential for HIPing are achieved during processing by two methods: firstly via the mechanical compression of the processing gas; and secondly by the heating and expansion of this gas within a fixed volume [6].

2.3.1 - Densification via HIPing

To HIP a work piece, a non-porous surface is required in order to apply the pressure. To appreciate the reason for this behaviour some knowledge of sintering theory is required. Sintering occurs when the heating of a body results in the closure of porosity [115]. The lowering of the total Gibbs free energy (ΔG) upon pore removal is the driving force for sintering [116].

ΔG varies between the bulk material, grain boundaries and surfaces. Surface sites such as pores have a greater value of ΔG than that found in the bulk material or at grain boundaries. Therefore, when the temperature of a material is sufficient to promote significant solid state diffusion or viscous flow, the system will aim to reduce its ΔG by eliminating these surface sites. The process starts by forming grain boundaries and necks between particles which is followed by the rounding of pores [117]. Sintering continues to cause pore shrinkage and the eliminated gases diffuse along the grain boundaries to areas of lower pressure, such as the body's surface or into larger pores. Finally, interconnected porosity is eliminated at approximately 95 % of theoretical density and the remaining residual porosity is eliminated at a slower rate [118].

Application of pressure to the body improves densification by bringing particles into closer proximity, as such, promoting the formation of grain boundaries by providing an opposing force to the internal pressure of the porosity. The primary driving force for pore retention is

the internal pressure of this porosity, which acts to oppose sintering action by forcing grain boundaries apart. Equation 2.10 shows the relationship between external pressure (P_e) and the total pressure for densification (P_T) where P_T may be considered the driving force behind sintering [117];

$$P_T = P_e + \frac{2\gamma}{r_p} - P_i \qquad \textbf{Equation 2.10}$$

where γ is the specific energy of the internal surface of the pore (J m^{-2}), r_p is the pore radius and P_i is the internal porosity of the pore.

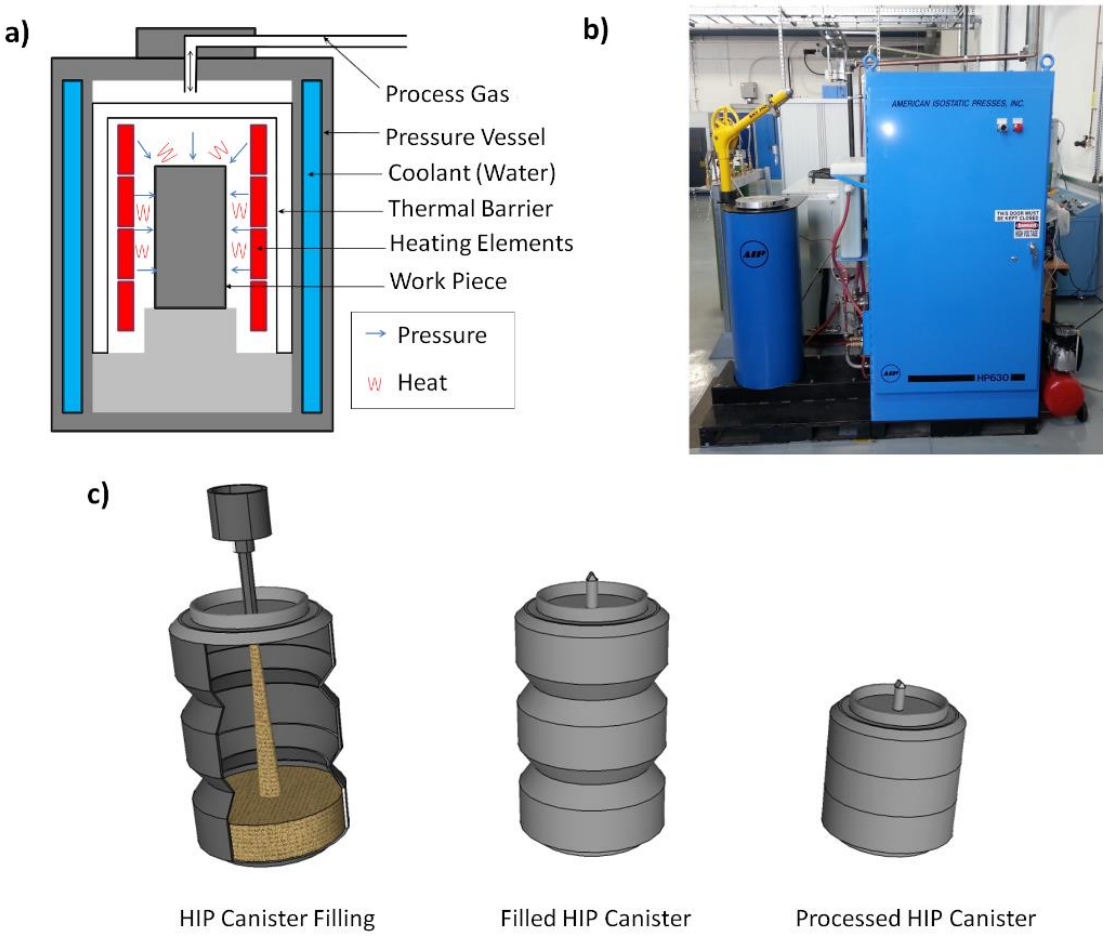

Figure 2.7 – a) Schematic of HIP pressure vessel during operation, b) a photograph of the University of Sheffield's AIP-630H research scale HIP and c) Schematic of canisters and associated collapse likely to be deployed for radioactive waste immobilisation.

This process provides the ability to produce a desired densification and microstructure by sintering in shorter time frames and using lower temperatures than are attainable in the absence of pressure.

Consideration of Equation 2.10 and Figure 2.8 explain why it is necessary to have a non-porous surface to effectively utilise the HIPing process [111, 113, 117]. HIPing utilises gas as the pressurising medium, this means that any porosity open to the processing gas will become highly pressurised. This eliminates the benefit of applying pressure as $P_e = P_i$. This is especially important for samples with interconnected porosity as once these pores have become isolated and start to shrink via conventional sintering their P_i will become greater than P_e. This means P_T is then lower under these circumstances than would otherwise have been observed in a similar, yet unpressurised regime.

The methodology is however extremely effective for removing sealed porosity formed at lower pressures, such as that found in castings. In this scenario P_e is now far greater than P_i. As such P_i can now be considered negligible and so P_T is greatly increased. Figure 2.8 provides a schematic illustration of the HIP process's ability to remove both external and internal porosity.

As mentioned above, a common use of HIPing is in the densification of powders. This and the densification of surface porosity can be achieved by reaction bonding, or, more commonly, by encapsulation of the powder in a deformable canister made of either metal or glass [111-113]. To minimise the potential for the retention of pressurised pores, these canisters are densely packed with powder before being sealed under vacuum prior to HIPing. A detailed description of the canning procedure as utilised in this study can be found in Section 3.3. The canister provides a non-porous surface on which the gas medium can apply pressure to the encapsulated materials.

The industrial benefits of HIPing over hot uniaxial pressing are numerous, including: the applicability to process variable shapes, increased uniformity of densification, isotropic microstructure formation, the ability for near net shape formation and densification, increased throughput, and no requirement for expensive die maintenance.

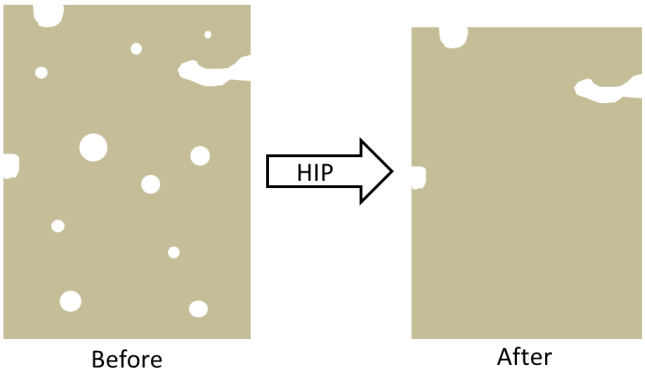

Figure 2.8 – Schematic illustrating the behaviour of both internal and surface connected porosity during HIPing. The internal porosity will be removed whereas any external pressure will be retained.

2.3.2 - HIPing for Radioactive Waste Immobilisation

There are several attributes of HIP technology which make it extremely attractive to the production of radioactive wasteforms [1, 119, 120]. Waste processing using a HIP process would operate on a batch process where the waste is pre-sealed and self-contained prior to processing. The radioactive waste therefore would not come into direct contact with the processing unit at any time. This has four key benefits;

1. A single plant could be used to process numerous types of waste as the interaction between the waste and the HIP rig do not need to be considered. As such, an active HIP facility could be used to process materials as diverse as glasses, cements, glass-ceramics, composite materials, ceramics and metals.
2. The waste is hermetically sealed during processing and therefore it is unlikely to result in any contamination of the rig. This minimises the production of secondary processing wastes, which are common in conventional vitrification processes e.g. corroded melters.
3. The batch process allows flexibility to readily optimise parameters such as waste loading, particle sizing and temperature for each run, providing flexible working condition within a single plant.
4. The batch methodology allows accountability for all materials being processed at any time; this is especially important when processing sensitive materials such as plutonium containing wastes.

Radioactive waste HIP canisters are likely to be produced from corrosion resistant stainless steels, as are currently utilised for waste storage canisters. This means, once processed,

HIPed canisters are suitably packaged for direct GDF disposal, although an additional overpack will likely be required for regulatory and transport purposes.

The dimensions of the work pieces alters significantly upon processing in a HIP, depending on several factors, such as initial can geometry and the compaction behaviour of material on sintering. Therefore, one potential issue is the packaging efficiency of HIPed waste materials once processed. However, canister designs are available which compact predictably to produce roughly cylindrical packages after HIPing. This provides an improved efficiency in the use of a GDF's limited storage capacity [119]. Further waste volume efficiency is found in the ability to process wastes at up to 100 % waste loadings using HIP technology, a threshold difficult to attain with almost any other waste processing technique. This is fundamental for the economics and real world application of this technology; as not only does it eliminate the need to purchase chemical additives, but also because the final waste disposal volume has been shown to have the greatest impact on the economics of GDF waste disposal [1, 19].

For the reasons laid out above, significant literature exists on the formation of radioactive wasteforms utilising HIPing and various reviews are available on the subject [119-121]. The development of HIPing as a methodology for radioactive waste immobilisation was most notably applied in the development of Synroc, a mixed ceramic material capable of immobilising HLW waste into solid solution of various titanate based phases [122]. A detailed review on Synroc development can be found in [123]. HIPing has also been used to successfully process plutonium wastes and residues into a glass ceramic, mixed magnox sludge-zeolite wastes and HLW at up to 50 wt % waste loading within a borosilicate glass [28, 120, 124]. Active HIPing facilities are currently under development or consideration for processing of wastes formed during the extraction of ^{99}Mo at ANSTO (Australia), plutonium residues from Sellafield (UK) and HLW calcines from reprocessing activities in Idaho (USA) [28, 119, 125, 126].

2.4 - Background on Waste Streams Investigated

2.4.1 - Tri-Structural Isotopic Fuel (TRISO) Particles

Some of the most promising next generation nuclear reactor concepts (Generation IV) are known as the High Temperature Reactors (HTRs), such as the 'pebble bed' modular reactor and the U.S. next generation nuclear plant [127]. The advantages of these systems include

passive safety mechanisms, the production of direct process heat for industrial applications, online refuelling, and an increase in thermodynamic efficiency.

The use of multi-layered spherical TRISO particles in HTR reactor fuel arrays is a key feature in the case for commercial use of HTRs and a fundamental part of the reactor design [128]. Bi-Structural Isotopic (BISO) and TRISO fuel particles have previously been irradiated in test reactors in the UK (Dragon Reactor), Germany (AVR Reactor) and China (HTR-10 Reactor) [129-132]. TRISO particles are engineered to be mechanically robust, corrosion resistant, dimensionally stable at high temperatures and have the ability to retain most fission products, not only under normal operating conditions, but also under envisioned accident scenarios [133].

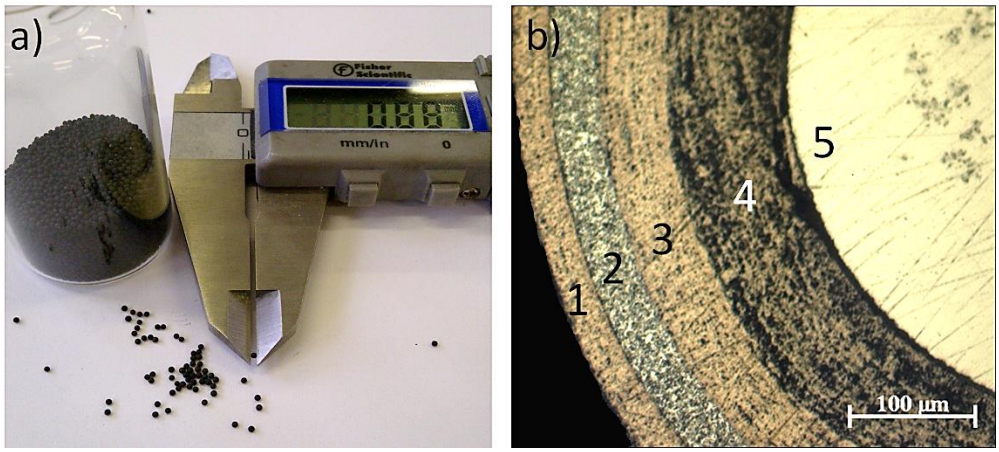

Figure 2.9 - a) Photograph of simulant TRISO particles used during the course of this investigation (callipers read 0.88 mm) and b) optical micrograph showing the layered structure of a sectioned TRISO particle where the numbers relate to the following isotropic layers 1) OPyC 2) SiC, 3) IPyC 4) BC and 5) UO_2 (illustration shows ZrO_2 simulant core).

A TRISO particle commonly consists of a spherical central core of UO_2 fuel, coated with four functional layers, as shown in Figure 2.9. Moving inward to the central fuel core, these protective layers are composed of: 1) an 'outer' pyrolytic carbon layer (OPyC); 2) a layer of silicon carbide (SiC); 3) an 'inner' pyrolytic carbon layer (IPyC); 4) a final layer of 'buffer' carbon (BC); and 5) the fissile fuel core (UO_2, $(U,Pu)O_2$). These layers work in concert to produce the favourable characteristics described above for HTR reactors [134]. TRISO particles have been mass produced to a high standard with a low failure rate, typically < 0.003% [135]. The combination of these factors makes TRISO particles a feasible option for use in a commercial reactor. TRISO particles are generally planned to be deployed in one of two forms, either as spherical graphite pebbles containing approximately 10,000 - 40,000

particles or in a more traditional fuel array, consisting of graphite fuel rods impregnated with TRISO particles [128].

It has been suggested that graphitic TRISO particle fuel arrays could be suitable for direct disposal in a GDF [136]. However, radiolysis of surrounding ground water has been shown to have a pronounced deleterious effect on the aqueous durability of graphite [137]. The interconnected porosity within the fuel arrays and the potential release of the radioactive ^{14}C, $^{137/135}Cs$ and fission product Ag content through this route brings the suitability of direct disposal pathway into question.

It has been noted that segregation of the spent fuel component (i.e. individual TRISO particles) from the fuel array would significantly reduce the volume of the HLW to be disposed of from any future HTR operations [137]. Even with the highest envisaged loading of TRISO particles per fuel array, the separation of these components would provide a 60% reduction in the volume of HLW produced (calculated from data in [138]). As previously noted, the volume of waste is the major contributor to the final cost of a GDF, therefore minimisation of HLW volume would be of considerable benefit in terms of cost reduction [1, 19]. With these two issues in mind, the development of a disposal strategy which minimises the volume of HLW for disposal while imposing an engineered barrier to radionuclide release, would be beneficial for any future deployment of TRISO particle-fuel.

Such a disposal strategy may also provide a disposal route for the existing stockpiles of irradiated BISO and TRISO particles. This stockpile is estimated at over 52 tons heavy metal equivalent worldwide [139]. These wastes are mostly classified as ILW due to the low burn up of the fuel during experimental trials. The problems associated with disposal of irradiated graphite as ILW, noted in section 2.1.2, mean that a disposal technology for TRISO fuel particles could also prove advantageous for a variety of other problematic graphitic waste streams. These include graphite fragments produced during the dismantling of graphite moderated reactor cores, irradiated graphitic dusts and highly contaminated advanced gas cooled reactor (AGR) sleeves.

Previous immobilisation methods have focused on the encapsulation of TRISO particles into a durable matrix. Encapsulated wasteforms are not usually considered ideal for HLW. This is due to the fact that degradation of the host matrix will lead to the direct contact of the waste with the environment, promoting incongruent release of radionuclides [1]. However, the OPyC coating of TRISO particles has a high aqueous durability and is expected to remain uncontaminated by fission product species during normal HTR operations. This makes

radionuclide release from encapsulated TRISO particles less of a concern than for comparable uncoated HLW waste streams.

Borosilicate glasses have been the focus of previous work on the encapsulation of TRISO particles [140]. The deleterious interaction of TRISO particles with a glass melt at high temperature were reported. Mixing TRISO particles directly with a glass melt resulted in low waste loadings, poor wetting of the glass to the fuel, and oxidation of the OPyC layer, whilst also producing large pores in the vitreous matrix. This oxidation of the OPyC results in the exposure of the SiC layer; this layer plays host to the highly radioactive fission products species. However, the same work also showed encapsulating TRISO particle in sintered glass composites provided a more successful encapsulation, as evidenced by the structural integrity, improved contacting properties, low porosity and lack of oxidative reaction in the OPyC layer.

Some promise has been shown in studies utilising reaction bonded silicon carbide ceramics to act as TRISO particle encapsulants [141]. However, the simulated wasteform was relatively porous and the stability of the SiC ceramic phase as a whole depends on the passivation provided by a thin layer of SiO_2. Further study should be carried out on the stability of SiC in aqueous environments to evaluate its stability over geological time frames.

An alternative approach to TRISO particle encapsulation has proposed the use of a graphite-glass composites, comprising the formation of a graphitic puck by hot uni-axial pressing followed by “encapsulation” of the puck with molten borosilicate glass [142]. Significant oxidation of the graphite, which could result in the release of radioactive $^{14}CO_2$ and ^{14}CO proved problematic for this route. This study also suggested powdering of the TRISO particles into a 1 µm powder to form the graphitic body. Such size reduction would prove prohibitive in practical terms, since processing routes requiring size reduction and dust formation for fission product bearing wastes should be strongly discouraged. Other recent work have focused on graphite matrices made from a mixture of powdered, irradiated graphite and TRISO particles [143]. A graphitic matrix containing TRISO particles was produced, the porosity was filled using borosilicate glass with a similar hot uniaxial pressing methodology to that described above. However, at these high processing temperatures, further study into potential oxidative losses of graphite must be considered.

The studies of TRISO immobilisation performed in this thesis have built upon earlier work on the encapsulation of TRISO particles in sintered glass matrices with the aim of utilising matrices with a high aqueous durability. The use of these higher durability matrices aimed

to minimise waste volume and further stabilise the TRISO particles for GDF disposal. The high temperatures required to produce fluid melts with high durability glass compositions usually prohibit their use in HLW immobilisation due to excessive volatilisation of fission products. However, these glasses may be considered as potential encapsulants of HLW using sintering methodologies because of the lower processing temperatures required. Therefore, a number of such glasses and various processing methods have been evaluated during this study.

2.4.2 - Prototype Fast Reactor (PFR) Raffinate

The prototype fast reactor (PFR) was the UK's second fast reactor and operated between 1974 and 1994, utilising a high plutonium content mixed oxide fuel (MOX) with a molten sodium coolant and an output capacity of 600 MW thermal [144]. This reactor was built to serve the UK's desire to develop commercially viable fast reactor technology, bridging the knowledge gap between the earlier operation of the Dounreay Fast Reactor (DFR) and the construction and operation of full scale commercial fast reactors [145].

Spent fuel from the PFR was reprocessed on the Dounreay site by dissolution in nitric acid to recover the reusable fissile material. During the recovery of this fissile fraction, the reprocessing operation also produced approximately 206 m^3 of an aqueous radioactive liquor, known as PFR raffinate [146]. This raffinate contains the vast majority of the radioactive material and fission products produced both during the operation of the PFR reactor and on the Dounreay site [147]. The raffinate varies in composition from those produced in the reprocessing of thermal reactor fuel, due to higher burn up and the variation in fission product cross section, which occurs from fast neutron irradiation [148].

The last PFR fuel to be reprocessed was passed through the Dounreay reactor fuel reprocessing plant in 1996. Since then the waste raffinate has been stored in underground tanks on the Dounreay site. The conditioning of this waste into a passively safe solid form has been identified as a priority in the Dounreay Site Restoration Plan (DSRP) [149]. The aim of such a treatment is to solidify the waste stream for long term storage or disposal. As noted in Chapter 1, the internationally accepted methodology to achieve this for fission product containing raffinate waste streams from reprocessing operations is to vitrify them using borosilicate glass [1]. This involves the incorporation of waste elements into a durable glass matrix and has been practised since the 1950's.

Vitrification was the planned immobilisation methodology for PFR raffinate waste until 2000, when this treatment methodology was challenged because of the low heat generating capacity of PFR raffinate. After having spent a decade in storage, the heat output of the raffinate was estimated to peak at 135 W m^{-3}, well below the 2000 W m^{-3} level required to qualify HLW in the UK, hence, PFR raffinate was reclassified as an ILW stream in 2004[1] [150].

A best practical environmental option (BPEO) assessment was subsequently undertaken by the UKAEA to determine the most favourable treatment method for the PFR raffinate [151]. The BPEO study acknowledged a number of potential treatment options for this waste including vitrification, evaporation, continued liquid storage and cementation. This study ultimately identified neutralisation and cementation in a new facility on the Dounreay site as the new reference strategy for treating PFR raffinate. Construction of this facility, known as D3900, is yet to begin at the time of writing.

The physical properties of cemented inactive PFR raffinate have been shown in laboratory studies to exceed those required for ILW disposal [147]. This was achieved by neutralising the raffinate with $Ca(OH)_2$ and NaOH then mixing this with a 1:1 ratio of pulverised fly ash and OPC. Although promising, it must be considered that PFR raffinate will contain an activity nearly twenty times greater than that seen in other, similar waste streams currently immobilised via cementation [152, 153].

Although fulfilling the required physical and heat generation criteria is essential in wasteform design, the identity, concentration and ability to retain radioisotopes should be the primary concern in developing a suitable wasteform matrix as outlined in Chapter 1. This is especially true of wastes to be stored at the Dounreay site due to the site location and envisioned disposal of wastes in a near surface store.

At the time of writing, no data has been made publically available on the performance of the cemented PFR wasteform with respect to radionuclide retention in an aqueous environment. It is considered likely that due to the high concentration of $^{135/137}Cs$ and the properties of cementitious wasteforms, outlined in Section 2.1.2, that the release rates from a cemented PFR raffinate wasteform will be significantly higher than would be observed in a vitrified

[1] Despite this PFR raffinate having a heat output which allows classification of ILW, it should be noted that a thermal output of 6 W m^{-3} is considered the safe limit for waste packages within the UK GDF concept [150]. A 100 W m^{-3} thermal output is expected to be suitable for individual waste packages. If near surface stores were to be considered unsuitable for this waste, in practise it may require treatment as HLW.

product. Furthermore, a vitrified product may also be produced at a similar, if not reduced cost, when lifetime waste management costs are considered. Reductions in cost may be realised by a combination of smaller scale plant requirements, production of a smaller volume of packaged and secondary wastes and the resulting decrease in storage, transportation and installation costs required for final disposal.

The purpose of the study performed in this thesis was to qualify this hypothesis and to provide an alternative option for PFR raffinate using barium silicate glasses as the disposal matrix. The barium silicate glass G73, has been selected as it was developed as a matrix for the immobilisation of other UK ILWs [154, 155]. The glass has a high aqueous durability and contains Fe_2O_3 as a control on the glass redox properties. The high barium content inhibits the formation of soluble 'yellow phase' in waste streams with high sulphur contents, such as the PFR raffinate.

2.4.3 - Clinoptilolite

The UK's early aim of developing a fleet of fast reactors, nuclear defence capabilities and the difficulties associated with the storage of Magnox fuel elements gave rise to the policy of reprocessing spent nuclear fuels [156]. During reprocessing operations the highly radioactive fission products in the fuel are separated from the reusable uranium and plutonium. This reprocessing of spent nuclear fuel is carried out at the Sellafield site in Cumbria, where, prior to reprocessing, the spent fuel is stored underwater in purpose built ponds [157]. In these ponds, corrosion of the fuel cladding can occur, leading to the release of small amounts of soluble radioisotopes into the pond water. These soluble isotopes primarily consist of the fission products ^{134}Cs, ^{135}Cs, ^{137}Cs and ^{90}Sr. The presence of these isotopes in the pond water poses difficulties for operational staff due to an increased dose uptake in the vicinity of the fuel storage ponds [157]. To mitigate this dose uptake, the pond water was regularly purged and replaced. This, however, also led to increased environmental releases of radioactivity from the Sellafield site. To counteract these problems the Site Ion Exchange Effluent Plant (SIXEP) commenced operation in 1985 with the aim of removing particulate materials and aqueous Cs/Sr from the fuel pond effluents prior to sea discharge.

The ion exchange material used in the pressurised columns to strip radio-caesium and radio-strontium from the pond effluent is a crucial component of the SIXEP plant. The exchange material utilised for this purpose is the natural zeolite mineral, clinoptilolite. This has the approximate chemical formula $(Na,K,Ca)_{2\text{-}3}Al_3(Al,Si)_2Si_{13}O_{36}\cdot 12H_2O$ and is sourced

from a deposit in the Mojave Desert, California [157]. The advantages of this material include; high selectivity for Cs and Sr over other cationic species, a high radiation stability, the physical strength to form an exchange bed, ready availability and low cost. The clinoptilolite is used in a granular form, as shown in Figure 2.10 a), to increase the rate at which effluents can be treated [157].

As with other zeolitic materials, the cation exchange capability of the material, is a result of the open channelled crystal structure and the presence of alumina tetrahedra in the structure [158]. The channels allow diffusion of species through the zeolite network and the tetrahedrally coordinated alumina provides localised anionic sites through which interstitial cations provide charge compensation. The crystal structure of clinoptilolite is shown in Figure 2.10 b) which highlights the different sites which interstitial Na^+, K^+ and Cs^+ ions take within the structure [159].

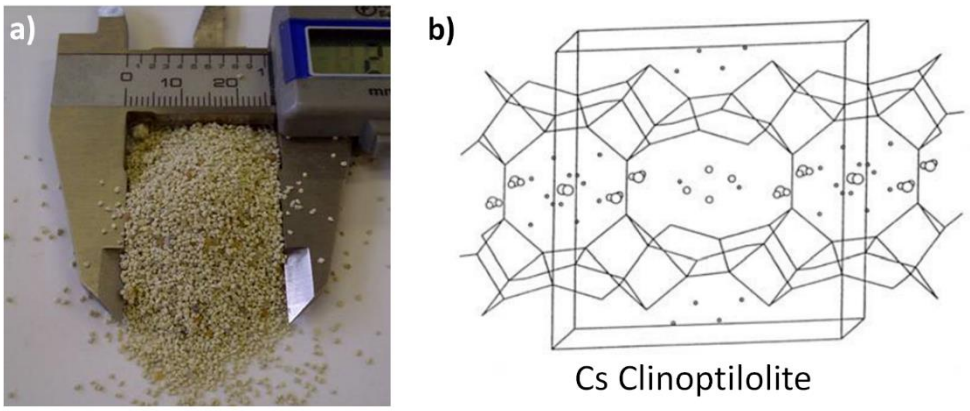

Figure 2.10 - a) Granular clinoptilolite, as utilised at SIXEP (Sellafield) and b) the atomic structure of clinoptilolite viewed along its c axis depicting the positioning of the cation sites in Cs exchanged clinoptilolite. Large circles represent cations, small circles represent water molecules and line intersections represent the cations of tetrahedrally coordinated oxide species (figure b) adapted from [159]).

The waste loading of Cs and Sr on the clinoptilolite is minimised to reduce heat generation and allow disposal of the spent material as ILW. Once an ion exchange bed is considered spent, the clinoptilolite is discharged to a storage tank fitted with a water based cooling system [157]. Estimates suggest that approximately 2,400 m^3 of spent clinoptilolite and sand filters will be produced by the end of SIXEP's operational life [160]. This unconditioned waste will therefore account for approximately 1 % of the total expected UK Intermediate level waste (ILW) inventory by volume and up to 4 % by activity [23, 160].

It could be argued that storage of this waste for approximately 300 years in above ground, monitored facilities would provide a suitable disposal option for these wastes. This would allow sufficient time for the short-lived isotopes which constitute the majority of the waste activity (^{90}Sr $t_{1/2}$ = 28.8 y, ^{134}Cs $t_{1/2}$ = 2.06 y and ^{137}Cs $t_{1/2}$ = 30.2 y) to decay to radiologically acceptable levels, as described in Chapter 1 (i.e. ten half-lives). However, the waste in its current granular state poses a dispersion risk in the event of a natural or anthropogenic breach of a storage facility. This means consolidation into a monolithic from would be necessary, even for above ground storage. If this waste were instead to be placed in a GDF it would still require pre-treatment into a monolithic form prior to transportation and disposal. This monolith should be resistant to aqueous corrosion in order to improve the passive safety of the waste [161].

As described in Section 1.2, the accepted methodology in the UK for treatment of ILW into a monolithic form is via cementation [23, 29]. However, traditional cements are unsuitable for the disposal of clinoptilolite due to the deconstruction of the zeolite network in the alkaline pore water, a problem which is also highlighted in Section 2.1.2 [47, 162, 163]. The deconstruction of this network leads to the release of the adsorbed Cs into the cement pore water. This is clearly undesirable due to the potential for subsequent environmental release as Cs accounts for over 90% of the radioactive inventory in clinoptilolite [47]. The cementation of clinoptilolite would also involve a fourfold increase in the final volume of waste for disposal [160]. This larger volume of waste would incur additional costs for emplacement in a GDF and in the construction of an alternative above ground storage facility [19].

Alternative vitrification routes for the immobilisation of clinoptilolite have been studied in order to overcome these issues. Sintered glass composites have been evaluated for the encapsulation of clinoptilolite, however, were unable to retain the Cs inventory in aqueous solutions [164]. Co-processing of a slurry of clinoptilolite with a variety of other waste streams/inactive additives at temperatures of 1150 °C using joule-heated ceramic melters (JHCM) has been investigated, where full scale tests utilising JHCMs have successfully produced glass monoliths from the clinoptilolite sand mixture [165-167]. Mixtures of clinoptilolite/sand were processed with a variety of either magnox sludge simulants or pile fuel cladding silo waste and/or glass forming additives. These studies showed this technology is capable of producing up to 974 kg of waste a day to a standard which passes the regulatory conditions for disposal provided by the US Environmental Protection Agency. Co-processing is required as the composition of clinoptilolite contains a high percentage of oxides which

act as network formers in a silicate melt (>90 wt %). This increases the temperature required to achieve a pourable melt fluidity for a clinoptilolite/sand melt to >1300 °C [51]. Such high temperatures are problematic for the design of radioactive-capable melters due to the potential for radioisotope volatilisation, especially for radio-Cs [168, 169].

Some issues remain which restrict the usefulness of JHCM for the immobilisation of clinoptilolite. Co-processing results in waste loadings of the dried clinoptilolite below 50 wt%. The vitrification of clinoptilolite under these conditions also requires the careful control of a cold cap, extensive off-gas monitoring and retrieval systems to account for volatile caesium loss. This volatile caesium loss has been shown to be as high as 10 % of the waste inventory. Other problems include the production of numerous secondary wastes and a high degree of porosity in the final sample.

An alternative methodology for performing the vitrification of clinoptilolite is to HIP the clinoptilolite-sand mixture. The use of a closed system during processing eliminates the potential for volatile losses during processing and the application of pressure promotes densification, lowering the operating temperature required to achieve vitrification. Investigation into the HIPing of clinoptilolite waste streams has previously been examined by co-processing clinoptilolite-sand mixture with magnox sludge simulant [120]. This method produced a dense glass ceramic monolith with 98% waste loading.

Chapter 6 investigates HIPed clinoptilolite wasteforms. Small amounts of inactive additives are used as the basis for this study, in place of the significant additive volumes previously utilised. Processing clinoptilolite as an individual waste stream is invaluable for two reasons; 1) the poorly defined characteristics of magnox sludges may introduce difficulties in the final processing of clinoptilolite waste streams; and 2) it is unlikely that both the magnox sludge and clinoptilolite waste streams will be made available for thermal conditioning concurrently. Therefore options to process these wastes individually are beneficial and could provide flexibility in future plant operations [170]. This thesis presents an investigation of the effect of HIPing clinoptilolite/sand in order to produce suitable wasteforms.

2.4.4 - SrTreat® Ion Exchange Material

SrTreat® is a commercially available ion exchange material, produced by Fortum Engineering, Finland, for the removal of Sr from aqueous solutions [171, 172]. It is based on a sodium titanate structure. Tri and tetra-titanate of alkali titanates have a crystal structure which allows for ionic diffusion and ion exchange to occur [173]. A schematic illustration of the

layered channel containing structures of these alkali titanates is included in Figure 2.11 b). The TiO_6 octahedra line up in distorted sheets, with alkali cations filling the interlayers. The exact arrangement of the sheets depends on composition but the generic structure is the same for the majority of members of the tri and tetra-titanate phases. SrTreat® is supplied as a granular solid for use in either ion exchange beds or columns and has a typical granular size of 0.30 - 0.85 mm [174].

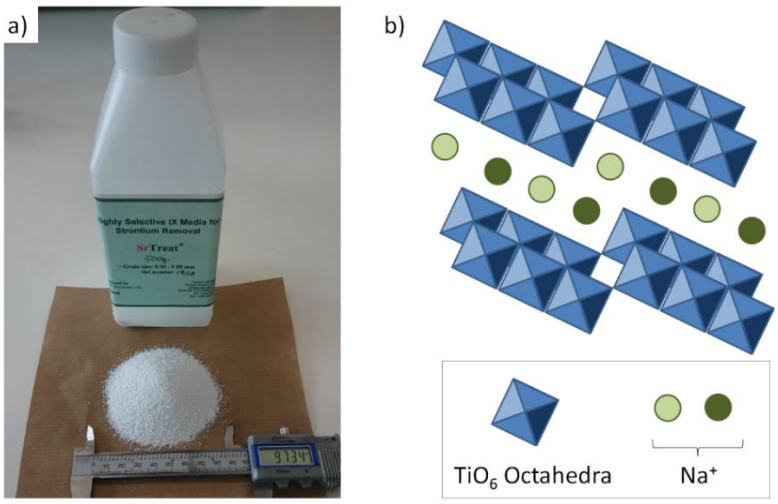

Figure 2.11 - a) Photograph of SrTreat® granules used during the course of this study and b) a schematic of crystal structure of $Na_2Ti_3O_7$ showing the channelled structure between the sheets of TiO_6 octahedral which provide the capacity for ion exchange observed in the tri and tetra-titanates (image adapted from [173]).

SrTreat® is a highly effective ion exchanger due to its selectivity for Sr over other common cations such as Na^+, K^+, Mg^{2+} and NH_4^+ making it especially useful for solutions where Sr is present in much lower concentrations than other cations [175, 176]. The selectivity of the material for Sr^{2+} against Na^+ is approximately $K_{Sr/Na}$ = 200,000 and is effective above pH 9. However, the effectiveness of the ion exchanger is reduced by the presence of either H^+ or Ca^{2+}, which are preferentially sorbed into the interlayer, as illustrated in Figure 2.12. This preferential exchange of H^+, reduces the effectiveness of SrTreat® under acidic conditions, limiting the conditions in which SrTreat® can be usefully applied to high pH solutions. SrTreat® is usually utilised at pH values >10 and performs, optimally at approximately pH 12 [174]. By utilising SrTreat® at high pH values, the problems associated with low selectivity for Ca^{2+} containing are also minimised. This is due to the precipitation of the majority of Ca^{2+} as $CaCO_3$ under high pH conditions, exposed to the atmosphere.

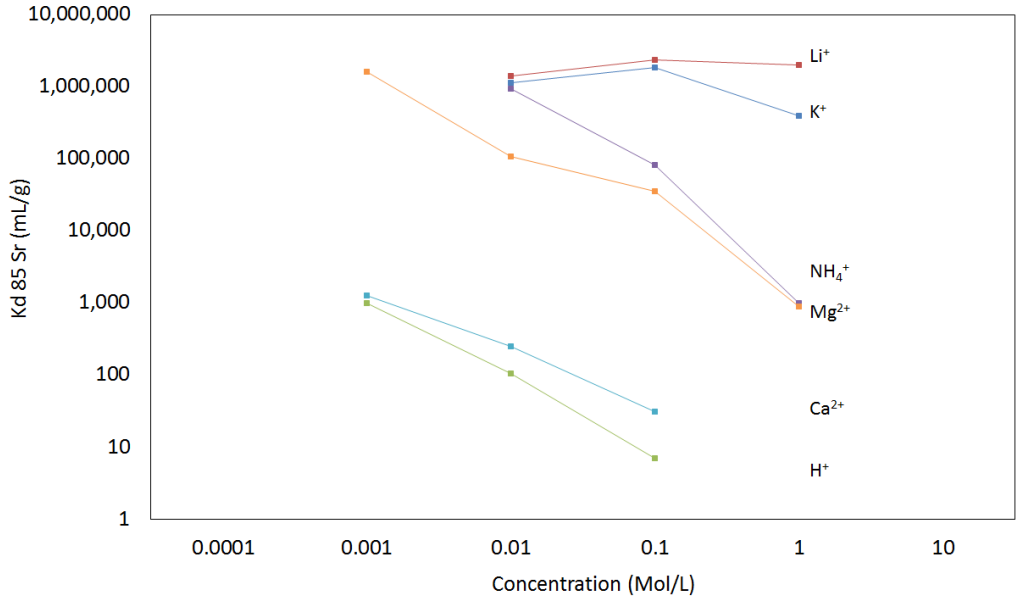

Figure 2.12 - Graph illustrating the capability of SrTreat® to extract Sr from solutions which contain other cations in varying quantities adapted from [176].

SrTreat® has been used in various instances around the globe to strip aqueous effluents of their Sr inventory and provide a reduction in waste volume by incorporating it into a solid matrix. Existing stockpiles of SrTreat® have been produced by stripping Sr from waste waters produced by nuclear powered icebreakers in Murmansk, Russia, from alkaline reprocessing effluent in Tokai, Japan and from contaminated waters at Savannah River, USA. Further details involving the industrial employment on SrTreat® are included in [172].

The necessity to condition of SrTreat® falls under similar grounds to that of clinoptilolite as described in Section 2.4.3. Although the crystal structure will not show the same pozzolanic collapse in high pH solutions seen in clinoptilolite, the propensity for powder dispersal through a loss of containment incident is of concern. This necessitates the formation of monolithic wasteform for the final disposal.

The heat treatment of Sr exchanged sodium titanates has previously shown the material will decompose at 870 °C, producing a mixture of $Na_2Ti_6O_{13}$ and a strontium titanate phase, tentatively identified as $SrTi_3O_7$ [175]. The formation of such a mixed crystallite wasteform is likely to produce a wasteform with durability acceptable for geological disposal.

The use of HIPing to process these waste streams would provide all the benefits stated in Section 2.3.2, including waste volume reduction, minimised porosity etc. Furthermore, if a suitable wasteform could be designed from spent SrTreat® utilising HIPing, improvements in future applications of this material can be speculated upon. In this instance SrTreat®

exchange columns could be readily manufactured to be sealed and function as a HIP canister at the end of life. This would provide ready handling of the spent exchange material and minimise the costs associated with final disposal by providing a complete disposal option for this ion exchanger.

This thesis includes a chapter studying the potential for the direct application of HIPing to create a monolithic wasteform form SrTreat® without the use of chemical additives. The aim of this work is to investigate the potential for application of the above hypothesis regarding future use, processing and handling of these waste streams. The results may also have significance to the global inventory of spent SrTreat® materials.

Chapter 3 - Experimental

This chapter will set out the basic principles underlying the experimental work and analytical techniques utilised in this thesis. Details of methodologies common to multiple chapters are included. Where considered appropriate, specific details of the materials, sample preparation, equipment identity and experiment parameters can be found in the experimental sections of each technical chapter.

3.1 - Vitrification

Vitrification is the term used to describe the production of a structurally amorphous material, such as an oxide glass. the most common methodology for producing vitreous materials involves the heating of mixture of chemical components, usually oxides, carbonates, sulphates and nitrates, to form a liquid melt [177]. This melt is subsequently held with a sufficient temperature to allow homogenisation of the viscous fluid, followed by cooling at a rate which is sufficiently high to prevent significant crystal formation. The glasses are then cast and in most cases annealed, a step aimed at increasing the physical stability of the final vitreous product. This works by cooling slowly through the T_g which allows for the dissipation of thermal energy. This process minimises the residual energy which is 'frozen' into the glass structure, decreasing the likelihood of future mechanical failures [107].
During the course of this PhD a number of oxide glasses were produced utilising the basic methodology set out below. The exact details of the processing regimes and batch reagents are provided in the experimental sections of the corresponding chapters.

3.1.1 - Batch Calculations

Batch reagents which decompose on heating are commonly used in place of oxide components in glass melts. This minimises the melting temperature, improves homogenisation, accounts for batch components unavailable as oxide reagents and produces cheaper, better quality glasses. As a result of this, to produce a melt of a certain composition, batch calculations are necessary in order to calculate the final composition [178]. A useful guide to the batch calculation methodology used during this thesis can be found in [51].

Once the batch calculations were complete, reagents were dried appropriately. Components accounting for ≥ 20 mol % were weighed with an accuracy of ±5 x 10^{-3} g and components

accounting for ≤ 20 mol % to ± 5 x 10^{-5} g. The batches were lightly ground then mixed by shaking in a sealed polyethylene bag to promote homogenous melting. The batches were then transferred to mullite or alumina crucibles for melting.

3.1.2 - Melting

During melting the components form a vitreous liquid phase [67]. In most cases this melt initially forms a liquid phase by a eutectic mixture of salts, such as Na_2CO_3 and $CaCO_3$, at a temperature significantly below the point a pourable melt is obtained [177]. This liquid then acts to dissolve the refractory components, such as SiO_2 and Al_2O_3. Glasses produced during this study used a combined temperature and time for melting sufficient to reduce the melt viscosity to allow pouring, homogenisation through convection and the release of 'seed' bubbles [61]. In the case of G73 melts produced in Chapter 5, in-melt stirring was applied to improve melt homogenisation.

All melts were performed in either an electric muffle furnace or a gas fired furnace. When using the gas furnace an overnight preheat was performed in an electric muffle furnace to heat the crucibles to 1000 °C – 1100 °C. These crucibles were then transferred to the gas furnace. This method minimises the risk of thermal shock to the crucibles whilst optimising the efficiency of gas usage by allowing a fast thermal ramp rate. After the dwell period the melt was cast into its final form. During the course of this work, casting was achieved using two methodologies. The first method produced a glass frit by pouring the melt into a bucket of water to quickly quench the glass and produce a granular material. The second method was used to obtain monolithic samples, in this case the glasses were cast into preheated steel moulds prior to annealing.

3.1.3 - Annealing

All monolithic glass samples produced were annealed to minimise residual stresses. The cast blocks were allowed to cool at an ambient rate until self-supporting before transferring to a muffle furnace set at a temperature 15 °C above the T_g, as estimated from literature sources. The furnace was set to hold this temperature for one hour before cooling to room temperature at a rate of 1 °C min^{-1}.

3.2 - Cold Press and Sinter (CPS)

Cold press and sinter (CPS) is one of the most common methodologies used for the solid state synthesis of ceramics [179]. CPS is a simple process performed in five stages;

i) The desired reagents are mixed to provide the most even distribution of components possible.
ii) This mixture is transferred to a uniaxial die.
iii) The powders are compacted in the die by the application of pressure which forms a fragile monolith, known as a 'green body'.
iv) The green body is ejected from the die.
v) The green body is heat treated to produce the final work piece.

This method has previously been suggested for the encapsulation of radioactive materials in a vitreous matrix [164, 180, 181]. In this thesis CPS was primarily used as a method of preparing materials for vitreous encapsulation.

Solid state reactions between particles can take place during firing which result in sintering. The densification which occurs in glass powders proceeds via three stages similar to those described in Section 2.3.1 [117, 118]. The initial shrinkage ($\Delta L/L_0$) can be determined using the Frenkel Equation shown in Equation 3.1:

$$\frac{\Delta L}{L_0} = \frac{3\gamma_s t}{2\eta\alpha}$$ **Equation 3.1**

Where γ_s = surface tension, *t* = isothermal sintering time, η = viscosity and *a* = particle size (assumes a uniform particle size exists).

Secondly, gas diffusion through the interconnected porosity becomes rapid and the rate of shrinkage becomes proportional to the ratio γ_s / η. As η is temperature dependant, the rate of sintering increases significantly with temperature. Finally, once the interconnected porosity is eliminated, the removal of the remaining internal porosity is proportional to the size and quantity of pores, viscosity and sintering time according to the Mackenzie-Shuttleworth Equation provided in Equation 3.2 [117]:

$$\frac{dD}{dt} = \frac{K\gamma_s n^{1/3}(1-D)^{2/3}(D)^{1/3}}{\eta}$$ **Equation 3.2**

Where *K* is a constant depending on geometry, *D* = bulk density fraction and *n* = number of pores m^{-3}.

During all three stages of vitreous sintering, the densification is limited by viscosity, as such, increasing the temperature will increase the rate of densification. However, at higher temperatures, the viscosity decrease can result in the deformation of the green body as it slumps under the effect of gravity. Hence, optimal densification of glass powders using sintering is achieved whilst sintering at a temperature above the glass T_g ($\eta \approx 10^{11.3}$ Pa s) but below its Littleton softening point ($\eta = 10^{6.6}$ Pa s) [61, 117].

3.3 - Hot Isostatic Pressing (HIPing)

HIPing is a methodology used in the heat treatment and densification of materials. It can be used for almost any material which does not emit volatiles during the desired densification regime and is most commonly applied to the densification of metals and ceramics. It utilises elevated temperatures whilst using an inert gas, such as Ar or He, to apply high pressure isostatically as described in Section 2.3.

The majority of samples discussed during this thesis were produced using the University of Sheffield's HIP Research HIP facility with an AIP-630H HIP rig. Details of the AIP-630H rig and its installation are included in Appendix I. The samples were all HIPed as powdered or granular materials, contained within 316 stainless steel canisters. A number of test samples were kindly processed using the HIP rig at NNL's Workington laboratory and under contract with Bodycote Chesterfield.

The canned samples were produced in a number of steps using 'the coin-tube' methodology to allow for the processing of powder samples, as shown in Figure 3.1.

a) Canister components were created by sectioning steel rod and steel tubing.
b) End caps were cut from steel rod. Lids were created by drilling a 6.5 mm hole into an end cap and welding a 150 mm x 6.35 mm (length x outer diameter) stainless steel pipe into this hole.

c) The canister was created by welding the bottom cap into the tube. An alternative design, where the base was created by crimping and welding the tube, was utilised for a number of samples discussed in Chapter 4.
d) The canister was filled with the powdered materials and compacted using a combination of vibration, tapping and/or uniaxial pressure to minimise internal void space.
e) The lid was welded onto the canister, a vacuum line was attached to the evacuation tube and the canister tested to test whether if it could hold a 3.3 Pa vacuum at room temperature. Once vacuum was achieved the canisters were placed in a furnace.
f) Water, solvents and volatile organic material were removed from the canister at elevated temperatures until the vacuum achieved was maintained at ~3.3 Pa.
g) The evacuation tube was then crimped in a hydraulic press. A second crimp was applied above this first crimp. The upper crimp was broken without disturbing the lower crimp and sealed using a weld in order to seal the canister under vacuum.
h) The volume, mass and dimensions of the work piece were recorded prior to processing in the HIP.

Details specific to the processing conditions, sample preparation and sample retrieval can be found in the experimental sections of each relevant technical chapter.

The HIP canister volumes were measured before and after processing using the principle of volume displacement in water. With this information, the waste volume reduction associated with processing can be calculated using Equation 3.3.

$$V_D = \frac{V_i - V_f}{V_i} \times 100 \qquad \textbf{Equation 3.3}$$

Where V_D is the volume decrease (%), V_f is the final processed canister volume and V_i is the canister's initial volume. The contraction of the packaged waste volume can be estimated by subtracting the known volume of the canister material before and after processing according to Equation 3.4.

$$V_{DM} = \frac{(V_i - V_{CM}) - (V_f - V_{CM})}{(V_i - V_{CM})} \times 100$$ **Equation 3.4**

Where V_{DM} is the volume reduction of the packaged waste simulant materials (%), V_{CM} is the volume associated with the canister material (cm^3) as calculated from the known geometric dimensions of the materials utilised. As the steel in the canister should only deform and show no associated volume decrease it can be assumed that all densification is associated with compaction of the packaged waste simulant.

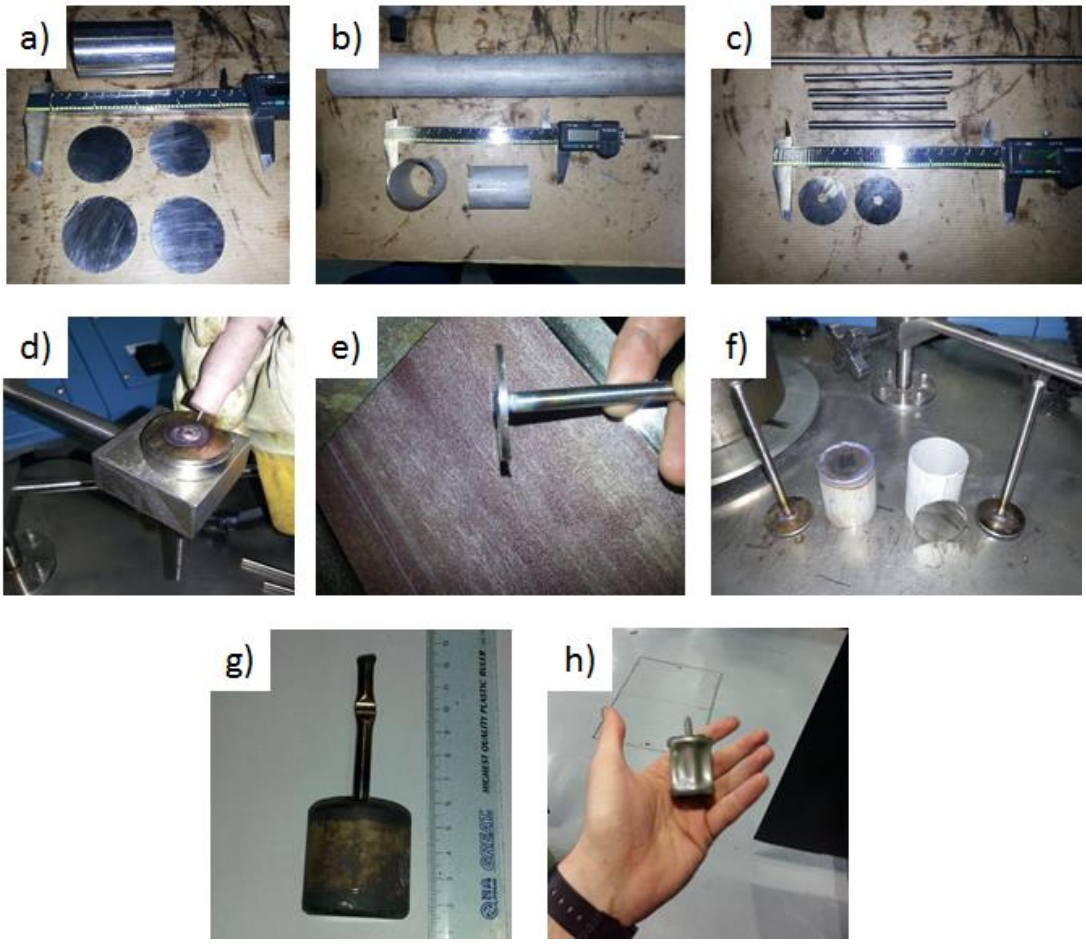

Figure 3.1 - Images of HIP canister manufacture a) solid steel rod cut into coins to provide end caps b) tubing cut to sample size c) end caps drilled with hole for evacuation tubing d) welding of evacuation tubing to end cap e) finishing of end caps f) canister components before filling g) a sealed canister pre-processing h) a processed HIP canister.

3.4 - X-Ray Powder Diffraction (XRD)

XRD is a powerful technique used to fingerprint crystal structures in a material. It utilises the fact that all crystal structures have defined inter-planar spacings. When a beam of X-rays is focused on the sample, diffraction of the X-rays occurs at each crystal plane. During diffraction coherent waves of radiation are produced with an increased intensity at specific angles. These coherent waves are produced by the interaction of the radiation with the crystal structure as described by the Bragg equation, given in Equation 3.5.

$$n\lambda = 2d\sin\theta \qquad \textbf{Equation 3.5}$$

Where *n* is an integer, λ = wavelength of the X-ray beam, *d* = inter-planar spacing distance and θ= the diffraction angle. The principles described by Equation 3.5 are illustrated in Figure 3.2 a).

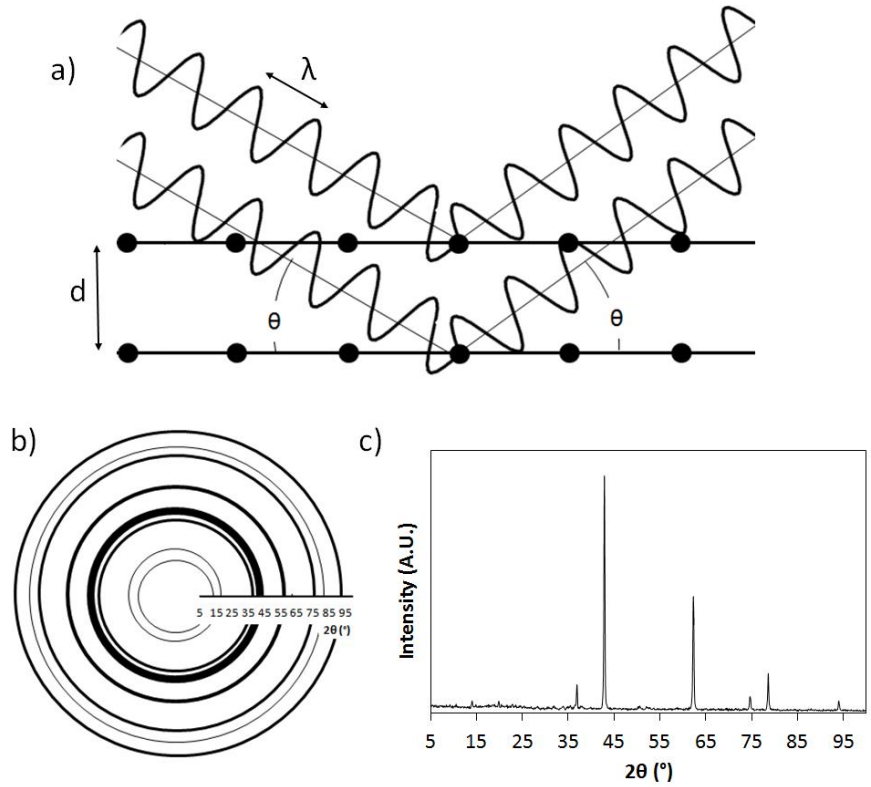

Figure 3.2 - a) Illustration of the principle described in Equation 3.5. Coherent diffraction of radiation is dependent on both the wavelength, angle of incoming radiation and the inter-planar distance of the crystal phase being studied b) schematic of the ring based diffraction patterns achieved by using a selection of randomly orientated MgO grains and c) is a measured powder diffraction illustrating a cross section of these rings.

Powder XRD is one of the most common uses of this phenomenon. In this technique a collimated X-Ray beam is focused onto a powdered sample with a flat surface of randomly orientated crystals. A detector is set to measure the beam of photons which are diffracted from these crystal structures at an angle of 2θ from the incident beam. The resultant beam has a conical form due to the random crystal orientation; these cones of radiation can be collated to form a diffraction pattern, as shown in Figure 3.2 b). If we take a line scan across this diffraction pattern we obtain an x-y pattern plotting intensity against 2θ as shown in Figure 3.2 c).

Most commonly, the powder XRD data is used to identify phases from this x-y plotted diffraction data. The pattern is compared against known compounds contained within the ICDD database using a software program such as Sieve4+ or WinXPow. This methodology can be used to identify multiple phases within the same sample.

XRD is also a useful technique for determining if a material is amorphous in nature. As no long range structural order is observed in amorphous materials, variations in the inter-planar spacing exists, therefore, the formation of a coherent diffracted beam at individual diffraction angles does not occur. Instead, an increased intensity across a wide range of 2θ angles, relating to diffraction from a range of short range interatomic distances, is observed. This type of feature in a diffraction pattern is commonly referred to as an 'amorphous hump' or more accurately as diffuse scattering.

3.4.1 - Experimental Parameters

Chapter 4: Powder X-ray Diffraction patterns were obtained for the glasses using a Philips PW1830 diffractometer using Cu K_α radiation (1.5418 Å), over the range $10° < 2\theta < 60°$ with a step size of 0.02° at a rate of 0.6° 2θ min^{-1}. The pattern for ABS-1 glass after sintering was collected on Siemens D500 diffractometer using Cu K_α radiation (1.5418 Å) over the range $10° < 2\theta < 60°$ with a step size of 0.02° at a rate of 0.6° 2θ min^{-1}.

Chapter 5: X-ray powder diffraction was performed on sub-75 μm powder with a Siemens D500 diffractometer, using Co K_α (1.7902 Å) radiation over a 2θ range of 15° to 85°, with a step size of 0.05° 2θ at a rate of 0.08° 2θ min^{-1}.

Chapter 6 & 7: Powder XRD patterns were collected using a Bruker D2 Phaser with Cu Kα radiation (1.5418 Å), over the range $5° < 2\theta < 70°$ with a step size of 0.02° at a rate of 0.6° 2θ min^{-1}. Patterns were also collected on the XC-SrT to study the sample carbonation

with time. These patterns were collected over the range of 24° < 2θ < 27° with all other parameters identical to those described above.

3.5 - Reflected Light Microscopy

Light microscopy allows the visual examination of structures below 100 µm, impossible to resolve with the naked eye. Reflected light microscopy was used during the course of this thesis as it facilitates the examination of the surface features of opaque samples. The reflected light microscope illuminates the samples from above and collects the reflected light through a series of lenses. These lenses focus the light to achieve an increase in the resolution of the area of interest [182]. Optical microscopy was performed on a Reichert-Jung Polyvar Met microscope equipped with a Zeiss AxioCam MRc.

3.6 - Scanning Electron Microscopy (SEM)

SEM is a technique primarily used for imaging surface topography and chemical analysis of materials. It is capable of resolving features < 0.2 µm in size, which would be impossible to resolve using optical microscopy [183]. The ability to look at features smaller than those observable using visible light is a result of the smaller wavelengths associated with electrons. An SEM image is created by focusing a beam of electrons with energies ranging between 5 - 30 KeV on a sample. A number of signals are produced by the interaction of an electron beam with a sample, a selection of which are shown in Figure 3.3 a). The uses of these signals is discussed further below. The returned signals and their intensity can then be collected by a detector to form an image.

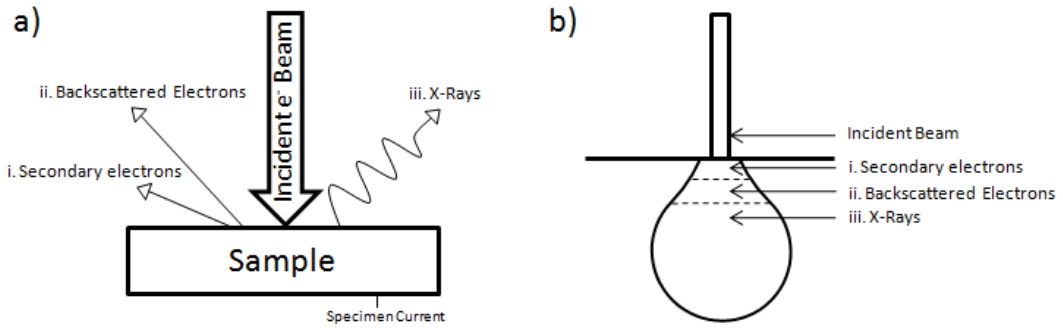

Figure 3.3 - a) A selection of the signals produced by the interaction of electrons with a bulk material and b) a schematic of the interaction volume of an electron beam, illustrating the regions from these signals are produced. (adapted from [184])

3.6.1 - Secondary electrons - SEM mode

Secondary electrons are the type of electrons most commonly associated with SEM imaging and typically have energies below 50 eV. These tend to be electrons which have been ejected from near the sample surface, as shown in Figure 3.3 b), due to inelastic scattering interactions with the incident beam. Secondary electrons only have enough energy to escape from the first few nanometres of the sample surface and therefore provide the smallest sampling depth for the beam and provide the highest resolution topographic images [183]. The images produced resemble grayscale images of 3-D objects as viewed with diffuse light. This is due to the likelihood of secondary electrons escaping the sample being dependent on the angle at which the beam is incident.

3.6.2 - Backscattered Electrons - Backscattered Electron Mode (SEM-BSE)

These electrons are used for imaging, diffraction and chemical identification in SEM. They are high energy electrons produced by the elastic scattering of the incident beam. Indication of chemical composition is provided as the likelihood of electrons backscattering increases proportionally with atomic number [185]. As such, more backscattered electrons are produced by heavier elements, which allows for the imaging of chemical detail.

3.6.3 - X-rays - SEM-Energy Dispersive X-Ray (SEM-EDX) Analysis

Appropriate sources of radiation, such as a high energy photons or electrons will ionise atoms by ejecting an inner shell electron. After ionisation the atom exists in an excited energetic state and in order to relax must refill the unoccupied position left in its electron shell. The atom achieves this by utilising an outer shell electron, which transitions between shells and fills the vacancy present in the inner shell [183, 186]. The electron which fills this vacancy has an excess energy associated with this move. This energy is in turn dissipated from the atom by one of two mechanisms; i) a photon of characteristic energy is ejected or ii) another outer electron (Auger electron) is ejected after absorbing the emitted photon. These processes are illustrated in Figure 3.4. SEM-EDX is primarily concerned with the first of the two mechanisms.

Due to the well-defined energy levels which exist between the electron shells in each element, the energy of the ejected photon can be used to determine both the element and the electron shell from which it was produced.

This methodology can be calibrated to provide semi-quantitative data on a sample's composition. Commonly in SEM-EDX the summation of these characteristic photons can be used to great effect in mapping the elemental composition. Lighter elements ($M_r \leq 20$) cannot be readily detected as the energy of emitted photons drops below the limitations of common detectors and the ratio of photon to Auger electron production decreases.

As photons do not interact with the material to the same extent as escaping electrons, the signal produced for SEM-EDX corresponds to a larger interaction volume than that seen for SEM-SE and SEM-BSE. Depending on the materials being studied and the energy of the incident electron beam, the detected signal can result from a depth of up to 5 µm within the sample. This effect therefore lowers the useful resolution attainable for chemical identification and quantification.

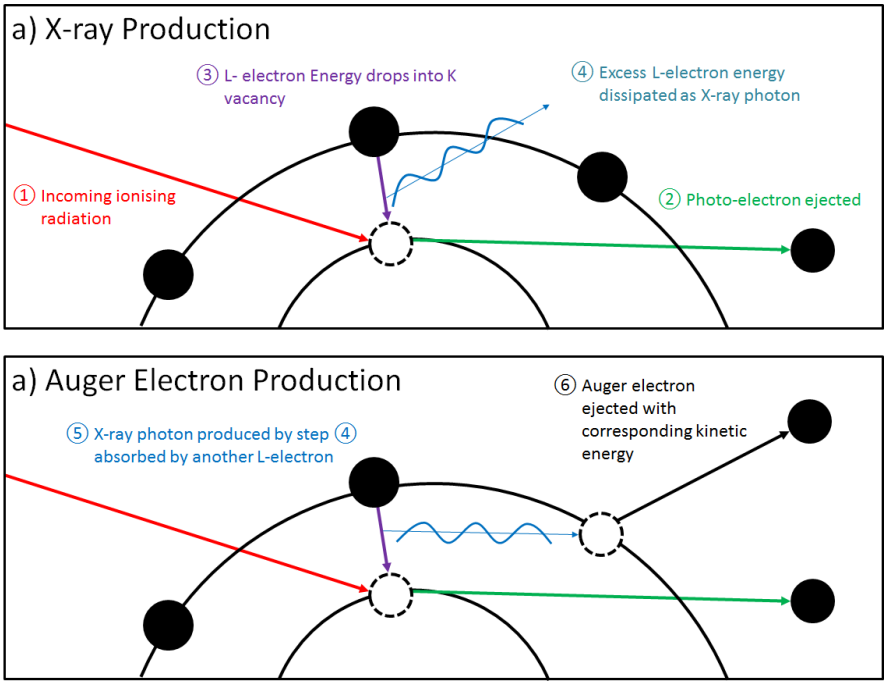

Figure 3.4 - Schematic of electron ejection produced by inelastic scattering of ionising radiation, followed by the electron transition and dissipation of excess energy as an X-Ray photon or b) an Auger electron. (figure adapted from [187]).

3.6.4 SEM - Wavelength Dispersive Spectroscopy (SEM-WDX/EPMA)

SEM-WDS, also known as electron probe micro-analysis (EPMA), works on the same principle as SEM-EDX. The difference between the two methodologies is in the mode of detection. SEM-EDX instruments use efficient energy dispersive x-ray detectors, able to detect the incident energy of all incoming photons based on the production of electron-hole pairs in the

detector. However, this methodology can lack resolution in elements where the characteristic photon energies are similar. EPMA achieves higher resolution and more accurate elemental composition quantification by utilising a wavelength dispersive detector. This detector has a series of crystals and uses the principle of diffraction (explained in Section 3.4 and Figure 3.2 a) to separate the characteristic X-ray photons of interest onto the detector.

SEM-WDS is less commonly utilised than SEM-EDX for a number of reasons. It only measures a small proportion of the produced signal (due to inefficiencies in the diffraction process), requires flat polished samples and needs well defined chemical standards for calibration. The benefits are more accurate quantification and the ability to detect, quantify and map trace and low atomic mass elements.

3.6.5 - Experimental Parameters

Chapter 4: SEM imaging was performed using a JEOL JSM 6400 SEM with an accelerating voltage of 20 kV at a working distance of 15 mm.

Chapter 5: Initial assessment and mapping presented in Figure 5.1 b) was performed as in Chapter 4 and analysed using the INCA mapping software package. Further imaging presented in Figure 5.2 was performed using an FEI Quanta 200 F SEM with an accelerating voltage of 30 kV and a working distance of 10 mm at Forschungszentrum Jülich. Analysis was performed using the Genesis EDX software package.

Chapter 6 and 7: Imaging was performed using an FEI Quanta 200 F SEM with EDX using an accelerating voltage of 20 kV and a working distance of 10 mm at Forschungszentrum Jülich. The EDX spot measurements were conducted until a count >2000 was obtained. Collection of maps was performed over an 8 hour period to allow data collection of quality sufficient to allow semi-quantitative analysis to be performed using pixel groupings.

Images for use in montaging were collected using a calibrated microscope stage with set movement along both the x and y axis. The magnification was set to provide a 0.5 µm pixel size. The Image J software suite was utilised for image analysis. Montaging was performed using 16 bit TIFF images by the determination of the picture overlap, creation of appropriate image stacks, followed by the performance of a montaging operation. No alterations were applied to the original brightness or contrast values during image manipulation.

Pixel data ranges were then selected based on their grayscale value. This separation was performed on the basis of grayscale values, where the grayscale variations had been cross

correlated with SEM-EDX spot measurements to determine composition. The pixel separation was performed by thresh-holding of the montaged data to create new images. The related pixel data was further quantified to allow the determination of its contribution to the overall area of the phase assemblage. This was also performed using the Image J software package.

The data presented in Figure 7.3 was collected using a Hitachi TM3030 fitted with EDX, using an accelerating voltage of 20 kV and a working distance of 10 mm. EDX mapping and analysis was performed using the Bruker Quantax 70 EDX software package.

EPMA: Sample CSXC-$NaAlO_2$ was analysed using EPMA with a Cameca SX 100 electron microprobe and a spot size of 1 µm. Maps (512 x 512 pixels) were taken for elements Si, Al, Cs and Sr using wavelength dispersive detectors and an accelerating voltage of 15 kV and a 100 nA current. Quantitative analysis was performed for the elements Si, Al, Na, K, Ca, Fe, Mg, Ti, Cs and Sr in 35 spots of interest which were identified via mapping. A 15 kV acceleration voltage with a 20 nA current was used for quantitative analysis. The quantification was calibrated using mineral standards for each element. The phase compositions given in Table 6.1 are averaged over a minimum of four spots.

3.7 - Thermal Analysis

During thermal analysis a small quantity of material (< 0.1 g) is heated in a crucible at specified rate with a standard used for calibration. This standard is most often an empty crucible identical to that in which the sample is contained. During the heating regime a difference in the measurement between the standard and the sample provides insight into the properties of the sample. The measurement which is taken is determined by the type of thermal analysis being performed and the information desired [188].

3.7.1 - Differential Thermal Analysis (DTA)

DTA measures the thermal change of the sample during heating by reference to the standard. DTA measures the temperature difference between the sample and the reference during a given heating regime [189]. The results are displayed as thermal analysis curves where the thermal change of the sample is plotted against temperature. This allows the identification of peaks as both endotherms and exotherms in the heating regime. These peaks or step changes identify the reactions and phase transformations which occur in the material at varying temperature. This is of particular interest in glass and polymer systems

as it allows for the determination of the T_g through the alteration observed in the heat capacity of these materials in this region.

DTA was used to determine the glass transition temperature (T_g) on a Perkin Elmer DTA 7, data was acquired over the range 25 – 1000 °C at a rate of 10 °C min^{-1}. The glass transition was determined by the extrapolation of tangents at the point of interest using the Netzsch Pyris software package.

3.7.2 - Thermo-Gravimetric Analysis (TGA)

This methodology measures the mass change which occurs in a sample during heating. Most commonly mass loss, indicating the formation of a gaseous product at a given temperature, is observed [190]. TGA will only indicate reactions where a mass change occurs and so is most often run in conjunction with DTA/DSC or mass spectroscopy to provide information on the reactive profile during heating. TGA was performed on a Perkin Elmer Pyris TGA 1 using Al_2O_3 crucibles in air from ~25 °C to 1000 °C at a rate of 10 °C min^{-1}.

3.8 - X-ray Fluorescence Spectroscopy (XRF)

XRF is a methodology used for identifying and quantifying the composition of solid samples and has been used as the primary method of the compositional analysis during the course of this thesis. XRF works using the same principle described in Section 3.6.3 where the ionising radiation takes the form of an X-ray beam. The sample ionisation causes the emission of the characteristic photons which are collected as the signal. The collected signal is proportional to the elemental composition and quantification can thus be obtained via calibration with known standards.

Large samples (~10 g) are used to improve counting statistics and are formed into pucks via either vitrification or encapsulation in low molecular mass wax. Most XRF instruments work with energy dispersive detectors. As in SEM-EDX, resolving spectral lines with similar characteristic energies can be problematic. Also the detection of low atomic mass components is difficult due to the attenuation of X-rays in air, the energy range of common detectors and increased proportion of Auger electron produced by these elements.

3.9 - Laser Particle Size Analysis (PSA)

Laser PSA is used to measure the particle size distribution of powders, most commonly in liquid suspension. A laser beam is passed through the powder suspension and the angular variation of the light scattered by the particle is measured. The scattering angle is dependent on the particle size, larger particles scatter light at a smaller angle and smaller particles scatter light at a larger angle. The measurements can be used to determine the distribution of particles sizes from a given suspension without knowledge of the solids light scattering properties by use of the Fraunhofer approximation. This returns data on the spread of particle sizes by assuming the existence of a spherical particle geometry.

Particle size was determined using a Coulter LS130 particle analyser with a 750 nm wavelength laser, settings of 45% PIDS and 7% obscuration. Sonication was applied during sample loading, measurements and intervals. Results were averaged over 15 runs of 120 seconds using triplicate samples. Calculation was performed using the Fraunhofer optical model, including PIDS conditions.

3.10 - Aqueous Durability Protocols

A number of standardised and non-standardised protocols exist for investigating aqueous dissolution of glass in aqueous solutions. These protocols aim to determine either the mechanism for dissolution, provide information on the elemental release rates or to produce a comparative assessment of product quality. Almost all protocols developed tend to focus on one of two things to provide the information relevant to leaching properties; i) the chemistry of the aqueous leachate; or ii) changes in the glass samples, such as the formation of alteration layers/mass loss. The most information can be gathered from protocol methodologies which analyse both the solution and the solid.

Due to the complexity of the aqueous dissolution mechanism of glass, as discussed in Section 2.2.3, designing a single protocol capable of providing all this information simultaneously is problematic. Therefore multiple protocols have been utilised during the course of this thesis to provide insight into both comparative qualities and where considered reasonable, to allow speculation on the dissolution mechanisms at work.

3.10.1 - Product Consistency Test (PCT)

This protocol was developed to determine the consistency with which HLW glasses were being produced, in terms of their aqueous durability and subsequently to provide a method to efficiently, readily and reproducibly test glasses anywhere in the world [191]. The PCT is an accelerated leaching experiment, carried out using powdered glass samples in an aqueous solution with a high surface area to volume ratio (SA/V). The elemental concentration of the leachate is analysed using ICP-AES or ICP-MS and normalised using the wasteform's elemental composition in order to provide a normalised elemental mass loss value (NL_i). This can in turn be used to provide a normalised elemental loss rate (NR_i).

Normalised mass losses were calculated using Equation 3.6.

$$\mathrm{NL_i} = \frac{\mathrm{C_i}}{\mathrm{f_i} \times \frac{\mathrm{SA}}{\mathrm{V}}} \qquad \textbf{Equation 3.6}$$

where NL_i is the normalised elemental mass loss of element i (g m^{-2}), C_i is the concentration of element i in solution (g m^{-3}), f_i is the fraction of element i in the unleached waste form and SA/V is the ratio of glass surface area to the volume of water (m^{-1}).

C_i is calculated according to Equation 3.7.

$$\mathrm{C_i} = \mathrm{C_{sample,average}} - \mathrm{C_{blank,average}} \qquad \textbf{Equation 3.7}$$

NR_i can be calculated from PCT testing in g m^{-2} day^{-1} using Equation 3.8.

$$\mathrm{NL_i} = \frac{\mathrm{C_i}}{\mathrm{f_i} \times \frac{\mathrm{SA}}{\mathrm{V}} \times t} \qquad \textbf{Equation 3.8}$$

where t is the time of sampling in days.

Experimental Parameters

The assessment followed the procedure of ASTM standard C 1285 – 02 (Product Consistency Test - PCT), using 18.2 MΩ H_2O at 90 °C in 15 ml PFA pots produced by Savillex unless

otherwise stated [192]. Samples were analysed in triplicate, with reference to duplicate blanks at intervals of 3, 7, 14 and 28 days. Leachate samples were performed on 1% HNO_3 acidified samples using either ICP-AES (Spectro Ciros ICP-AES instrument, University of Manchester) or ICP-MS (Agilent 7500cx at the University of Manchester or a DRC PerkinElmer SCIEX ICP-MS ELAN 6100 at Forschungszentrum Jülich). The stated error is three time the maximum standard deviation measured between the data obtained from the triplicate samples as measured via ICP-AES unless otherwise specified. NL_i were calculated according to Equation 3.6 and NR_i were calculated according to Equation 3.8.

3.10.2 - MCC-1

The MCC-1 protocol is the ASTM standard test method for the dissolution of monolithic samples of glass and glass ceramic wasteforms [193]. It is similar to the PCT test, however, it utilises a low SA/V with a monolithic sample. This results in solution saturation being reached more slowly, allowing a more accurate interpretation of initial dissolution rates. The other major benefit of this protocol is the ability to examine the surface layers which form during dissolution and to correlate these with the concentration of leached elements in solution. This can provide useful mechanistic insights into the dissolution of the glass matrix as described in Section 2.2.3. NL_i and NR_i values were calculated using an identical methodology to those in PCT experiments.

Experimental Parameters

MCC-1 experiments were performed and analysed according to ASTM Standard C1220-98. This test methodology is identical to the method described above for the PCT experiments with the following alterations; monolithic samples were placed in 60 ml PFA jars fitted with a sample basket exception and a SA/V of 10 m^{-1} was used [193].

In Chapter 4 the experimental method deviated from the ASTM standard as cylindrical rather than cuboidal monoliths were used. The surface area of the composite pellets was calculated geometrically using the Image J software package. Scaled images were taken of both the faces of the cylinder, which were used to calculate the surface area and circumference of each face. The thickness of the pellets was measured using Vernier callipers. NL_i and NR_i values were calculated as per the PCT experiment.

3.10.3 - Single-Pass Flow-Through (SPFT) Experiments

The SPFT experiment has been employed extensively to determine the kinetics of glass dissolution in aqueous solutions [194-200]. The experiment is beneficial as it minimises the uncertainty inherent in static experiments which result from the solution based effects described in Section 2.2.3. By performing the experiment in a solution which is constantly replenished, the effects on dissolution from glass components in solution are minimised. This allows for the separation and independent study of a range of the parameters which affect the kinetic properties of glass dissolution. These include the effects of pH, temperature, solution composition and alteration layers.

The normalised elemental loss rate for each element can be calculated using Equation 3.9.

$$NR_{i,j} = \frac{C_{i,j} - C_{i,0} \times q}{f_i \times S} \qquad \textbf{Equation 3.9}$$

Where $NR_{(i,j)}$ is the normalised elemental loss rate for element i at sampling j (g m^{-2} day^{-1}), $c_{i,j}$ is the concentration of element i at sampling j (g m^{-3}), $c_{i,0}$ is the average concentration of i observed in the eluent, q is the flow rate (m^3 day^{-1}), f_i is the elemental fraction of i in the glass wasteform (dimensionless) and S is the surface area of the glass (m^2).

The experimental methodology is outlined below and has been reviewed and validated in [201].

3.10.4 - Implementation of SPFT

Samples for SPFT were prepared using the HIP as described in Section 3.3 and the relevant technical chapters. For each composition under investigation, samples were synthesised and prepared in triplicate using an identical methodology. After processing in the HIP the welds on the canister lids were removed using a Buehler Abrasimet cutting saw. This allowed for the removal of the sample end caps. The sample was then placed in a bench vice and pressure applied to the canister walls to produce a set of fragments/powder from the monolith via fracturing.

The retrieved sample from each canister was powdered using a hardened steel percussion mortar and sieved to obtain the 106-180 µm powder fraction. The following cleaning regime was utilised to remove residual fines from the powders. The powders were washed three

times with ethanol from a squirt bottle, using three times the volume of powder. The ethanol was then decanted after each wash. The powders were then covered with ethanol and placed in an ultrasonic bath for 2 minutes. This process was repeated in triplicate prior to drying the powders in a 110 °C oven for 24 h. A BET surface area was recorded using a Coulter SA 3100 BET surface area analyser, to allow comparison of the BET and geometric surface areas.

The reactor vessels utilised in the SPFT experiments were 60 ml PFA jars fitted with a 53 mm PFA closure containing two 3.175 mm tube ports. PFA tubing (3.175 mm OD) was used to connect the reactor vessels to both the pump and effluent input/outputs. All PFA based lab wear was provided by Savillex. A Watson Marlow 205S pericyclic pump fitted with an eight station pumping cassette was used to pump the eluent solutions, this allowed for up to 8 solution compositions to be utilised using a single pump.

Prior to beginning the experiment all vessels were cleaned and prepared according to the ASTM PCT standard, as described in [202]. A solution of 1 x 10^{-4} M HNO_3 was used to flush the reactor vessels and tubing for four days to determine if any contamination was present in the vessels or lines and to stabilise the pump flow rate. Three samples were taken during this period and analysed via ICP-MS for contamination prior to insertion of the samples into the reactor vessels. When reactor vessels were not in use, a continuous flow of 1 x10^{-4} M HNO_3 eluent was maintained.

Prior to the insertion of samples in the reactor vessels, 10 L of eluent was prepared for each reactor vessel to be used. Five eluents were used in this study to provide a pH range from 2-10 at 90 °C. These eluents are described in Table 3.1. Un-buffered solutions were selected for pH 2, pH 4 and pH 7 to limit the introduction of solubilising organic materials in the eluent. The pH change of all eluents was modelled using the PhreeqC geochemical modelling code with the LLNL database to provide the pH at 90°C and is provided in Table 3.1.

A 30 ml sample of the eluent solution was taken for analysis immediately after preparation and 24 hours later. These samples were used to measure the input pH and to prepare ICP-MS samples in order to provide the background concentration of the eluent for blank subtraction.

To start each experiment the reactor vessels were removed from the oil bath, taken apart and the existing eluent discarded. Care was taken to avoid contamination of the vessel interior during sample insertion. The vessel was rinsed with the new eluent and 10 ml of eluent was added to the vessel before the powder sample. This eluent helped to eliminate

static charging in the powders and subsequent 'jumping'. The samples were inserted into each reactor vessel to obtain the desired log(Q/S) range and resealed. The pump was turned to maximum speed until the first flow from the test vessel was observed, then returned to the desired pumping rate. The pump rate (Q) was set to 2.5 x 10^{-4} m^3 day^{-1} and the log(Q/S) was varied by alteration of sample mass in the reaction vessel.

The flow rates used and log(Q/S) were determined with reference to data obtained by static experiments and the available literature, to ensure the reaction lay in the forward rate regime, where log(Q/S) < -7.1 and the concentrations in solution would be measurable via ICP-MS. The NR_i from the PCT static batch experiments after three days were used with Equation 3.8 to estimate the expected change in concentration during testing.

From this information it was determined that measurable concentrations would be best determined near the point where log(Q/S) = -7.1. The exact experimental conditions used are presented in Chapters 6 and 7.

Buffer solution	**Reagents to make 10L of solution**	**pH (25°C)**	**pH (90°C) ***
0.01 M HNO_3	HNO_3 (6.86 ml, 15.2 M) in 10L distilled water	2.00	2.00
0.0001 M HNO_3	HNO_3 (75 µL of 15.2 M) in 10L of distilled water	4.00	4.01
Deionised water	Deionised water	5.7 - 6.8 (CO_2 dependant)	6.22**
LiCl : LiOH (0.004 M : 0.001 M)	LiCl (1.6956 g) and LiOH (0.2395 g) in distilled water (9.995 L). Acidified with 0.5 M HNO_3 (5 ml).	10.68	9.07
LiCl : LiOH (0.004 M : 0.004 M)	LiCl (1.7 g), LiOH (0.96 g)	11.57	9.97

Table 3.1 - List of Buffer solutions, their respective compositions and pH values. *modelled using PhreeqC geochemical program- database LLNL. **assuming degassing of solution at 90 °C.

During the experiment, the effluent was collected in storage vessels. These were weighed during sampling to determine the flow rate during the experimental period. Samples of ~35 ml of effluent solution were collected. 13 ml of each solution was filtered to determine whether colloids or solids were present in the solution. Both the filtered and unfiltered

samples were prepared and submitted for ICP-MS analysis as undiluted, 1:10 and 1:100 solutions to provide a range of analysis possibilities for the various elements using ICP-MS. The remaining solution was used to record a pH reading for the sample.

The SPFT set up which was utilised is shown in Figure 3.5.

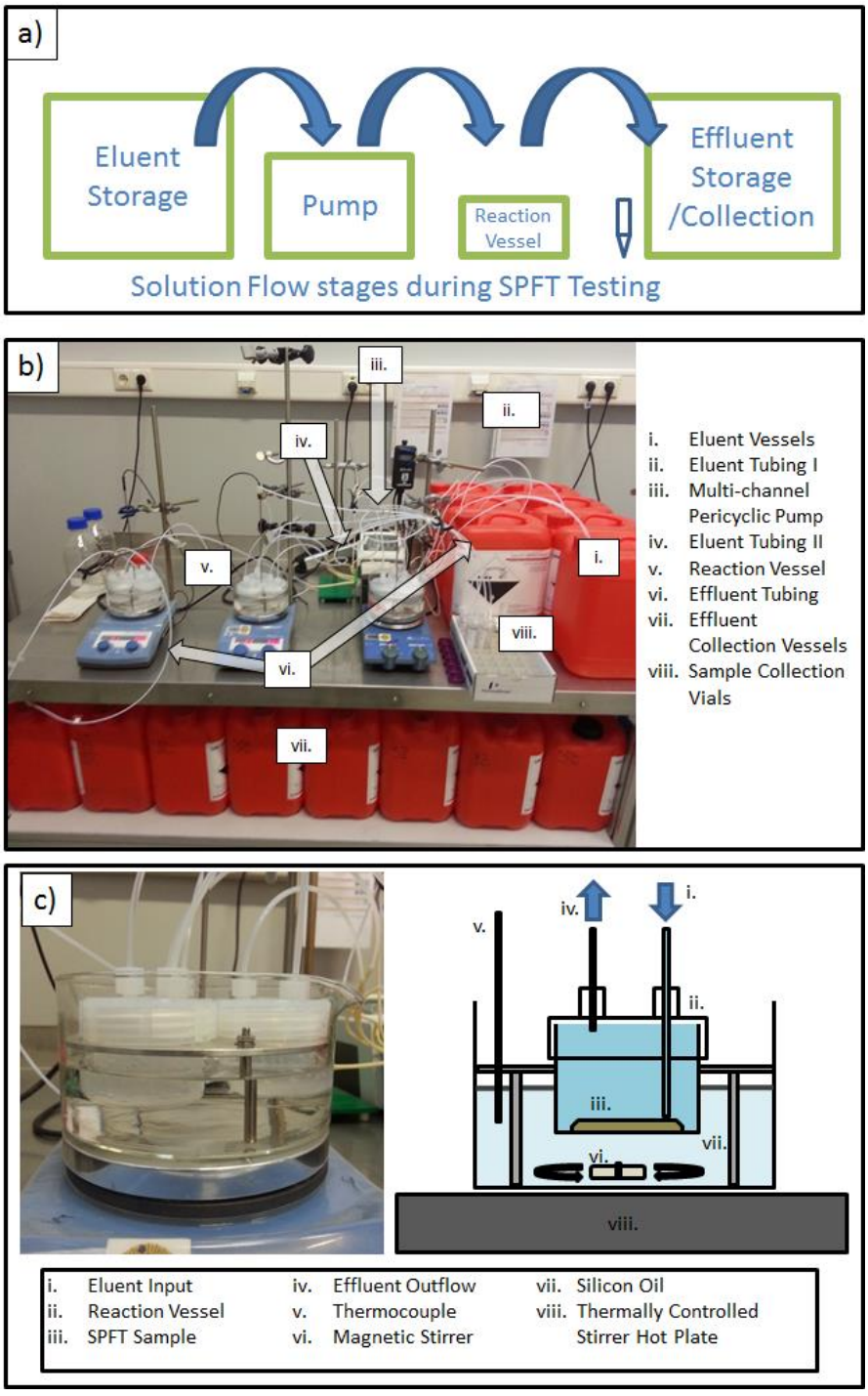

Figure 3.5 - Images illustrating a) the main stages of solvent flow during SPFT b) the experimental set up utilised and c) the reaction vessels.

3.11 - Inductively Coupled Plasma - Chemical Analysis (ICP)

ICP is a methodology used to quantify the concentration of elemental species in a solution [203]. The two most commonly utilised methods are ICP-Atomic Emission Spectroscopy (ICP-AES) and ICP-Mass Spectroscopy (ICP-MS). Both methods produce a sample signal using a similar methodology, however, the detection techniques and sensitivity vary greatly. These differences are outlined in Sections 3.11.1 and 3.11.2.

In both methods acidified solutions are passed through a nebuliser to create a fine aerosol, this is then injected into a plasma flame of ionised Ar atoms (Ar^+) and electrons. In the plasma, collisions of the sample with the high energy Ar^+ ions and electrons cause the excitation and ionisation of the sample atoms. Due to the sensitivity of these techniques they are ideally carried out in a clean room with the purest reagents possible in order to avoid contamination of the samples.

3.11.1 - ICP-AES

The emission of characteristic photons associated with electron excitation, as described in Section 3.6.3, is used to quantify elemental concentration in ICP-AES. Each element has a characteristic photon emission wavelength, the photons produced are then separated using a diffraction grating prior to detection using a photomultiplier. The final signal count obtained is proportional to solution concentration and is quantified via calibration with standards of known composition. Detection limits for ICP-AES can be as low as 0.1 - 10 ppb, although for accurate quantification, concentrations around 100 times greater are required.

3.11.2 - ICP-MS

ICP-MS ionises atoms as described in Section 3.6.3. These ionised atoms are then passed into a vacuum chamber through a number of cones to create a beam of plasma. This beam passes through a hexapole collision cell to lower the kinetic energy of the incoming ions, is then deflected to split the ionic component from the photons and this separated ionic component then enters a quadrapole mass spectrometer. Here the mass to charge ratio of ions allows for separation of the ions prior to detection. As in ICP-AES, elemental signal intensity is proportional to concentration and quantification of the sample is achieved by comparison with calibration of standards. Detection limits for ICP-MS can be as low as 0.01 - 1 ppt, although for accurate quantification, concentrations around 100 times greater are required.

3.12 - Mechanical Testing

The behaviour of vitreous wasteforms takes that of brittle, fracture prone materials. It is important to qualify the potential for fracturing in these materials as it is possible any such fracturing would result in readily dissolved fines [204]. Fracture toughness has been reported to be the primary property of interest in determining the propensity for wasteform fracture [205].

The fracture toughness and hardness were measured in this study utilising the Vickers indentation methodology. This method applies a defined load to a polished sample with parallel sides using a square pyramidal diamond tip. The load is held for a set time and then the indent and any fractures emanating from the indent are measured. A typical indent from Vickers hardness testing is displayed in Figures 3.6 b) and c).

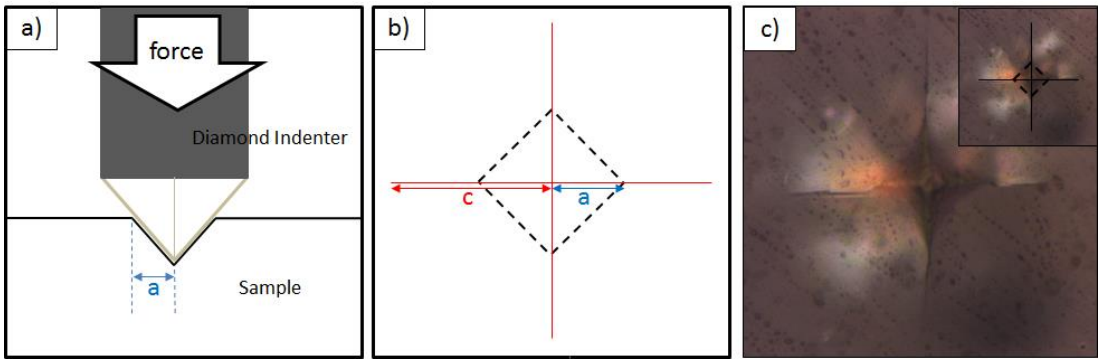

Figure 3.6 - Schematics of a) the indentation process and b) a typical indentation profile with the dimensions of both the crack for use with Equations 3.13 and 3.14. c) a typical indent as obtained during measurements in this thesis, with an inset picture illustrating the indents characteristic features.

The Vickers hardness (H_v) in Pa was calculated using Equation 3.10.

$$H_v = \frac{1.854P}{(2a)^2} \qquad \textbf{Equation 3.10}$$

where *P* is the load in Newtons, and *2a* is the average diagonal length of the impression in m.

Fracture Toughness (K_c) was calculated using Equation 3.11 [205].

$$K_c = \frac{0.0824P}{c^{3/2}} \qquad \text{Equation 3.11}$$

where c is average crack length in m.

The Vickers hardness indentation test methodology was used to determine both hardness (H_v) and fracture toughness (K_c) following the procedure described by Connelly in [205] and Equations 3.12 and 3.13 respectively. Indentation was performed on a Mitutayo HM-101. Sixty indents were made at each of three indentation loadings; 0.98 N, 1.96 N and 2.94 N (twenty indents at each force per sample, error ± 0.02 N). The load was held for 20 seconds. Samples were left for 24 hours prior to analysis using optical microscopy. The results quoted are those obtained from the 1.96 N loading due to the higher number of acceptable indentations (a minimum of fifteen per sample).

3.13 - Vertical Scanning Interferometry (VSI)

Vertical scanning interferometry is utilised to produce a topographical image of an objects surface. It makes use of the wave like behaviour of beams of light. When these beams have wavelengths in phase they provide constructive interference and when they are out of phase they will show destructive interference [206]. A VSI instrument utilises this principle by shining a collimated light beam onto a beam splitter to produce a pair of light beams. The first, a reference beam, travels a known distance, reflecting off a mirror while the second beam is shone onto the sample surface. They are then re-collimated and detected by a camera [207]. A schematic of the operation of a white light vertical scanning interferometer is shown in Figure 3.7.

When the distance travelled by the two beams is identical, the beams will be in phase, producing positive interference and the detector will show the brightest region, when they are completely out of phase the detector will measure the darkest region. These patterns are known as fringes.

To produce a topographical image the interferometer moves the interferometry objective by known distances to vary the sample beam length. Modern computers and cameras can detect the fringe patterns for every pixel in an image and the topological image is then computed from the data based on the brightest fringe patterns [208].

VSI has been utilised recently not only to study the surface topography of samples but also to quantify the retreat of a surface during dissolution and to measure the differential retreat rates of different crystallites over a wide field of view [209-211].

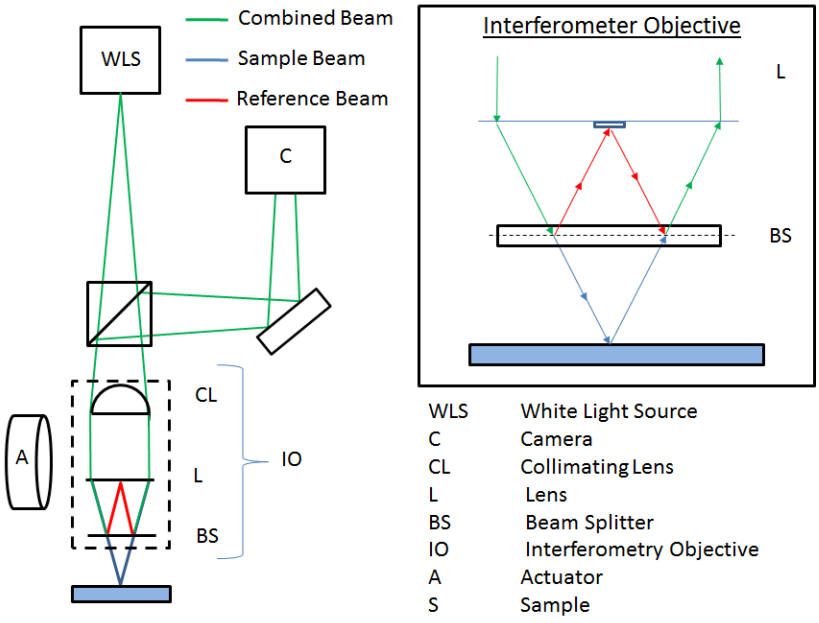

Figure 3.7 - Schematic of vertical scanning interferometer, fitted with a Mirau interferometer aperture. The paths taken by each beam is displayed with the inset of the Mirau interferometry objective. (Figures adapted from [207, 208]

VSI analysis was performed at MARUM (Zentrum für Marine Umweltwissenschaften, Univeristät Bremen). A Ziemetrics Zemapper optical profilometer with a 2048 x 2048 pixel CCD camera, Nikon objectives (5x, 20x and 50x), white light LED illumination (centre wavelength = 560 nm) and a Mirau objective was used. This instrument was mounted on air-suspension tables in a vibration-isolated laboratory. The instrument was also fitted with a P-736 piezodriven nano-positioning X,Y stage and E-710 digital piezo-controller. All measurements and analysis were performed using the Spip v.6.2.6 software package.

3.14 - Dilatometry

Dilatometry can be used to measure the TEC of a material. The material is placed inside a furnace where a linear variable differential transformer (LVDT) is in contact with the end of the sample [212]. As the sample is heated the LVDT produces a signal proportional to the expansion of the sample. By calibration of this movement with samples of known TEC, the linear TEC of the material can be calculated. In the course of this study all stated TEC are provided from an averaged combination of 10 runs with a relative standard deviation (RSD) < 5% obtained. A fused SiO_2 standard was used as to calibrate the instrument before each set of analyses.

Dilatometric analysis was used to determine the TEC of cuboidal glass monoliths with dimensions of 5 x 5 x 15 mm. Monoliths were cut from the annealed melt using a diamond edged slow saw. Dilatometry was performed on a Netzsch DIL 402C dilatometer from 25 - 300 °C with a heating rate of 2 °C min^{-1}. The TEC was determined using the Netzsch Proteus software package.

3.15 - Helium Pycnometry

Helium pycnometry is a method for measuring the volume of sample whether it be monolithic or powdered. The knowledge of the volume and samples mass then allows for calculation of a samples density. The principle of operation is based upon the pressurisation of two chambers of known volume. By measuring the deviations in pressure of gases pumped into these chambers from calibration, the volume supplied from the sample can be calculated.

All pycnometry measurements made in the course of this thesis were performed with an AccuPyc 1340 II pycnometer. The following parameters were used; 200 purges of the chamber followed by 50 cycles using an equilibration rate of 35 Pa min^{-1} at 25 °C in a 1 cm^3 chamber and a fill pressure of 86.2 KPa .

3.16 - Archimedes Density Measurements

The density of monolithic samples were measured using the Archimedes principle according to Equation 3.12. All sample measurements were performed in triplicate with new samples. Water was used as the immersion medium, with an assumed water density at 25 °C of 0.9977 g cm^{-3}.

$$\rho_{sample} = \frac{mass_s \times \rho_{H_2O}}{mass_{s.i} \times (mass_{s,d} - mass_s)} \qquad \textbf{Equation 3.12}$$

Where ρ_{sample} is the monolith density in g cm^{-3}, $mass_s$ is the initial monolith mass, ρ_{H2O} is the density of water, $mass_{s,i}$ is the measured mass of the immersed sample and $mass_{s,d}$ is the mass of the sample once removed from the vessel and pat dried with a paper towel.

3.17 - Geochemical Modelling

Geochemical modelling is a method which utilises thermodynamic data, kinetic data or a combination of the two to simulate the behaviour of chemical reaction in systems relevant to both solution based and geological systems [213]. It has been utilised in the course of this thesis to provide information on the saturation of phases of interest under set conditions and of the alterations in solution pH dependant on temperature.

This modelling was performed using the PhreeqC geochemical modelling code (v3-12-8538, provided by the United States Geological Survey). Data was input using either known or measured variables which the model used to calculate the equilibrium values. All data utilised in this study was collected using the Lawrence Livermore National Laboratory (LLNL) thermodynamic database.

Chapter 4 - Encapsulation of TRISO Fuel Particles in Sintered Glass Composites

4.1 - Chapter Introduction

Tri-Structural Isotropic (TRISO) coated particulate fuel is a key component in concepts for Generation IV high temperature nuclear reactors. This study investigated the suitability of four glass compositions for the encapsulation of simulant TRISO particle fuels, with comparison to the SON68 base glass previously studied for this purpose (SON68 is an inactive simulant of the French R7T7 HLW glass). The chapter is separated into three sections; firstly the study of soda lime silicate (SLS) glass compositions, secondly a study of an optimised alumina-borosilicate glass composition (ABS-1) and finally the application of HIPing to the production of these composite wasteforms.

The main body of Sections 4.3 and 4.4 are based on the two following publications. The currently unpublished work in Section 4.5 describes the application of HIPing to wasteform processing. Alterations to the structure and the text have been applied where necessary to create a cohesive narrative.

1. P.G. Heath, C.L. Corkhill, M.C. Stennett, R.J. Hand, W.C.H.M. Meyer, N.C. Hyatt, Encapsulation of TRISO particle fuel in durable soda-lime-silicate glasses, *Journal of Nuclear Materials*, **436** (2013) p.139-149.
2. P.G. Heath, M.C. Stennett, O. J. McGann, R.J. Hand, N.C. Hyatt, The Use of High Durability Alumino-Borosilicate Glass for the Encapsulation of High Temperature Reactor (HTR) Fuel, *MRS Proceedings* **1518,** (2013), p.3-8.

4.2 - Materials and Experimental

4.2.1 - Materials

TRISO Particle Simulant

A non-active TRISO particle-fuel simulant was supplied by PBMR Ltd (South Africa) for use in these studies. This simulant contained a surrogate zirconia core (ZrO_2) in the place of UO_2. The density of the simulant was measured using helium pycnometry and determined to be

2.6640 ± 0.0005 g cm^{-3}. An average particle radius of 0.87 mm ± 0.03 mm was recorded across a range of 50 particles using Vernier callipers. TRISO Particles are described in more detail in Section 2.4.1 and the layered structure is illustrated in Figure 4.1 a).

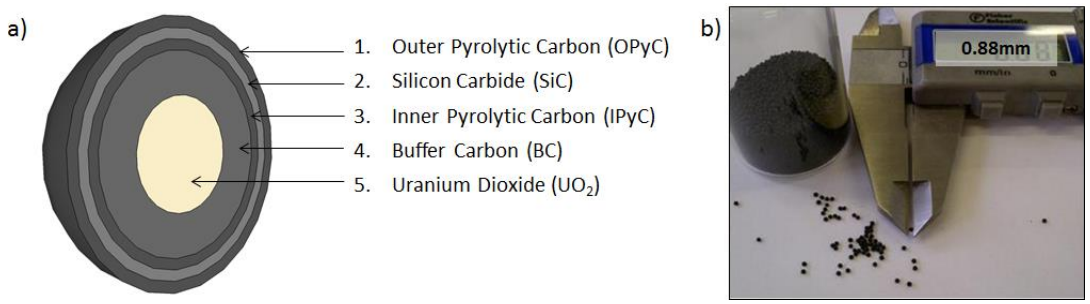

Figure 4.1 - a) Illustration of the layers structure of TRISO fuel Particles (ZrO_2 surrogated for UO_2 in this study) and b) image of TRISO particle simulant utilised in this study.

SLS Glasses

Three different compositions of SLS glasses were prepared for use in this study which are identified from this point as SLSA, SLSB and SLSC. The nominal and analysed compositions of these glasses are provided in Table 4.1. Batches were produced using appropriate quantities of analytical grade reagents (SiO_2, $NaCO_3$, $CaCO_3$, H_3BO_3 and $(MgCO_3)_4.Mg(OH)_2.5H_2O$, >99 % purity). Batches were made to produce 500 g of glass and preheated in alumina crucibles overnight at 1100 °C. These crucibles were then transferred into a preheated, top loading gas furnace. This furnace was subsequently ramped to 1500 °C and left to dwell at this temperature over a five hour period. The melts were poured into pre-heated blocks prior to annealing at 525 °C for one hour. Cooling to room temperature was then performed with a ramp rate of 1 °C min^{-1}. Glass powders were produced using a Temer ring and puck mill. These powders were sieved to collect the sub-75 µm fraction for use in pellet formation as described in Section 4.2.3. The mean particle size of the powdered glasses SLSA, SLSB and SLSC was measured at 37 ± 27 µm, 39 ± 30 µm and 31 ± 23 µm respectively using laser PSA.

SON68 Glass

Batches were made to produce 200 g of glass using appropriate quantities of analytical grade reagents (SiO_2, $NaCO_3$, $CaCO_3$, Li_2CO_3, $Al(OH)_3$, $(ZnCO_3)_2.(Zn(OH)_2)_3$, ZrO_2, and H_3BO_3, >99 % purity). The melt was produced in a mullite crucible by ramping to 900 °C at 3 °C min^{-1} in an electric muffle furnace and then ramping to 1350 °C at 10 °C min^{-1}. The melt was left to dwell at this temperature over a two hour period. The melt was poured into pre-heated steel

blocks before annealing at 500 °C for one hour. Cooling to room temperature was subsequently performed at 1 °C min^{-1}. An identical preparation and analytical procedure to that employed for the SLS glasses was performed. The mean powder particle size of the sieved fraction was determined to be 48 ± 33 µm using laser PSA.

ABS-1

Batches were made to produce 500 g of glass using appropriate quantities of analytical grade reagents (SiO_2, $NaCO_3$, $CaCO_3$, $Al(OH)_3$, $MgCO_3$, and H_3BO_3). Batches were preheated in alumina crucibles in an electric muffle furnace overnight at 1100 °C, these were then transferred to a top loading gas furnace before ramping to 1650 °C at a rate of approximately 10 °C min^{-1}. The melts were left to dwell at this temperature for a two hour period before casting. Melts were collected either as a monolith or as a frit. An identical preparation and analytical procedure to that used for the SLS glasses was performed. The mean particle size of the sieved fraction of ABS-1 glass powder produced was 40 ± 20 µm measured using laser PSA.

4.2.2 - Sample Preparation and Analysis

Pellet Formation

Glass pellets (~2 g) were formed by the uniaxial pressing of glass powders in a 13 mm hardened steel die, using a load pressure between 15 - 40 MPa. Depending on their composition, pellets were sintered at three temperatures between 650 °C and 800 °C for 15, 30 and 60 minutes. This data was used to define a densification profile for each glass. Powder XRD was performed on the sintered glass pellets to determine if they maintained their amorphous nature during heat treatment.

Compositional Analysis

Compositional analysis was performed using X-ray Fluorescence Spectroscopy (XRF) on a Phillips PW2404 XRF Axios by AMG Superalloys (formerly LSM analytical). Compositional analysis for boron was performed via acid digestion of the sample and ICP-AES analysis, also performed by AMG Superalloys.

Glass component (mol %)	Sample I.D.				
	SLSA	**SLSB**	**SLSC**	**SON68**	**ABS-1**
SiO_2	69.00 [68.23]	74.00 [74.86]	74.00 [76.76]	60.50 [53.29]	72.20 [72.24]
Na_2O	15.00 [13.31]	15.00 [12.73]	15.00 [13.04]	7.00 [5.81]	7.10 [7.16]
CaO	15.00 [12.90]	10.00 [8.70]	5.00 [4.52]	5.75 [4.34]	2.60 [2.68]
B_2O_3	1.00 [1.72]	1.00 [1.20]	1.00 [1.53]	16.10 [19.54]	8.20 [8.23]
Al_2O_3	- [1.75]	- [0.14]	- [0.71]	2.60 [8.32]	8.60 [8.63]
MgO	- [< 0.03]	- [0.03]	5.00 [2.32]	- [0.07]	0.10 [0.98]
P_2O_5	- [< 0.12]	- [< 0.07]	- [< 0.12]	- [< 1.10]	- [< 0.05]
Fe_2O_3	- [< 0.13]	- [< 0.08]	- [< 0.13]	- [0.15]	- [< 0.05]
SO_3	- [< 0.07]	- [< 0.04]	- [< 0.07]	- [< 0.06]	- [< 0.05]
K_2O	- [< 0.08]	- [< 0.05]	- [< 0.08]	- [0.30]	- [< 0.05]
BaO	- [< 0.13]	- [< 0.08]	- [< 0.13]	- [1.12]	- [< 0.05]
Li_2O	- [< 0.02]	- [< 0.01]	- [< 0.03]	5.30 [1.22]	- [< 0.05]
ZnO	- [< 0.07]	- [< 0.04]	- [< 0.07]	2.40 [3.70]	- [< 0.05]
ZrO_2	- [< 0.10]	- [< 0.06]	- [< 0.10]	0.35 [0.86]	- [< 0.05]
Density ($g\ cm^{-3}$)	2.578 ± 0.003	2.535 ± 0.003	2.486 ± 0.003	2.522 ± 0.003	2.360 ± 0.003
TEC ($10^{-6}\ K^{-1}$)	11.4 ± 0.2	11.2 ± 0.2	10.6 ± 0.2	8.62 ± 0.2	7.2 ± 0.2
T_g (°C)	595 ± 5	583 ± 5	555 ± 5	527 ± 5	610 ± 5

Table 4.1 - Properties of all glasses produced in this chapter including composition as batched, composition as analysed via XRF ICP-AES analysis, theoretical density from pycnometry of powder samples, thermal expansion coefficients from dilatometry and glass transition temperature (T_g) from DTA. Errors on XRF measurements estimated to ±2 % of presented values. Numbers in [brackets] indicate analysed composition.

Composite Formation and Preparation

Composite pellets were formed by an identical process to that described above yet with the addition of 10 wt% TRISO particle simulant mixed into the glass powders prior to pressing. Pellets and composites were sintered in a tube furnace, either under air or in a reducing atmosphere of 5% H_2/N_2. Temperatures between 700 ˚C and 750 ˚C were used with dwell times between 15 and 360 minutes.

Sintered composites were sectioned using a diamond edged slow saw, cold mounted in resin, then ground and polished to a 1 μm finish for examination via optical and electron microscopy. Grinding was performed using 600 and 1000 grit diamond matrix plates and polishing using lapping pads with 6 μm , 3 μm and 1 μm diamond pastes.

HIPing of ABS-1 Glasses

The HIPing of ABS-1–TRISO particle composite was performed using two different canister designs and sizes. Tube-coin canisters were produced with a diameter of 38.1 mm and an approximate internal volume of 60 cm^3, as described in Section 3.3. These canisters were processed with waste loadings of 0 wt%, 10 wt%, 20 wt%, 30 wt%, 40 wt% and 50 wt% TRISO particles by BodyCote, Chesterfield. The canisters were filled using vibratory packing. The canisters underwent a vacuum bake out prior to sealing to obtain a 3.3 Pa vacuum at a temperature of 300 °C. HIPing was performed at 750 °C with a dwell time of 30 minutes, ramp rates of 10 °C min^{-1} and temperature dependant pressure profile.

A second set of canisters were produced using a modified tube-coin design with an outer diameter of 15.1 mm. The coin base of the canister was substituted for a flat base produced by pressing the tube to form a crimped parallel surface which was sealed with a butt weld. This allowed for sample mounting using a vice without the application of pressure to any region of the canister which contained sample. Unfortunately it also excluded the use of vibratory packing due to the inability of these canisters to stand on a vibratory table. Otherwise, all processing parameters were identical. All canisters were HIPed at the University of Sheffield's HIP facility using an AIP 6-30H HIP.

HIP sample Retrieval

The retrieval of the sample from the canisters was attempted with varying success using numerous processing techniques, as is discussed further in Section 4.5.1 and 4.5.2. The basic methodology in each case involved mounting the canister, sectioning the canister to obtain a monolith and preparing the monolithic sample for study. Mounting methodologies included the use of clamp-vices, micro screw vices, hot wax mounting and torque adjusted

clamp vices. Sectioning was performed or attempted utilising a Buehler Isomet 5000 fitted with a 0.9 mm diamond blade, a Buehler Abrasimet abrasive saw fitted with a 1.6 mm diamond blade, a Buehler Isomet slow saw fitted with a 0.3 mm diamond blade and with a Struers Sectotom 500 fitted with a hard ferrous precision abrasive blade.

Successful monolith recovery was best achieved using the Struers Secotom 500 with the hard ferrous blade and the 15.1 mm HIP canisters. The retrieved monolith samples were mounted in resin and polished to a 0.25 µm finish by hand grinding using P1200 SiC grit paper followed by polishing with 6 µm, 3 µm, 1 µm and 0.25 µm diamond pastes.

Aqueous Durability Experiments

Durability assessment of the glass materials was carried out on powders produced from sintered pellets of SLSA, SLSB, SLSC, SON68 and ABS-1 glasses. PCT type testing using 18.2 MΩ H_2O, 90°C and a SA/V between 2085 m^{-1} and 2270 m^{-1} (dependent on glass density for 75-150 µm glass fraction as noted in Table 4.1) was performed. MCC-1 type testing was also performed on SLSA with a SA/V of 10 m^{-1} and otherwise identical conditions.

4.3 - SLS Glass Compositions

SLS glasses were chosen as the initial base glass for this study because of their commercial importance and compositional simplicity [106]. These glasses were used to develop a test methodology for determining the quality of the composite wasteforms and to provide insight into compositional variations which may be necessary to produce an improved wasteform.

4.3.1 - SLS Glasses - Results

Chemical Compatibility

The chemical compatibility of the glasses and TRISO particle simulant, i.e. the degree to which the OPyC is oxidised to form gaseous CO_2, was evaluated by sintering composites of each formulation at 700 °C for six hours, in air and under a reducing 5% H_2/N_2 atmosphere. When sintering under air a complete oxidative reaction of the OPyC layer occurred, resulting in the exposure of the SiC layer as displayed in Figure 4.2 a). The use of a reducing atmosphere eliminated this oxidative reaction, as shown in Figure 4. 2 b). The OPyC remained completely intact under a reducing 5% H_2/N_2 atmosphere, even when sintered for several hours.

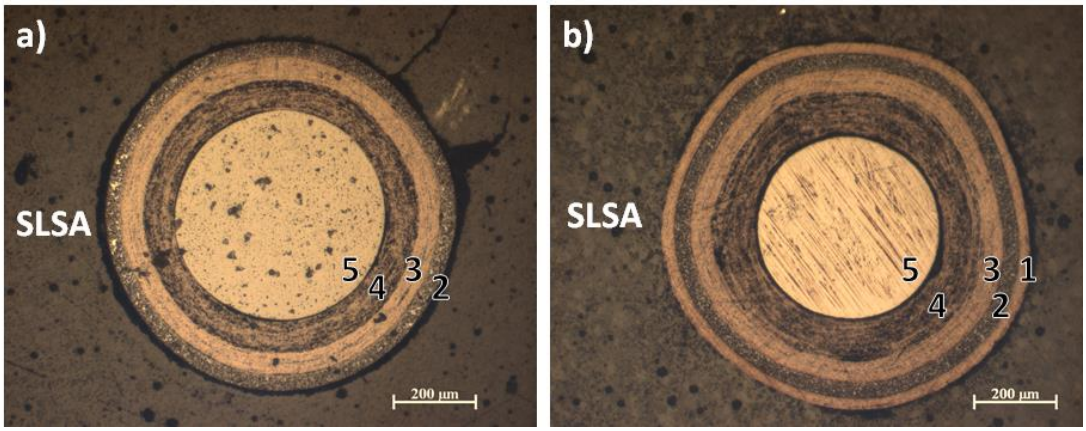

Figure 4.2 - Composite of TRISO particles and SLSA sintered for six hours at 700 °C in a) air and b) (5%) H_2/N_2 atmosphere.

Two methods were utilised to determine the loss of the OPyC layer through volatilisation. The first measured the crucible masses before and after sintering the composite wasteforms. These measurements were constant within ± 0.01 g. The total mass of OPyC contained in each sample was calculated to account for approximately 0.02 g. This analysis therefore indicates that there is no large scale depletion of the OPyC. However, these estimates are prone to a high degree of error due to the number of assumptions required and the potential for mass losses from other sources such as water desorption from the glass powders.

Matrix	Heat Treatment Applied	Average Thickness of OPyC Layer (µm)
Epoxy Resin	None	30 ± 1.7
SLSA	700 °C , 30 minutes, 3 °C min^{-1} ramp rates	31 ± 2.0
SLSB	700 °C , 30 minutes, 3 °C min^{-1} ramp rates	31 ± 2.5
SLSC	700 °C , 30 minutes, 3 °C min^{-1} ramp rates	31 ± 2.4

Table 4.2 - Dimensions for the OPyC layer of TRISO particle simulant both with and without encapsulation in SLS glass compositions sintered under (5%) H_2/N_2 atmosphere.

To better quantify the loss of the OPyC layer, measurements were made on both the untreated TRISO particles and on the TRISO particles after encapsulation. This allowed the characterisation of the physical of the OPyC retreat during oxidation. 150 measurements of OPyC layer thickness were taken on sectioned TRISO particles exposed to no heat treatment

(15 particles, 10 measurements per particle) and an average layer thickness was recorded. This was repeated using TRISO particles in sintered composites (3 compositions, 5 particles per composite, 10 measurements per particle). The results of these measurements are displayed in Table 4.2.

Densification Regimes

Sintering regimes capable of yielding near fully dense compacts of the SLS glass composites were determined. The potential for the oxidation of the OPyC with prolonged sintering times required optimisation of the sintering regime. The optimised sintering regime should produce dense compacts, free of interconnected porosity in the shortest possible time using the lowest possible temperature. This combination would also be beneficial for any future industrial use of the processing technique. Glass pellets (2 g) without TRISO particle additives were sintered under a 5 % H_2/N_2 atmosphere, using nine different sintering regimes, with variations in temperature (650 °C, 700 °C and 750 °C) and time (15, 30 and 60 minutes).

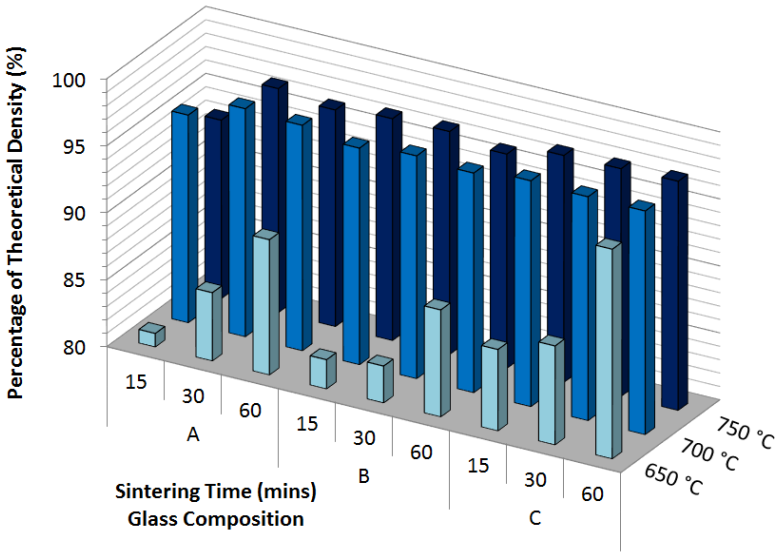

Figure 4.3 - Densification matrix for 2 g pellets of SLS glass compositions across a range of temperatures and times. Errors ± 0.1 %.

The density of these sintered glass pellets was measured using the Archimedes method (precision of ± 0.1 % in quoted densities) to build the sintering and densification matrix provided in Figure 4.3. The three compositions behaved similarity during sintering. SLSC was the most readily densified however this will not be discussed further as a detailed analysis of the effect of composition on sintering of SLS glasses was not performed in this thesis.

Sintering at 600 °C for up to one hour could not produce specimens in excess of 90% of theoretical glass density in all three formulations. Specimens sintered at 700 °C for 30 minutes produced sintered bodies in excess of 95 % of the theoretical density. The attainment of this level of densification is significant as it is indicative of the removal of the interconnected porosity from a sintered body [118]. Little improvement in densification was observed with further increases in either the temperature or the duration of processing.

Composite Characterisation

Glass-TRISO particle composites were produced for formulations SLSA, SLSB and SLSC by sintering at 700 °C for 30 minutes under a 5% H_2/N_2 atmosphere. Figure 4.4 shows that composites of all three glass formulations showed near identical oxidation of OPyC, wetting of TRISO particles by the matrix and residual porosity. Effective densification of all pellets was evident, with a volume reduction between 25 - 30 % (± 5 %). Oxidation of the OPyC in each composite was negligible as shown in Figures 4.4 a-f and Table 4.2. The OPyC layer was found to have a constant thickness of 31 ± 2.5 µm both before and after encapsulation into sintered composites. The wetting of the all three SLS compositions to the OPyC layer was poor. A region of non-contact between the glass matrix and TRISO particle was quantified at 12.9 ± 4 µm, from 120 measurements across 10 particles. This non-contacting area is highlighted in Figures 4.4 d-f. The degree of wetting varied between particles as seen in Figure 4.4 c), however, no particle in any composite showed evidence of effective contact over more than half its perimeter.

In the composites of all three glasses, radial cracks emanated from the TRISO particles into the sintered glass matrix as shown in Figures 4.4 a-c and Figure 4.5. These cracks were often interconnected, producing pathways to nearby particles, as shown in Figure 4.4 b). Residual porosity was retained in composites of all formulations, as displayed in Figures 4.4 g-i.

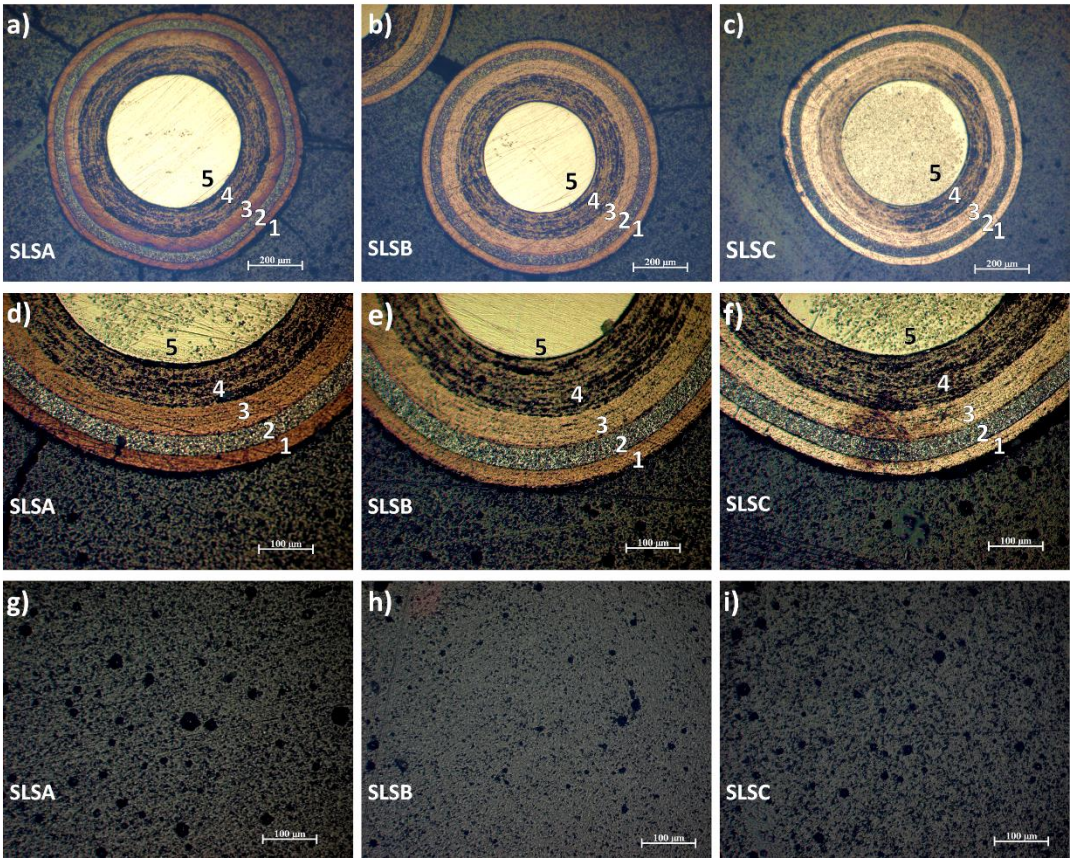

Figure 4.4 - Analysis of glass – TRISO particle composite pellets sintered at 700 °C for 30 minutes under a N_2/H_2 atmosphere of SLSA (a, d and g), SLSB (b, e and h) and SLSC (c, f and i). TRISO particle and matrix integrity (a, b and c), wetting behaviour of matrix with the OPyC (d, e and f) and matrix porosity (g, h and i) are displayed.

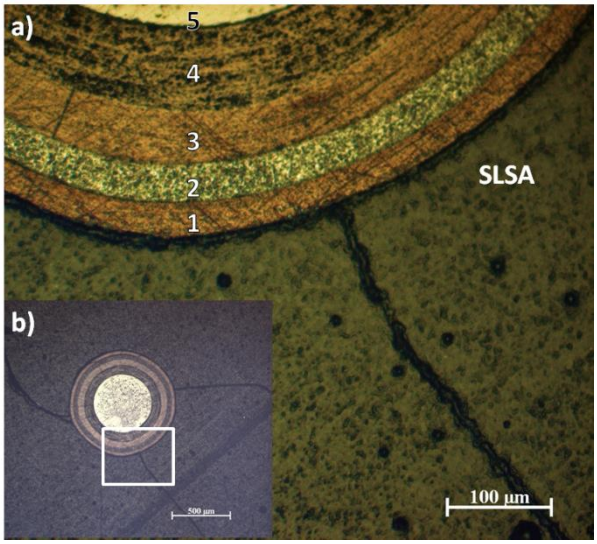

Figure 4.5 - Sintered SLSA-TRISO particle composite a) illustrating radial crack emanating from particle and b) showing the same particle at a lower magnification displaying the extent of the damage to the glass matrix.

Several of these pores were over 10 µm in size, yet this porosity did not appear to be interconnected, as is consistent with a measured density > 95 % of theoretical for the sintered glass compacts.

Crystallisation

Glasses were analysed after sintering using powder XRD. All compositions were found to be amorphous when produced from the melt as indicated by the diffuse scattering shown in Figure 4.6 a). Figure 4.6 b) shows that SLSA and SLSC remained amorphous during the sintering regime. However, a partial crystallisation of α-cristobalite (PDF 04-007-5019) was observed in SLSB.

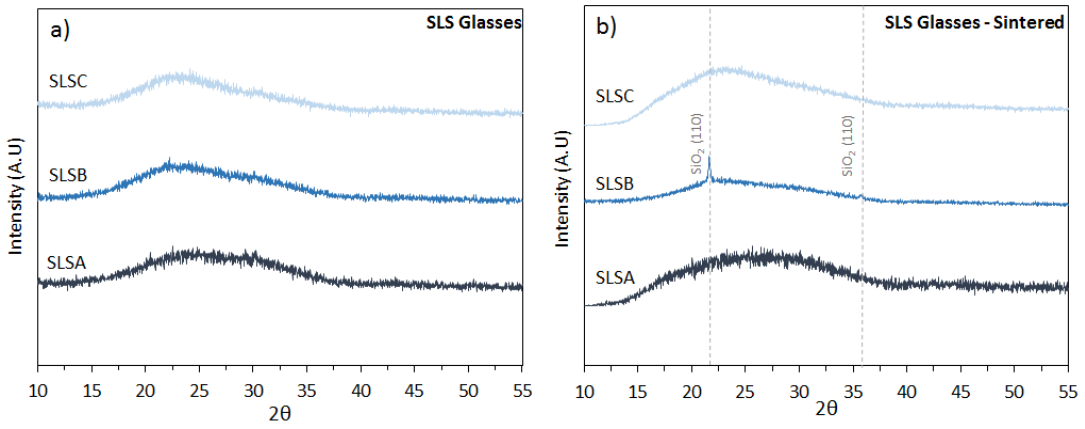

Figure 4.6 - a) powder XRD patterns for SLS glasses prior to sintering and b) after sintering at 700 °C for 30 minutes.

Durability Experiments

PCT: The durability of the glasses after sintering at 700 °C for 30 minutes under a 5% H_2/N_2 atmosphere was assessed using the PCT methodology [192]. The durability of the SON68 base glass was also analysed using an identical methodology. This was performed to allow comparison between SLS glasses and previous work on the immobilisation of TRISO particles in borosilicate glass formulations [140]. The NL_i of Si, B, Na and Ca from each glass composition are displayed in Figure 4.7. A comparison of the NL_i values between the four glass compositions is provided in Figure 4.8. The alteration in pH during these experiments is displayed in Figure 4.9 and Table 4.3 provides a summary of the NL_i and NR_i values after 28 days for these four elements common to each glass composition.

	Time (Days)	NL_i (g m^{-2})				NR_i (g m^{-2} day^{-1})			
		Boron	Calcium	Sodium	Silicon	Boron	Calcium	Sodium	Silicon
SLSA	3	8.61×10^{-2}	9.19×10^{-2}	5.07×10^{-1}	1.07×10^{-1}	2.87×10^{-2}	3.06×10^{-2}	1.69×10^{-1}	3.55×10^{-2}
	7	1.93×10^{-1}	3.00×10^{-2}	7.22×10^{-1}	1.90×10^{-1}	2.75×10^{-2}	4.29×10^{-3}	1.03×10^{-1}	2.71×10^{-2}
	14	2.79×10^{-1}	2.85×10^{-2}	9.61×10^{-1}	2.64×10^{-1}	1.99×10^{-2}	2.03×10^{-3}	6.86×10^{-2}	1.88×10^{-2}
	21	3.36×10^{-1}	2.33×10^{-2}	1.13×10^{0}	3.07×10^{-1}	1.60×10^{-2}	1.11×10^{-3}	5.36×10^{-2}	1.46×10^{-2}
	28	3.92×10^{-1}	2.01×10^{-2}	1.29×10^{0}	3.54×10^{-1}	1.40×10^{-2}	7.19×10^{-4}	4.62×10^{-2}	1.26×10^{-2}
SLSB	3	3.19×10^{-1}	5.48×10^{-2}	1.24×10^{0}	2.91×10^{-1}	1.06×10^{-1}	1.83×10^{-2}	4.12×10^{-1}	9.71×10^{-2}
	7	4.98×10^{-1}	1.98×10^{-2}	1.74×10^{0}	4.54×10^{-1}	7.12×10^{-2}	2.83×10^{-3}	2.48×10^{-1}	6.48×10^{-2}
	14	6.84×10^{-1}	1.93×10^{-2}	2.32×10^{0}	6.08×10^{-1}	4.89×10^{-2}	1.38×10^{-3}	1.66×10^{-1}	4.34×10^{-2}
	21	8.49×10^{-1}	1.66×10^{-2}	2.80×10^{0}	7.53×10^{-1}	4.04×10^{-2}	7.92×10^{-3}	1.33×10^{-1}	3.59×10^{-2}
	28	1.03×10^{0}	1.48×10^{-2}	3.35×10^{0}	8.96×10^{-1}	3.67×10^{-2}	5.30×10^{-4}	1.20×10^{-1}	3.20×10^{-2}
SLSC	3	2.98×10^{-1}	1.21×10^{-1}	1.01×10^{0}	2.55×10^{-1}	9.94×10^{-2}	4.04×10^{-2}	3.38×10^{-1}	8.51×10^{-2}
	7	3.24×10^{-1}	7.89×10^{-2}	1.24×10^{0}	2.79×10^{-1}	4.62×10^{-2}	1.13×10^{-2}	1.78×10^{-1}	3.98×10^{-2}
	14	4.69×10^{-1}	4.45×10^{-2}	1.54×10^{0}	4.00×10^{-1}	3.35×10^{-2}	3.18×10^{-3}	1.10×10^{-1}	2.86×10^{-2}
	21	5.72×10^{-1}	4.32×10^{-2}	1.86×10^{0}	4.76×10^{-1}	2.72×10^{-2}	2.06×10^{-3}	8.86×10^{-2}	2.27×10^{-2}
	28	6.59×10^{-1}	3.75×10^{-2}	2.09×10^{0}	5.42×10^{-1}	2.35×10^{-2}	1.34×10^{-3}	7.48×10^{-2}	1.93×10^{-2}
SON68	3	2.86×10^{-1}	1.47×10^{-1}	2.21×10^{-1}	1.18×10^{-1}	9.52×10^{-2}	4.91×10^{-2}	7.37×10^{-2}	3.94×10^{-2}
	7	3.89×10^{-1}	1.59×10^{-1}	2.97×10^{-1}	1.41×10^{-1}	5.56×10^{-2}	2.27×10^{-2}	4.25×10^{-2}	2.02×10^{-2}
	14	4.21×10^{-1}	1.42×10^{-1}	3.16×10^{-1}	1.46×10^{-1}	3.01×10^{-2}	1.02×10^{-2}	2.25×10^{-2}	1.04×10^{-2}
	21	4.52×10^{-1}	1.35×10^{-1}	3.35×10^{-1}	1.50×10^{-1}	2.15×10^{-2}	6.41×10^{-3}	1.60×10^{-2}	7.14×10^{-3}
	28	4.89×10^{-1}	1.32×10^{-1}	3.59×10^{-1}	1.56×10^{-1}	1.74×10^{-2}	4.73×10^{-3}	1.28×10^{-2}	5.57×10^{-3}

Table 4.3 - Normalised elemental mass loss and normalised elemental loss rates from PCT experiments at 90 °C in 18.2 MΩ water for elements common to SLSA, SLSB, SLSC and SON68 glasses sintered at 700 °C for 30 minutes.

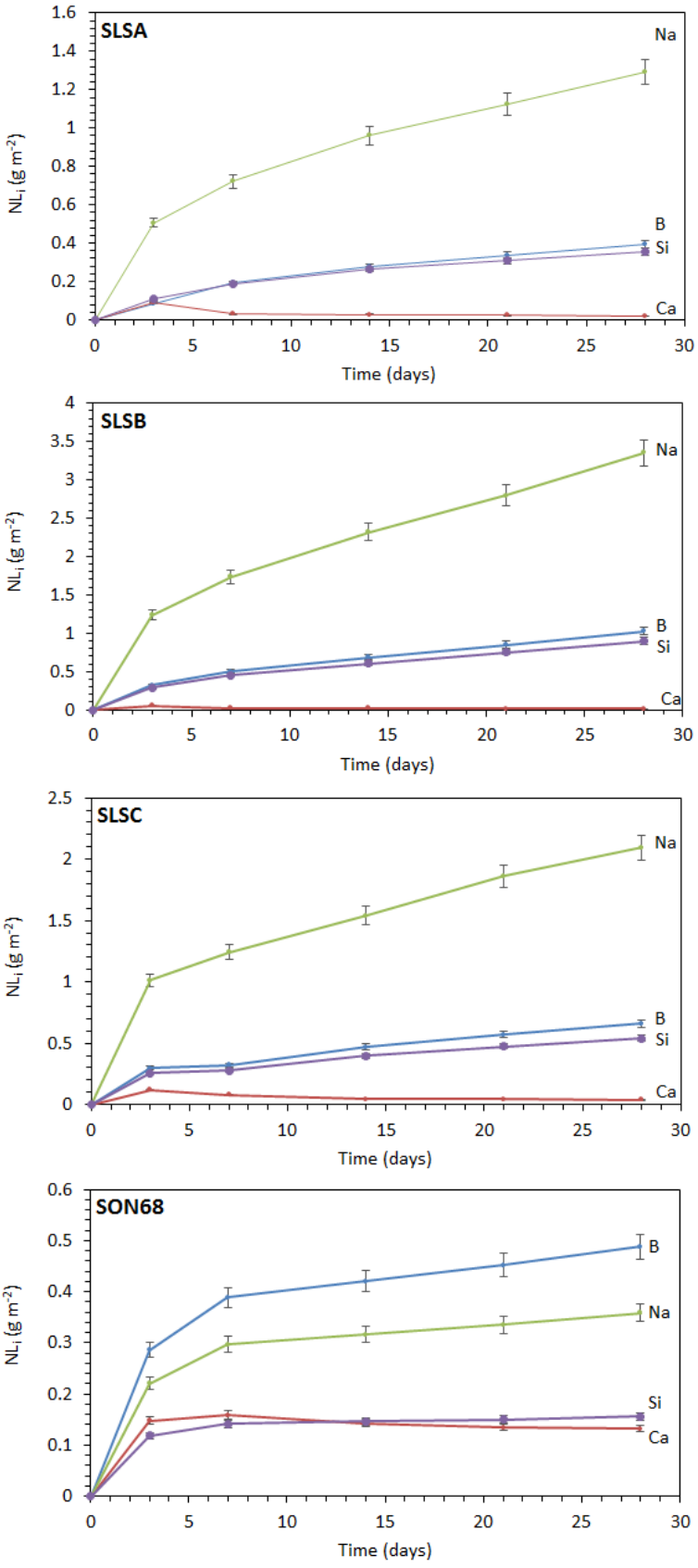

Figure 4.7 - Comparison of normalised elemental mass losses for Si, B, Na and Ca from PCT experiments on SLSA, SLSB, SLSC and SON68 sintered at 700 °C for 30 minutes from PCT experiments at 90 °C in 18.2 MΩ water.

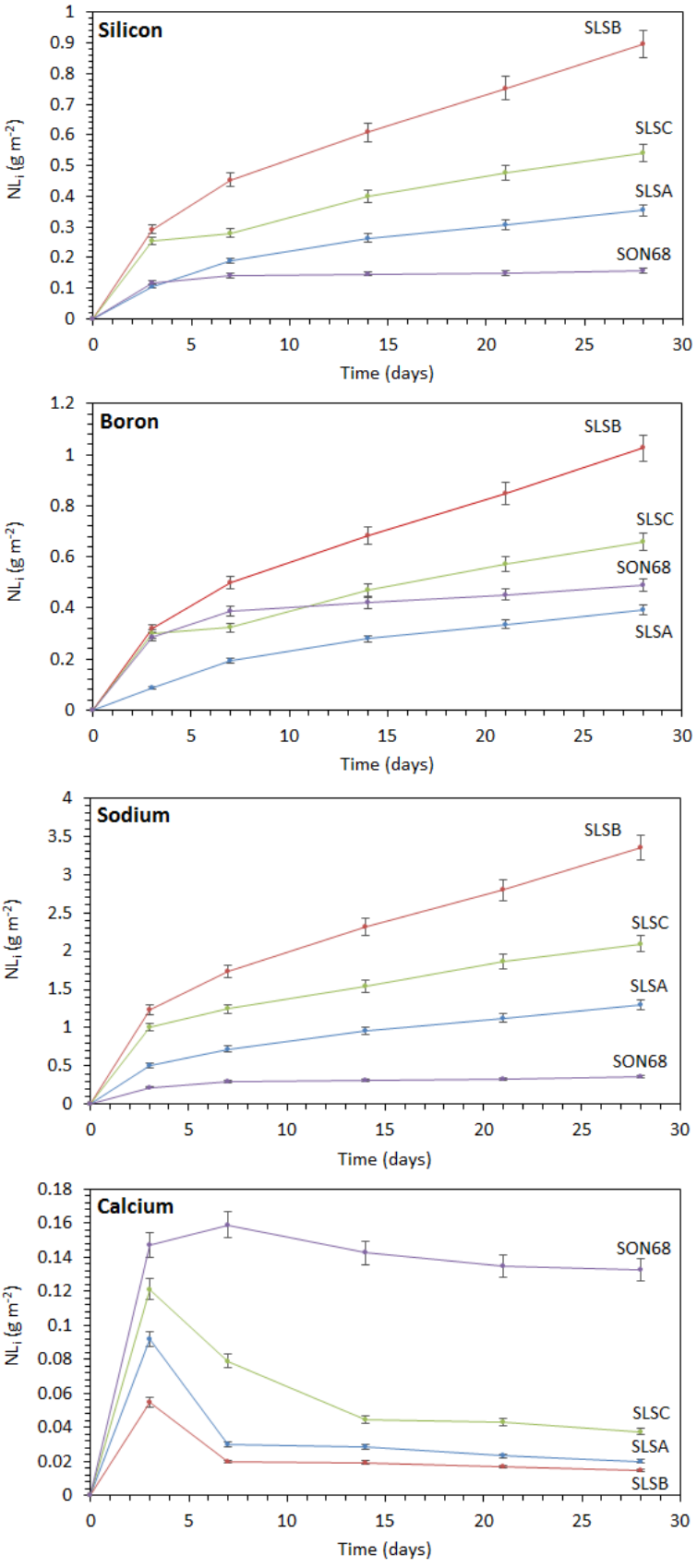

Figure 4.8 - Comparison of normalised elemental mass losses from PCT experiments on SLSA, SLSB, SLSC and SON68 sintered at 700 °C for 30 minutes from PCT experiments at 90 °C in 18.2 MΩ water.

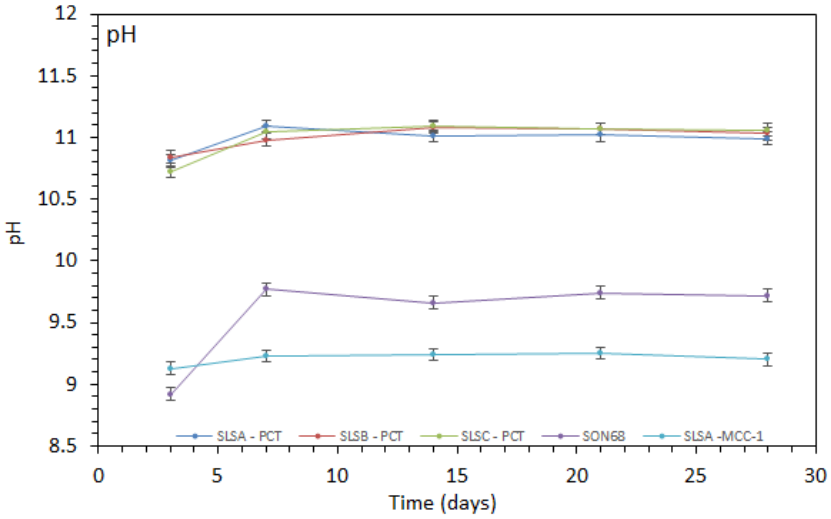

Figure 4.9 - Alteration of solution pH during PCT testing in 18.2 MΩ water at 90 °C in for SLSA, SLSB, SLSC and SON68 after sintering at 700 °C for 30 minutes.

The durability of the tested formulations were all within the same order of magnitude and increase in the following order; SLSB < SLSC < SON68 < SLSA based upon NL_B as determined during PCT experiments. The SLS formulations showed higher residual NR_i values than the SON68 formulation as illustrated in Figure 4.7 and Table 4.3. In the case of the SLS compositions, the NL_{Si} and NL_B were lower than that for the modifier Na, and higher than the modifier Ca. The measured NL_{Ca} decreased with time, suggesting that solution saturation of Ca was reached in all glasses. Buffering of leachate solutions for the three SLS compositions was similar, reaching a pH of 11 after 3 days. The SON68 glass buffered to a pH of 9.7. The alteration of the leachate pH over the course of the experiment is displayed in Figure 4.9.

MCC-1: SLSA-TRISO particle composites were also studied using the MCC-1 method [21], to allow comparison of the dissolution between high and low SA/V conditions in the SLS glass compositions. The results of this experiment are shown in Figures 4.10 and Table 4.4. The MCC-1 experiment on SLSA showed that the NL_{Ca} was similar to NL_{Na}. NL_{Si} and NL_B were significantly lower than that of the glass modifiers. Steady state dissolution rates did not appear to be reached for any element. NR_i values obtained under MCC-1 conditions were between 20 and 50 times higher than those measured for SLSA under the PCT conditions. The pH increased steadily during the experiment to a maximum pH value of 9.4.

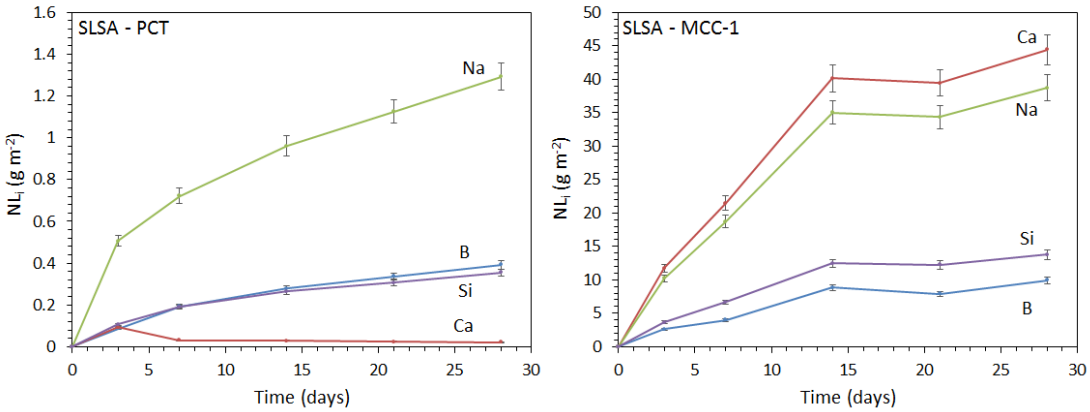

Figure 4.10 - Comparison of the normalised elemental mass losses and dissolution behaviour from SLSA during PCT and MCC-1 experiments at 90 °C in 18.2 MΩ water. SA/V were set at 2160 m^{-1} and 10 m^{-1} for the PCT and MCC-1 experiments respectively.

Element	NR_i - SLSA (g m^{-2} day^{-1}) Measured after 28 days	
	PCT	MCC-1
Si	0.0125 ± 0.0005	0.491 ± 0.008
B	0.0140 ± 0.0002	0.354 ± 0.005
Na	0.039 ± 0.001	0.69 ± 0.02
Ca	0.0007 ± 0.0001	0.033 ± 0.002

Table 4.4 – Normalised elemental loss rates of SLSA after 28 days under PCT and MCC-1 experimental conditions at 90 °C in 18.2 MΩ water.

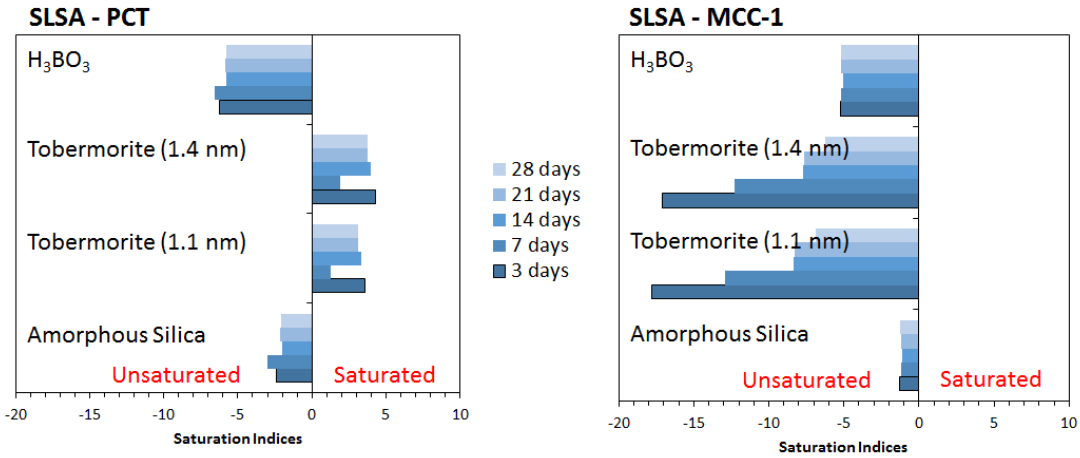

Figure 4.11 - Comparison of saturation indices for the leachate used in aqueous dissolution experiments on SLSA glass at 90 °C in 18.2 MΩ water.

Geochemical modelling of the leachate resulting from SLSA dissolution experiments under both PCT and MCC-1 regimes were conducted using PHREEQC. Saturation indices for the following species are displayed over the course of the experiment in Figure 4.11; boric acid, amorphous silica and tobermorite. Tobermorite is a calcium silicate hydrate known to precipitate from non-aluminium containing glasses as an alteration product [214]. The PCT leachates were determined to be further from solution saturation with respect to amorphous silica and H_3BO_3 than under MCC-1 conditions. The calcium silicate phases were above the point of saturation in the leachates under the PCT conditions but not under MCC-1 conditions.

Mechanical Testing

Results for Vickers hardness and fracture toughness are shown in Table 4.5 and Figure 4.12. Vickers hardness values of the glass-TRISO composites across all formulations were comparable within the precision attainable. Fracture toughness measurements gave a spread of data with composites of SLSA and SLSB performing slightly better than SLSC and SON68. All the sintered composites performed favourably in comparison with the reported values of hardness and fracture toughness for HLW waste glasses currently deployed worldwide [52, 205].

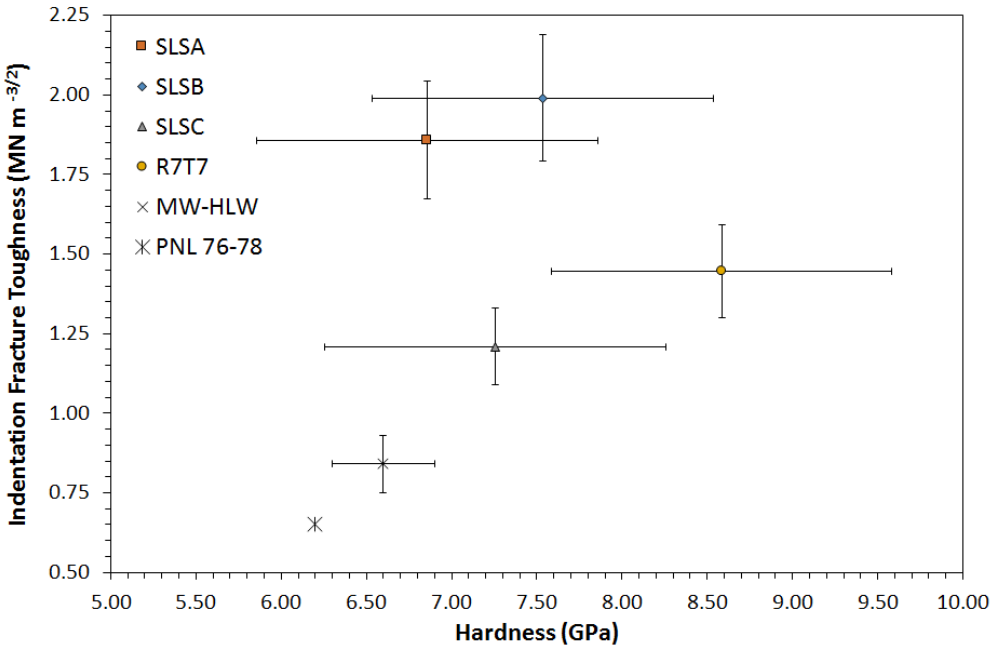

Figure 4.12 - Vickers hardness plotted against indentation fracture toughness for SLSA, SLSB, SLSC and SON68. Data points for HLW glasses currently in use are included for comparison.

Glass Formulation	Hardness at 1 kg loading (GPa)	Indentation Fracture Toughness at 1 kg loading (M N $m^{-3/2}$)
SLSA	6.9 ± 0.7	1.9 ± 0.2
SLSB	7.5 ± 0.8	2.0 ± 0.2
SLSC	7.3 ± 0.8	1.2 ± 0.15
SON68	8.6 ± 0.9	1.4 ± 0.15
MW-HLW [52]	6.6 ± 0.3	0.84 ± 0.09
PNL 76 – 78 [205]	6.2	0.65

Table 4.5 - Tabulated results from Vickers Hardness testing of sintered TRISO-glass composites with comparison to existing HLW nuclear waste glass for hardness and indentation fracture toughness. Both properties were determined with a 1 kg loading. No error provided in [205] for PNL 76-78. [52, 205].

4.3.2 - SLS Glasses - Discussion

With the exception of aqueous durability, little variation in the properties of importance were determined between the SLS formulations. The characteristics of chemical compatibility, porosity, wetting and radial cracking were similar across composites of the glass formulations SLSA, SLSB and SLSC.

OPyC oxidation

The SLS glass compositions studied as encapsulants for TRISO fuel show some promise for this purpose when alterations in sintering atmosphere are implemented. Complete oxidation of the OPyC layer was observed when composites were sintered under air. This oxidation removes the outer protective layer of the TRISO particle, exposing the fission product-bearing SiC layer to the glass matrix. In the event of matrix degradation, the removal of this layer could promote the rapid release of the fission products, such as ^{110m}Ag and $^{135/137}$Cs, which can diffuse through the TRISO structural layers [215, 216]. As such retention of the OPyC in final wasteform is desirable. We have demonstrated that this deleterious reaction between the matrix and OPyC can be readily avoided by sintering under a mildly reducing 5% H_2/N_2 atmosphere. This illustrates that the sintering atmosphere is an important variable which can be applied to glass formulations which would otherwise be considered unsuitable for the encapsulation of TRISO particles.

The potential for the oxidation of the OPyC layer was further minimised by the study of sintering regimes. The shortest possible combination of time, with the lowest temperature capable of producing compacts in excess of 95% theoretical density, was determined to be 700 °C for 30 minutes. This sintering regime provided a degree of densification expected to

eliminate interconnected porosity in a sintered body. This is essential for the encapsulation of the TRISO particles from aqueous solution.

The two methods utilised to characterise OPyC oxidation cannot decisively determine that there is no change in the OPyC layer. However, the combination of techniques determines the maximum possible loss of OPyC during composite sintering is < 10%. This level of loss would still leave the OPyC as a functional barrier to radionuclide release from the SiC layer. Therefore, the results were deemed acceptable to determine that the SLS glass compositions tested have the chemical compatibility required to behave as useful encapsulants for TRISO fuel particles.

TRISO particle-glass contacting behaviour

Wetting describes the behaviour of a liquid contacting the surface of a solid. The use of the term in the context of the glass matrix-TRISO particle interaction may not be appropriate. This is because it is not clear that the glass component is indeed behaving as a free flowing liquid during sintering. As such, it may be more appropriate to refer to areas where matrix-TRISO particle interaction occurs as having 'contacting' behaviour, promoted by sintering action, rather than 'wetting' *sensu stricto*.

Contacting is an important consideration as a low level of contact between the matrix and TRISO particles promotes the existence of voids around the TRISO particles. These voids in turn create the potential for the entire surface area of the TRISO particles to be exposed to aqueous solution in the event of dissolution or cracking of the encapsulating matrix. Therefore, the composite wasteforms described in this study do not yet show the necessary coating properties for TRISO particles to produce a high quality wasteform, whereby the encapsulants directly binds to the embedded material.

Composite Integrity

The data presented in Section 4.3.1 shows that these glasses are not suitable for immobilisation of TRISO particles. The mismatch in the TEC values between the glass and the TRISO particle is great enough to cause fracturing in the processed matrix with radial cracking emanating from each particle.

Glass composite aqueous durability

Comparison of SLS Glasses: The aqueous durability of the sintered SLS glasses used for encapsulation is equivalent to that reported for similar commercial SLS glass [217]. This shows that the sintering process does not have a pronounced deleterious effect on the

aqueous durability of the materials in spite of the partial crystallisation in SLSB. The NL_i of network formers Si and B to solution is lower than that of the modifier cation Na, as shown in Figure 4.7. This indicates the involvement of an ion exchange process in the corrosion mechanism in agreement with glass dissolution theory.

These results show a marked difference in aqueous durability based on small variations in the composite glass formulation. The release of most elements from SLSA is a factor of three smaller than that observed for SLSB and a factor of two smaller than that observed for SLSC. Due to the lower mole fraction of silica in SLSA, it was expected that this glass would have the lowest aqueous durability.

There are three possible explanations for the above behaviour. The first involves the previously noted presence of SiO_2 crystallites in sintered SLSB. The precipitation of cristobalite from the glass solution will reduce the molar composition of SiO_2 in the glass network structure. As such, this composition will have a proportionally increased quantity of modifier components to SiO_2. As explained in Section 2.2.2 this is well documented to result in a decreased aqueous durability.

An alternative explanation would be that the increased durability in SLSA may be explained by the greater alkali earth to alkali ratio, promoting cross linking in the glass network and blocking ion exchange pathways for sodium release [218]. The increased durability of SLSC relative to that of SLSB could also be a result of a mixed alkali earth effect [218]. The use of a mixture of alkali earth ions has been suggested to create a difference in cation field strength, significant enough to polarise non-bonding oxygen atoms in the glass structure [219]. This polarisation is thought to strengthen bonding between the cations and non-bonding oxygen atoms, thus decreasing diffusion of modifier cations from the structure, the rate of ion exchange and the rate of hydrolysis.

A third explanation for this behaviour, which is considered most probable, is that the presence of Al_2O_3 impurities in the glasses causes this trend. These impurities most likely occur as a result of crucible corrosion during melting. As shown in Table 4.1, the molar ratio of alumina increases in the same order as that of the aqueous durability (SLSB < SLSC < SLSA). Additions of alumina have been shown previously to increase aqueous durability of SLS glasses, as discussed further below [220].

Comparison of SLS Glasses with SON68: SON68 borosilicate glass was tested using an identical methodology to that for the SLS composite glasses in the PCT experiment. The NL_i of both silicon and boron in SON68 over the 28 day test period was lower than those

observed for any SLS composite glass tested. This result is contrary to what may be expected from a glass with a significantly lower molar ratio of silica than the SLS composite formulations.

The difference in attained steady state dissolution between the SLS composite formulations and SON68 glass is likely to also be affected by leachate buffering effects creating differences in the pH, as shown in Figure 4.9. The SON68 glass buffers the solution to pH 9.7 within three days, while the SLS composite glasses buffers the solution to pH 11 in the same time. This effect is correlated with the increasing mole% of Na in the glass composition. The Na is removed by the ion exchange mechanism at the start of the dissolution process, exchanging for a protonated species and increasing solution pH through the formation of OH^- groups in solution. This results in the pH increases noted. The higher boron and aluminium content of the SON68 glass, noted in Table 4.1, will also help to buffer the solution to a lower pH according to Equations 4.1 - 4.3 [26 - 28].

$(\equiv Si\text{-}O)_yB_{(3-y)}Na^+_{(y-3)} + H_2O \rightarrow 3(\equiv Si\text{-}OH) + (y-3)(\equiv Si\text{-}ONa) + H_3BO_3$ **Equation 4.1**

$H_3BO_3 + H_2O \leftrightarrows B(OH)_4^- + H^+$ **Equation 4.2**

$Al_2O_3 + 2OH^- + 3H_2O \rightarrow 2[Al(OH)_4]^-$ **Equation 4.3**

It can be seen in Figure 4.7 that after seven days the NL_i for boron, silicon and sodium in the SON68 experiments reaches a steady state. This may be indicative of solution saturation with respect to silicon at the lower pH values that the leachate buffers to. This is an important consideration in the analysis of these results, as in a GDF facility, the pH buffering will likely not be controlled by the glass dissolution itself, but the surrounding environment.

The dissolution of silicate glasses is well documented to be dependent on pH according to the term $10^{\sim 0.4pH}$ [196, 199, 200, 221]. As such, the rate of glass dissolution at pH 11 is expected to be 2.5 times greater than at pH 10 assuming all other factors remain constant. In addition, the solution saturation level of silicon is approximately ten times greater at pH 10.7 than at pH 10, due to the stabilisation of the silicate anion [222]. These factors combine to adequately explain the differences in the dissolution profiles of the SLS composite and the SON68 glasses.

Comparison of Monolithic and Powder Experiments: Monolithic SLSA–TRISO particle composites were investigated using the MCC-1 durability experiment. This experiment

produced an NR_i between 20 and 50 times greater (depending on the element) than that seen in the PCT experiment of SLSA, as shown in Table 4.4 and Figure 4.10. It is a well-established that an increased SA/V lowers the NL_i of glasses in static tests [109]. The higher SA/V provides a more rapid approach to solution saturation of silica, the initiation of protective crystallite layer formation and affinity limiting effects. The process of glass dissolution in aqueous solution results in the partial hydration of the glass network to form an amorphous layer of $SiO_{4-x}(OH)_x$. It has been suggested, as explained in more detail in Section 2.2.2, that this layer acts in concert with precipitated phases such as calcium silicate hydrates (CSH), as a passivating barrier to minimise further dissolution, thus, lowering the dissolution rate [85]. In the SLSA composite glass tested, the solution is not saturated with respect to amorphous silica for either type of experiment, as shown in Figure 4.11. However, geochemical modelling indicates that the solution is closer to equilibrium for the MCC-1 experiment than in the PCT experiment. This indicates that the saturation of silica is not the cause of the difference observed in NL_i.

Under PCT conditions, a decrease in the NL_{Ca} was observed with time for the SLSA composite, while the network formers B and Si were still being released into solution as displayed in Figure 4.8. This is indicative of the precipitation of a calcium-bearing phase. No such effect was observed under MCC-1 conditions. Geochemical modelling of the PCT leachates indicates that the solution was beyond the saturation limit for twelve of the twenty seven thermodynamically possible calcium bearing phases included in the database, including tobermorite ($Ca_5Si_6(O,OH)_{18}.5H_2O$), shown in Figure 4.11. It has been suggested that tobermorite is a major constituent of CSH gel layers likely to exist in a glass alteration phase, which may passivate dissolution [23, 35]. The MCC-1 leachate was not saturated with respect to any of the Ca-Si phases contained in a CSH gel, such as tobermorite (Figure 4.11). Disregarding possible errors from the geochemical model, we may infer that the enhanced dissolution rates in the MCC-1 experiment compared to the PCT experiment, are the result of saturation with respect to calcium silicate hydrates and the subsequent protective effect provided in the PCT experiment.

It should be noted that inaccuracies in the calculation of sample surface area may partially contribute to the observed results. The surface area of the composite pellets was measured geometrically. Cracks in the composite samples and the finish of the pellets exterior could not be accounted for using this determination of surface area. This may result in an under estimation of the surface area and, therefore an increase in the calculated NL_i. However, the error involved should be below ± 5 % and would not negate the trends noted above.

Physical properties

The Vickers hardness and fracture toughness of the composite glasses and SON68 were determined to be comparable with those of HLW glasses currently employed for nuclear waste immobilisation, as shown in Table 4.5 and Figure 4.12 [205]. The results provided may be subject to some inaccuracy, because annealing of the composite materials was precluded by the potential removal of the polished surface finish by sintering action. It may be assumed that the mild compressive stresses created during polishing will have a positive effect on the values obtained for Vickers hardness and indentation fracture toughness due to surface compression. Nevertheless, the trends are expected to be meaningful.

4.3.3 - SLS Glasses - Conclusions

The SLS glasses studied showed some promise for the purpose of TRISO particle encapsulation. A simple alteration in the processing atmosphere was shown to allow the effective densification of glass-TRISO particle composites, without an oxidative reaction of the OPyC layer. The mechanical properties of Vickers hardness and fracture toughness for the sintered glass composites compared favourably to glasses currently employed as wasteforms in the nuclear industry.

The durability of the sintered SLS glasses was also shown to be comparable to that of as-cast analogues known for their high durability. Small variations were noted between the glass formulations tested, likely a result Al_2O_3 impurities introduced during processing. Leachate pH was shown to have a dramatic effect on the dissolution of the glasses as shown by comparison with a borosilicate glass. Strong variations in NL_i were observed for SLSA, dependant on the SA/V of the experiment used. This is most likely a result of reaching saturation with respect to a calcium silicate hydrate phase in the leachate solution.

However, significant issues preclude the use of SLS glasses for the encapsulation of TRISO particles. The mismatch between the TECs of the glasses and TRISO particles proved detrimental to the wasteform integrity. This mismatch resulted in the propagation of large radial cracks from the TRISO particle into the matrix. The contact between TRISO particles and the glass matrix was also poor.

The problems encountered here demonstrate the difficulties of increasing wasteform durability. The determining factors for production of an effective wasteform for TRISO particles from sintered glasses will involve matching of TECs and increasing chemical durability. The issues identified could potentially be mitigated by increasing the

mole fraction of B_2O_3 in the glass, as this would lower the TEC, T_g and the viscosity, as such, preventing cracking, lowering processing temperatures and promoting contact [223]. Al_2O_3 additions would likely have a positive effect both on aqueous durability and in lowering the TEC. However, they also increase temperatures required for processing, which in turn increases the potential risk of OPyC oxidation.

4.4 - ABS-1 Compositions

As described above, the development of a higher durability encapsulant for TRISO particles requires improvements in the coupling of TEC, contacting properties and aqueous durability. It was believed these properties are likely be improved for silicate glasses which contain a mixture of B_2O_3 and Al_2O_3. To determine a glass composition capable of providing these improvements, the glass compositional database Sciglass 5.0 was utilised. This database allows a user to search through over 250,000 oxide glass compositions and compare their properties with data available from the literature. To determine the most appropriate glass formulation only compositions containing a mixture of SiO_2, B_2O_3 and Al_2O_3 as network formers were selected based upon observations in Section 4.3 and to keep the major glass forming components non-toxic and commercially available. These compositions were then filtered according to the availability of information on aqueous durability, glass transition temperature and melting parameters in the database. Compositions without this information available were excluded to minimise the number of compositions to be investigated. This provided a shortlist of glass compositions for review.

The parameters for selection of the favoured glass composition to be investigated for use in TRISO particle encapsulation are listed below.

1. Data available which suggests the composition provides a high level of aqueous durability.
2. A glass transition temperature below 700 °C.
3. Readily melted in large quantities, from common and inexpensive starting materials.
4. Previous study into the composition for use in radioactive waste immobilisation.

The glass selected for further investigation had previously been investigated in the US for the encapsulation of HLW calcines via sintering, where it was designated as composition SG7A. A review of this work is available in [224]. For the purpose of this study this glass composition

will be referred to as alumino-borosilicate 1 (ABS-1). The composition and basic properties of this glass are given in Table 4.1.

4.4.1 - ABS-1 Glass - Results

Sintering Regime and OPyC Oxidation

As discussed in Section 4.3.2 the retention of the TRISO particles' OPyC layer is desirable during high temperature encapsulation. To minimise the risk of OPyC oxidation during processing, the minimum time and temperature required to achieve a density in excess of 95% of the theoretical density was determined. As seen in Table 4.6 optimal conditions were obtained by sintering at 750 °C for 30 minutes. Composite ABS-1-TRISO green bodies showed a volume reduction during sintering of ~30 %.

The effect of atmosphere was also investigated to determine if the presence of oxygen in the sintering process would have the same deleterious effect on OPyC oxidation as found for the SLS glass compositions. The behaviour of ABS-1 is identical to that described for SLS glasses and is shown in Figure 4.13. Retention of the OPyC layer was observed under a reducing 5% H_2/N_2 atmosphere but completely lost when sintered in air. The presence of the 5% H_2/N_2 reducing atmosphere played a crucial role in the retention of the OPyC layer during sintering.

Sintering Regime		Temperature (°C)		
		700	750	800
Time (minutes)	15	81 ± 1%	85 ± 1%	90 ± 1%
	30	95 ± 1%	97 ± 1%	97 ± 1%
	60	94 ± 1%	97 ± 1%	97 ± 1%

Table 4.6 - Densification regime of ABS-1 glass pellets as a function of temperature and time displayed

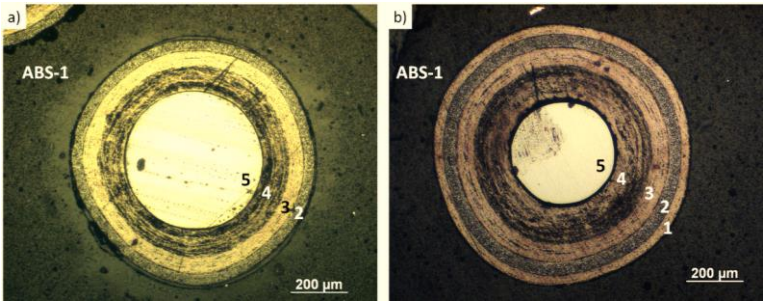

Figure 4.13 - Optical micrographs of ABS-1 – TRISO particle composites sintered for 30 minutes at 750 °C in a) air and b) 5% H_2/N_2 atmospheres.

Crystallisation

The ABS-1 glass was obtained from the melt as a fully amorphous material as shown in Figure 4.14 a). However, ABS-1 shows partial crystallisation on sintering with the precipitation of TiO_2 observed (rutile, PDF card - 00-003-1122). Where this TiO_2 originated from is unclear as the XRF data analysis shows < 0.05 wt% TiO_2 in the starting materials. This phase is unlikely to affect the dissolution behaviour of the glasses and is not deemed likely to prove detrimental to the final wasteform.

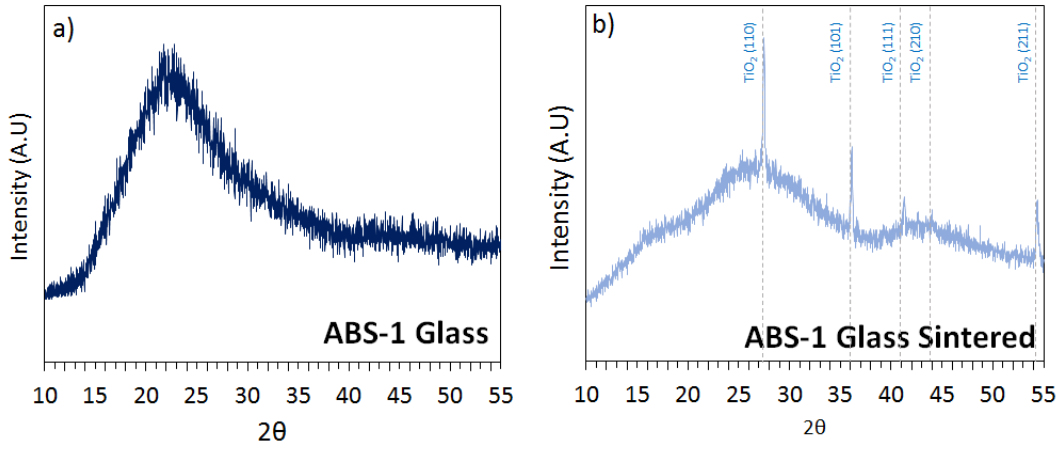

Figure 4.14 - Powder XRD patterns ABS-1 before and after sintering with TiO_2 peaks indexed.

Composite Characterisation

Figure 4.15 shows SEM-BSE images of the sectioned ABS-1 - TRISO particle composites, sintered for 30 minutes at 750 °C and Figure 4.16 depicts the same samples with SEM-BSE and optical microscopy. The radial cracking in SLS glass composites, described in Section 4.3.1, was not apparent upon inspection of ABS-1 sintered composites. The use of ABS-1 has also improved the interaction of the glass matrix with the TRISO particles. An average gap between the TRISO particles and ABS-1 matrix was calculated from 120 measurements across 10 particles to be 2.7 ± 3 µm. This is a substantial improvement on the average of 12.9 ± 4 µm gap observed for SLS compositions.

Although the density of the sintered glass matrix exceeds 95% of its theoretical density, Figure 4.15 a) and Figure 4.16 d) show that a small amount of residual porosity remains. This does not appear to be interconnected and so should not prove excessively detrimental to wasteform performance.

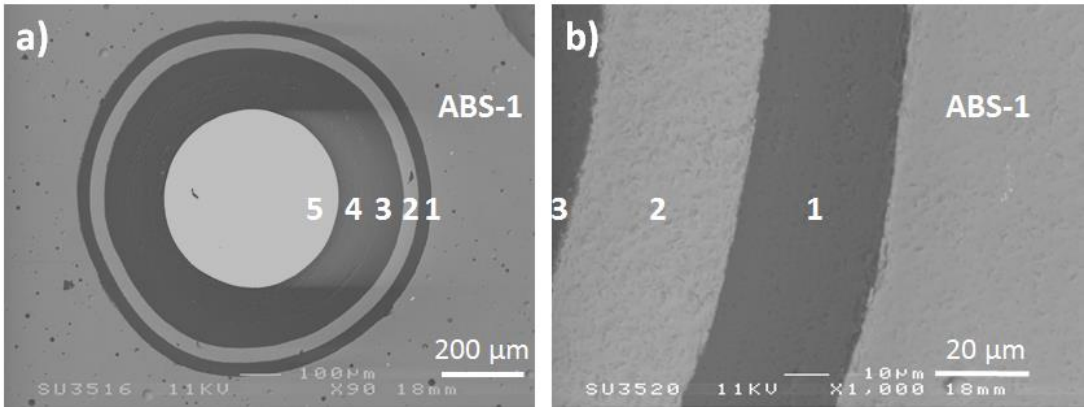

Figure 4.15 - Back-scattered SEM images of a) TRISO particle embedded in ABS-1 b) OPyC-ABS-1 interface of the composite.

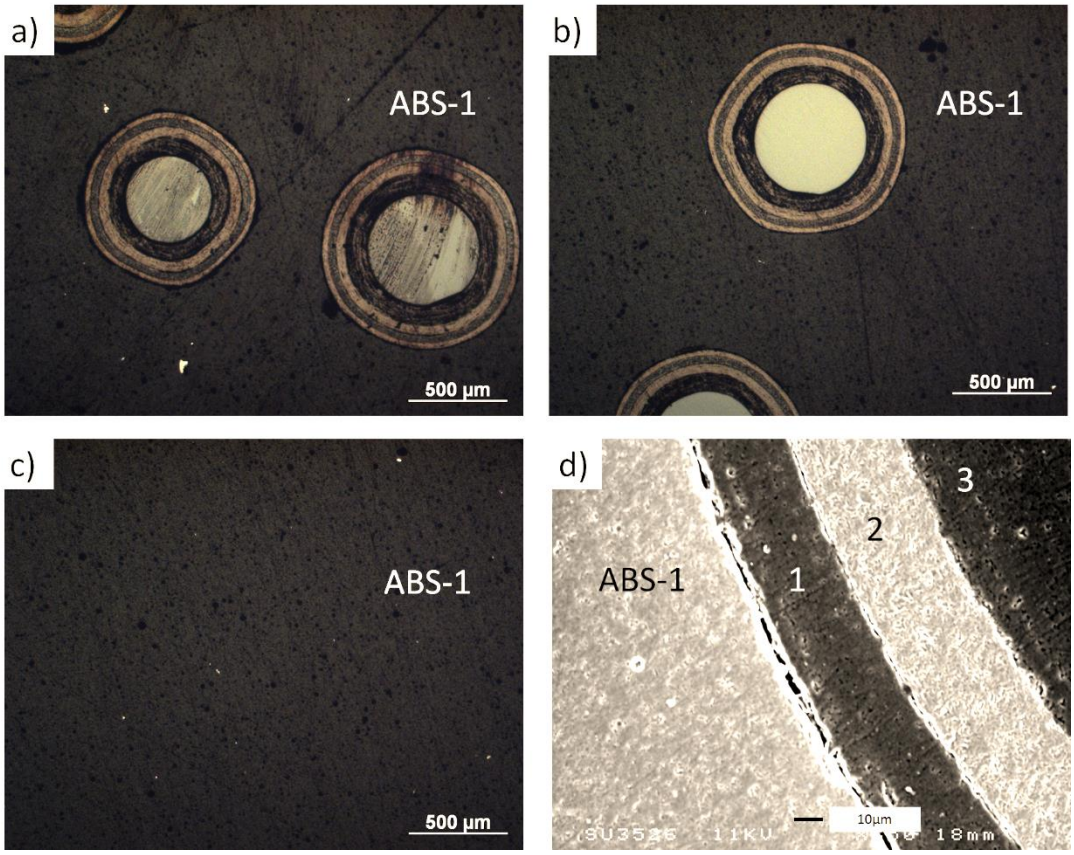

Figure 4.16 - a) and b) display optical micrographs of ABS-1 TRISO- particle composites sintered at 750 °C for 30 minutes, c) displays the residual porosity and crystallisation of the glass matrix and d) is a secondary SEM image of the interaction of the ABS-1 matrix with the TRISO particles OPyC layer.

Aqueous Durability Experiments

A PCT experiment was performed on powdered samples of sintered ABS-1 glass at 90 °C in 18.2 MΩ water with a SA/V of 2270 m^{-1}. The NL_i values from the 28 day sampling of ABS-1 are displayed in Table 4.7. The solution buffered to a pH of 9.3 ± 0.2 after three days, this value remained constant up until the 28 day sampling point. Figure 4.17 displays the NL_i obtained during PCT experiment of the ABS-1 and the saturation indices for selected phases of interest important in the dissolution process of Al and Mg containing glasses. These include amorphous silica (SiO_2), analcime ($NaAlSi_2O_6 \cdot H_2O$), sepiolite ($Mg_4Si_6O_{15}(OH)_2 \cdot 6H_2O$) and tobermorite ($Ca_5Si_6O_{16}(OH)_2 \cdot 4H_2O$) [84, 225].

The NL_i values follow the order $NL_{Na} > NL_B > NL_{Si} > NL_{Al} > NL_{Ca} > NL_{Mg}$. All elements show an initial rapid release at up to three days, however, after this point the degree and behaviour of subsequent release can be split into three different trends. NL_{Na} and NL_B are highest throughout the experiment. The rate drops rapidly after three days then continues to steadily drop throughout the remaining sampling points. Al and Si show mid-level NL_i values with a steady state rate for dissolution reached after three days. Ca and Mg both show a decrease in rate after three days and a steady drop in NL_i throughout the experiment.

A comparison of NL_i for ABS-1, SLSA and SON68 base glass from PCT experiments under near identical test conditions is displayed in Table 4.7 and Figure 4.18. The trend between SLSA and SON68 is discussed in detail in Section 4.3.2. Figure 4.18 clearly identifies the significant increase in aqueous durability of the ABS-1 composition over both the SLS and borosilicate glass compositions. Dissolution rates for ABS-1 are improved by almost an order of magnitude in comparison to SLSA or SON68 and display more stable characteristics in terms of their elemental release behaviour.

	ABS-1	SON68	SLS
NL_{Si} (g m^{-2})	4.97×10^{-2}	1.56×10^{-1}	3.54×10^{-1}
NR_{Si} (g m^{-2} day^{-1})	1.77×10^{-3}	5.57×10^{-3}	1.26×10^{-2}
NL_B (g m^{-2})	1.11×10^{-1}	4.89×10^{-1}	3.92×10^{-1}
NR_B (g m^{-2} day^{-1})	3.97×10^{-3}	1.74×10^{-2}	1.40×10^{-2}
pH (as buffered from 3 days sampling)	9.3 ± 0.2	9.7 ± 0.2	11.0 ± 0.2

Table 4.7 - Comparison of normalised elemental mass losses and normalised elemental loss rates for silicon and boron from sintered ABS-1, SON68 and SLS subjected to a 28 day PCT experiment at 90 °C (precision ± 5 %).

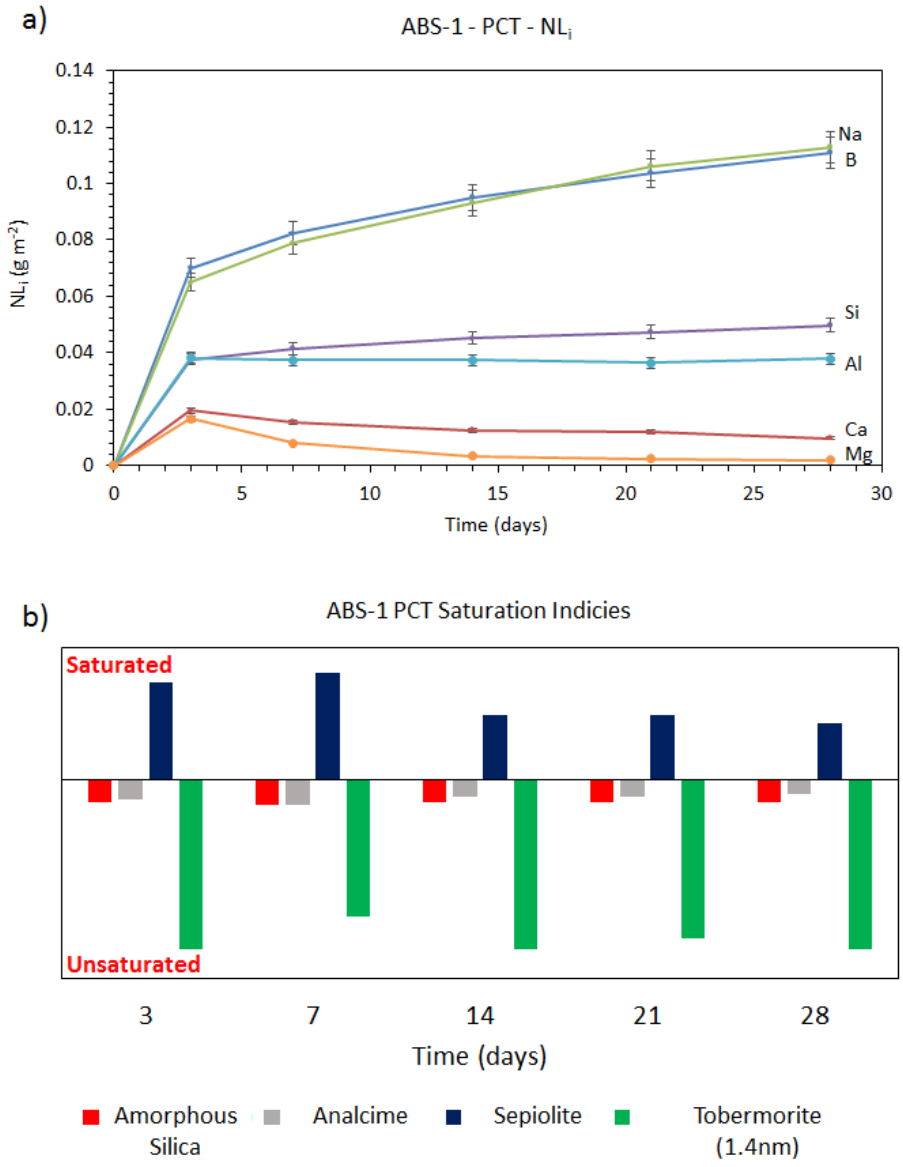

Figure 4.17 - a) Normalised elemental mass losses of ABS-1 glass sintered at 750 °C for 30 minutes from PCT experiments at 90 °C in 18.2 MΩ H_2O and b) saturation indices for phases from the same PCT experiments on ABS-1 as modelled using the PhreeqC geochemical code.

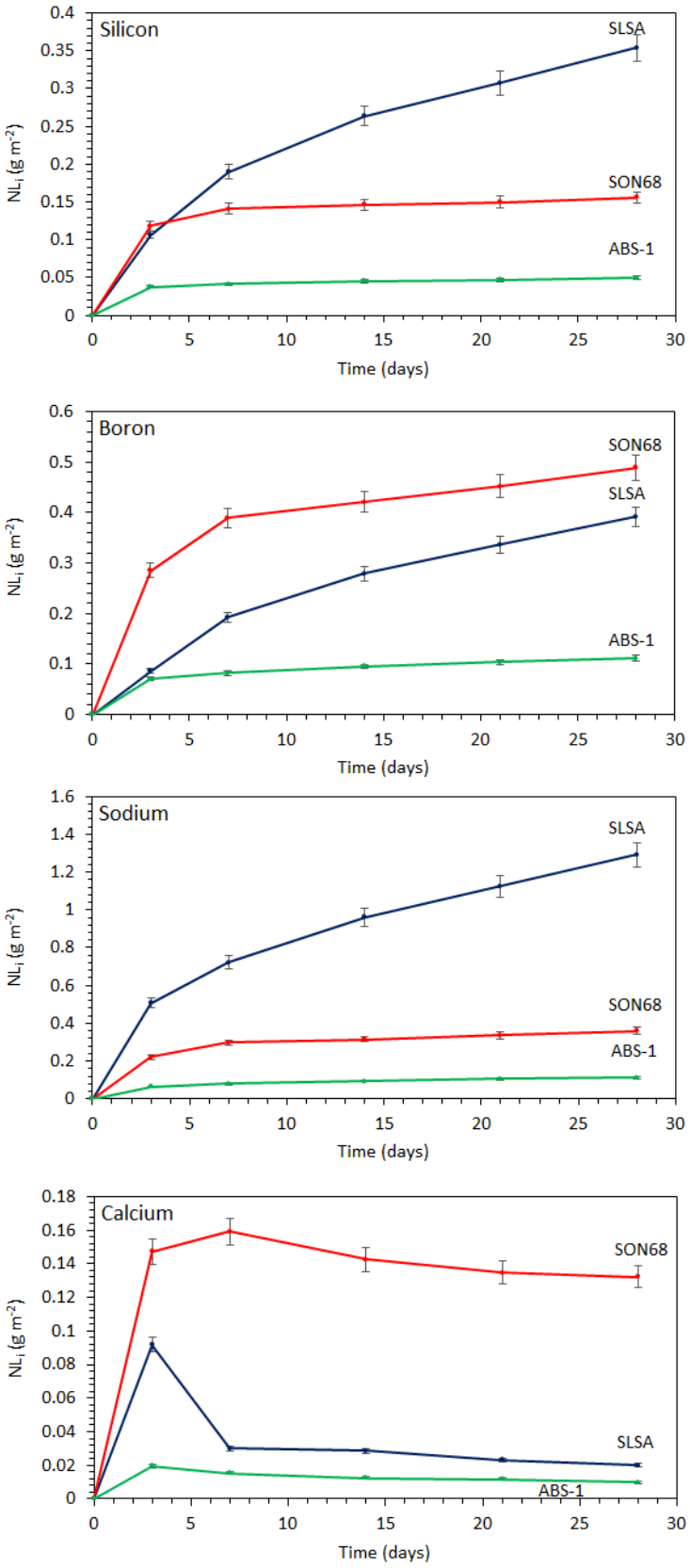

Figure 4.18 - Comparison of normalised elemental mass losses of the common elements in glass compositions SLSA, ABS-1 and SON68 from PCT experiment on powdered sintered glasses at 90 °C in 18.2 MΩ water.

Mechanical Properties

The ABS-1 sintered glass composites were of comparable quality to those of the SLS and SON68 compositions. Measurements from Vickers hardness testing and indentation fracture toughness gave results of 7.3 ± 0.8 GPa and 1.7 ± 0.2 M N $m^{-3/2}$ respectively. These results compare favourably with glasses currently employed for the disposal of HLW glass wastes, as described in Figure 4.12.

4.4.2 - ABS-1 Glass - Discussion

OPyC Oxidation and Composite Formation

The behaviour of the ABS-1 glass in terms of the oxidation of the OPyC is almost identical to that described for the SLS glass compositions. As these glasses have already been noted to provide acceptable chemical compatibility, it also stands that the chemical interaction of the ABS-1 with the OPyC is acceptable. However, to produce composites lacking interconnected porosity requires an increase in sintering temperature when compared with SLS compositions, from 700 °C to 750 °C. This higher sintering temperature is likely to be a direct result of the inclusion of over 8% Al_2O_3 into the network structure. Al_2O_3 is well documented to increase both the network connectivity and the glass transition temperature as described in Section 2.2. The increase in glass transition temperature may mean that to obtain a fluidity of the glass capable of introducing significant particle necking requires processing at higher temperatures.

Composite Quality

A marked improvement in the quality of the composite is observed through the use of ABS-1 glasses. The radial cracking observed in the SLS composites is eliminated to produce a fracture free composite wasteform as shown in Figures 4.13 b), 4.15 and 4.16. This is likely a result of the decreased TEC of ABS-1. This decrease is a result of the increased cross linking created by the addition of Al_2O_3 resulting in a TEC (7.2 x 10^{-6} K^{-1}) which more closely matches that of graphite (~5 x 10^{-6} K^{-1}), the main component by volume of TRISO fuel particles [115]. Without the stress profile created by the TEC mismatch, the cracking in the composite matrix is no longer evident in ABS-1 composites.

The contacting properties are also improved in the ABS-1 – TRISO particle composites, with some particles showing direct contact of the OPyC layer with the glass matrix, as shown in Figure 4.15 b). However, this degree of contacting is not evident across all particles as shown in Figures 4.13 b) and 4.16 d). Contact of the TRISO particles with the glass matrix still

requires improvement to prevent the potential for water ingress around particles. The contact of the glass matrix with the TRISO particles was expected to be improved by the application of pressure during the sintering process, attainable using a methodology such as uniaxial hot pressing, spark plasma sintering or HIPing (see Section 4.5).

Aqueous Durability

Figure 4.17 shows that the dissolution mechanism involves an ion exchange process, due to the favoured release rate of both Na and B from the glass. The combination of the NL_i data in Figure 4.17 a) with the solution saturation data from PhreeqC geochemical modelling, shown in Figure 4.17 b) illustrates that the release of network formers Si and Al are potentially linked to the concentration of Mg and Ca in solution. Once Al and Si reach a certain concentration in solution they could preferentially combine with Mg and Ca to form an alteration layer of sepiolite, chabazite or phillipsite. When sufficient levels of these components are available in solution, precipitation occurs resulting in decreased concentrations of Mg and Ca in solution. This would result in the steady state release of Si and Al.

Figure 4.18 and Table 4.7 illustrate the vast improvement in aqueous durability of ABS-1 when compared to SON68 and SLS. It was shown that across common elements ABS-1 has NL_i values approximately an order of magnitude lower than the other compositions. As the matrix in all glasses tested is based upon a silicate network, the dissolution rate of silica can be considered the limiting factor to the degradation of the matrix. Table 4.7 shows the calculated NL_{Si} and NL_B after 28 days. The rate of silicon dissolution is approximately an order of magnitude lower for ABS-1 than for SLSA and SON68. Although static test conditions result in significantly different buffered solution conditions, Table 4.7 shows that SON68 and ABS-1 should be considered to have comparable pH values. This indicates that the assertion based on the improved durability of ABS-1 over SON68 can be made with confidence. The test conditions are unfavourable to make a direct comparison with the SLS glasses although it is expected that the ABS-1 glass would outperform these compositions.

The improvement of the ABS-1 glass by comparison to SLSA and SON68 glasses may be due to the precipitation of alteration layers on the glass surface. The saturation indices for the phases phillipsite-Ca ($CaAl_2Si_5O_{14}.5H_2O$), chabazite ($CaAl_2Si_4O_{12}.6H_2O$) and sepiolite ($Mg_4Si_6O_{15}(OH)_2:6H_2O$) are all positive in the leachate solutions of the ABS-1 glass. As explained in Section 2.2.2 these phases are known to form as a result of glass dissolution [225]. If this is the case then further investigation should be performed to determine if this

passivation layer exists and also if it is broken down over time. If the passivation layer were to be broken down then it may result in the resumption of the dissolution process as described in Section 2.2.2 for high Al_2O_3 containing glasses.

4.4.3 - ABS-1 Glass - Conclusion

Alumino-borosilicate glass has been shown to have superior properties by comparison to glass compositions previously investigated for TRISO immobilisation. Improvements include the elimination of composite circumferential cracking and radial cracking, improved contacting of the OPyC layer by the glass and an aqueous durability over an order of magnitude greater than that of other glasses tested.

ABS-1 glasses show favourable qualities for TRISO encapsulation however some refinements in the processing methodology are required to remove the remaining composite porosity and improve the contacting properties of the wasteform. The application of pressure during the sintering process was expected to improve wetting by forcing the vitreous matrix onto the TRISO particles whilst removing the residual porosity by decreasing the resistance to sintering from internal pore pressurisation.

4.5 - ABS-1 HIPed Composites

It was decided the application of pressure to improve composite's properties should be performed using HIPing. HIPing has a relatively high technological readiness level for nuclear waste production and is regularly utilised during conventional materials production. Other benefits of this technology are described in Section 2.3. The results of this investigation are presented below.

4.5.1 - ABS-1 HIPed Composites - Results

HIP Compaction

Initial evaluation of the HIPed canisters showed the expected collapse of the canister walls, indicative of sample densification. An analysis of the compaction behaviour of the 38.1 mm canisters with respect to waste loading is shown in Figure 4.19. This displays both the compaction of the sealed package and the densification of the packaged waste stream according to Equations 3.9 and 3.10 respectively.

An illustration of the degree of canister deformation can be seen in Figure 4.21 a) for the 30 wt% loaded samples.

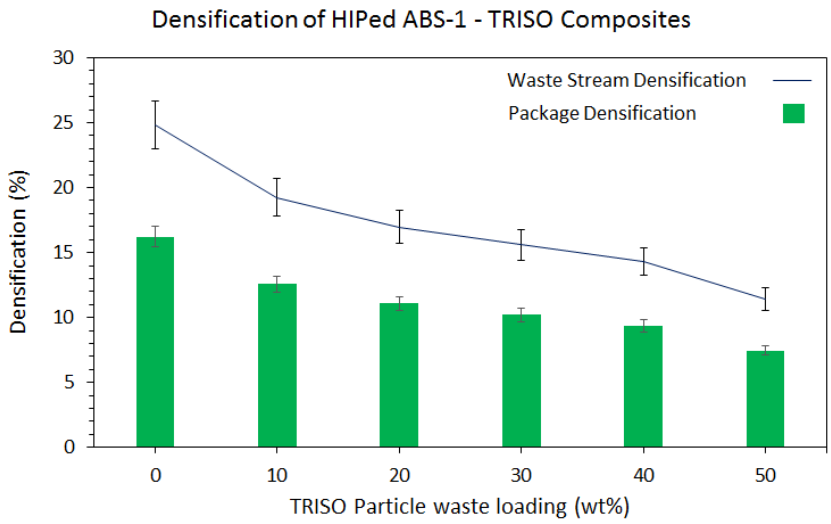

Figure 4.19 - Graph showing the densification behaviour of ABS-1 – TRISO particle composites HIPed in 38.1 mm tube-coin canisters. The bar chart is plotted according to Equation 3.3 and the line graph is plotted according to Equation 3.4.

Figure 4.19 shows that the degree of densification observed in both the waste package and waste stream is dependent on the waste volume addition. It also highlights the efficiency of canister powder packaging, which was achieved utilising vibratory packaging for these waste streams. Assuming complete densification of the glass has been achieved after HIPing, the canister can be packed with sub-75 µm glass powders and TRISO to a green density of ~65 % using this methodology. This explains the lower degree of canister wall deformation, as shown in Figure 4.21 a) than observed in the other waste streams presented in this thesis.

Table 4.8 illustrates the difference that canister design had on the filling and subsequent densification properties of the HIPed ABS-1 – TRISO particle composites. Densification values are presented of the 0 wt% and 10 wt% TRISO particle loadings of the modified 15.1 mm diameter tube-coin canisters.

A significantly greater volume reduction in the 15.1 mm modified canisters was observed after processing. This has been attributed to an inability to package the glass powders as efficiently in this canister design, due to the inability to vibratory pack or mount in a uniaxial press. Despite the inefficiency in the initial packaging, this canister design was essential for the study of the TRISO composites, as will be described below.

	38.1 mm Tube-coin Canister		15.1 mm Modified Canister	
	0 wt%	10 wt%	0 wt%	10 wt%
Waste package densification (%)	16.2 ± 0.8	12.6 ± 0.6	32 ± 1.6	28 ± 1.4
Waste stream densification (%)	25 ± 2.0	19 ± 1.4	38 ± 2.4	34 ± 2.3

Table 4.8 - Comparison of the waste package densification and waste stream densification (calculated using Equations 3.3 and 3.4 respectively) of 38.1 mm and 15.1 mm HIPed ABS-1 – TRISO particle canisters at 0 wt% and 10 wt% loadings.

Sample Retrieval

As noted in Section 4.2.3, various methods of obtaining a sample for study were attempted with varying degrees of success. The main issues encountered were due to the mixed hardness of materials within the HIPed composite. Cutting samples effectively requires the matching of cutting tools to materials. However, as the composite contains significant quantities of graphite, glass, ceramic and metal, there was no cutting material suited to the range of materials present in this composite available. Diamond blades are most effective for the sectioning of the hardest materials in the composite (ABS-1, SiC and the ZrO_2 TRISO particle core). Although diamond blades are able to cut through metals they take significant wear during this process as the diamond cutting surface is removed from the bonding of the blade. The alternative is to match the cutting tool to the stainless steel canister by the use of a hard ferrous cutting tool. The consequence of this method when applied to cutting the harder materials present, is that the process becomes slow and creates significant heat and abrasive damage in the glass and ceramic sample matrix. A brief discussion of the results of various sectioning techniques are included below.

Buehler Isomet 5000 (0.6 mm diamond blade): This was the first sectioning methodology utilised as it allows samples with a diameter up to 80 mm to be mounted with a controlled vice pressure and to be sectioned effectively using a set feed rate and blade RPM, minimising damage to samples by the selection of cutting parameters. The precision mounting is beneficial as it minimises the chances of cracks forming in the HIPed materials after processing. A medium gauge precision diamond blade provides strength and durability with a low degree of abrasive damage to the cutting plane surface and should provide a minimum product finish of P600 grade.

However, this method proved highly unsuitable for the processing of HIPed ABS-1 – TRISO particle composites. Figure 4.20 provides a schematic illustrating the mechanism by which this methodology is prone to failure. The poor bonding between the YSZ core and BC layer in

the simulant TRISO particles results in the removal of this core during sectioning. This hemisphere, up to 0.2 mm in diameter, is then trapped in the cutting plane, which due to the high hardness of YSZ (approximately 12 GPa [226]) acts as a large abrasive bead causing extensive damage to both the sample surface and the expensive consumables required. Once this effect became apparent this methodology was stopped and plans to utilise diamond core drilling were also discarded.

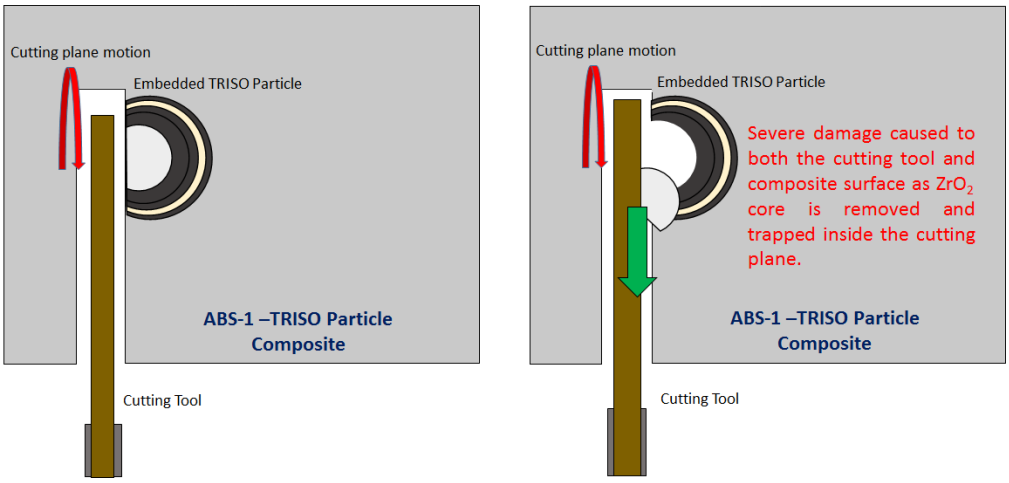

Figure 4.20 - Schematic illustrating the difficulties involved with sectioning large ABS-1 TRISO particle samples due to the removal of the poorly adhered ZrO_2 cores from the simulant particle. These cores become trapped in the cutting plane between the rotating tool and sample surface causing significant, if not catastrophic damage, to both the sample surface and cutting tool.

***Buehler Isomet Slow Saw (0.3 mm diamond blade)**:* The same vices used with the Isomet 5000 can be utilised with the Isomet slow saw. The use of lower RPM and thinner blades minimises the cutting plane depth. This means sectioned core hemispheres can no longer be trapped in the cutting surface and less damage was induced on the sample surface. However, this method was unsuitable due the excessive time required to section samples (over 36 h to make a single 38.1 mm cut), deformation of the blade (sample mass is too great for blade even with maximum counterbalance applied) and damage to diamond blades through the removal of the bonded diamond by the steel canister.

Buehler Abrasimet abrasive saw (1.6 mm diamond blade): The use of a strengthened 1.6 mm diamond blade lowers the quality of surface finish but also reduces the potential for damage to the blade and the cost for its replacement. This method proved effective for the sectioning of the canisters, however the necessity to use a clamp vice created uncertainty in the origin of cracking with the samples, as is discussed below. The failure of the above

sectioning techniques necessitated the production of smaller modified canisters to determine the origin of the cracking and provide samples suitable for microscopic investigation.

Struers Secotom 500 (hard ferrous abrasive blade): This was most successful sectioning method and was used only for the smaller 15.1 mm modified coin tube canisters at 0 wt% and 10 wt% TRISO particle loading. The improved coolant application of the Secotom alongside the ability to control both cutting feed rate and blade RPM made it possible to use a hard ferrous precision abrasive blade to cut composites without creating excessive heating or abrasive damage in the sample. This method was performed with the smaller samples for two reasons. Firstly to minimise the amount of harder material requiring sectioning, reducing the possibility of sample damage and secondly the altered canister design has a flat bottom. This allowed vice mounting without the application of any pressure to the canister regions containing brittle materials, reducing the potential of fracturing occurring in the wasteform. As a result of these alterations any cracking in these smaller canisters is most likely to be a direct result of processing effects.

38.1 mm canister properties

As described above no methodology was found to be entirely suitable for the sectioning of these larger composite canisters. Either the canisters could not be opened or the origin of cracking in the composite was uncertain due to the use of a uncontrolled clamping force during sectioning. As a result no comparison of the sample morphology and matrix interaction from these canisters is presented for discussion.

Figure 4.21 illustrates the cracking observed in the 38.1 mm 0 wt% TRISO loaded HIP canister sectioned with a Buehler Abrasimet. The fracture pattern observed on canister opening was analysed by comparison to fracture patterns of known origins in cylindrical glass rods [227]. This analysis indicates that cracking was initiated at the point marked “crack origin” in Figure 4.21. Further, it indicates that the cracking is likely to be due to lateral pressures applied to the cylinder surface. Finally, as no TRISO particles are present in the sample it is known this cracking is not an effect of waste loading, but a result of sample preparation or processing. However, it was unclear from this data if the lateral pressure which caused the fracturing is a result of the HIP pressuring fluid the clamping required during sample retrieval.

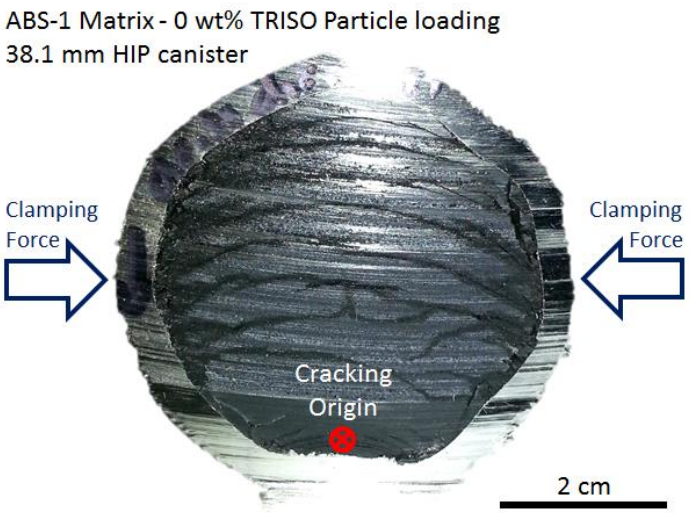

Figure 4.21 - Image of ABS-1 canister sectioned using the Buehler Abrasimet. The direction of the clamping force is indicated.

X-ray Computed Tomography (XCT)

Figure 4.22 illustrates the results of a preliminary scan made on the 30 wt% loaded, 38.1 mm ABS-1 – TRISO particle composite canister using computed XCT performed at the Henry Mosley Facility, University of Manchester. It was hoped that by studying a small 10 mm area of the sample, a resolution high enough to identify any cracking inside the canister may be achieved. Unfortunately, this was not possible due to the beam attenuation through the 2 mm thick stainless steel canister. The resolution obtainable did allow the identification of zirconia core the TRISO particles. However, it was not possible to distinguish between the other layers of the TRISO particles and the ABS-1 matrix. Based on the results of this preliminary data, a more in depth study of the canister was not attempted and the data collected was of no benefit in determining the origin of matrix cracking within the processed canisters. The preliminary data did allow identification of the distribution of particles in the composite from the location of the YSZ core. From this data we know that the TRISO particles are well dispersed in the matrix and do not agglomerate, float or sink during processing.

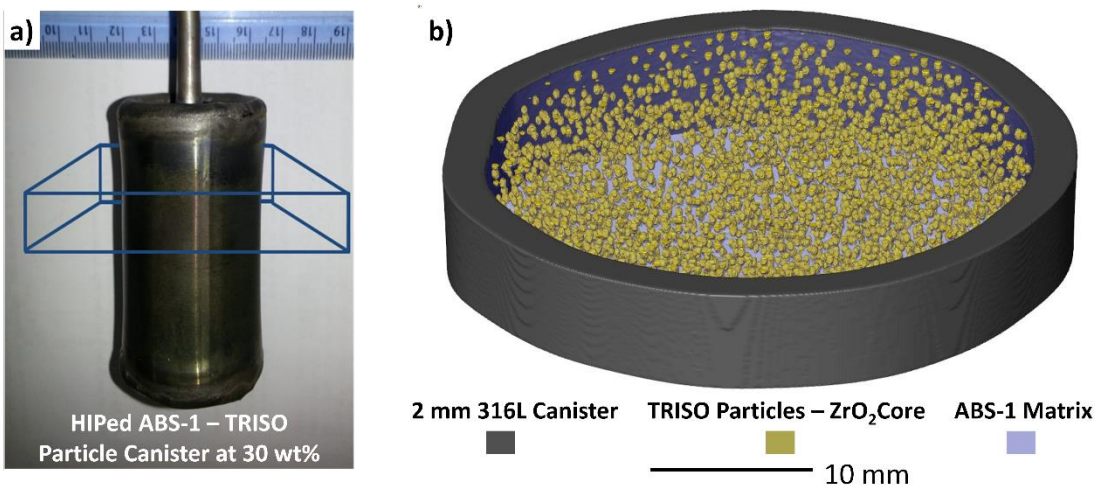

Figure 4.22 - a) Image of HIPed ABS-1 – TRISO particle composite super imposed with the approximate area scanned via XCT and b) the section of this canister studied in the preliminary XCT study illustrating the dispersion of TRISO particles in the processed canister.

15.1 mm HIP Canisters

Due to the difficulties described above in determining the source of the cracking within the 38.1 mm HIP canisters, 15.1 mm canisters were produced. Figure 4.23 displays the microstructure of these canisters at both 0 wt% and 10 wt% loadings. It was seen that the TRISO particles are well encapsulated and contained within the ABS-1 structure and that no significant oxidation of the OPyC layer has occurred during this processing. The micrographs show that significant cracking in the wasteform is present in both the unloaded and waste loaded samples. The canisters show a crescent shape after compaction and the main fractures run parallel with the crescent length. Both samples show similar fracture behaviour where the major crack structure runs parallel to the sample length. Buckling of the glass matrix occurs at the inside of the crescent curve. The most significant cracking occurs in both samples at the edge of the crescent. As no pressure was applied to this sample during sectioning the cracking observed in both samples is expected to be a result of the processing methodology.

The microstructure of the TRISO particles encapsulated in the HIPed ABS-1 matrix is shown in Figure 4.24. Here it is clear that the TRISO particles do not show any oxidation of the OPyC layer. The absence of radial cracks in or around the particles show no issues remain for the mismatched TECs.

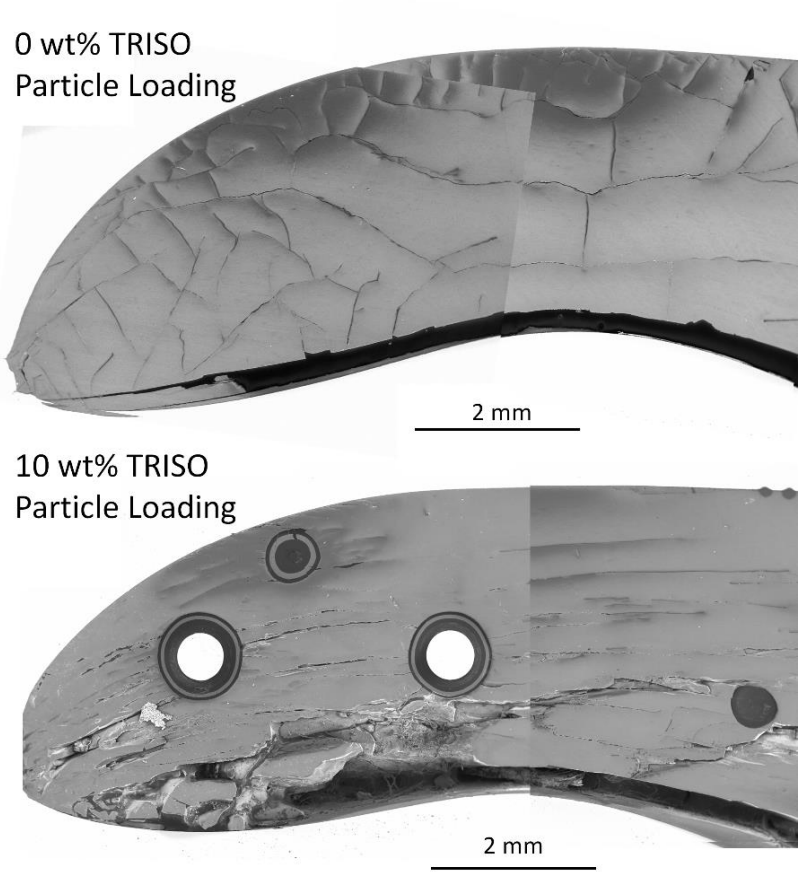

Figure 4.23 - Combined SEM-BSE micrographs for the 15.1 mm HIPed ABS-1 – TRISO particle composites at 0 wt% loading and 10 wt% loading.

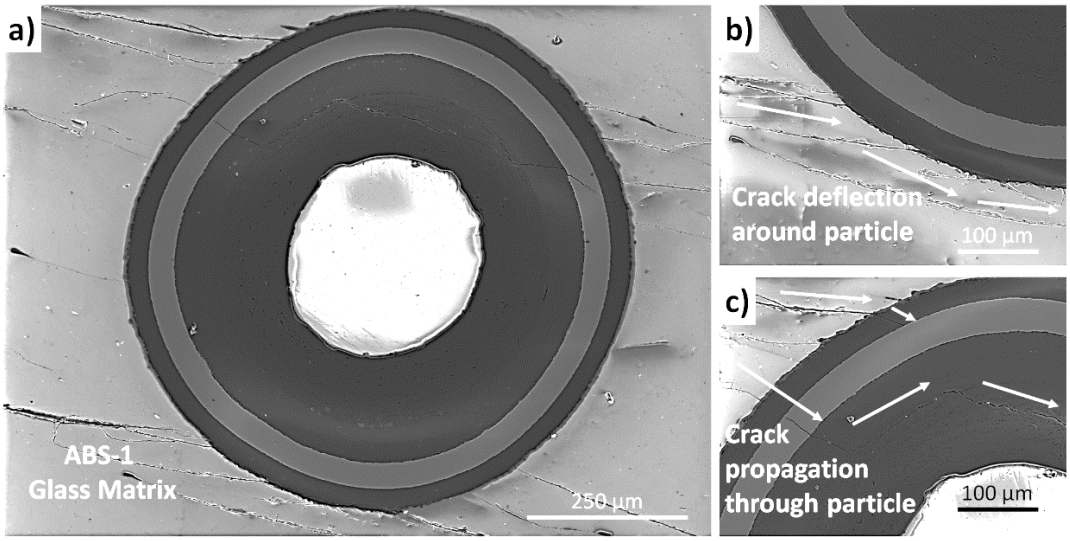

Figure 4.24 - a) SEM-BSE micrographs of the encapsulated TRISO particles from the 15.1 mm modified tube-coin canister loaded with 10 wt% TRISO particles b) Illustrates the deflection of cracking around the OPyC layer of the TRISO particles and c) the propagation of the cracking into the OPyC, SiC, IPyC and BC layers.

Figure 4.24 a) shows that despite the lack of TEC based cracking around the particles, matrix cracking extending to the particle surface is evident when HIPing is used as the processing methodology. When these cracks meet the encapsulated particles, one of two behaviours is noted in the crack propagation. The first is a deflection of the crack around the OPyC layer of the particle, as seen in Figure 4.24 b). The second is the propagation of the crack into the TRISO particle itself, as seen in Figure 4.24 c). This cracking shows preferential propagation through the junctions of the particle layers, but are also seen to pass uninterrupted through multiple layers. These cracks pass through all four layers of the TRISO particle as shown in Figure 4.24 c).

The interaction zone between the particle and the matrix is displayed in Figure 4.25. The lack of a coating interaction is evident from the gap which exists between the OPyC and ABS-1 matrix. This gap is 1.5 ± 0.4 µm, as averaged across 125 measurements, over 5 particles. The small error seen across this large range of measurements indicates this gap is inherent to the materials as processed and not an artefact of the sample preparation methodology. Further evidence for this is seen in the morphology of the ABS-1 and OPyC layer. Figure 4.25 highlights areas of the interaction surface labelled a - l where it can be seen that a perfect correlation between the OPyC surface morphology with the ABS-1 matrix exists.

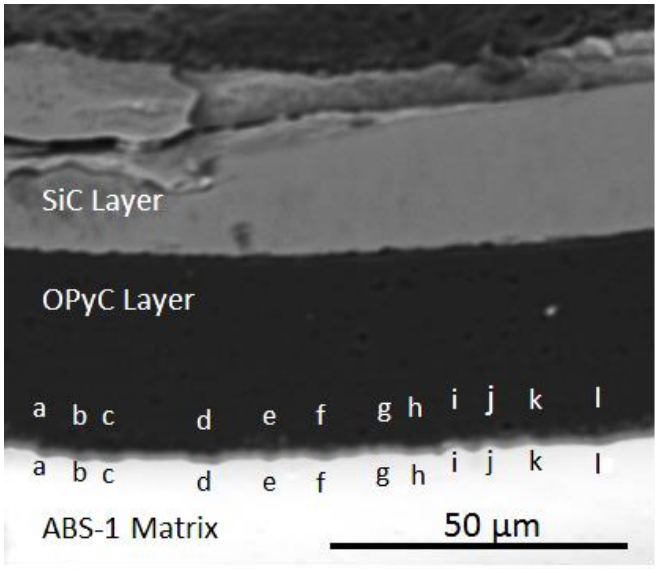

Figure 4.25 - SEM-BSE micrograph of the interaction zone between the ABS-1 matrix and OPyC layer in the 10 wt% loaded 15.1 mm HIPed ABS-1 – TRISO particle composite.

4.5.2 - ABS-1 HIPed Composites - Discussion

Densification behaviour

The behaviour shown in Figure 4.19 shows that effective densification of these composite materials can be achieved via HIPing. The differences in densification observed between the 38.1 and 15.1 mm canisters shows how vibratory packing is much more effective than the tap and press method used to fill the 15.1 mm canisters. The comparison of the 0 wt% loaded canisters shows the canister packing efficiency of the 15.1 mm canister is only 65 % of that seen in the 38.1 mm canister packaged via vibratory packing. The SEM-BSE micrographs in Figures 4.23 - 4.25 also illustrate the effective densification of the composites has occurred as evidenced by the lack of porosity in the ABS-1 matrix. From this densification behaviour and the lack of OPyC oxidation seen in Figures 4.23 – 4.25, we know the processing temperature used in the processing of these samples is appropriate.

Sample Preparation and Sample Cracking

Sample Preparation: As summarised in Section 4.5.1, the sample preparation of the heterogeneous composite materials pose many issues, which in turn affected the ability to analyse the larger samples of the HIPed composites. The major drawback was the inability to open the larger canisters without application of large lateral clamping force to the canister walls and use of a saw without controllable blade rotation or pressure application leading to aggressive sectioning conditions. This resulted in several issues for the analysis of the larger samples including: the complete removal or destruction of TRISO particles from the composites; large regions of fracturing in the ABS-1 matrix; large amounts of material removal and a poor surface finish. This poor surface finish can be seen in Figure 4.21 which shows the 0 wt% loaded canister sectioned using the Abrasimet saw. The aggressive nature of this sectioning can be seen in the burring of the canister edges and visible notches from the cutting plane of the sample surface.

Not only did this sectioning method prevent effective polishing and sample preparation for microscopic study, but the data gleaned from the canister behaviour in respect to the larger scale matrix cracking could not be considered diagnostic, due to the high lateral pressures on the sample during sectioning. The fracture patterns, as shown in Figure 4.21, are characteristic of a load applied at a minimum of two places to the lateral surface of a cylindrical glass tube [227]. This behaviour could be described by either the application of too great a pressure during processing, whilst below the glass T_g or from the clamping forces used during sectioning.

To determine whether this highly detrimental cracking was a result of the processing parameters, 15.1 mm canisters were designed to enable sectioning of the canister with a less aggressive methodology eliminating clamping forces. The decrease in the amount of hard materials within these smaller diameter canisters allowed the use of the hard ferrous abrasive blade and determination of cracking origins.

Cracking Origins: The canisters produced allow for a comparison of the crack morphology and for some speculation on their source. As no external force capable of causing cracking was applied to the 15.1 mm canisters post processing, we know all cracking in these samples is a direct result of the material processing parameters. As the 0 wt% loaded canisters show this fracturing it can be determined that the cracking is a result of the interaction of the canister with the glass and not because of the presence of TRISO particles. Unfortunately, the smaller canisters compacted into a crescent shape, most likely as a result of the lower packing density achieved prior to HIPing. This makes analysis of the cracking patterns more difficult.

Major cracks in both the 0 wt% loaded and 10 wt% loaded samples follow the length of the crescent shape, with an increased degree of cracking in the corners. Despite the complexity of the cracking patterns in the 15.1 mm patterns, some information can be related back to fracturing in the larger samples. It is most likely that the fracturing results from excessive lateral pressure on the canister during processing, whilst below the glass T_g, as discussed above. However, caution should be used in the assignment of this due to the potential for vibrationally induced cracking during sectioning.

Effects of Cracking on Wasteform Quality: Cracking is the major issue precluding the use of HIPing for processing TRISO particles into an ABS-1 encapsulated composite. These cracks propagate from the surface of the canister to the OPyC surface where contacting is poor. This means fluid could rapidly transfer from a breach in the container, along this crack network to the OPyC layer [228]. This fluid would then fill the gap which exists between the glass and the particle and provide a release mechanism for the radionuclides to the environment.

If this did not already preclude the use of HIPing (using these parameters) then the micrograph shown in Figure 4.24 c) illustrates why the wasteform in its current form should not be considered for use. The cracking of, not just one, but all of the protective layers of the TRISO particle should be considered the greatest possible failure of an encapsulation methodology for TRISO particles. This would open the internal structure of particles to

dissolution and promote the release of the most soluble fission products contained in these layers, as well as promoting the direct dissolution of the TRISO particle fuel core [228].

The parameters utilised in the processing of the HIPed composites were chosen to provide a short dwell period with effective densification, while not exceeding the pressure that TRISO particles are designed to sustain [229-231].

Crack Propagation into the TRISO Particles: Figure 4.24 c) indicates that the cracking of the particles is not a direct result of the pressure applied to the particles, but is instead a propagation of cracking occurring in the ABS-1 matrix. This has already been attributed to the lateral pressures applied to the glass during processing whilst below T_g. From analysis of the HIP data logs it is known that the highest pressure applied to the densified composite canister, after passing below the glass T_g, was at 610 °C with an applied pressure of 82 MPa. An inference on fracture behaviour can be made from the fracture properties described in Sections 4.3.1 and 4.4.1. These indicate that the ABS-1 has a fracture toughness at the lower end of that seen in sintered SLS glass compositions. The load required to initiate this type of cracking mechanism in isostatically loaded cylindrical SLS glass compositions has previously been measured at between 76.5 MPa and 85 MPa [227]. This could therefore explain the presence of cracking in the sample. However, 76.5 MPa should not be assumed to be the lowest pressure at which cracking is initiated in the ABS-1 glass composition and a study of the HIPing parameters should be performed.

Requirements for Optimisation of Processing Parameters: Processing of the TRISO – ABS-1 glass composites should be readily achieved without application of high pressures to the densified solid matrix. This can be done by simply processing at a lower pressure. 40 MPa should be capable of readily deforming canisters such as those used in this study. Alternatively if higher pressures were required for the densification of the waste stream, decreasing the pressure below that known to initiate cracking, before passing through T_g, would likely eliminate this crack formation.

Contacting: The fracturing in the TRISO particles has been noted to form as an extension of the fracturing in the ABS-1 matrix. Inferences can thus be made on the origin of the gap which exists between the ABS-1 matrix and the OPyC layers of the TRISO particles. This gap must not exist at the point of crack initiation as the fracture plane in the particles would then not follow the same path as those seen in the ABS-1 matrix. It can therefore be assumed that at processing temperatures where the cracking is initiated, the particles are in contact with

the ABS-1 matrix. The above observation supports the earlier conclusion that this matrix cracking is a result of the excessive pressurisation from the HIP processing fluids below T_g.

Evidence supporting this is displayed in Figure 4.25, where it can be seen that micron sized features are present at the OPyC surface which are an exact match for the solidified surface of the ABS-1 matrix. Two mechanisms could account for the creation of this gap. The first would be a non-wetting interaction between the particles and matrix at elevated temperature, followed by contraction of both the ABS-1 matrix and the TRISO particles. Evidence in support of this theory is presented by the uniform nature of the gap distance noted in section 4.5.1, which suggests the formation of this gap is a result of the materials fundamental properties, such as TECs.

An alternative explanation may be proposed involving the relaxation of the stresses and fractures in the processed canister on sectioning. This process of sectioning the canister would allow for stress relief, springing open the canister, resulting in the opening of the fracture structure of the encapsulated materials. This would create movement in the fractured regions of the ABS-1 which could then pull away from the poorly wetted, yet contacting, TRISO particles. Evidence for this hypothesis is seen in Figure 4.23, where the sectioned canisters are displayed and the open structure of the cracks can be seen. However, the data is inconclusive as to which of these mechanisms may be responsible for the formation of the gap between the ABS-1 and TRISO particle matrix.

4.5.3 - ABS-1 HIPed Composites - Conclusion

From the results presented above it is clear that as processed in this study HIPing of ABS-1 with TRISO particles produces a wasteform unsuitable for geological disposal. The range of failings is listed below.

1. **Incomplete contacting between the matrix and the TRISO particles** – A gap of 1.5 ± 0.4 µm exists between the matrix and the OPyC layer of the TRISO particles.
2. **Cracking of the ABS-1 matrix** – Cracks exist throughout the entire structure of the composite structure, these would allow water ingress to contact the encapsulated TRISO particles.
3. **Cracking of the TRISO particles** – The ABS-1 cracking propagates through the OPyC, SiC, IPyC and BC layers of the TRISO particle vastly increasing the potential for radionuclide release into the environment.

The data does, however, support the idea that encapsulation of TRISO particles in an ABS-1 matrix via HIPing, using modified parameters, is likely to produce an effective wasteform. This is expected based on the following considerations;

1. XCT scanning shows a homogeneous distribution of TRISO particles throughout the waste stream with no sinking, floatation or agglomeration in the canister processing.
2. Effective densification of the wasteform occurs up to 50 wt% of the TRISO particles in these composite materials.
3. The cracking of the TRISO particles is considered an extension of matrix cracking. Therefore alterations of processing parameters, which would eliminate matrix cracking would eliminate the most deleterious cracking observed.

The following work packages should be performed in an attempt to improve the final properties of the wasteform and determine whether the analysis of the data performed above is accurate.

1. **Alteration of the HIP cycle parameters** – The processing of canisters of ABS-1 with 0 wt% TRISO particles should be performed at a range of HIP pressures from 20 MPa to 100 MPa. This would determine the point at which densification can be achieved and whether the cracking is a result of the lateral pressure on the canister during HIPing.
2. **Waste loaded study** – If step 1 proves successful in optimising a process cycle to densify the glasses without the presence of matrix fracturing, waste loaded samples should be attempted. This will determine if the TRISO particle cracking was a product of matrix cracking or not.
3. **Waste loading study** – If the cracking of TRISO particles is no longer evident a variety of waste loadings should be processed with the optimised parameters to study the effect of particle-particle interaction in the composites. XCT should be utilised to determine the particle distribution in the canister after processing.
4. **Active Study** – As UO_2 fuel kernels have almost twice the density of ZrO_2 the distribution of un-irradiated UO_2 TRISO particles should be studied to ensure no sinking of particles occurs during processing.
5. **Scale up Studies** – The ability to process this waste in larger canisters should be investigated to determine the potential for industrial scale up of the optimised waste processing route.

4.6 - Conclusions and Future Work

Although a final acceptable waste stream has not been created the development of a matrix material optimised for encapsulation of TRISO particles at low temperatures has been performed. The suggestions presented for future work in Section 4.5.3 are considered likely to produce a wasteform for spent TRISO fuel both optimised for the GDF storage and scalable to a level practical for industrial implementation.

Section 4.3 details the production of TRISO particle - SLS glass composites, determined their aqueous durability, densification profiles, fracture toughness and Vickers hardness. All of these properties were found to be comparable or superior to glasses currently employed for the disposal of HLW glasses. Sintering at 700 °C for 30 minutes was found to remove all interconnected porosity from the composite bodies and oxidation of the outer pyrolytic carbon layer during sintering was prevented by processing under a 5% H_2/N_2 atmosphere. However, the outer pyrolytic carbon layer was not effectively wetted by the encapsulating glass matrix and significant matrix cracking occurred as a result of TEC mismatches. The aqueous durability of the TRISO particle-SLS glass composites was investigated using PCT and MCC-1 experiments, in combination with geochemical modelling. It was found that durability was dependent on the saturation of the solution with respect to silicon and calcium.

In Section 4.4 an identical methodology was applied to the study of ABS-1 glasses in the production of TRISO particle – glass composites. These glasses show significant improvement over SLS and the SON68 glasses in terms of both aqueous durability, which was over an order of magnitude higher and via the elimination of TEC mismatch. However the coating of the TRISO particles by the ABS-1 matrix was still considered unsuitable and required further improvement.

In an attempt to address this coating issue, pressure was applied during densification via HIPing, the results of which are outlined in Section 4.5. This study showed the process parameters used in composite manufacture were unsuitable for the encapsulation of TRISO particles due to the application of excessive lateral pressure during processing. This in turn initiated significant cracking of the ABS-1 matrix. This cracking not only degraded the matrix integrity, but propagated into the TRISO particles, causing the unacceptable failure of the isotropic layers themselves. Future work is proposed based on the hypothesised fracturing mechanisms. This suite of work is expected produce an optimised wasteform for TRISO particle encapsulation utilising an industrially relevant processing methodology.

This study provides significant advancements in the preparation of TRISO particle encapsulated wasteforms, both in terms methodology used and the final products obtained, which are listed below;

1. Increased the waste loading from the ~ 5 wt% previously processed to 50 wt%.
2. Increased the aqueous durability of the glasses utilised by over an order of magnitude, an important characteristic for the encapsulation of spent fuel elements.
3. Optimised the composition of glass formulation used by matching the properties to those of the TRISO particles, eliminating TEC cracking likely to be induced in both borosilicate and SLS glass compositions.
4. Investigated the potential for HIPing of the wastes as an industrial process
    a. Determined the most effective methodology to study and section composites with difficult mechanical properties.
    b. Analysed cracking patterns in HIPed samples to suggest improved processing parameters for the HIPing of ABS-1-TRISO particles composites.

The potential for the use of non-borosilicate, sintered glass composites for the encapsulation of TRISO particles has been confirmed, although further refinements in processing parameters are required.

Chapter 5 - Prototype Fast Reactor Raffinate

5.1 - Chapter Introduction

This chapter investigated the possibility of using vitrification as an immobilisation technique for the processing of PFR wastes. The current baseline for processing of PFR is via cementation, however, as has been described in Section 2.1, the ability of cement to effectively retain certain radioisotopes is poor. This study provides information on the feasibility of an alternative methodology for PFR immobilisation in the event that cementation is deemed unsuitable for these wastes. As any future commercial fast reactor operations will require fuel reprocessing, this investigation should also be considered relevant to the disposal of other fast reactor raffinates.

The primary challenge for the immobilisation of PFR raffinate in glass is expected to result from the high sulphur content in the raffinate. The G73 glass composition was developed to immobilise sulphur bearing ion exchange wastes, and has already been shown to be effective for the immobilisation of a number of other ILW waste streams [155]. As such it was selected as the base glass for this investigation into PFR vitrification.

An inactive simulant for the PFR raffinate was used to create G73 glasses loaded with 10 wt%, 15 wt% and 20 wt% PFR raffinate. These glasses were analysed for composition, amorphous nature, aqueous durability, thermal and mechanical properties. A short discussion of the potential benefits of PFR raffinate vitrification over cementation is included in the discussion, including identification of the potential cost savings associated with management via vitrification and future work required.

5.2 - Materials and Experimental

5.2.1 - Materials

Raffinate Simulant

This proof of concept study was carried out using an inactive surrogate for the PFR raffinate wastes. This inactive surrogate was formulated on the assumption that the PFR raffinate would be treated using an evaporation or calcination step in order to produce a solid calcine. The composition was thus formulated using the data available from the literature on the

average composition of four PRF tanks at the Dounreay site [151]. The chemical composition of this hypothetical, calcined PFR raffinate was used as the basis for the simulant waste design in this study. The average composition, as used for these calculations, is provided in Table 5.1. The simulant waste stream used varied in a number of ways from that stated in the above reference. Any altered or excluded elements are identified below and in Table 5.1.

For reasons of practicality any elements with concentrations <15 mg L^{-1} were excluded (Ag, As, Cm, Dy, Eu, Gd, Ge, Hg, Ho, In, Nb, Np, P, Pb, Pd, Rb, Rh, Sb, Se, Sn and Tc). These elements were considered to be present in concentrations below that applicable for the purpose of these scoping experiments. The one exception to this was Pd which exists in the waste stream at a concentration of ~150 mg L^{-1} and yet was excluded on an economic basis. The omission of these elements accounts for < 2.8 wt% of the mass of the total waste stream. Radioactive elements with concentrations < 15 mg L^{-1} were substituted for relevant concentrations of inactive surrogates (Ce for U and Sm for Am).

Glasses

Three glasses were produced and characterised in this study. These glasses were based on a G73 barium-silicate base glass composition [154], with PFR raffinate simulant incorporated at 10 wt%, 15 wt% and 20 wt% waste loadings. These glasses are identified from this point as G73, G73-10, G73-15 and G73-20 respectively. Glasses were produced from batch to provide 250 g of glass. The components of the raffinate simulant were batched in either their oxide or carbonate forms according to their molar proportions to obtain the specified waste loading. The following analytical grade chemicals were used for batching; $Al(OH)_3$, $Na_2B_4O_7.10H_2O$, $BaCO_3$, $CaCO_3$, CdO, CeO_2, $Cr(NO_3)_3.9H_2O$, Cs_2CO_3, CuO, Fe_2O_3, La_2O_3, Mn_2O_3, MoO_3, Na_2CO_3, Nd_2O_3, $NiCO_3$, Pr_6O_{11}, RuO_2, Na_2SO_4, SiO_2, Sm_2O_3, $SrCO_3$, TeO_2, TiO_2, Y_2O_3 and ZnO. The glasses were heated in mullite crucibles with stirring to 1200 °C at 10 °C min^{-1} and held at temperature for 3 hours. The glasses were poured into blocks and annealed at 500 °C for one hour before cooling to 25 °C at 1 °C min^{-1}.

Included in Simulant (surrogate element used)		Excluded from Simulant	
Element	*ppm*	*Element*	*ppm*
Na	9,711	*Rh*	15
Cu	8,725	*Cm*	4
Fe	3,837	*Nb*	3.5
Zn	3,566	*Dy*	2.4
Cd	2,540	*Ag*	<1.3
S	1,351	*As*	<13
Ni	1,277	*Co*	<0.4
Cr	669	*Ge*	<1.3
Cs	509	*Hg*	<0.3
Nd	462	*Ho*	<1.3
Am (Sm)	405	*In*	<4
Al	350	*Np*	<13
Ce	304	*P*	<2.7
U (Ce)	168	*Pb*	<1.1
La	163	*Rb*	<1.3
Pr	158	*Sb*	<1.3
Mo	154	*Se*	<1.3
Pd	150	*Sn*	<0.3
Ca	138	*Tc*	<1.3
Sm	123	*Eu*	15
Y	112	*Gd*	15
Te	74	*Pd*	150
Sr	60		
Mn	45		
Ru	60		
Ba	39		
Ti	36		

Table 5.1 - Average composition of PFR raffinate as characterised in [151]. Brackets indicate where the use of an appropriate inactive simulant was applied. The right hand columns identifies elements excluded from the simulant based on both low concentrations in the raffinate and on an economic basis.

Nominal wt% [Analysed wt%]	Sample ID				
	G73 Base	PFR Calcine	G73-10	G73-15	G73-20
SiO_2	40.8	-	36.76 [34.29]	34.72 [33.40]	32.68 [32.58]
BaO	36.5	0.09	32.90 [41.21]	31.07 [41.61]	29.25 [38.61]
Fe_2O_3	6.3	11.68	6.81 [7.88]	7.09 [7.78]	7.36 [7.56]
CaO	8.1	0.41	7.35 [4.55]	6.97 [4.54]	6.58 [4.40]
Li_2O	3.1	-	2.77 [-]	2.61 [-]	2.46 [-]
Na_2O	2.5	27.88	5.06 [1.64]	6.33 [2.38]	7.60 [3.30]
CuO	-	26.26	2.33 [2.83]	3.49 [3.98]	4.66 [5.05]
B_2O_3	2.1	-	1.87 [0.46]	1.76 [0.56]	1.66 [0.46]
ZnO	-	9.45	0.95 [1.08]	1.42 [1.55]	1.89 [1.93]
CdO	-	6.18	0.62 [0.74]	0.93 [1.05]	1.24 [1.35]
SO_3	-	7.18	0.72 [0.72]	1.08 [0.79]	1.44 [0.86]
Al_2O_3	0.6	1.41	0.64 [0.86]	0.68 [0.85]	0.72 [1.20]
NiO	-	3.46	0.35 [0.55]	0.52 [0.71]	0.69 [0.86]
Cr_2O_3	-	2.08	0.21 [0.48]	0.31 [0.56]	0.42 [0.66]
Cs_2O	-	1.15	0.12 [0.36]	0.17 [0.42]	0.23 [0.52]
Nd_2O_3	-	1.15	0.11 [0.15]	0.17 [-]	0.23 [0.23]
Sm_2O_3	-	0.30	0.03 [0.10]	0.05 [0.14]	0.06 [0.19]
CeO_2	-	0.97	0.10 [0.05]	0.15 [0.10]	0.19 [0.12]
MoO_3	-	0.49	0.05 [0.06]	0.07 [0.08]	0.10 [0.09]
Y_2O_3	-	0.30	0.03 [0.035]	0.05 [0.05]	0.06 [0.06]
La_2O_3	-	0.04	0.04 [0.03]	0.06 [-]	0.08 [0.04]
Pr_6O_{11}	-	0.04	0.04 [0.04]	0.06 [0.06]	0.08 [0.09]
RuO_2	-	0.17	0.02 [-]	0.03 [-]	0.03 [-]
SrO	-	0.15	0.02 [0.60]	0.02 [0.12]	0.03 [0.07]
TeO_2	-	0.20	0.02 [-]	0.03 [-]	0.04 [-]
TiO_2	-	0.13	0.01 [-]	0.02 [-]	0.03 [-]
Mn_2O_3	-	0.14	0.01 [0.08]	0.02 [0.08]	0.03 [0.09]

Table 5.2 – Compositions of base glass, simulant calcined PFR raffinate and glasses produced. Compositions of glasses provided both as batched and [as measured by XRF] (boron analysis via dissolution in HF and ICP-AES). Numbers in [brackets] indicate analysed composition.

Glass monoliths were prepared for SEM-EDX, Vickers hardness testing and fracture toughness testing by grinding with P600 and P1000 diamond matrix plates followed by polishing with 6 µm, 3 µm, 1 µm and 0.25 µm diamond pastes.

Powder samples were prepared for XRD and XRF analysis by powdering to a sub-75 µm size fraction using a hardened steel ring and puck mill.

5.2.2 - Experimental

Liquidus Measurement: The liquidus temperature for each sample was measured by placing a 20 cm long mullite boat filled with sub-75 µm glass powder into a tube furnace. The samples were left to equilibrate at 1200 °C for 24 hours, then the temperature gradient along the length of the boat was measured using a retractable thermocouple at 5 mm intervals. The boats were removed and fast quenched in air. The point of crystallisation was measurable to within 1 mm by optical examination of the crucibles and was then correlated with the measured temperature to obtain the liquidus temperature. Results of thermal analysis and density are displayed in Table 5.3.

Glass Property	Sample ID		
	G73-10	G73-15	G73-20
Density (g cm^{-3})	3.512 ± 0.002	3.572 ± 0.002	3.574 ± 0.003
Glass Transition Temperature (°C)	470 ± 10	483 ± 10	484 ± 10
Liquidus Temperature (°C)	1045 ± 10	1075 ± 10	1020 ± 10

Table 5.3 - Properties of glass wasteforms produced at varying PFR raffinate waste loadings including the density, liquidus temperature and glass transition temperature.

Compositional Analysis: XRF analysis was performed using a Phillips PW2404 XRF Axios instrument to obtain compositional data. B_2O_3 content was determined by dissolution of glass powder in HF followed by analysis of leachate using a Perkin-Elmer Optima 5300 dual view Inductively Coupled Plasma Atomic Emission Spectroscopy (ICP-AES). Both sets of analysis were performed at the School of Earth Sciences, The University of Manchester. Results are displayed in Table 5.2.

PCT Experiments

PCT experiments used a 75 µm – 150 µm size fraction in 18.2 MΩ H_2O at 90°C with a SA/V between 1499 m^{-1} and 1525 m^{-1}.

5.3 - Results

5.3.1 - Glass Formation

Glasses with the addition of 10 wt%, 15 wt% and 20 wt% PFR simulant were produced in this study. These glasses formed readily and were easily poured from the melt at 1200 °C, with no evidence of un-dissolved batch found. However, a small degree of corrosion was evident in the crucibles. The glasses formed were amorphous, with no evidence of large scale crystallisation, as shown by the powder XRD in Figure 5.1 a). Only diffuse scattering was observed, indicating an amorphous atomic structure. The lack of contrast in both the SEM-BSE imaging and SEM-EDX mapping analysis, displayed in Figure 5.1 b), illustrates that no chemical segregation is present in the glass on a macro-scale.

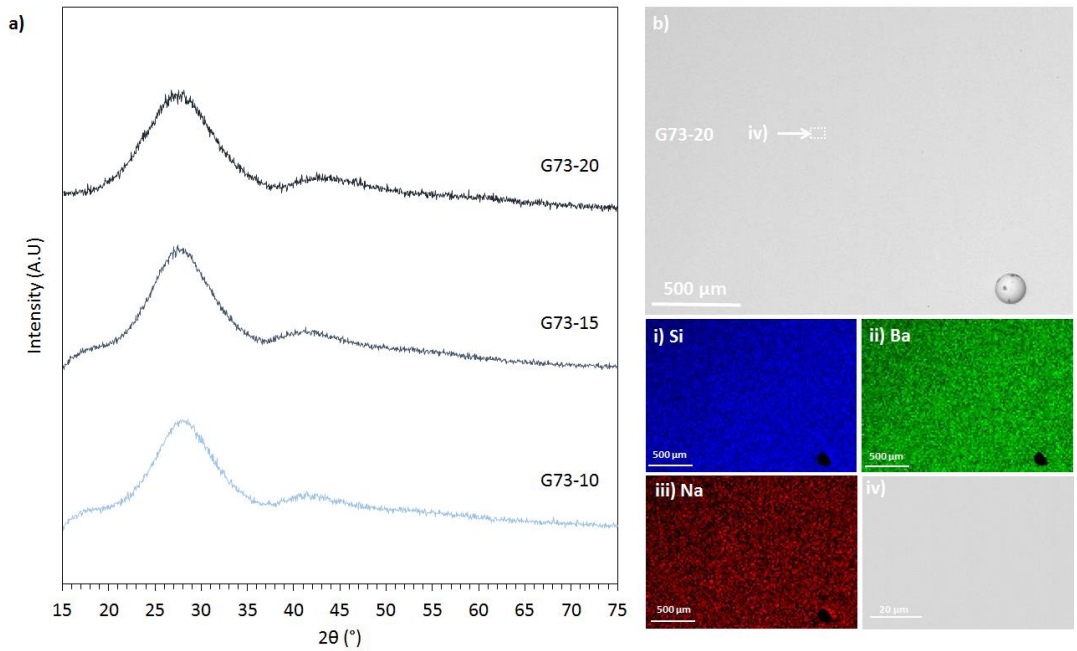

Figure 5.1 - a) Powder XRD patterns of G73 PFR raffinate loaded glasses, displaying diffuse scattering characteristic of amorphous material and b) SEM-BSE image displaying homogeneity of G73-20 glass matrix, set above i) - iii) SEM-EDX maps of key elements for b) and iv) a higher resolution BSE-SEM of G73-20 glass matrix identified in b) which taken illustrates the absence of crystalline materials in the final waste product.

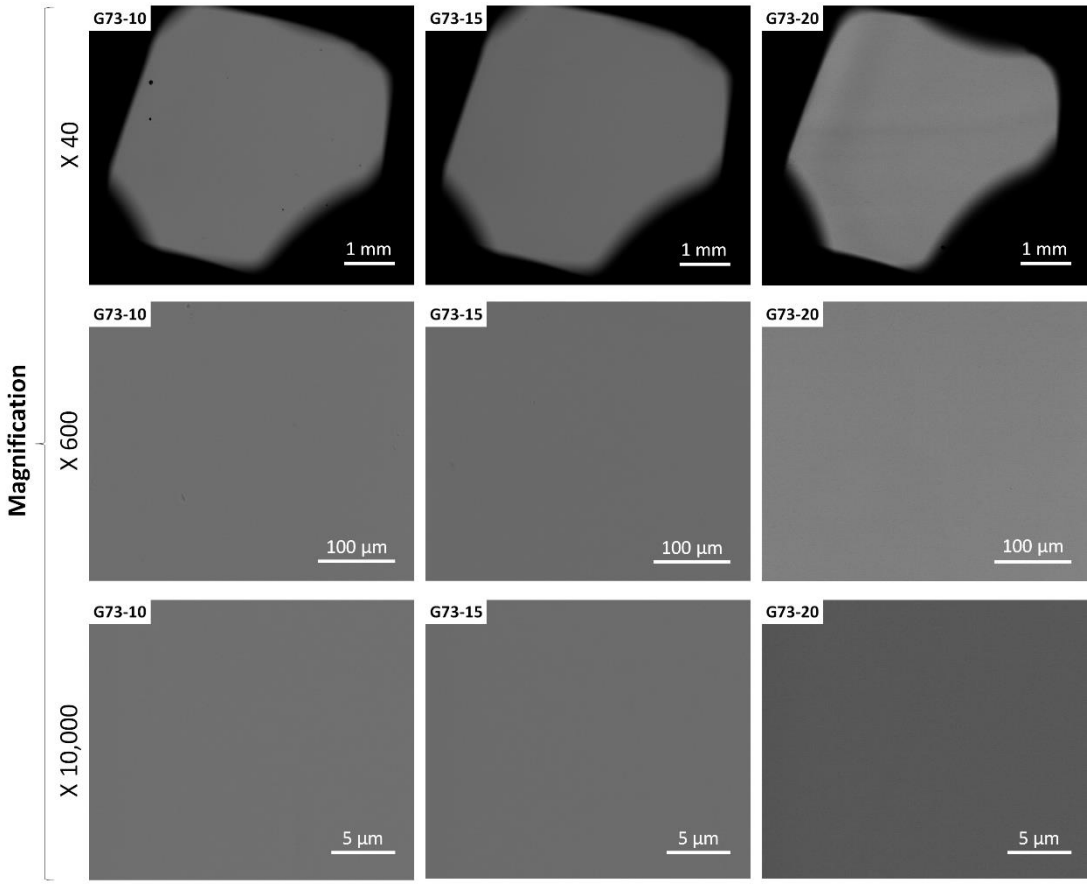

Figure 5.2 - SEM-BSE images of the three waste loaded glasses G73-10, G73-15 and G73-20 at various magnifications. The lack of image contrast suggests chemical homogeneity within the sample.

No contrast in the SEM-BSE grayscale was observable in any of the three glasses, as shown in Figure 5.2. This indicates no crystallisation or compositional phase separation is present in the glass at the scales investigated. This is true from a mm to a sub-micron scale (images obtained at x10,000 having a single pixel resolution of 25 nm). No differences in crystallisation behaviour were noted between the three glass compositions and no sulphate phases were observed to be present despite the majority of sulphur being retained within the glass.

5.3.2 - Glass Composition

The composition of the three glasses produced was analysed using XRF analysis and ICP-AES, the data for this is provided alongside the nominal batched compositions in Table 5.2. The quantification using XRF compositional data was interpreted with caution, due to the unavoidable overlap of multiple spectral lines and limitations in software when studying a

system with a high numbers of component elements. As such the following comments on composition and waste retention are used primarily as a guide to qualify glass properties.

The analysed compositions all showed a decrease in the mole % of glass forming constituents and corresponding increase in mole % of waste constituents with increased waste loading. This is concurrent with retention of waste oxide components in the glass. This was true of 19 out of the 26 of the constituent oxides. There were seven noted exceptions to this trend, five in the waste constituent oxides (Cs_2O, Cr_2O_3, La_2O_3, Nd_2O_3 and SrO) and two in the glass matrix constituent oxides (Al_2O_3 and B_2O_3).

5.3.3 - Aqueous Durability

The aqueous durability of the glasses was assessed using the PCT methodology [110]. Results of the PCT aqueous durability experiments are displayed in Figures 5.3 - 5.5 and Tables 5.4 - 5.5. Graphs are provided for the elements which were detectable by ICP-AES in concentrations higher than that those measured in the blanks. NR_i from 28 days testing are provided for selected elements in Table 5.4. Figure 5.3 shows that the solutions for all three waste loaded glasses buffered to pH 10.2 ± 0.2 after 3 days. There was no further measurable fluctuation of pH during the course of the experiments.

NR_i ($g\ m^{-2}\ day^{-1}$)	Glass Composition		
	G73-10	G73-15	G73-20
B	3.33×10^{-2}	3.28×10^{-2}	3.24×10^{-2}
Na	1.69×10^{-2}	2.17×10^{-2}	1.84×10^{-2}
Si	7.18×10^{-3}	8.40×10^{-3}	7.19×10^{-3}
Ca	5.89×10^{-3}	3.62×10^{-3}	4.95×10^{-3}
Mo	4.44×10^{-3}	4.78×10^{-3}	6.38×10^{-3}
Ba	4.43×10^{-3}	3.10×10^{-3}	1.47×10^{-3}
Cr	3.48×10^{-4}	1.64×10^{-4}	2.30×10^{-4}
Cu	4.93×10^{-6}	1.45×10^{-6}	0.00
Al	0.00	0.00	2.91×10^{-4}
Fe	0.00	0.00	0.00
Ni	0.00	0.00	0.00
Sr	0.00	0.00	0.00
Zn	0.00	0.00	0.00

Table 5.4 – Normalised elemental loss rates for the three waste PFR waste loaded glasses measured after 28 days. Data is from PCT experiments of the wasteforms at 90 °C in 18.2 MΩ water.

Table 5.4 shows that only nine out of 26 of the elements of interest; B, Si, Na, Ca, Mo, Ba, Cr, Cu and Al were detectable in concentrations above that observed in the blanks. Seven of these are present in both the glass frit and waste stream compositions whereas Si and B are present only in the batched frit. Table 5.4 and Figure 5.3 show no discernible difference between the three glasses tested in the terms of their elemental NL_i. The NL_i of elements tracked well for all three waste loadings and most of the variations in NL_i are within the experimental error (± 5% NL_i). This indicates that increasing waste loading does not significantly impact the aqueous durability of the G73 glass with the addition of up to 20% PFR raffinate simulant waste loading. Barium is the one notable exception to this observation. The NL_{Ba} shows that Ba starts to be removed from solution after 7 days in G73-20, 14 days in G73-15 and 21 days in G73-10.

Table 5.4 and Figure 5.4 shows that in all three glasses NR_i was highest for the network former B (3.24×10^{-2} g m^{-2} day^{-1} – 3.33×10^{-2} g m^{-2} day^{-1}) and the alkali modifier Na (1.69×10^{-2} g m^{-2} day^{-1} – 2.17×10^{-2} g m^{-2} day^{-1}). The other measurable components had an NR_i approximately an order of magnitude lower than that of B and Na. The lowest NL_i values were observed for Al and Cr (< 1.7×10^{-4} g m^{-2} day^{-1}).

Figure 5.4 suggests that steady state dissolution rates do not appear to be reached for any element tested during the time frame of this experiment. This is indicated by the gradual changes in the slope of the plots of NL_i and from the presence of peaks and troughs in the elements closest to the detection limit, as is the case in the dissolution profile of Al. However, it looks probable that all present alkali earth elements (Ca, Sr, Ba) started to precipitate from solution during the experiment, as shown by the decrease in their NL_i with time. This is particularly evident in the case of Sr where the NL_{Sr} drops to near zero after 14 days from its highest concentration after seven days.

The NR_B and NL_{Si} shown in Table 5.5 highlights the stability of the glass network by comparison with SON68 glass, tested via a comparable methodology, as described in Section 4.3 and [232]. The NR_{Si} is also below that previously determined for UK HLW glasses (MW25) under similar test scenarios [233].

Figure 5.5 illustrates the changes in saturation indices, obtained by geochemical modelling using the PhreeqC code, for the PCT experiments on the three glass compositions. The species displayed in this figure are of importance as either potential alteration layers, affinity limiting species or potential crystalline precipitates. It can be seen that the behaviour of all three glasses is broadly similar. The experiment solutions only reach saturation with one of

the phases tested, tobermorite 14 Å, which may precipitate as a calcium-silicate hydrate alteration product on the powders. For the duration of the experiment, all solutions remain unsaturated with respect to amorphous SiO_2, boric acid, analcime and all barium phases contained in the LLNL database.

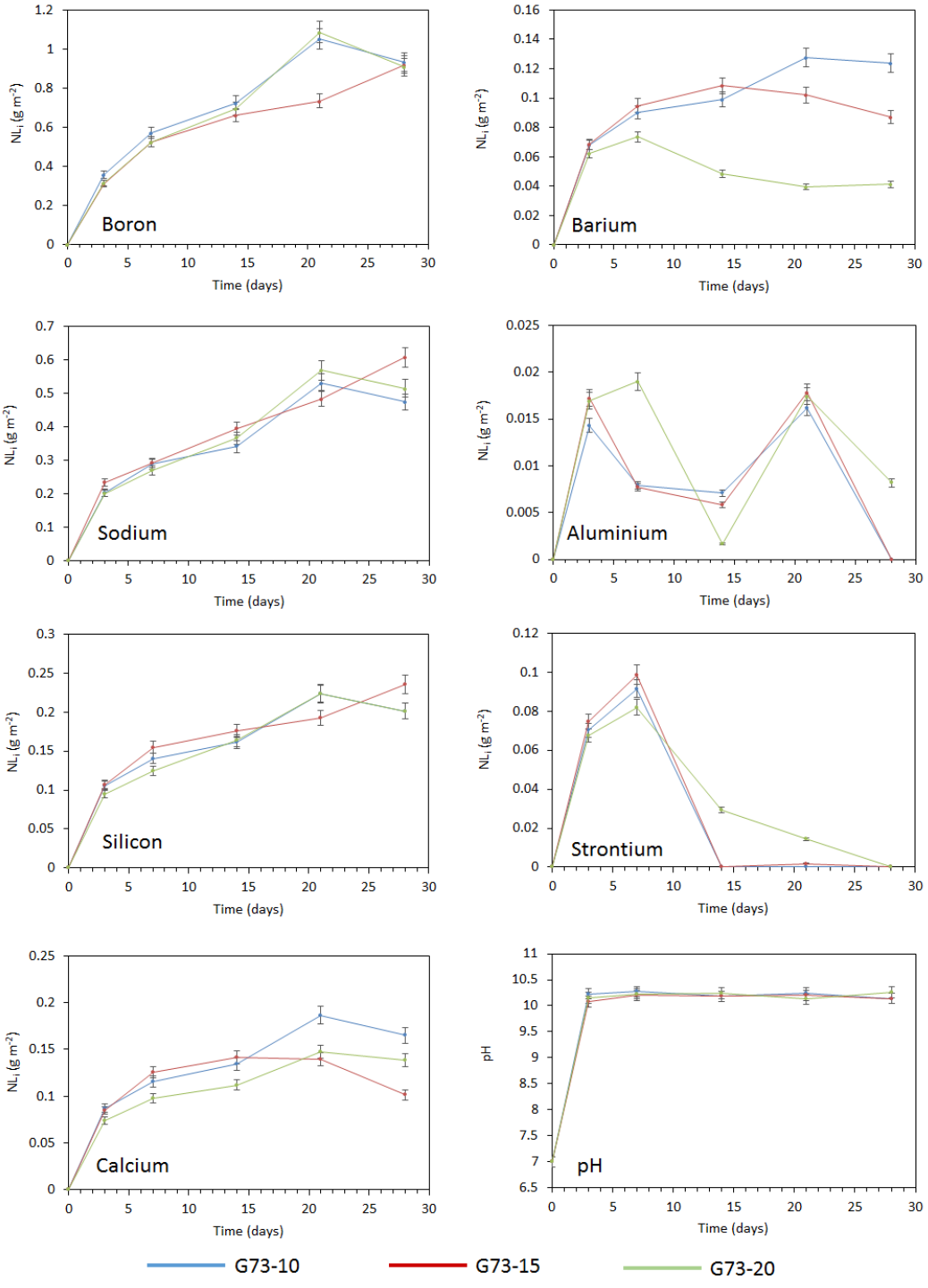

Figure 5.3 – Graphs displaying the normalised elemental mass loss with varying levels of PFR raffinate loading from PCT experiments at 90°C in 18.2 MΩ water with a SA/V of 1499 m^{-1} -1525 m^{-1} dependant on glass density.

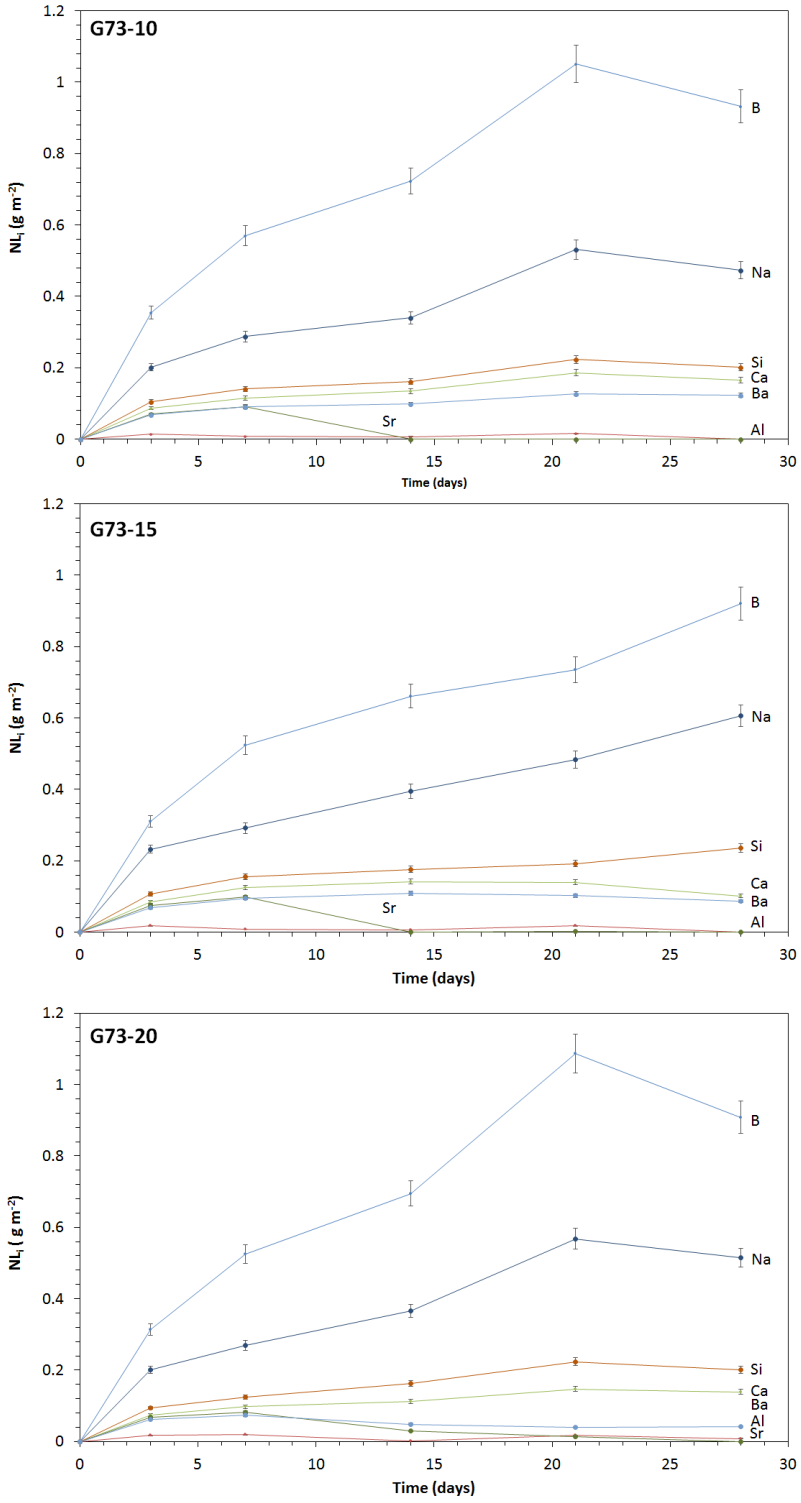

Figure 5.4 – Graphs displaying differences in normalised elemental mass losses for PFR waste loaded glasses from PCT experiments at 90°C in 18.2 MΩ H_2O with a SA/V of 1499 m^{-1} -1525 m^{-1} dependant on glass density.

Glass Composition	NL_i after 28 days (g m^{-2})		NR_i after 28 days (g m^2 day^{-1})	
	NL_B	NL_{Si}	NR_B	NR_{Si}
G73-15	0.9196	0.2351	0.0328	0.0083
SON68 [232]	0.4886	0.1559	0.01745	0.0055
MW25 [233]	-	-	-	0.020

Table 5.5 – Comparison of network dissolution limiting normalised elemental mass losses and normalised elemental dissolution rates between SON68 glass, British magnox waste HLW glass and G73-15 waste loaded glasses tested, under PCT conditions at 90 °C in 18.2 MΩ water.

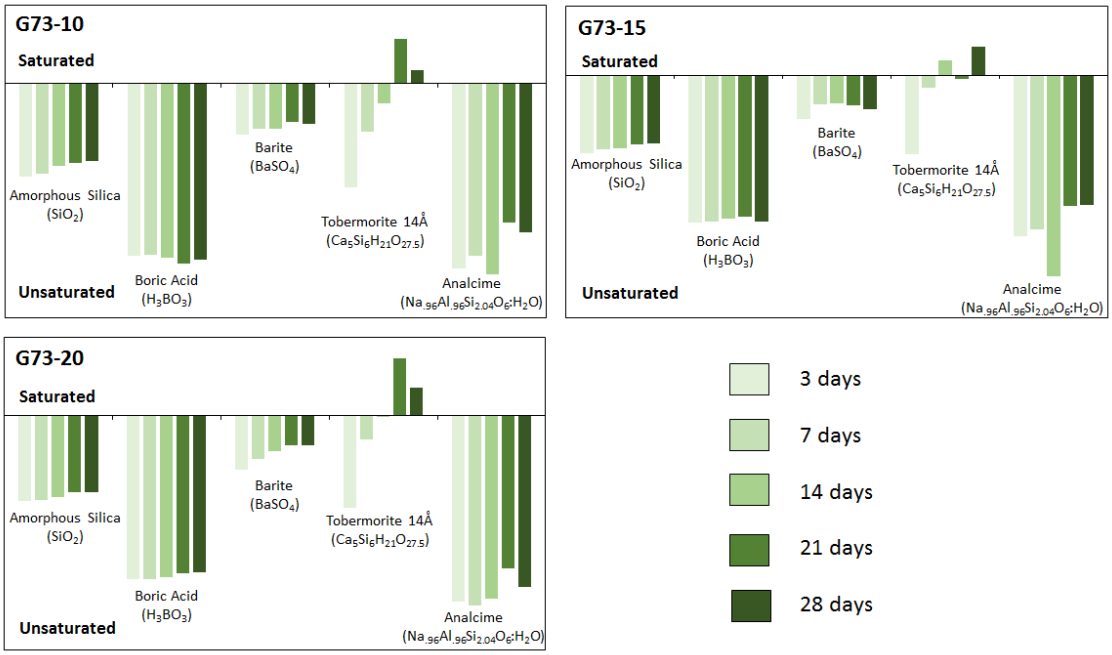

Figure 5.5 – Changes in saturation indices over time for key species and phases involved in the dissolution process for G73 PFR loaded glasses, as obtained from PhreeqC geochemical modelling of the dissolution data.

5.3.4 - Thermal Properties

Table 5.1 shows the glass transition temperature, point of melt fluidity and measured liquidus temperature for the three waste loaded glasses. The T_g are comparable within error for increases in waste loading and correspond well with the transition temperature previously reported for the same base glass loaded with organic exchange resins [154]. The liquidus temperature of the glasses were all below 1100 °C, similarly, no correlation with increased waste loading was found.

5.3.5 - Mechanical Testing

The results from mechanical testing of the glass compositions for Vickers hardness and fracture toughness are shown in Figure 5.6. All compositions performed better than existing HLW glass compositions for fracture toughness and were comparable or superior in terms of Vickers hardness [52, 205]. The lowest waste loaded glass, G73-10, performed slightly better than the G73-15 and G73-20 glasses with respect to indentation fracture toughness. The hardness of the glasses with varying waste loading was equivalent within measurable precision

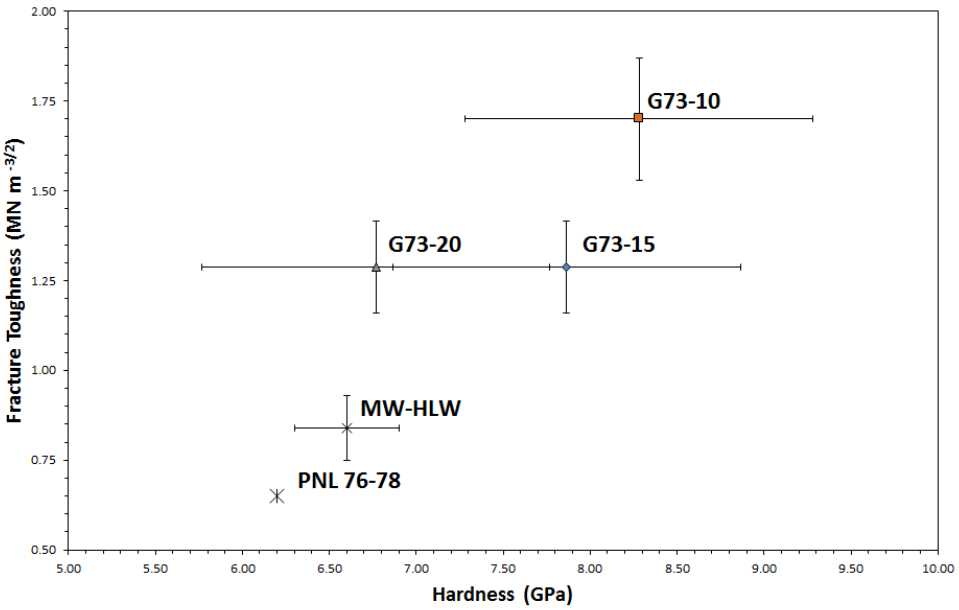

Figure 5.6 – Fracture toughness and hardness values of G73 PFR raffinate waste loaded glasses obtained using the Vickers indentation methodology with comparison to waste glasses currently used for HLW immobilisation. Errors correspond to 3 x the measured standard deviation.

5.4 - Discussion

5.4.1 - Choice of Raffinate Simulant

A number of waste component elements were excluded from the waste simulant used in this study as has been noted in Section 5.2. These omissions resulted in a variation of the overall finished glass composition, at 20 wt% waste loading, against that expected in a full waste loaded simulant, of only ≤ 0.54 wt%. This was considered to be a good approximation and acceptable compromise for this initial investigation. The exclusion of Rh, Ru and Pd make up

the greatest proportion of the simulant omitted from these formulations by wt%. Although these elements may have significant implications on melter design, they are insoluble in silicate melts and therefore unlikely to affect the vitreous wasteform produced [234]. Any future detailed studies should, however, plan to address any issues arising from the exclusion of these components.

The use of surrogate elements in place of radioactive isotopes was employed for reasons of practicality. While this is not ideal, the surrogate elements selected (U replaced with Ce and Am with Sm, on a molar basis of overall composition) were deemed the most appropriate for the study, based upon considerations of coordination number, ionic radii and potential oxidation states [1]. Thus a simulant wasteform has been produced which can be considered broadly representative of that which would be produced as a result of PFR raffinate vitrification. Clearly the addition of missing components and optimisation of the simulant raffinate should be applied if further study is to be undertaken.

5.4.2 - Crystallisation and Amorphous Character

It can be stated with confidence that PFR loaded G73 glasses exist within a stable glass forming region of the phase diagram up the 20 wt% loadings utilised in this study. The diffuse scattering and absence of sharp peaks in the powder XRD pattern indicates that no significant crystallisation had occurred (> 0.5 wt%). SEM-EDX mapping and SEM-BSE imaging with up to 100 nm resolution provided evidence that no phase separation had occurred in these samples. Crystallisation in radioactive waste glasses, when produced from the melt, is undesirable for several reasons including; the possibility for the precipitation of soluble radionuclide containing phases; the potential for decreased aqueous durability of the matrix, due to the removal of refractory components; the potential for swelling of crystal phases as a result of damage from self-irradiation, the negative effects on pouring and radiogenic heating from in-melt crystallisation. The absence of significant crystallisation and minimal evidence of crucible corrosion indicate that a high quality glass wasteform has been obtained which should be both stable and amenable to the processing of PFR wastes.

5.4.3 - Glass Composition

As noted in Section 5.3, the data collected on glass composition in this study has to be treated with caution. This data does not warrant significant discussion, as due to the number of elements included in the waste stream, spectral signal overlap is an inevitable factor.

However, some positive inferences on the quality of the wasteform produced can be taken from this XRF data. The noted trend that the concentration of most waste components in the glasses increases with waste loading is suggestive that the wasteform is incorporating the waste components. This wasn't true in all cases. Most notably Cs showed no trend in composition with waste loading. This requires further investigation as Cs is prone to volatilisation within boron containing glass melts. What is happening to this Cs during processing should be determined and steps taken to minimise this volatile loss fraction as far as possible.

A substantial loss of the oxides B_2O_3 from batch was observed during melting. B_2O_3 showed losses of between 64.38 mol % and 71.05 mol % compared to batch calculations. As such, no trend according to waste loading should be assigned to this elements. The accuracy of the boron data was deemed to be inaccurate. A standard glass sample of similar composition was measured using an identical methodology and the results produced were 3 x lower than expected. The increased concentration of Al_2O_3 noted is likely to be a result of corrosion of the mullite crucible and the inclusion of corroded material into the final wasteform. This corrosion may also account for the anomalous increase in the concentration of Fe_2O_3 when compared to the batched composition. In order to accurately quality the chemical composition of these complex glasses the use of chemical dissolution and quantification via ICP-AES/MS would be more suitable.

5.4.4 - Aqueous Durability

The glasses produced can be considered to perform well in aqueous solution as an immobilising matrix for the PFR raffinate waste stream. The NR_{si} measured after 28 days PCT experiments at 90 °C was 8.3 x 10^{-3} g m^{-3} day^{-1}. The UK HLW MW25 glass, has a NR_{Si} of ~2 x 10^{-2} g m^{-2} day^{-1} under identical experimental conditions [233]. This comparison shows that these wasteforms have a comparable product quality to glasses currently utilised for UK HLW disposal; as such they should be considered suitable the immobilisation of ILW. Furthermore the waste loaded G73 glasses made in this study also behave comparably in similar tests performed on the French HLW base glass, SON68, as described in Chapter 4. Only eight of the 19 waste constituent elements from the PFR raffinate were detectable by ICP-AES above background levels, Na, Ca, Mo, Ba, Cr, Cu, Sr and Al.

The low release rates measured under these aggressive conditions are promising and support the hypothesis that vitrification will produce a waste stream superior to that

provided by cementation. It has to be assumed that the NL_{Cs} would have been measurable and in a worst case scenario would be present with a NL_{Cs} similar to that seen for NL_{Na}. However it should be expected that the Cs release would be lower than that measured for Na.

The high rates of Na and B release after 28 days imply that an ion exchange mechanism for matrix dissolution is prevalent during dissolution. The gradual decrease in the slope of the NL_{Si} up to 28 days shown in Figure 5.3 indicates that the rate of network hydration is reduced during the course of the experiments. The most likely reason for this is the affinity affect or formation of alteration product on the glass surface. The NL_i of alkali earth elements Ba, Sr and Ca were decreased over during the course of the experiment, most likely due to precipitation from solution.

Geochemical modelling provides insight into the possible behaviour of these glasses in solution. The reduction in the slope of the NL_{Si} curve could be attributed to either the movement of amorphous silica towards saturation, indicating an affinity based mechanism; or alternatively via the precipitation of alkali-earth silicate hydrates. The trend for alkali-earth silicate hydrates is to reach saturation around the middle of the test period, as is illustrated in Figure 5.5 for tobermorite 14 Å. This correlates with the decrease in NL_i noted for the alkali-earth species.

As no trend was identified in the saturation indices for simple alkali-earth salts or for non-silicate containing alkali-earth phases, the glass dissolution behaviour can be attributed to the precipitation of an alkali earth rich silicate hydrate phases on the glass surface. This would prove beneficial as it would act as a secondary immobilisation technique to the release of harmful elements from the wasteform such as Ba and Sr, even after their initial release to solution while also lowering the steady state dissolution rate of the glass network.

5.4.5 - Thermal and Mechanical Properties

Thermal Properties: All glasses tested have a liquidus temperature below 1100 °C, which is beneficial for nuclear waste vitrification. This is based on the requirement to minimise volatile losses of radioactive components caused by high melt temperatures, especially that of Cs, when processed at temperatures above 1200°C [51, 168, 169]. As the glasses produced in this study have been shown to retain the majority of their Cs inventory after processing at 1200°C, the retention of Cs should be expected to be even higher with the utilisation of lower melt temperatures. These glasses should be recast with a lower processing temperature in order to test this hypothesis.

Mechanical Properties: The mechanical properties of the glass have been shown to be improved by comparison with those currently employed for radioactive waste disposal. This means that the waste should, at a minimum, pass compliance tests for storage in HLW canisters. Packaging in 3 m^3 boxes should also be possible based on the mechanical properties of these packages and the lack of internal voidage which would be expected in the final product.

5.4.5 - Implications of this work

It is unlikely that cement will be able to effectively immobilise the whole range of elements present in this waste stream as has been discussed in Section 2.1.2 [235]. A cementitious wasteform could be subject to increased dissolution and release rates due to its inherent porosity and increased internal surface area. Radioisotopes sorb to the surface of cements and can thus be more readily removed from the disposal matrix waste through changes in ground water chemistry. The high solubility and potential for removal of many of these waste elements; especially Cs, which by activity makes up over 60% of the radioactive inventory, is of significant concern [146]. These factors necessitate treatment of this waste using the most robust methodology possible to minimise potential radioisotope migration during interim or GDF storage. Vitrification is likely to offer an environmentally improved solution over the current baseline.

This study has demonstrated that a high quality product may be obtained by vitrification of PFR raffinate using G73 barium silicate glass. The benefits of vitrification go beyond the improvements in wasteform quality described in Section 5.4 and may also offer fiscal incentives for implementation. If this PFR raffinate waste were to be calcined and treated via vitrification, a substantial waste volume reduction would be achieved.

Current NDA plans are to cement this raffinate in 500 L drums with a target waste loading of 0.305 m^3 per drum. With 212.1 m^3 of raffinate to process this would result in 397 m^3 of packaged waste for disposal (696 x 500 L drums with a displacement volume of 0.57 m^3 each) [146]. If vitrification, at only 15 wt% loading were utilised for the same purpose, the volume of waste produced would be reduced to below 14.4 m^3 of glass. Conceivably, this could be processed inside refractory lined 3m^3 boxes, using in container vitrification technology, such as that marketed by Kurion. Assuming 70% of the box capacity (2.57 m^3) could be filled, each 3m^3 box would hold 1.8 m^3 of vitrified product. This means the waste could be fully conditioned using just eight 3 m^3 boxes, producing a total waste volume for disposal of

28.6 m^3. This treatment methodology would therefore eliminate >368 m^3 of ILW from the UK waste disposal inventory. The heat generation, surface activity limits and containment limits for impact of this hypothetical G73-15 waste stream have been calculated to be within NDA guidelines for a 3 m^3 ILW box[2] [236].

If the assumption is made that a small scale modular vitrification plant could be constructed at a similar cost to that of the cementation plant, an estimate of the potential financial savings for treatment of ILW via vitrification can be deduced. At the time of writing disposal of UK ILW had a projected disposal cost of £25.9k m^{-3} [237]. This alone would equate to a minimum cost saving of over £9.5 M on the GDF disposal of this waste stream alone.

This price does not include any of the associated costs of interim storage, waste packaging or transport to the GDF facility. The following assumptions have been made in the production of the total cost savings provided in Table 5.6:

Cost of Interim Storage: Estimated at £10.7k based on the projected cost of £321M for an protected EPS2 type ILW store holding 30,000 m^3 of waste [238, 239].

Cost of 500 L drum: £4 k based on estimated materials and manufacturing costs.

Cost of refractory lined 3 m^3 box: £40k based on the assumption of comparable costings for the provision of the refractory lined 3 m^3 box with that of the advanced double skinned 3 m^3 box [240].

Transport costs: Assumed to be £1.25 k/m^3 costs provided in [241].

The decreased risk to public health, improved quality of final wasteform, improved long term stability, smaller footprint on the Dounreay ILW stores and the reduced waste management cost, combine to provide a compelling case for treatment of these wastes using vitrification when compared with cementation.

It is recommended that further review of the cemented wasteform should be made available in order to allow a more detailed comparison of each treatment methodology. Data already exists detailing vitrification of PFR raffinate into both G73 ILW glass and standard HLW compositions. Equivalent data on the cementitious wasteform, especially concerning its waste retention and stability in aqueous environments should be produced in order to

[2] Calculation based upon reported inventory of radioisotopes for this waste stream and accounting for the concentration of activity achieved by vitrification. This packaged waste will meet specifications imposed for a square corner 3 m^3 box.

provide a valid comparison. The necessity for this review has been acknowledged by Dounreay Ltd and should be completed before cementation of this material is begun. This will provide confidence in the treatment methodology selected and reduce the potential for an expensive and complicated reworking of unsuitable waste packages in the future [149-151].

	Cementation	**Vitrification** *G73-15*	**Projected savings from use of vitrification technology**
Waste container	500 L drum	Refractory lined 3 m^3 box	N/A
Waste volume (m^3)	347	14.4	332.6
Packaged waste volume (m^{-3})	397	28.6	368.4
Cost of packaging materials	£2.78M	£0.32M	£2.46M
Cost of Interim storage	£3.18M	£0.23	£2.95M
Cost of GDF disposal*	*£10.28M*	*£0.74M*	*£9.54M*
Cost of Transport*	*£0.50M*	*£0.04M*	*£0.46M*
Expected saving *(GDF relocation)*		£15.41M	
Expected Saving *(Long-term near surface storage)*		£5.25M	

Table 5.6 – Projected lifetime waste management volumes and costs for PFR raffinate as both cemented and vitrified products. *As the Scottish government has a policy of long term near surface storage for these higher activity radioactive wastes, costs associated with GDF and transport may not be relevant to this assessment, although they should not be excluded from consideration.

5.5 - Conclusion and Future Work

During the course of this investigation it has been shown that the proposed processing methodology shows promise for PFR immobilisation. A high quality vitreous wasteform has been produced from the simulated calcine of PFR raffinate. Retention of the waste stream has been demonstrated to be possible using a G73 barium silicate glass at up to 20 wt% loading.

The product was homogeneous in nature, readily forming a stable amorphous solid with no detrimental crystal formation and thermal properties conductive to the industrial processing

of ILW. The final wasteform, at up to 20 wt% loading, were also of a high quality in terms of their aqueous durability and mechanical properties. All glasses performed comparably to glass compositions currently in use, both in the UK and internationally, for the immobilisation of HLW. The aqueous durability was higher than that of current UK HLW glasses and should be considered a stable matrix for ILW under storage and disposal conditions. The mechanical properties of the wasteform also matched or exceeded those currently in use for HLW glasses, in both the UK and USA, and therefore, should be amenable to transport and storage in either 500 L HLW flasks or 3 m^3 ILW waste packages.

The volume reduction and concentration of the waste associated with this vitrification step would not result in the re-classification of the waste as HLW. This is important as a reclassification to HLW would require consideration of heat dissipation in storage, introducing significant extra costs for disposal, as well as increasing the final volume required in a storage vault. The immobilisation methodology proposed would result in a decrease in the waste disposal volume of approximately 368 m^3 by comparison to cementation. With an assumption of comparable plant costs, this vitrification could offers a potential reduction in cost for final disposal of up to £15.4M. However, any potential cost reduction must be qualified against numerous other site operations, as such the primary driver for the alteration of the baseline processing technology be based upon the expected improvements in wasteform quality.

The G73-15 vitrified product provides a high quality alternative to the immobilisation of PFR raffinate by cementation, and as such deserves further investigation. Six significant areas of study are still required to confirm the benefits of this processing over cementation which are listed below.

1. A review of the cemented PFR waste should be produced and made available with emphasis on the chemical retention of radionuclides during storage in aqueous solution. This of key importance as the ability of cements to effectively retain the PFR waste inventory over geological time frame is doubtful. This requires qualification before processing begins to prevent the necessity for difficult and expensive future wasteform reworking.

Further work should be performed on the G73 glass compositions including the following.

2. Production of a glasses using a raffinate simulant inclusive of all simulant elements. The addition of these elements should be studied for their effect on the glasses with waste loading up to 20 wt%.

3. Quantification of the retention of waste components in the glass wasteform during processing. This should be performed by complete dissolution of the glass followed by quantification by ICP-AES/ICP-MS to avoid spectral overlap.
4. Further testing of the aqueous durability properties, including the dissolution at high pH to simulate the dissolution rates with disposal in a cementitious backfill.
5. A detailed review of both the costing and wasteform properties should be performed to compare the G73 glasses with conventional borosilicate compositions or cemented products.
6. Concern could arise due to the chemo-toxicity of the barium released from these glasses [242]. However, the low NL_{Ba} observed in this study should mean this is of negligible concern. Further investigation may be required to appreciate how the barium released complexes with surrounding ground water and therefore its resulting solubility what the potential impact of this on the surrounding population may be.

Chapter 6 - Clinoptilolite Ion Exchange Material

6.1 - Chapter Introduction

Clinoptilolite is an ion exchange material in use at the SIXEP plant, Sellafield, to remove radioactive Cs and Sr from aqueous solution prior to discharge. This material exists in a granular form which requires consolidation prior to disposal in a GDF facility. It is, however, unsuitable for cementation due to the pozzolanic collapse and resulting release of its Cs inventory. HIPing has been investigated for its ability to immobilise this material. This chapter presents work illustrating the capability to process clinoptilolite into a glass-ceramic wasteform which should be considered suitable for GDF disposal.

The aqueous durability of these wasteforms was tested using PCT, MCC-1 and SPFT experimental methodologies. Vertical Scanning Interferometry (VSI) and SEM imaging were used to provide a powerful and novel method of elucidating the effect of phase separation on the properties of aqueous dissolution.

6.2 - Materials and Experimental

Clinoptilolite

The clinoptilolite (CLINO) used in this study was sourced from the same deposit in the Mojave desert as that currently used in the SIXEP plant, Sellafield. The material was kindly supplied to the ISL group by Sellafield ltd. The density was measured at 2.222 ± 0.002 g cm^{-3} via helium pycnometry. The stated average particle size was 628 µm. An average particle size of 0.7 mm ± 0.1 mm was measured across 150 particles using Vernier callipers.

Ion Exchange

Ion exchange of the CLINO was performed using non-active isotopes of Cs and Sr. CLINO (1 kg) was placed in a solution of deionised H_2O (1.25 L, 18.2 MΩ) with $CsNO_3$ (11.2 g, Sigma-Aldrich, 99.99%) and $Sr(NO_3)_2$ (0.55 g, Sigma-Aldrich, ≥99%). This was left at room temperature for 28 days and agitated for one minute, once every seven days. The Cs and Sr exchanged clinoptilolite (CSXC-CLINO) were washed with deionised H_2O (5 x 2L washes, 18.2 MΩ) and dried overnight in a 90 °C oven. After drying, the simulant was created through the addition of 10 wt % quartz sand (SiO_2 > 99.5%) as per the physical description of the waste stream at Sellafield, obtained from the NDA's waste stream data sheet [160]. Table 6.1 gives

the bulk clinoptilolite compositions before and after ion exchange, as measured using XRF on a Phillips PW2404 XRF Axios with ~10 g of powdered material. This exchange process represents both a significantly higher residency time and proportion of both Cs and Sr than found in the effluents and waste streams on the Sellafield site. The loading of 1 wt % Cs was chosen as the lowest concentration of Cs readily quantifiable by SEM-EDX and XRF analysis.

CPS testing for selection of additives and processing parameters

Five 1 g pellets of CSXC-CLINO were made using the CPS method in a uniaxial press with 13 mm hardened steel die at a pressure of 30 MPa. These pellets were pressed with the addition of $NaAlO_2$ at 0 wt%, 2.5 wt%, 5 wt%, 7.5 wt% and 10 wt%. These pellets were sintered at 1300 °C for two hours in an electric muffle furnace with set ramp rates of 10 °C min^{-1}.

Batching and Canister Preparation

Canisters were created according to the coin and tube design described in Section 3.3. Prior to canister loading the clinoptilolite was calcined at 700 °C for 6h. Samples were top filled with simulant to determine the approximate mass required to fill the canister. Once the approximate volume of simulant required to fill the canister was determined, the material was prepared prior to filling by the addition and mixing of either 5 wt% anhydrous $NaAlO_2$ (Sigma-Aldrich >99.95%) or 5 wt% anhydrous $Na_2B_4O_7$ (Sigma-Aldrich, >99%). The samples produced by HIPing the CSXC-CLINO simulant with these additives are identified from this point as CLINO-$NaAlO_2$ and CLINO-BORAX respectively. The components were mixed by shaking in a polyethylene bag before top filling the canister.

No grinding was performed to mimic an industrial production line, avoiding the creation of fission product containing dusts. The canister lid was utilised to uniaxially press the powders in order to obtain a higher packing density. The canisters were sealed by autogenous TIG welding before being baked out under vacuum. The bake out of the canisters was performed at 300 °C to a vacuum level of ~3 Pa. Once vacuum was achieved the evacuation tube was crimped to seal the canister. A second crimp was applied and broken above the sealing crimp. This was immediately sealed with a weld. The volume of the canister was recorded by measuring using the principle of water displacement.

Oxide Composition (Wt %)		SiO_2	B_2O_3	Al_2O_3	Na_2O	K_2O	CaO	Fe_2O_3	MgO	TiO_2	Cs_2O	SrO	BaO	SO_3	Theoretical Density (g cm^{-3})	Monolithic Density (g cm^{-3})	Percentage Densification (%)
SIXEP Active Inventory [160]		-	-	-	-	-	-	-	-	-	0.002	$7x10^{-5}$		-	-	-	-
Starting Materials	CLINO*	76.5	-	13.6	3.8	1.8	1.9	1.1	0.8	0.1	< 0.1	< 0.3	0.1	-	-	-	-
	CSXC-CLINO*	76.1	-	13.1	3.1	1.9	2.1	1.2	0.7	0.2	1.0	0.5	0.1	0.1	2.222 ± 0.002	-	-
CSXC-$NaAlO_2$	Batched	74.6	0.0	14.3	4.5	1.6	1.8	1.0	0.6	0.2	0.9	0.4	0.1	-	-	-	-
	HIPed*	73.4	0.0	13.1	4.0	2.7	2.3	1.5	0.5	0.2	1.1	0.5	0.3	0.2	2.453 ± 0.003	2.40 ± 0.01	97.7 ± 2
CSXC-BORAX	Batched	74.6	2.7	11.2	5.0	1.6	1.8	1.0	0.6	0.2	0.9	0.4	0.1	-	-	-	-
	HIPed*	73.5	0.58	10.3	5.7	2.6	2.5	1.7	0.4	0.5	1.1	0.6	0.3	0.2	2.397 ± 0.002	2.38 ± 0.01	99.3 ± 2

Table 6.1 - Composition of clinoptilolite before (CLINO) and after exchange (CSXC-C) with $Cs_{(aq)}$ and $Sr_{(aq)}$ at room temperature for 28 days (excluding SiO_2 added to create simulant) with comparison to the active loading of radio Cs and Sr as seen in waste stream stored at Sellafield [160]. Compositions of CSXC-$NaAlO_2$ and CSXC-BORAX as calculated from batch and as measured by XRF and ICP-MS after HIPing. * indicates measured composition, errors approximately 5 % of stated value. The exception is B_2O_3 where the error is substantially higher, potentially ± 100% of stated value as will be discussed later. Theoretical density stated measured on pulverised products via helium pycnometry, monolithic density measured in triplicate using the Archimedes methodology.

Hot Isostatic Pressing (HIPing)

HIPing was performed at the University of Sheffield's research HIP facility using an AIP-630H HIP. Processing was performed using a molybdenum furnace with an argon pressurising medium at 1200°C, a 100 MPa pressure was applied for 2 hours with 10 °C min^{-1} heating and cooling rates. The volume of the canister was measured after processing via the displacement of water.

Sample Retrieval

Powder samples were retrieved by sectioning the welds of the canister lids with an abrasive saw, pressure was applied to the canister walls using a vice. This pressure created significant fragmentation in the processed wasteform, allowing the collection of fragmented and powdered material. Further size reduction was performed using a hardened steel percussion mortar. The powders obtained by this process were separated into appropriate size fractions by sieving.

Larger monolithic samples were obtained by sectioning the lids and walls from the canister using an Isomet 5000 linear precision saw fitted with a 0.9 mm diamond blade. The canister was then mounted for sectioning using a combination of hot wax mounting and vice mounting to minimise the potential fracturing effects due to excessive clamping forces. The retrieved monolith was further sectioned to obtain appropriate monoliths using an Isomet low speed saw fitted with a 0.3 mm diamond wafering blade. Monoliths were prepared for investigation by grinding using P1200 grit SiC papers and polishing with 6, 3, 1 and ¼ µm diamond pastes.

Static Aqueous Durability Experiments

PCT type protocols were performed with a particle size of 106-180 µm and a SA/V ratio between 2150 m^{-1} and 2200 m^{-1} for PCT. MCC-1 experiments were performed on samples polished to a 0.25 µm finish with a SA/V of 10 m^{-1}. Both used a temperature of 90 °C and 18.2 MΩ H_2O.

SPFT Experiments

The methodology utilised to perform SPFT is described in more detail in Section 3.10.3 and 3.10.4. A detailed study of the aqueous durability of both CSXC-$NaAlO_2$ and CSXC-BORAX was performed in this chapter. A matrix of the experimental conditions is provided in Table 6.2. The methodology used is outlined in Section 3.10.4. SPFT was performed using the following pH values at 90 °C; 2, 4, near neutral (~6), 9 and 11 with an approximate log(Q/S) of -7.0.

Two other suites of experiments were performed on each wasteform. These were to study variations in temperature and log(Q/S) at pH 4. The first alterations were in log(Q/S) which were performed at 90 °C at pH 4 with log(Q/S) values of approximately -6.4, -6.7, -7.0 and -7.25. The variations in temperature were made at pH 4 and log(Q/S) -7.0 with variations in temperature of 50 °C, 70 °C and 90 °C.

Solution pH	Temperature	Log(Q/S)
2	90	-7.00
4	50	-7.00
	70	-7.00
	90	-7.00
	90	-6.40
	90	-6.70
	90	-7.25
Near Neutral	90	-7.00
9	90	-7.00
11	90	-7.00

Table 6.2 – Matrix of conditions used during SPFT testing of CSXC-$NaAlO_2$ CSXC-BORAX.

6.3 - Results and Discussion – Part I – HIPing of Clinoptilolite

The results and discussion of this chapter have been separated into two sections. Section one will provide information on the treatment of clinoptilolite utilising the process of HIPing, the physical properties and the phase assemblages of the product formed. Section two will provide information on the aqueous durability of the products produced by HIPing clinoptilolite.

6.3.1 - Selection of Additives and Processing Parameters

Use of additive

To determine what effect increasing the amount of fluxing agent available may have on the formation of a waste stream, pellets with varying amounts of $NaAlO_2$ were prepared and placed in a mullite boat for heat treatment. As clinoptilolite has previously been reported to form a vitreous product between 1200 °C and 1400 °C, this heat treatment was performed at 1300 °C for two hours. [243]. The products formed after heat treatment are illustrated in Figure 6.1.

Figure 6.1 – Products formed by the heat treatment of 1g, 10mm diameter CSXC-CLINO pellets with the addition of $NaAlO_2$ between 0 wt % - 10 wt % at 1200 °C for 2 hours.

Due to the collapse of the pellets into each other during processing only qualitative results of this test were considered appropriate. All pellets show a structural collapse indicating vitrification occurred at these processing temperatures. It is clear from collapse of the pellets that the fluidity of the materials at this processing temperature increases with the addition of $NaAlO_2$. A qualitative, visual assessment based on transparency of the products indicates that the degree of crystallisation decreases with increasing additive concentration. Foaming and residual colouration in the 0 wt% and 2.5 wt% loaded samples suggest that formation of the glass phase was not complete under these conditions. Samples with 5 wt%, 7.5 wt % and 10 wt% $NaAlO_2$ additive show no evidence of foaming yet have grey/white colouration and inclusions present in the collapsed pellet.

TGA

The TGA of CSXC-CLINO was performed with ramp rates of 10 °C min^{-1}. The TGA is provided in Figure 6.2 and illustrates three regions of mass loss up to 1000 °C. First, a rapid loss of mass occurs to approximately 300 °C; second, a slower rate of mass loss continues up until approximately 640 °C and finally a loss regime occurs from 640 °C to 750 °C. These mechanisms are not discrete and some overlap is seen in the gradual transition of the rate of mass loss between 300 °C and 400 °C. The total mass loss observed during this treatment is 12.95 wt%. The initial loss between 25 °C and 300 °C is 10.40 wt% and accounts for the majority of the total mass loss, the middle period between 300 °C and 700 °C accounts for 1.90 wt% and the final mass loss event accounts for the remaining 0.65 wt%. This behaviour

is similar to that reported elsewhere for the dehydration of clinoptilolite and has been attributed to the loss of water from the zeolite structure, where the variation in distinct thermal mass loss events relate to water molecules bound within the zeolite structure with varying degrees of strength [243, 244]. The results presented here show the bands identified in the literature for each type of water have been shifted to higher temperatures and that final stability is achieved at the higher temperature of 750 °C as opposed to 700 °C. Both of these effects have been attributed to the faster ramp rates utilised in the course of this study and it is believed the samples otherwise correlate well with the available literature. An alternative suggestion would be that the presence of Cs in the structure affects the dehydration properties via alterations in the crystal structure. This has not been investigated further in this study.

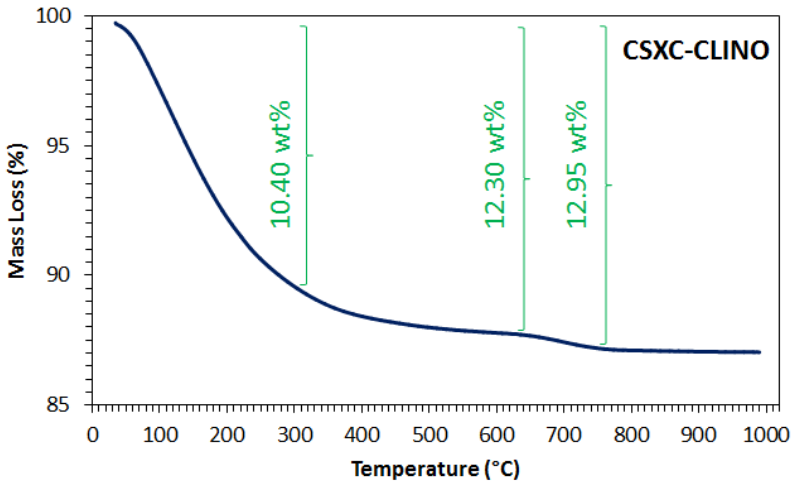

Figure 6.2 – TGA analysis of CSXC-CLINO performed with a ramp rate of 10 °C min^{-1}.

6.3.2 - Characterisation of HIPed Wasteforms

Canister densification

Inspection of the HIPed canisters showed effective densification had occurred. Using Equation 3.4 the total volume decrease associated with HIP processing was measured at 49 ± 5 % and 47 ± 5 % for CSXC-$NaAlO_2$ and CSXC-BORAX respectively. This shows the densification of the samples is comparable within error. The average reduction in waste volume, calculated using Equation 3.5, were 64 ± 5 % and 62 ± 5 % for CSXC-$NaAlO_2$ and CSXC-BORAX respectively.

XRD

Powder XRD patterns for the CSXC-CLINO, CSXC-$NaAlO_2$ and CSXC-BORAX are displayed in Figure 6.3. It is clear that a complete breakdown of the clinoptilolite structure (PDF 00-047-1870) has occurred during heating, by comparison of the CSXC-CLINO pattern with those of CSXC-$NaAlO_2$ and CSXC-BORAX. HIPing the CSXC-CLINO with $NaAlO_2$ and NaB_4O_7 produces materials with similar XRD patterns.

Both HIPed samples show evidence of diffuse scattering, indicative of an amorphous phase in the material. The presence of this amorphous hump and sharp crystal peaks in the powder XRD pattern informs us that a glass-ceramic has been produced during HIPing. The presence of crystalline silica is observed in both samples, as identified from the peaks corresponding to α-quartz (PDF 00-005-0490) and α-cristobalite (PDF 04-008-7819). α-quartz is the dominant crystalline peak in both samples. CSXC-$NaAlO_2$ contains peaks which have been indexed as a mixed feldspar (PDF 00-001-0739) in the powder XRD pattern and indicates the presence of other crystallites in this sample potentially in quantities >5 wt%.

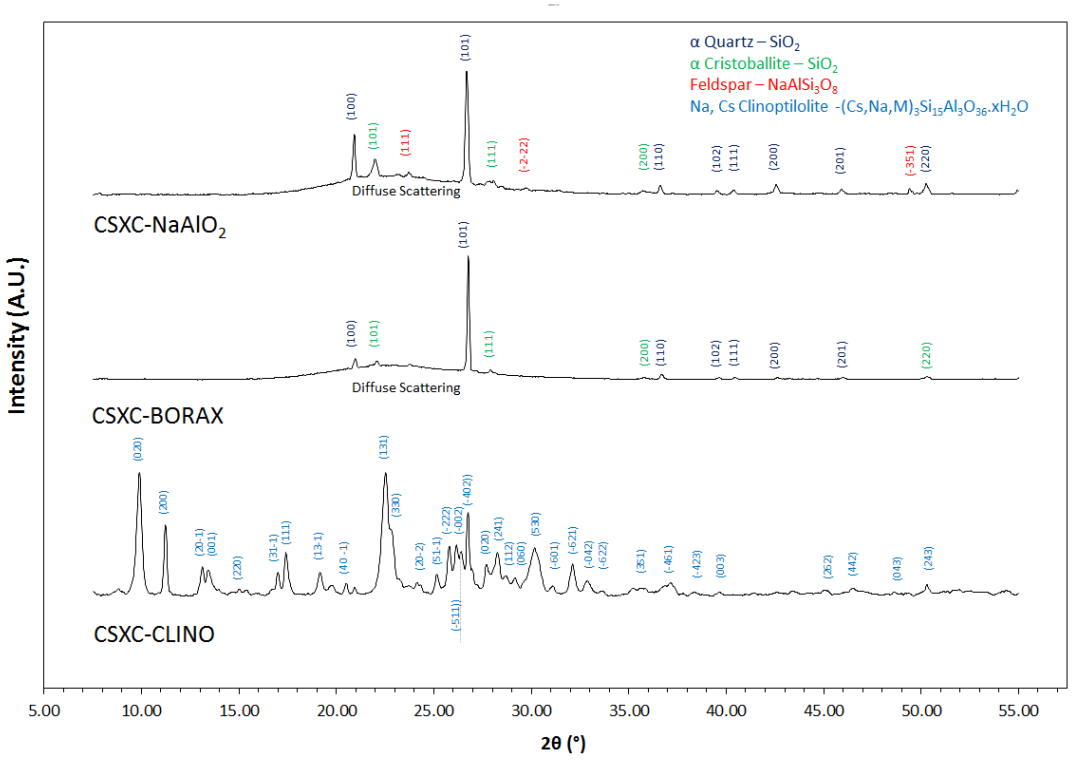

Figure 6.3 - XRD patterns for CSXC-CLINO, CSXC-$NaAlO_2$ and CSXC-BORAX highlighting Miller indices (hkl) of key reflections.

6.3.3 - Analysis of HIPed Wasteforms using Electron Microscopy

Overview of wasteforms

SEM-BSE imaging and SEM-EDX analysis was performed on both compositions to characterise their morphology, homogeneity, chemical segregation, identify any regions in which Cs and Sr concentrate and determine the identity of inclusions present unable to be detected via powder XRD analysis. SEM-BSE images in Figure 6.4 provide an overview of the wasteform properties of both CSXC-CLINO and CSXC-BORAX.

Similarities and differences can be identified between the CSXC-BORAX and CSXC- $NaAlO_2$ from this preliminary data. The SEM-BSE imaging shows good correlation with the phases identified by powder XRD analysis. Both wasteforms primarily consist of an alumino-silicate glass. A number of differences between the vitreous phases in the two samples are clearly visible when imaged via SEM-BSE, as shown in Figure 6.4. CSXC-$NaAlO_2$ has a relatively homogeneous greyscale across its vitreous phase. However, the vitreous phase in CSXC-BORAX exhibits two distinctly separate regions, indicating that significant compositional variations exists within the glass. These variations in glass composition are globular in nature, with the darker greyscale regions (Glass B) interspersed within the lighter greyscale glass regions (Glass A). The compositional variations of the glasses are provided in Table 6.3. The CSXC-BORAX glass was measured by SEM-EDX and that of CSXC-$NaAlO_2$ glass was measured by a combination of SEM-WDX and SEM-EDX. When CSXC-$NaAlO_2$ is mapped using EPMA, similar morphologies and compositional variations can be observed in the vitreous phase, as will be discussed below.

Interspersed within the vitreous phase of both wasteforms, regions of darker grey scale value, ranging in size from 30 µm to 500 µm exist. These were identified by SEM-EDX as SiO_2. The presence of these SiO_2 inclusions correlates with the identification of quartz and cristobalite in the powder XRD patterns. In most instances the presence of these SiO_2 inclusions is associated with circumferential cracking. These cracks surround the inclusion and propagate through both the vitreous phases and the inclusion itself. Radial cracking of the SiO_2 inclusion is also prevalent. Both types of cracking are highlighted in Figure 6.5.

The amount of SiO_2 present varies between the two wasteforms. CSXC-$NaAlO_2$ has qualitatively more SiO_2 inclusions. An attempt to quantify this difference is presented later in this section. Both the number and size of these SiO_2 inclusions is greater than that observed in the CSXC-BORAX sample. The SiO_2 inclusions in CSXC-$NaAlO_2$ have a diameter in the range 100 µm, whereas those present in CSXC-BORAX are in the order of 10 µm. Conversely the

CSXC-BORAX has qualitatively more bright spots in its SEM-BSE image indicating a greater presence of small inclusions in the CSXC-BORAX than CSXC-$NaAlO_2$.

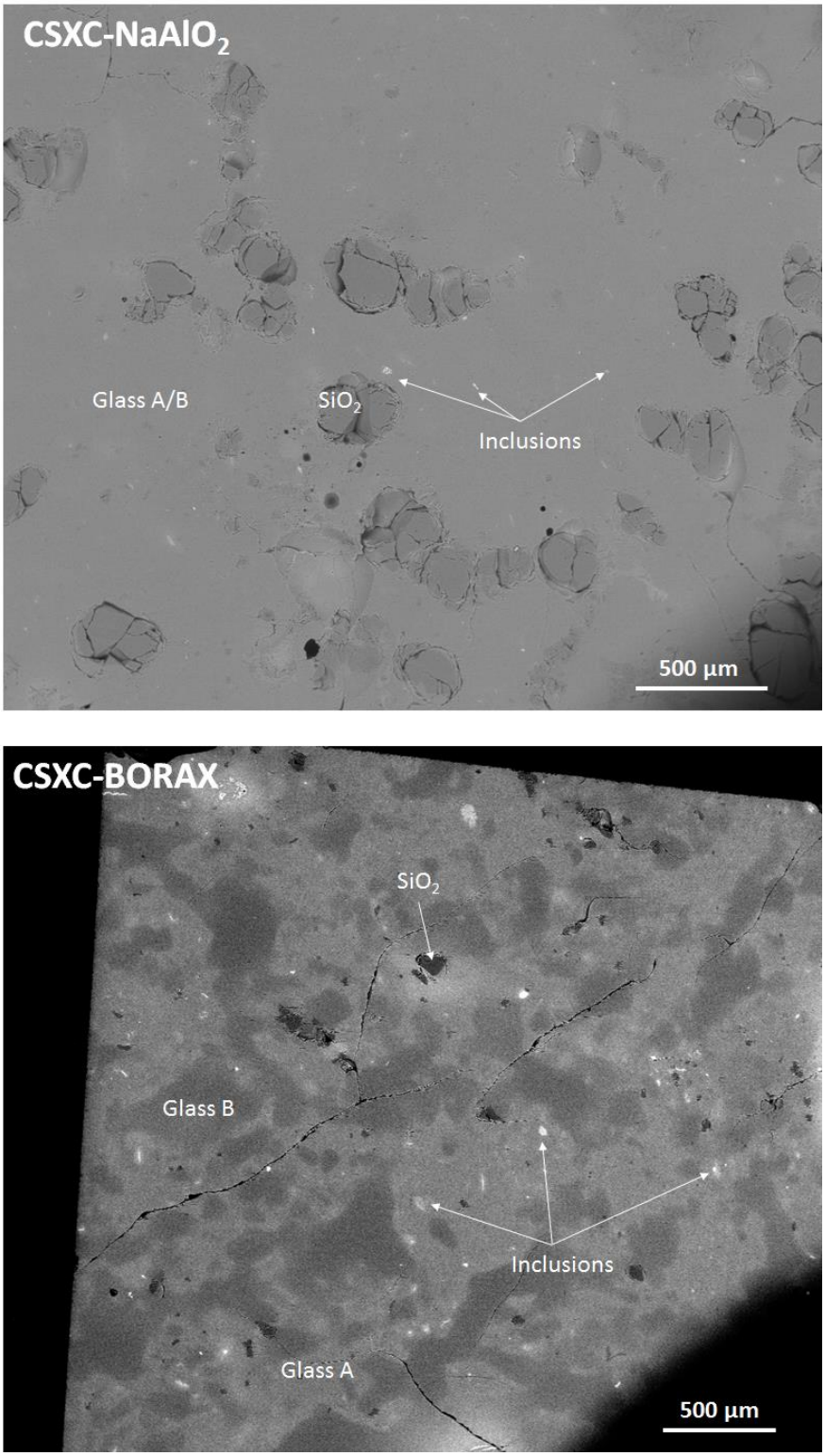

Figure 6.4 - SEM-BSE images of both CSXC-$NaAlO_2$ and CSXC-BORAX identifying the presence of major phases.

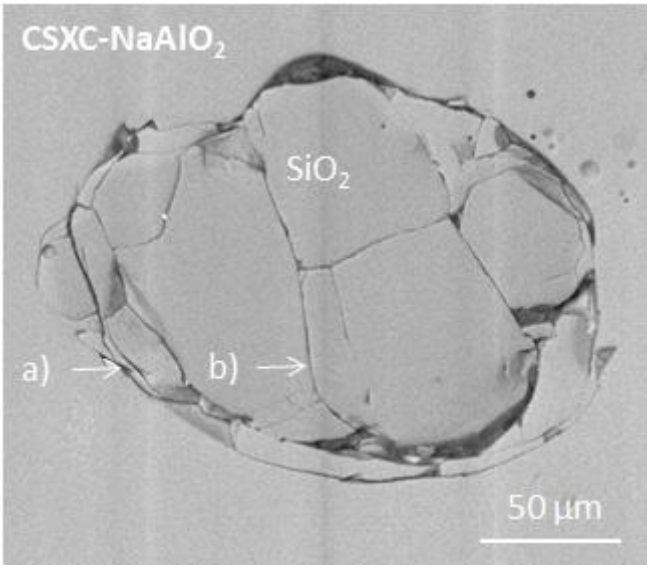

Figure 6.5 – SEM-BSE of a SiO_2 inclusion embedded in CSXC-$NaAlO_2$ highlighting a) the radial cracking emanating around the inclusion and b) the radial cracking which emanates through the inclusion.

Both CSXC-$NaAlO_2$ and CSXC-BORAX contain a variety of inclusions with brighter greyscale values, with variable dimensions and morphologies. These inclusions range in size from agglomerations of micron sized inclusions to inclusions tens of microns in size. None of these inclusions were detectable in the powder XRD patterns, suggesting they are either vitreous or present in quantities < 5 wt%.

Figure 6.4 and 6.5 identify some localised minor porosity in both samples. Figure 6.4 shows that significant fracturing exists in the CSXC-BORAX, which has been put down to the sectioning methodology used. This fracturing is believed to be an artefact of sample preparation, as discussed in Section 4.5.

It was noted that the SEM-BSE image of CSXC-$NaAlO_2$ shows no evidence of the mixed feldspar phase which was identified in the powder XRD pattern provided in Figure 6.3.

CSXC-$NaAlO_2$ SEM-WDX

As noted above, the presence of feldspar in the CSXC-$NaAlO_2$ was identified in the XRD pattern of CSXC-$NaAlO_2$ but not using SEM-BSE imaging. To elucidate this, SEM-WDX mapping was performed in conjunction with quantitative spot analyses. The mapping results are displayed in Figure 6.6 and the results of the analysis of the two vitreous phases which were identified are displayed in Table 6.3.

From the mapping data in Figure 6.6, it is apparent that the morphology and compositional variation of the vitreous region of CSXC-$NaAlO_2$ is similar to that imaged in CSXC-BORAX using

SEM-BSE. Compositional variations are evident in globular morphologies within the glass structure as identified previously for CSXC-BORAX. The composition differs primarily in the concentration of SiO_2 and Al_2O_3 present within the regions. The globular regions identified as Glass B contain a higher proportion of Al_2O_3 than is seen in the surrounding glass structure identified as Glass A.

The presence of the mixed feldspar phase was also identified in these maps. This phase is always associated with Glass B and is observed within the globular morphological regions as shown in the phase map in Figure 6.6. Quantitative EPMA spot measurements made across five of the particles gives an average nominal composition for this feldspar of $NaCa_{0.5}Al_2Si_2O_8$.

Oxide Component	CXCC-$NaAlO_2$ *		CSXC-BORAX **	
	Glass A	Glass B	Glass A	Glass B
SiO_2	76.1 ± 1.7	70.5 ± 1.5	72.5	66.2
Al_2O_3	13.6 ± 0.9	16.9 ± 1.4	13.8	12.7
B_2O_3	-	-	-	-
Fe_2O_3	0.7 ± 0.2	0.9 ± 0.2	-	-
Na_2O	2.9 ± 0.2	3.7 ± 0.3	5.5	5.3
K_2O	2.3 ± 0.1	2.3 ± 0.1	2.1	1.9
CaO	1.0 ± 0.3	1.4 ± 0.2	0.8	2
Cs_2O	1.2 ± 0.1	1.0 ± 0.1	1.7	1.5
SrO	0.4 ± 0.1	0.4 ± 0.1	-	-
TOTAL	98.2	97.2	-	-

Table 6.3 - Composition of the vitreous phases identified in Figures 6.4 and 6.6 for both CSXC-$NaAlO_2$ and CSXC-BORAX where * indicates analysis was performed by SEM-WDX (error ± 2 SD across measurements assigned to each phase) and ** indicates that analysis was performed with a mixture of SEM-EDX and SEM-WDX (error set to experimental error of ± 2.5 %).

The SEM-WDX mapping and the quantitative measurements provided in Table 6.3 show that the Cs is well distributed throughout the vitreous regions and is present in both compositional variations. Although a higher concentration is observed in the regions of Glass A, the segregation is considered minimal and the distribution is relatively homogeneous. The one exception to this is noted around the pore (bottom right corner of maps) where a region of enriched Cs concentration was observed. Five quantitative EPMA spot measurements were taken within this rim and the Cs_2O was measured to average 1.3 ± 0.15 wt%. The small variation in the total concentration and the high counts seen in this porosity for other

mapped elements indicates that this is likely to be an effect of the changing morphology of the sample surface leading to increased counts.

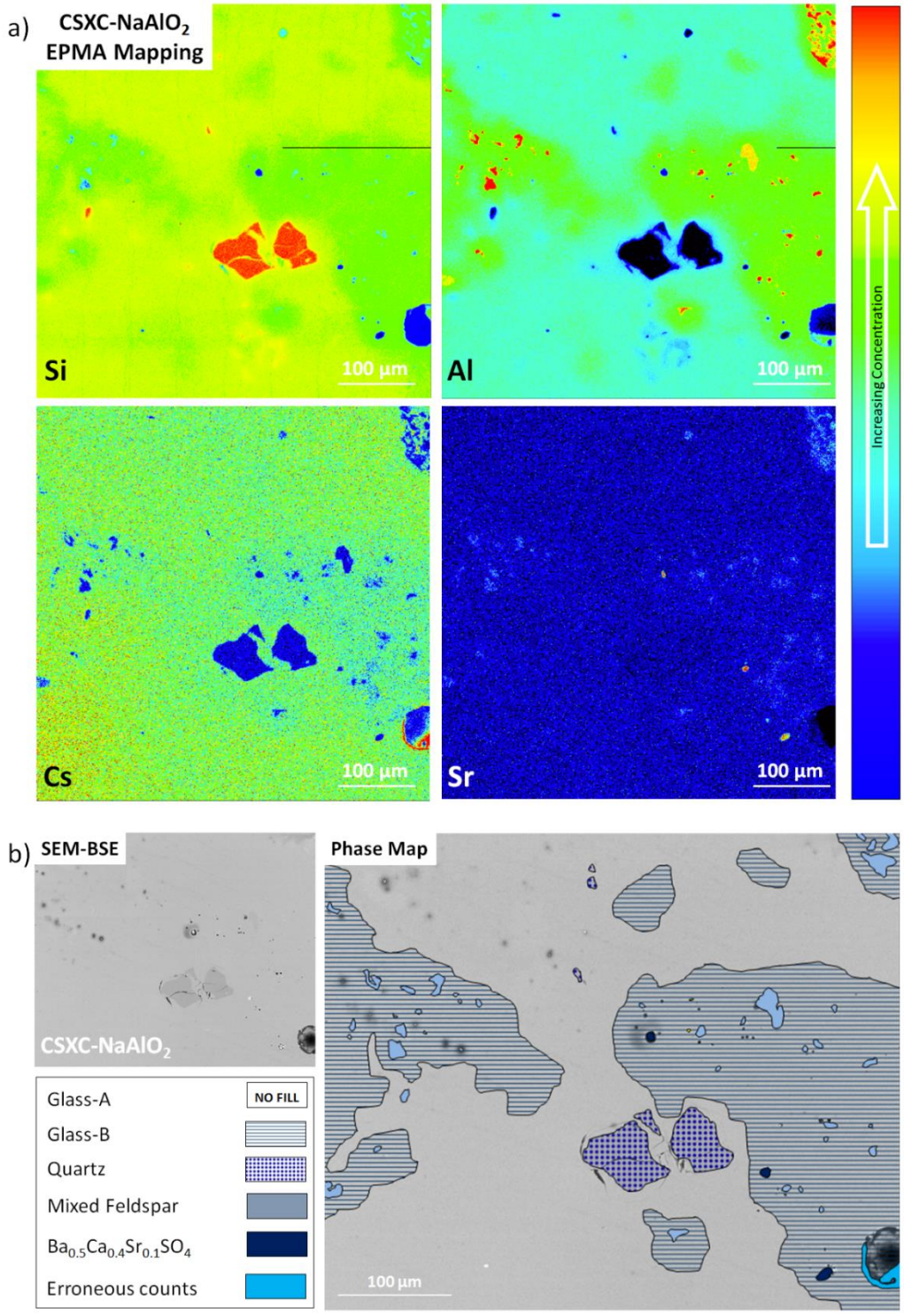

Figure 6.6 – a) SEM-WDX maps of CSXC-$NaAlO_2$ for Si, Al, Cs and Sr and b) Phase mapping of CSXC-$NaAlO_2$ produced using a combination of data from the SEM-BSE image (inlaid), the SEM-WDX mapping shown in a) and quantitative spot analysis performed across the sample.

The presence of Sr rich regions is also highlighted in Figure 6.6 and is discussed further below. These inclusions were identified using a mixture of SEM-EDX and SEM-WDX measurements as a mixed alkali earth sulphate phase, with an average composition $Ba_{0.5}Ca_{0.5}Sr_{0.1}SO_4$.

Identification of Mixed Inclusions and Bright Phases

As described above both CSXC-$NaAlO_2$ and CSXC-BORAX were shown to contain an array of inclusions and phases displaying brighter greyscale values from SEM-BSE analysis. Both wasteforms contain inclusions of SiO_2, Fe_2O_3 and mixed alkali earth sulphates which are displayed for CSXC-$NaAlO_2$ and CSXC-BORAX in Figures 6.7 and 6.8 respectively.

The morphology and cracking of the SiO_2 inclusions has been described previously. The Fe_2O_3 exists as regions of elongated sub-micron to micron scale inclusions encapsulated in the glass phase. The mixed alkali sulphate phases range in size from under 10 µm to over 100 µm and do not appear to have a well-defined crystalline structure from the absence of angular shapes. The presence of TiO_2 was also found in the CSXC-$NaAlO_2$ wasteform as an agglomeration of approximately micron sized inclusions.

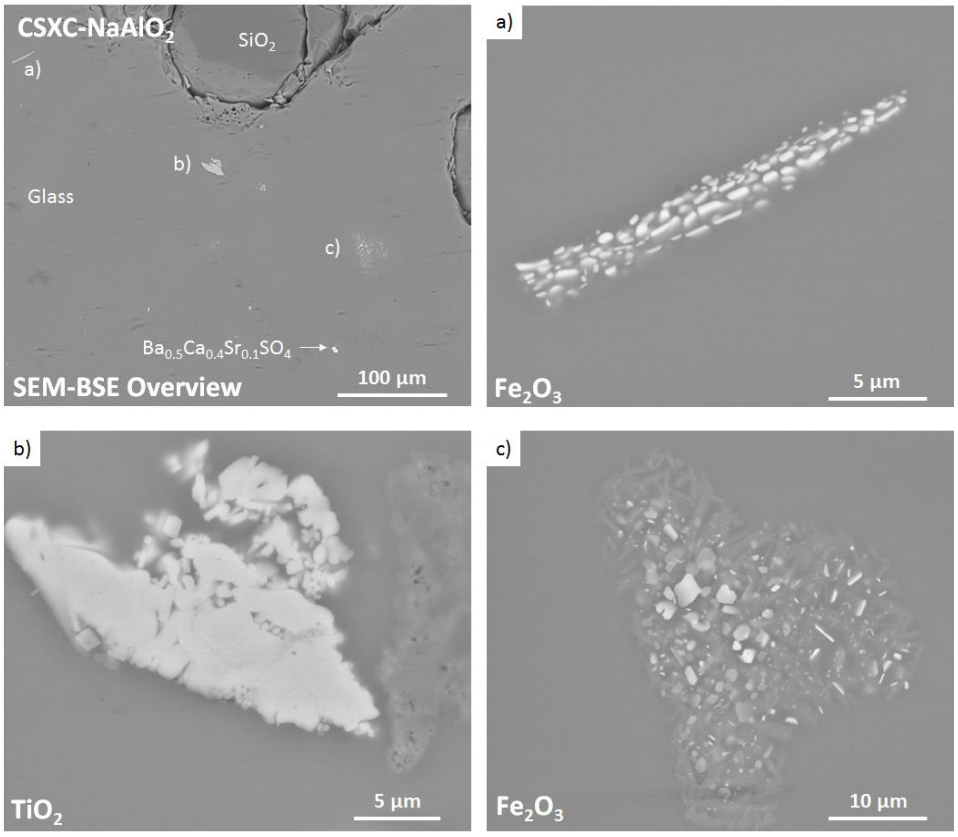

Figure 6.7 – SEM–BSE images giving examples of the bright phase inclusions found in the SEM-BSE imaging of CSXC-$NaAlO_2$. Compositional identification was performed using SEM-EDX.

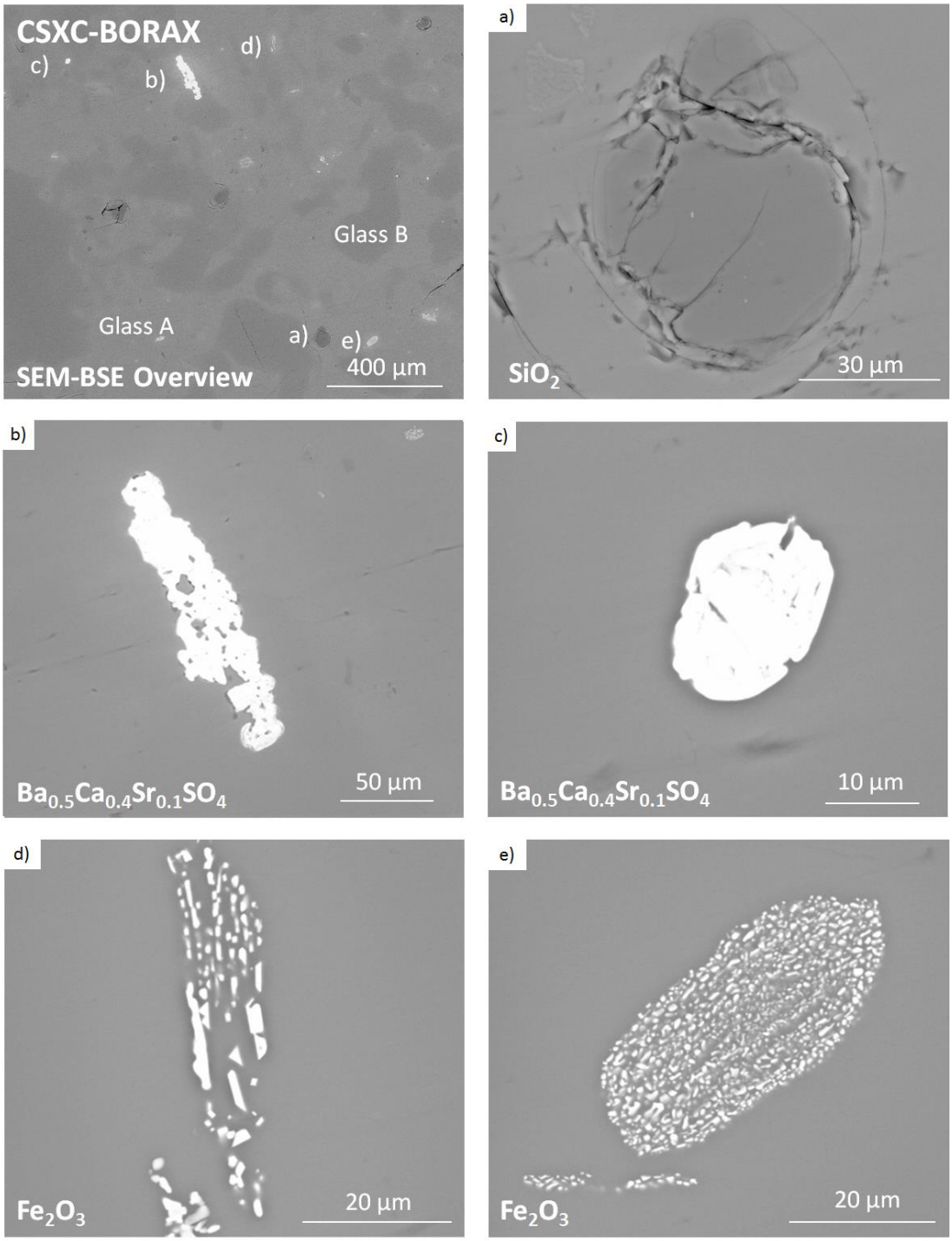

Figure 6.8 - SEM–BSE images giving examples of the bright phase inclusions found in the SEM-BSE imaging of CSXC-BORAX. Compositional identification was performed using SEM-EDX.

Quantification of Phase Assemblages

Figure 6.9 and Figure 6.10 show images created by montaging 30 SEM-BSE images taken of CSXC-$NaAlO_2$ and CSXC-BORAX respectively. This method allows for the analysis of an area of the sample large enough to be considered representative yet with a resolution sufficient to detail the smaller inclusions quantitatively. The images produced provide analysis of an area of 4.7 mm^2, with a resolution of ~1 μm^2 based on an individual pixel size of 0.5 μm^2. SEM-BSE greyscale images were compared with SEM-EDX measurements to identify where correlation between the two existed. It was observed that separation of SiO_2, Glass A (and Glass B in CSXC-BORAX), mixed inclusions and the combination of cracking and porosity, could be performed using this technique with an RSD of ± 5 %. The technique was, however, limited as no separation of the mixture of inclusions could be accurately performed. Also the second vitreous phase present in CSXC-$NaAlO_2$, which is discussed above, could not be determined using this methodology. The montages were thresholded to provide masks of the separated phase and inclusions which are displayed in Figures 6.7 and 6.8 and measurements of the corresponding pixel data from these images was performed to obtain the proportional area occupied by each phase in the montage. The results of this measurement are shown in Table 6.4.

Phase Identity	**Measured Area (%)**	
	CSXC-$NaAlO_2$	**CSXC-BORAX**
Miscellaneous Inclusions	0.4	0.2
Glass A	89.8	76.3
Glass B		22.0
SiO_2	4.6	0.7
Porosity and Cracking	0.7	0.7

Table 6.4 – Semi-quantitative analysis of volume contribution from the major phases in CSXC-$NaAlO_2$ CSXC-BORAX present from SEM-BSE image montaging and greyscale compositional analysis. Estimated error ± 5%.

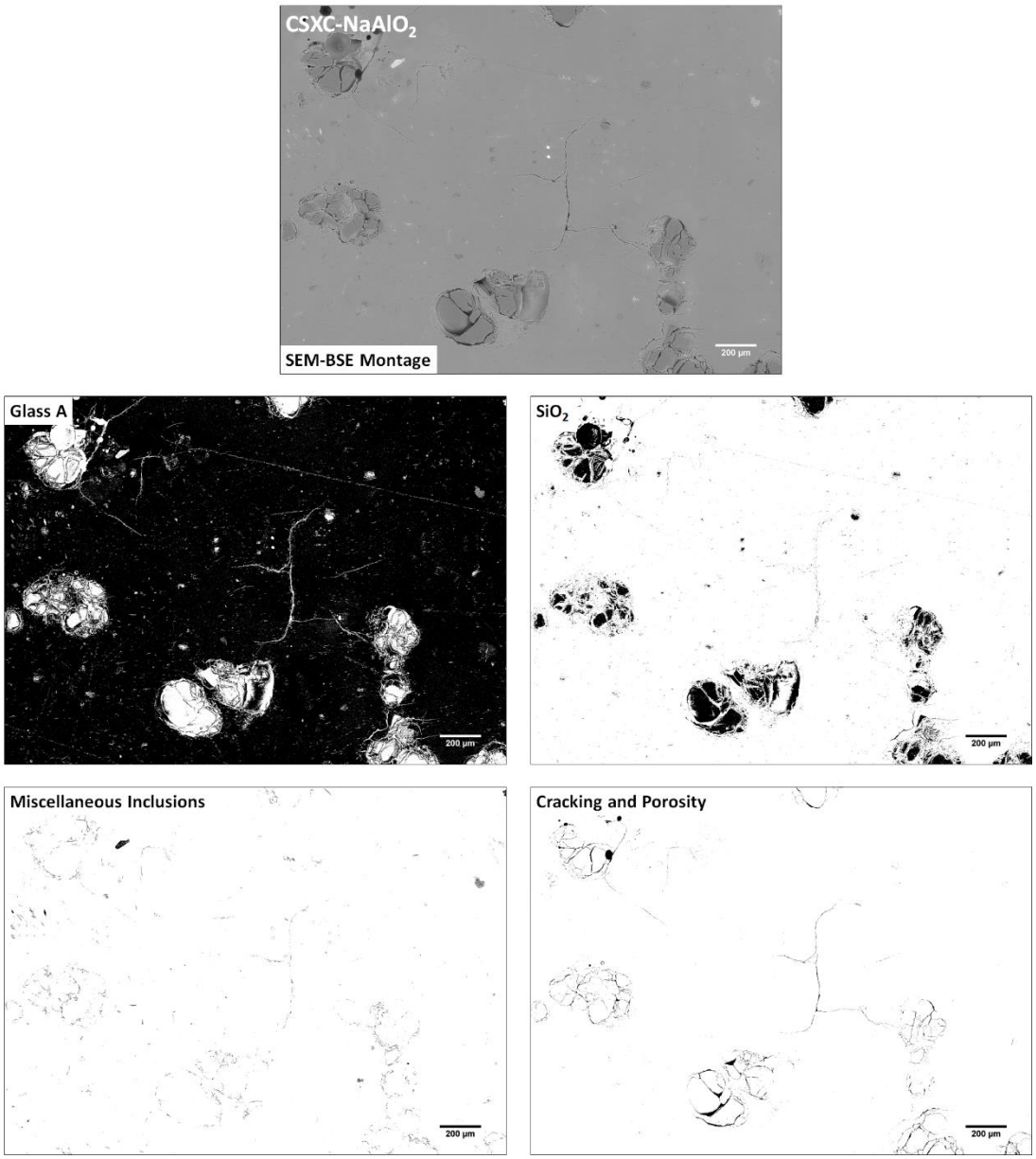

Figure 6.9 – Montaged SEM-BSE images of CSXC-$NaAlO_2$ including masks created by thresh-holding the montaged image for Glass A, SiO_2, miscellaneous inclusions and cracking and porosity.

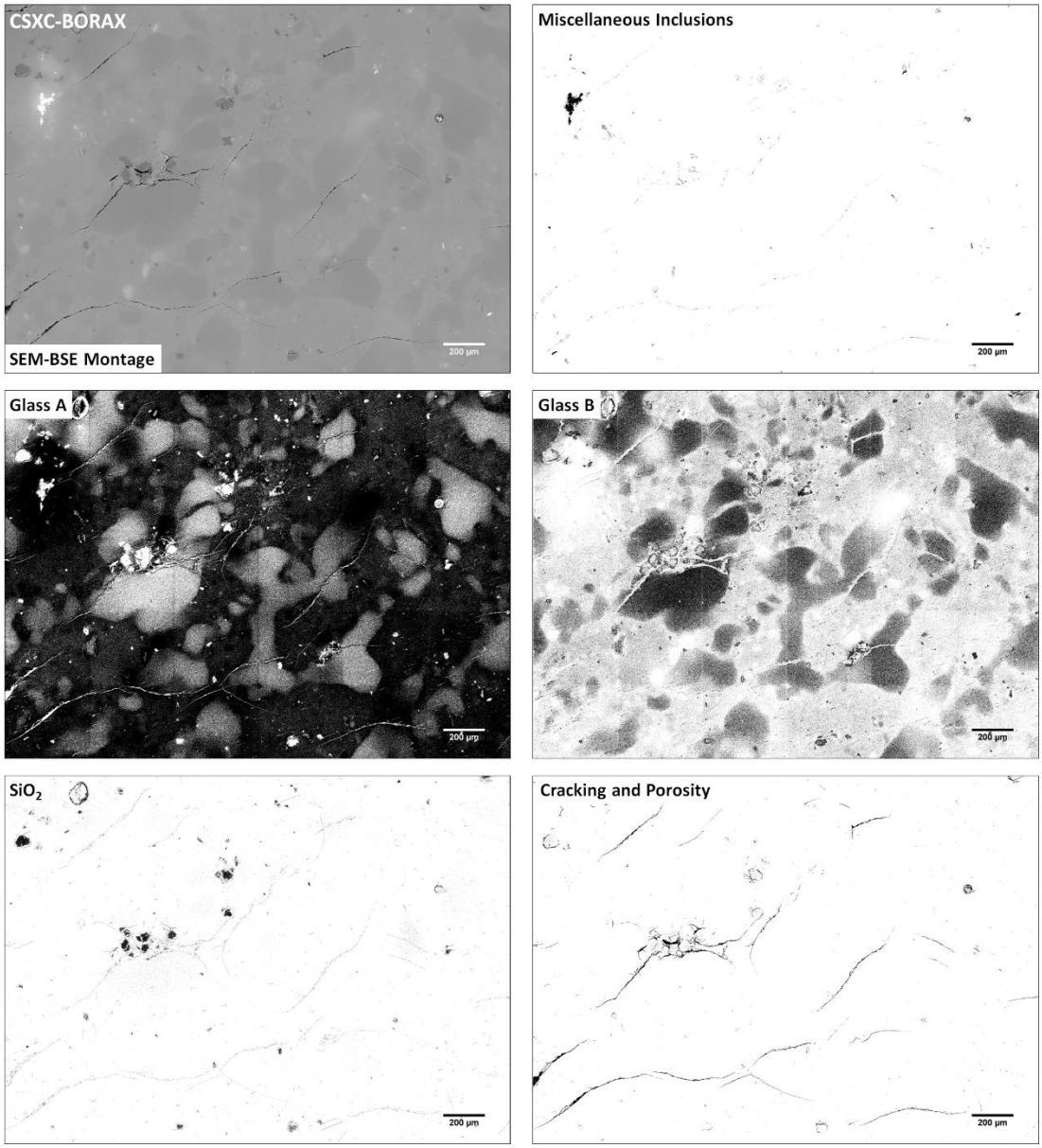

Figure 6.10 – Montaged SEM-BSE images of CSXC-BORAX including masks created by thresh-holding the montaged image for Glass A, SiO_2, miscellaneous inclusions and cracking and porosity.

6.3.4 - Discussion - Processability of Clinoptilolite via HIPing

The results relating the potential applicability of HIPing to the processing of clinoptilolite are provided in Sections 6.3.1 – 6.3.3. The combination of these results indicates that HIPing is a promising methodology for the treatment of clinoptilolite and has the potential to be applicable on an industrial scale.

Several factors are important when considering the utilisation of HIPing at an industrial scale. The study performed was designed to address a number of these issues which may arise when considering commercial utilisation of HIP technology.

Canister Suitability

Any large scale application of HIPing for radioactive wastes is likely to utilise a corrosion resistant stainless steel canister. This canister would act as the primary containment vessel for the processed wasteform. To provide evidence that this is possible, the HIP canisters used throughout this study was made from 316 stainless steel. This means the waste had to be processed at temperatures below 1375 °C in order to avoid any potential melting of the canister material [245]. The temperature used should ideally be as low as possible in order to maximise throughput, decrease processing cost and minimise the potential for the canister to form eutectic melts during processing. Based on these considerations, as well as the literature available on the vitrification of clinoptilolite described in Section 6.3.1, the selected processing temperature was set at 1200 °C [243].

Additive Additions

The use of inactive additives should ideally be minimised as far as possible in order to increase waste loadings, plant throughput, lower costs and expedite the conversion of the waste stream into a passively safe form. For these reasons it was desirable that the waste loading be maximised as far as possible. It was determined, however, that providing an additional source of modifier cation could provide benefits for the processing these wastes, promoting glass formation and increasing glass fluidity during processing.

Figure 6.1 illustrates the qualitative processing benefits that small additions can have to the glass forming ability of clinoptilolite. Small incremental additions of $NaAlO_2$ were observed to increase the fluidity of the heat treated product. As 5 wt% was the minimum addition of $NaAlO_2$ capable of causing a complete, non-foaming collapse of the pellet structure, it was decided this quantity of additive would be utilised for the production of wastes by HIPing. The decision was made to utilise both $NaAlO_2$ and $Na_2B_4O_7$ as additives. Both were chosen

to increase the amount of Na to act as a fluxing agent during glass formation. $NaAlO_2$ was selected to provide this flux, with the addition of Al to the melt which was hoped to be beneficial with respect to the glass aqueous durability. $Na_2B_4O_7$ was selected to provide the Na flux, as well as B to the glass which is known to decrease the viscosity of silicate melts and may therefore promote the formation of a more homogeneous glass.

Degassing Requirements

To use HIPing in the production of radioactive wasteforms, it is the necessary to minimise the formation of gaseous decomposition products during processing of the sealed canisters. If volatilisation equivalent to a weight loss > 0.5 wt% occurs during the HIP cycle it is generally accepted the microstructure of the resulting wasteform will be porous. Therefore, prior to canister sealing it should be shown that the volatilisation which will occur using selected processing parameters is < 0.5 wt%.

Clinoptilolite exists on the Sellafield site as a slurry and has the potential to take up large amounts of water after drying. This therefore necessitates the use of either a calcination step and/or vacuum bake out prior to HIPing. Calcination can be readily performed in the nuclear industry at temperatures up to 940°C, whereas large scale vacuum evacuation of a canister is only likely to be applicable where the canister can be rapidly evacuated below 300 °C [246]. The data in the literature concerning the degree of water removal from the clinoptilolite structure below 300 °C is unclear [244]. To determine which of these processes would be more readily applicable TGA of the clinoptilolite was performed. The results presented in Figure 6.2 show that, at rapid ramp rates to 300°C, the waste stream would still have the capability to lose ~2.4 wt% during processing, making this process unsuitable for effective degassing. It was decided that a combined calcination/evacuation approach was most likely to produce a material suitable for processing without the introduction of significant porosity in the end product. The calcination conditions were set to a temperature of 700°C for 3 hours, consistent with the TGA data obtained and the maximum temperature shown from the literature to produce complete dehydration of clinoptilolite. It is expected that in an industrial setting, where moisture exclusion and atmospheric control can be readily implemented in the process line, that calcination alone would provide sufficient dehydration of this waste stream.

Volume Reduction

An important practical benefit of HIPing is the ability to reduce the volume of particulate wastes, reducing the necessary size of any future GDF and providing lifetime waste

management cost savings over the reference scenario. It was observed that significant compaction of the processed canisters was achieved using the selected processing parameters. Canister compactions of approximately 50 vol% were attained showing that effective densification of the waste occurs during HIPing. Discussion of the total possible densification is not included as no attempt was made to investigate the canister packing density. The packing density of the sealed canister is of key importance in the determination of the degree of compaction which can be expected during HIPing. Without investigation of this parameter any further discussion of densification potential would lack context in a practical sense.

Monolith Formation

The primary aim of this study was to produce a suitable monolithic wasteform from the slurries of SIXEP waste currently existing on the Sellafield site. The processed HIP canisters were shown to produce a physically robust monolithic wasteform and therefore the primary aim of this project was successfully achieved. The physical stability of this wasteform is shown in the ability to readily obtain monoliths, evident due to the necessity of using aggressive sectioning methodologies for sample retrieval from HIP canisters. The phase assemblages of the monoliths obtained are discussed in Section 6.4.2. Although the general behaviour indicates that a robust monolithic wasteform has been formed, no quantitative evaluation of this property was performed. The heterogeneous nature of the product would invalidate micro-indentation experiments. Compressive and tensile testing experiments were precluded as larger samples would have been required. From a qualitative analysis it is expected that the mechanical properties of the wasteforms will readily exceed any criteria for transport and disposal, however, further work should be conducted to confirm this.

6.3.5 - Discussion - Wasteform Phase Assemblage

General Comments on Phase Assemblage

The use of thermal treatments should only be employed for ILW treatment when they offer the best available technology. Such solutions can be achieved by increasing the quality of the wasteform, reducing the volume of waste for disposal or improving its processability. In the case of clinoptilolite it is inevitable that a) the product quality will be improved and b) that the volume will be reduced by use thermal treatment methods. This is due to increase in volume and the pozzolanic reaction, which results in the release of a large proportion of the radio-Cs inventory into the pore water when processing via cementation. As such,

clinoptilolite should be considered wholly unsuitable for cementation [47]. A description of the phase assemblages produced by HIPing is provided to highlight the significant improvements in product quality and justify the suitability of this method for purpose.

Similarities between CSXC-$NaAlO_2$ and CSXC-BORAX

The majority of features in terms of the phase assemblages and microstructure for both CSXC-$NaAlO_2$ and CSXC-BORAX are comparable. The XRD analysis provided in Figure 6.3 shows that there has been a complete collapse of the original clinoptilolite structure resulting in the formation of a glass ceramic in both compositions. This was the intended outcome for the processing of this waste and shows that effective processing of clinoptilolite has been achieved. The presence of a vitreous silicate phase is considered ideal due to the general ability of these phases to chemically incorporate Cs and Sr, as well as other minor fission products into its structure.

The physical structure of the wasteform is of a high quality. The comparison of the pulverised powder density for the wasteform, as measured by helium pycnometry, with the monolithic density, as measured by the Archimedes method, indicates that both formulations achieved densities near 100 % of their theoretical value.

As may be expected from the slight deviation between the measured theoretical and monolithic densities, some porosity remains in the glass. However, this porosity is minimal, well contained and localised, therefore it has no significant impact on wasteform quality. This porosity may result from the rapid and favourable rehydration of the clinoptilolite occurring in air between the initial calcination and canister sealing [247]. Alternatively the use of $NaAlO_2$ and $Na_2B_4O_7$ as a source of flux may not be considered ideal as these reagents are hydroscopic and may introduce entrained water into the sealed system. In either case, this porosity is likely to be wholly avoidable with slight alterations to the processing equipment or formulation, readily achievable on an industrial scale. Calcination and packaging of powders could be performed under an inert or moisture controlled atmosphere until canister sealing is completed. Alternatives to the introduction of flux to aid glass formation could be investigated. Suggestions for process alterations and the potential benefits of these alternative methods will be discussed below.

Fracturing

Figure 6.5 shows that neither wasteform produced is completely fracture free. The fractures observed in CSXC-BORAX are believed to a result of the aggressive sectioning methodology required during sample retrieval. This fracturing could also result from thermal shock or the

release of stored energy in the vitreous wasteform, although such a determination is not possible from the data available.

The smaller cracking features observed around the quartz SiO_2 grains in both CSXC-$NaAlO_2$ and CSXC-BORAX are, however, resultant of a fundamental property of the wasteform and require further discussion. These cracks have been attributed to the α-β phase transition which quartz undergoes at 573 °C. These cracks are a result of the decrease in volume and change in the TEC which are associated with this change [248, 249]. Although this cracking should not be considered ideal in a radioactive wasteform, the cracks are localised to the regions of SiO_2 inclusions and are not interconnected. As a result of this localisation it should not be considered that this cracking is prohibitive to the use of these materials as an effective wasteform. This assumption does require further investigation, as these fractures may provide nucleation sites for larger fracturing and thus lower the overall physical integrity of the sample. Any future examination into properties of these wasteforms should aim to determine what effect these fractures have on wasteform integrity.

Although not ideal, the physical attributes of these wasteforms far surpass those expected for cementitious ILW and are considered to be suitable for ILW immobilisation. Further study to optimise and quantify the physical stability are required.

As noted above, the wasteform consists primarily of a vitreous matrix which encapsulates a number of inclusions. These are discussed in further detail below.

Vitreous Phases in CSXC-$NaAlO_2$ and CSXC-BORAX

As highlighted in Table 6.4, $\gtrsim$ 89 vol% of the two wasteforms produced is comprised of vitreous silicate phases. The glass present in the wasteform exhibited vitreous phase separation. Qualitative analysis of the morphology of the two wasteform compositions is provided in Figures 6.5 and 6.6. It was clearly visible that two major compositions exist in each wasteform. One of the compositions is identified as the major phase 'Glass A' which acts as an 'encapsulant' for the second phase 'Glass B'. Glass B is present with a globular morphology as localised regions in the order of hundreds of microns in size.

It is hypothesised that the formation of these two phase separated glasses occurs in two stages. First the clinoptilolite which is in contact with the $NaAlO_2$ or $Na_2B_4O_7$ additive will melt at a lower temperature. This incorporates the additive material into a vitreous structure creating Glass B. The remaining clinoptilolite then collapses at higher temperatures, forming Glass A. However, the overall viscosity of the material is not low enough to allow effective homogenisation via convective mixing.

The comparable morphologies of these vitreous phase separations and the compositional variations, as measured by EPMA and SEM-EDX for CSXC-$NaAlO_2$ and CSXC-BORAX respectively, support the above hypothesis. In the case of CSXC-$NaAlO_2$, regions of Glass B are enriched with respect to Al_2O_3 and Na_2O and depleted in terms of SiO_2. Glass B in CSXC-BORAX has decreased in terms of SiO_2 and Al_2O_3. It is expected from the contrast in SEM-BSE images that concentration of B_2O_3 also occurs in Glass B in CSXC-BORAX although, due to limits on detector capability, no quantification of B_2O_3 content was possible in this thesis. Although no enrichment was noted for Na_2O in Glass B, these measurements were performed using SEM-EDX, quantification of Na with this method is often prone to error and should not be considered conclusive.

The lack of homogenisation in the vitreous phase is suggestive that, at the processing temperature used, the glass is still highly viscous and precluded an effective convective flow within the canister. In this case the lack of homogenisation roughly represents the original packing of the canister, where the additive chemicals are found residing in the interstices between the clinoptilolite and sand particles. A lack of homogenisation is unavoidable for cementitious wastes and as such it should not be considered prohibitive for the use of these thermally treated products as an ILW wasteform. However, a lack of homogenisation is not an ideal situation for radioactive wastes and efforts should be made to increase product homogeneity where possible. This is because heterogeneity complicates effective prediction of long term properties. The lack of homogenisation often leads to regions of increased solubility in a wasteform, as has been observed in this study and is discussed further in Section 6.4.4.

There are three methods which would promote the homogenisation of the vitreous phases produced by HIPing clinoptilolite. The first would be to mill the clinoptilolite with the fluxing additives used in this study prior to canister packaging. This option is to be avoided at all costs due to the potential for production of radioactive fines and the complications this would add to any processing line. Secondly, alterations in the HIPing processing parameters could be made, whereby increased temperatures or dwell times were used. However, the increase of temperature or time would make the methodology less favourable for use on an industrial scale.

The exclusion of these two options leaves the final option of making improvements to the additive formulation as the favoured option for future improvements in the homogenisation of the wasteform. A suggestion for an optimised process is presented below based on the understanding gathered during this project.

Suggestions for Improvements in the HIPing of Clinoptilolite

It has been shown that the additions of fluxing agents promotes collapse of neighbouring clinoptilolite at decreased temperatures. Improved results may be obtained by the dissolution of the clinoptilolite into a silicate melt formed at lower temperatures. This method would involve the addition of a pre-formed glass frit, with a low T_g and melting point, to the canister before packaging most likely a borosilicate base glass as currently used for HLW immobilisation. Ideally, this glass would be added in sufficient quantities and with adequately controlled mixing to allow it to fill the interstices of the clinoptilolite particles.

It is proposed that the above mechanism may work as follows; as the glass frit passes through its T_g,, several hundred degrees below that of the melting temperature for clinoptilolite, sufficient pressure could then be applied to cause the collapse of the HIP canister. This would force the low T_g glass to coat the clinoptilolite particles. As the temperature was ramped up this glass would start to dissolve the sand and clinoptilolite grains until point that the clinoptilolite was vitrified or that the grains were completely dissolved into the surrounding melt.

It is expected that the final vitreous product from this process would be more homogenous and that the sand inclusions would be more effectively solubilised. Even in the case of a non-heterogeneous glass formation the results would likely result in an aqueous durability improved by comparison to that of Glass B (see section 6.4 for more detailed discussion). In the new methodology, the dissolution of clinoptilolite into the glass frit would result in the addition of Al_2O_3 and SiO_2 to the melt potentially improving the aqueous durability of the wasteform.

The above proposal would necessitate a decrease in waste loading. To function effectively, significantly more than 5 wt % additive would be required to provide an effective coating of the clinoptilolite. However, for treatment by HIPing, a decrease in the waste loading by weight % does not necessarily result in an increased number of canisters requiring processing. If it is assumed that the clinoptilolite grains are roughly spherical and a non-ideal packing density of ~60 % can be obtained, this would leave 40 vol% of the canister as voidage. By assuming the more likely non-spherical packing of clinoptilolite particles, these octahedral voidage sites are able to accommodate spheres with a radius of ~30 % that of the larger grains without any further expansion in the packaged volume [250].

Using glass frit as interstitial particles with a radius ~ 15% of the clinoptilolite particles radius (~45 μm), it should be possible to achieve a packing value in the interstitial regions similar to

that seen for the clinoptilolite in the canister as a whole. Therefore, if we make the following assumptions, the effect of increased additive on canister production can be predicted; 1) 60% packing of the clinoptilolite grains can be achieved; 2) sufficiently homogenous mixing can practically be attained for the glass frit to fill the interstitial sites 3) the 40 vol% of interstitials can be packed at 50 vol%; and 4) that the interstitial filling glass frit will have a similar packing density to the clinoptilolite. This results in the calculation that when using a glass frit powder of 90 µm diameter or below, up to 20 wt% glass addition can be made to the canister, without any decrease in the quantity of radioactive waste loading per canister, although it would inevitably increase the final volume of waste package as processed.

Inclusions

As described previously the wasteform produced is a glass ceramic. The general presence of the inclusions is not considered to be detrimental to the performance of either the wasteform produced, or the processing of the waste when utilising HIP technologies. Unlike the use of conventional melters, where crystallites and precipitates can cause significant issues with the functioning of the melter, HIPing can readily accommodate up to 100 % crystalline materials. Also the radiation induced damage and subsequent swelling of the crystals is unlikely to be detrimental to the wasteforms during prolonged storage. This is a result of the lower activity found in these ILW wasteforms. However, as briefly discussed above, in the case of fractured SiO_2 inclusions, some inclusions may be considered non-ideal and further investigation of this may be necessary in order to support a safety case for disposal. A brief discussion of the major inclusions present in the wasteforms is presented below.

SiO_2: The XRD patterns of both CSXC-$NaAlO_2$ and CSXC-BORAX identify the presence of both quartz and cristobalite crystals. The presence of SiO_2 crystallites could result from one of two processes during HIPing. The first would indicate the sand, added to simulate the particulate filter, is not completely dissolved into the vitreous phase during processing. The second would be that cooling of this silicon rich melt results in crystallisation.

There is evidence to support both possibilities. The presence of cristobalite is often indicative of the devitrification of silicate melt which would provide support for the notion that the presence of crystalline silica is due to precipitation from the silica rich melt [251]. However, the larger particle size, fracture patterns and morphology of the visible grains are suggestive of incomplete solubilisation of the batched sand. It is considered most likely that both mechanisms are occurring. Determination of which mechanism is prevalent could readily be

performed by processing a sample of pure clinoptilolite without the addition of sand as a particulate filter.

The solubilisation of the sand's surface and its effective encapsulation is crucial for the effective immobilisation of the SIXEP clinoptilolite/sand waste. As the sand filter acts as a particulate filter prior to the ion exchange in the SIXEP plant design, it will contain quantities of radionuclides on its surface. At a minimum, the surface of these sand particles should be well coated or solubilised to ensure these radioisotopes are taken into the glass structure. This is clearly achieved in both compositions with effective wetting and digestion of the SiO_2 grains achieved. As CSXC-BORAX contains approximately 4 vol% less SiO_2 inclusions than CSXC-$NaAlO_2$ from an otherwise identical batch, it can be assumed the addition of boron helps in the digestion of these SiO_2 grains. This is because on a mole for mole basis, boron additions decrease the viscosity of melts in silicate glasses promoting solubilisation.

Fe_2O_3: Several regions within the glass have been identified by SEM-EDX as sub-micron iron rich inclusions. The most likely identity of these inclusions was determined to be Fe_2O_3. This was in spite of the unavoidable measurement of a small proportion of glass forming elements in these sub-micron features in the SEM-EDX measurement. The presence of these inclusions could be explained by numerous mechanisms.

The first possibility is precipitation of FeO/Fe_2O_3 from the melt in concentrated regions. As the clinoptilolite used is a natural mineral, it is not considered unlikely that some iron rich grains are present. With the lack of effective mixing these regions could remain concentrated and precipitate from solution even if they were initially digested. Alternatively the presence of these inclusions could result from the partial dissolution and oxidation of the steel wire used as a vacuum line filter during the canister evacuation. Finally, they could be result of the 'burn through' of the canister during welding which has subsequently been encapsulated. The mechanism by which these inclusions formed were not investigated as their presence was not considered detrimental to the overall quality of a wasteform intended for the immobilisation of ILW wastes.

Mixed alkali earth sulphates: Numerous isolated regions of mixed alkali earth sulphate were found embedded within the glass structure of both compositions, with the nominal composition $Ba_{0.5}Ca_{0.4}Sr_{0.1}SO_4$. The mechanism by which this phase forms has not been investigated although some speculative discussion is presented. Sulphate was measured by XRF analysis at < 0.1 wt% in the CSXC-CLINO prior to HIPing. As limits for sulphate solubility in silicate glass melts are not commonly below 0.3 wt%, it was hoped that the glass would

directly accommodate these levels of sulphur into the structure without the formation of sulphate salts [252].

The presence of mixed alkali sulphate salt therefore indicates that a sulphate rich phase, such as gypsum, may present in the CSXC-CLINO prior to HIPing. Such a phase is likely to exist in a natural mineral product. As the fluidity and convective flow of the glasses during processing is low, these inclusions would be localised in the melt resulting in localised increases in SO_3 concentration. This could then cause the formation and precipitation of the mixed alkali earth phases observed. This provides a potential explanation for the presence of these phases in both CSXC-CLINO and CSXC-$NaAlO_2$ compositions.

The alkali earth sulphate is considered the property most detrimental to the integrity of the wasteform. Although not highly soluble, the alkali earth sulphates should not be considered ideal matrices for the immobilisation of radioactive wastes. This is because some Sr partitions into these regions and will be locally enriched in a phase of higher solubility than seen in the glass matrix.

The presence of these sulphate phases, although not desirable, was not considered restrictive to the potential use of these materials as ILW wasteforms. Compositional measurements and quantification of the phase assemblage showed that the majority of the Sr inventory is retained in the vitreous phase. This vitreous phase has been determined to be stable in aqueous dissolution as in Section 6.4.3. Therefore, the potential for the release of Sr into solution should be considered to be low.

The impact of the alkali sulphate phases is minimal as these inclusions are well encapsulated within a non-porous, high durability glass matrix. As industrial HIPing process would produce a roughly cylindrical wasteform with a low SA/V ratio, this would minimise the number of surface accessible sulphate inclusions. As these inclusions were not interconnected throughout the matrix, contact of these inclusions with aqueous solution will be determined by the global retreat of the glass and are overestimated in all tests performed during the course of this study.

Finally, as the loading of Sr is approximately four orders of magnitude higher in these simulant wastes than exists the real life waste stream, it is debatable how representative this segregation of the Sr into this phase is likely to be.

Feldspar and $NaAlO_2$: A mixed feldspar phase was identified in the XRD and SEM-EDX analysis for CSXC-$NaAlO_2$. The presence of this phase is not likely to be detrimental to the integrity of the wasteform. It is a naturally occurring mineral which can be considered a suitable phase

for the immobilisation of ILW and is well encapsulated within the vitreous phases. The SEM-WDX mapping shown in Figure 6.6 shows this phase only exists within the regions of Glass B. This indicates that the glass in these regions is saturated with respect to Al_2O_3 resulting in the precipitation of this alumina from solution during cooling as a mixed feldspar. This can be considered a direct result of the $NaAlO_2$ addition, as the presence of feldspar was not identified in the XRD trace of CSXC-BORAX. Figure 6.6 shows that a number of feldspar inclusions are locally enriched with respect to Sr. However, unlike the case of the mixed alkali sulphate, the concentration of Sr in this phase is not considered problematic as it should be expected to behave as a durable matrix for the retention of Sr in aqueous solutions.

The phase mapping in Section 6 identified numerous regions as mixed feldspar, however, there is some evidence that $NaAlO_2$ is also retained or precipitated in these regions. A decrease in Si concentration is correlated with a number of regions of increased Al. If these areas were feldspar, this should not be expected; therefore the most appropriate explanation is that some $NaAlO_2$ is also retained in the wasteform.

6.4 - Results and Discussion - Part II - Aqueous Durability

6.4.1 - Static Aqueous Durability Experiments - Solution Analysis

PCT Experiments

The results of PCT type experiments of the CSXC-$NaAlO_2$ and CSXC-BORAX are displayed in Figures 6.11 - 6.12, Figure 6.15 and Table 6.5. Figure 6.11 displays data obtained from PCT experiments on CSXC-$NaAlO_2$ and CSXC-BORAX. This figure provides plots of NL_i against time for each element from both CSXC-$NaAlO_2$ and CSXC-BORAX, illustrating the relationship between the individual NL_i values. Figure 6.12 provides plots of NL_i against time for each element of interest for both CSXC-$NaAlO_2$ and CSXC-BORAX. This allows comparison of the dissolution behaviour in the two wasteforms. The errors are set to ± 10 % based on RSD values of concentrations, as measurement using multiple ICP-MS measurements. The pH data is shown for the experiment in Figure 6.12 showing an initial rapid increase to approximately pH 9.2. Despite some minor variation the pH roughly stays constant at this value throughout the duration of testing. 28 days. Figure 6.15 provides the same comparison as Figure 6.12 with the addition of data from MCC-1 experiments, described later in this section, which allows comparison of NL_i under different experimental methodologies. Table 6.5 displays both the NL_i and NR_i from PCT and MCC-1 experiments after 28 days sampling.

The behaviour of CSXC-$NaAlO_2$ during PCT experiments shown in Figures 6.11 and 6.12 illustrates that, within the expected error margins, the majority of elements obtain a stable value of NL_i during the testing period. The exceptions to this are Ba and Cs. NL_{Ba} decreases over time, which indicates that Ba is likely to be precipitating from solution as the experiment progresses. NL_{Cs} shows a decrease from the initial sampling to the 14 day sampling point, however it is then increased in the last two sampling points.

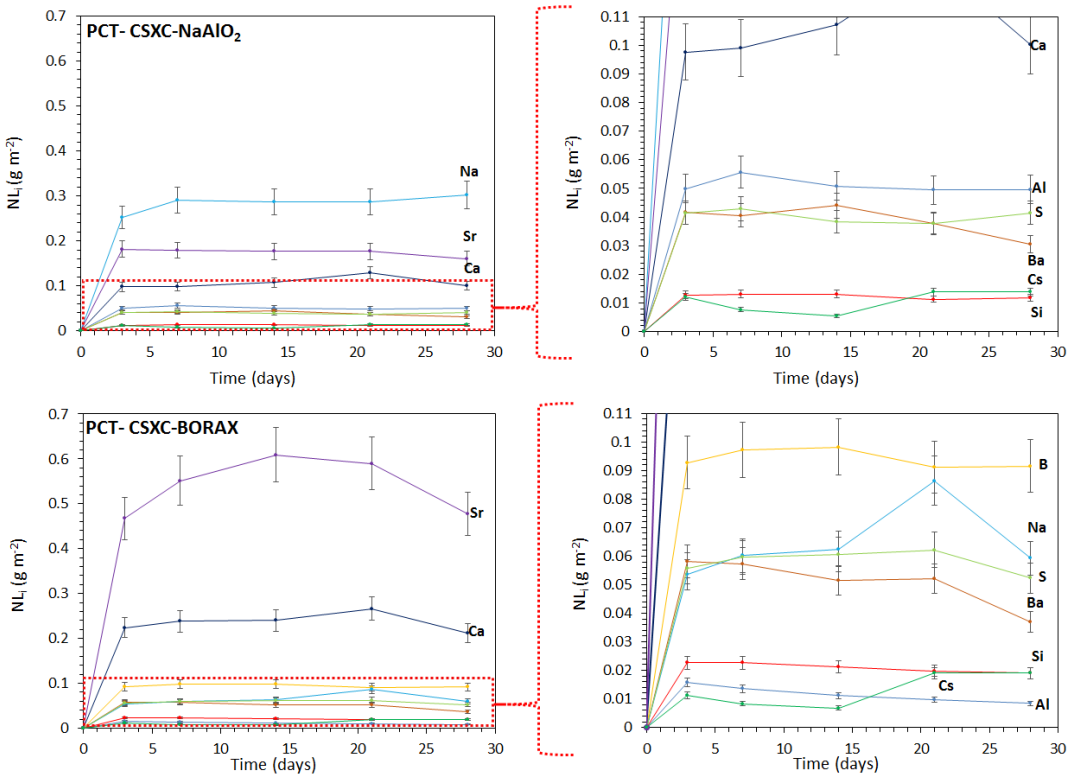

Figure 6.11 – Normalised mass losses of selected elements from PCT experiments on CSXC-$NaAlO_2$ and CSXC-BORAX at 90°C with a SA/V of ~2000 m^{-1} in 18.2 MΩ water.

The NL_i values obtained from CSXC-BORAX follow four different trends over the course of this PCT experiment, which are most clearly observed in Figure 6.12. NL_{Cs} follows the same trend as was noted was noted in CSXC-$NaAlO_2$. The second noted trend is where a large initial increase of NL_i occurs, followed by a gradual decrease. This is the case for NL_{Si}, NL_{Al} and NL_{Ba}. The third trend noted is that the NL_i first reaches a steady value until the final sampling point prior to a decrease in the NL_i, as is the case for NL_{Ca}, NL_{Sr}, NL_{Na} and NL_S. The final trend is only observed for NL_B which attains a steady value of NL_B after 3 days and shows no deviation from this outside of the expected error.

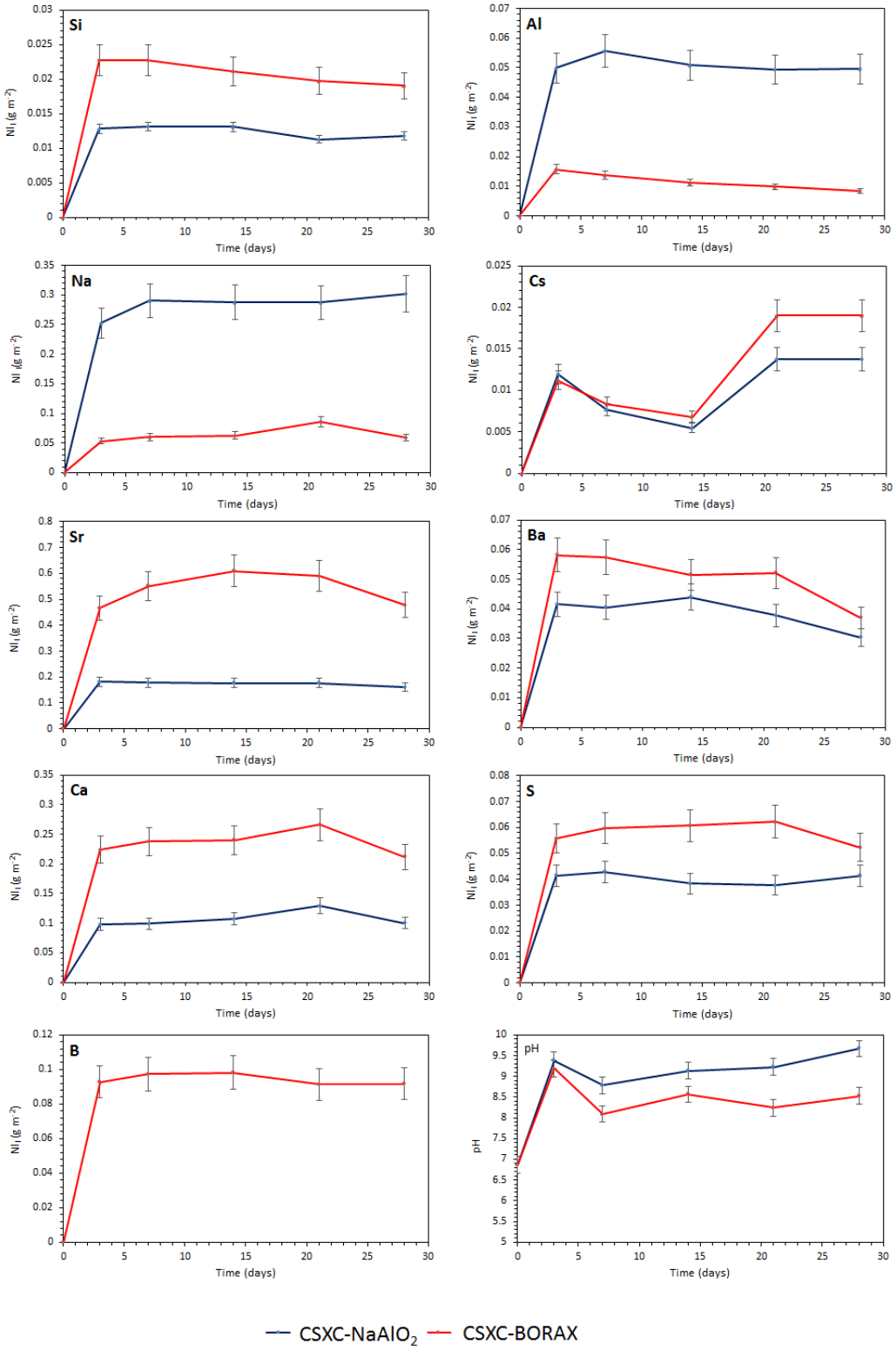

Figure 6.12 – Graphs comparing the normalised elemental mass loss of key elements from PCT type experiments on CSXC-$NaAlO_2$ and CSXC-BORAX at 90°C with a SA/V of ~2000 m^{-1} in 18.2 MΩ water.

Although the descriptions provided above appear to show the behaviour of the two wasteforms is very different, when looking at the generic behaviour of these glasses with

respect to the release of major elements several similarities are evident. After 28 days of testing both CSXC-$NaAlO_2$ and CSXC-BORAX both show the following trends in the values of NL_i, the values of which are provided in Table 6.5; $NL_{Si} \leq NL_{Cs} < NL_{Ba} < NL_S < NL_{Ca} < NL_{Sr}$. These NL_i values are all comparable within at least the same order of magnitude. This suggests that the dissolution behaviour concerning the majority of elements in the wasteforms is similar. Although all the NL_i values for these elements are within the same order of magnitude, it should be noted that the NL_i of the above mentioned elements is higher in CSXC-BORAX after 28 days than was determined for CSXC-$NaAlO_2$. The NL_i of Sr and Ca from CSXC-BORAX were up to three times greater than was observed for CSXC-$NaAlO_2$.

However, the NL_i of Na and Al differ more significantly between the two wasteforms. NL_{Na} and NL_{Al} are both an order of magnitude greater in CSXC-$NaAlO_2$ than was observed from CSXC-Borax. A comparison of the behaviour of NL_B is impossible due to the absence of B from the composition of CSXC-$NaAlO_2$.

MCC-1 Experiments

Figure 6.13 displays data obtained from MCC-1 experiments on CSXC-$NaAlO_2$ and CSXC-BORAX. This figure provides plots of NL_i against time for each element of both CSXC-$NaAlO_2$ and CSXC-BORAX, which highlight the relationship between individual NL_i values. Figure 6.14 provides plots of NL_i against time for each element of interest in both CSXC-$NaAlO_2$ and CSXC-BORAX which allows comparison of the dissolution behaviour between the two wasteforms. The error from these experiments was determined from the RSD on the concentrations of multiple identically prepared samples, as measured by ICP-MS. This error was large by comparison to that previously observed for MCC-1 type experiments (± 5%) and was set to ± 25 % of the measured value. The origin of this larger error is discussed later in this section. The pH data is shown for the experiment in Figure 6.14 showing a gradual increase during testing to a peak of approximately pH 8.5 after 28 days. Figure 6.15 provides the same comparison as Figure 6.14 with the addition of data from PCT experiments described earlier in this section. This allows comparison of NL_i under different experimental methodologies. Table 6.5 displays both the NL_i and NR_i values from PCT and MCC-1 experiments from the 28 days sampling.

In the case of CSXC-$NaAlO_2$ Figure 6.13 shows that the comparison of individual NL_i values is unlikely to prove conclusive. No pronounced differentiation based on behaviour can be made from Figure 6.13. Figure 6.14 shows that three different trends exist within the plots of NL_i for CSXC-$NaAlO_2$. NL_{Si}, NL_{Ba} and NL_{Cs} all increase steadily over the course of the testing. NL_S,

NL_{Ca}, NL_{Na} and NL_{Al} all increase in NL_i over the course of testing, however the rate at which these changes occurs varies between sampling points, accelerating towards the end of the experiment. Finally NL_{Sr} at first shows a steady increase but after 28 days drops significantly.

The values of NL_i obtained for CSXC-BORAX follow two different trends as can be seen more clearly in Figure 6.14. NL_{Sr} increases gradually at first with a large increases after 21 days. NL_{Si}, NL_{Al}, NL_{Na}, NL_{Cs}, NL_{Ba}, NL_{Ca} and NL_B increase over time steadily over the course of the experiment.

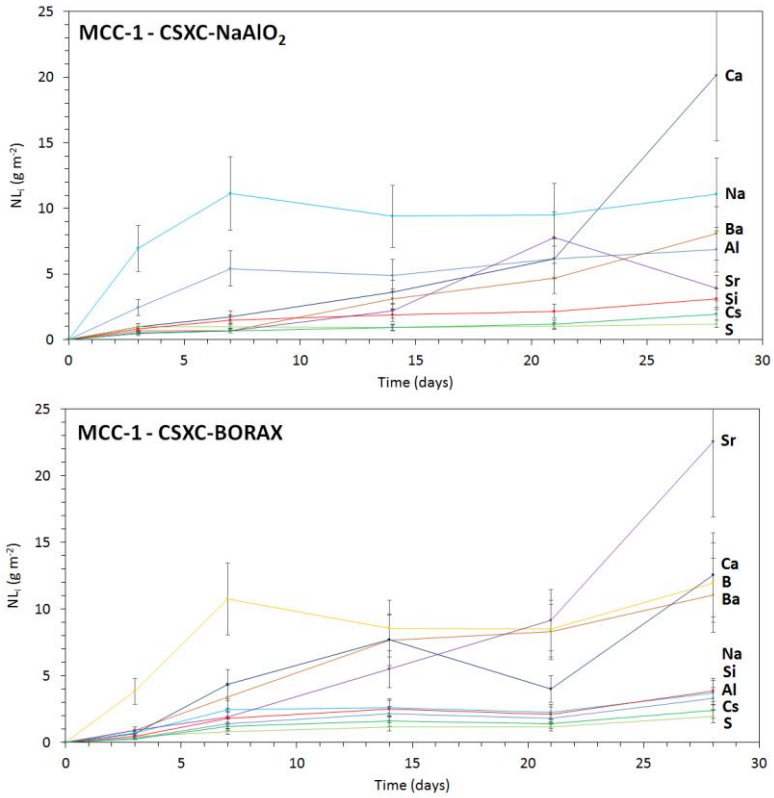

Figure 6.13 – Normalised elemental mass losses of selected elements from MCC-1 type experiments on CSXC-$NaAlO_2$ and CSXC-BORAX at 90°C with a SA/V of ~10 m^{-1} in 18.2 MΩ water.

Due to the large experimental error no comparison is made here of the significance of variations in NL_i within each experiment. It can however be surmised from Figure 6.14 that both CSXC-$NaAlO_2$ and CSXC-BORAX produce similar profiles to each other for all but three of the key elements. NL_{Sr} shows a decrease in CsXC-$NaAlO_2$ after 28 days testing, whereas it shows an increase in the case of CSXC-BORAX. As in the PCT experiments described above, the most apparent variation is observed for NL_{Al} and NL_{Na}. Here the release in the CSXC-$NaAlO_2$ sample is over an order of magnitude greater than that of the CSXC-BORAX. As in the

PCT experiments a comparison of NL_B is not possible due to the composition of CSXC-$NaAlO_2$ containing no boron.

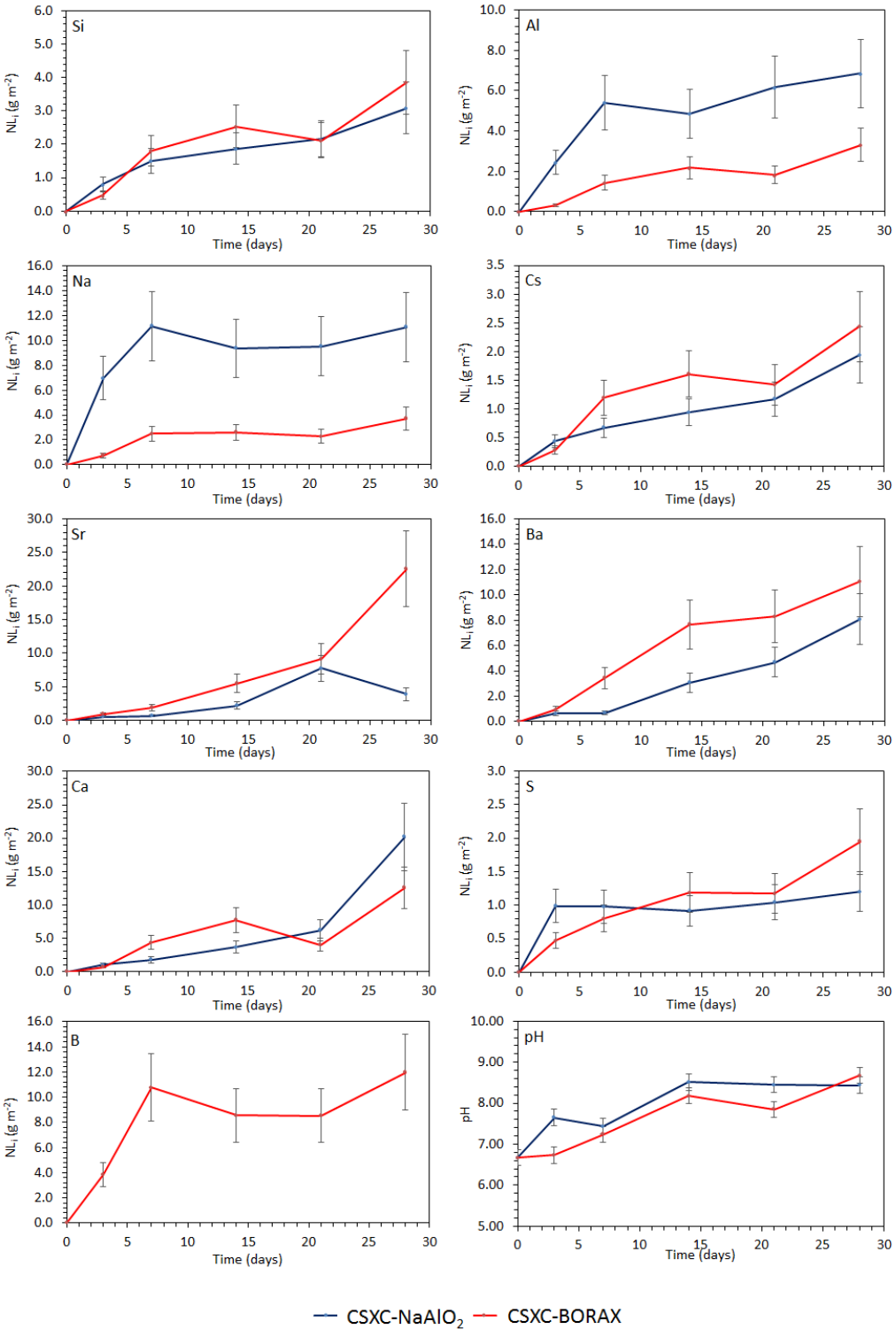

Figure 6.14 – Graphs comparing the normalised elemental mass loss of key elements from MCC-1 type experiments on CSXC-$NaAlO_2$ and CSXC-BORAX at 90°C with a SA/V of ~10 m^{-1} in 18.2 MΩ water.

Comparison of PCT and MCC-1 Experiments Solution Releases

Figure 6.15 provides a comparison of the results obtained from PCT and MCC-1 experiments on CSXC-$NaAlO_2$ and CSXC-BORAX. In all cases the NL_i from each composition is between one and two orders of magnitude higher when tested by MCC-1 experiments than observed in PCT experiments.

MCC-1 experiments consistently show a greater slope in the NL_i vs. time than is observed from PCT experiments throughout the course of testing. This shows the NR_i is always greater in the MCC-1 experiments.

Plotting the combined results on a log scale helps to illustrate where consistencies in the behaviour of elemental release behaviour from each composition exist in both experiments. Three behaviours can be noted with respect to the consistency of behaviour. The first is that NL_i values from each composition are broadly similar when examined with comparable experimental methodologies. This is true of NL_{Si}, NL_{Cs}, and NL_S.

The second behaviour observed was evident when consistent and significant differences existed between each composition tested under both experimental methodologies. This is the case for NL_{Na}, NL_{Al} and NL_{Sr}. NL_{Na} and NL_{Al} are over an order of magnitude greater for CSXC-$NaAlO_2$ than for CSXC-BORAX in both experiments. NL_{Sr} shows the CSXC-BORAX consistently releases Sr in greater quantities in both experiments than is seen for CSXC-$NaAlO_2$.

The third behaviour is shown when no correlation of behaviour between composition and experimental methodology are observed. This is the case with NL_{Ca} and NL_{Ba}. NL_{Ca} shows roughly equivalent behaviour of the compositions during MCC-1 experiments, but a greater NL_{Ca} from CSXC-BORAX during PCT experiments. NL_{Ba} shows higher release from CSXC-BORAX during MCC-1 experiments but roughly similar behaviour of each composition during PCT experiments.

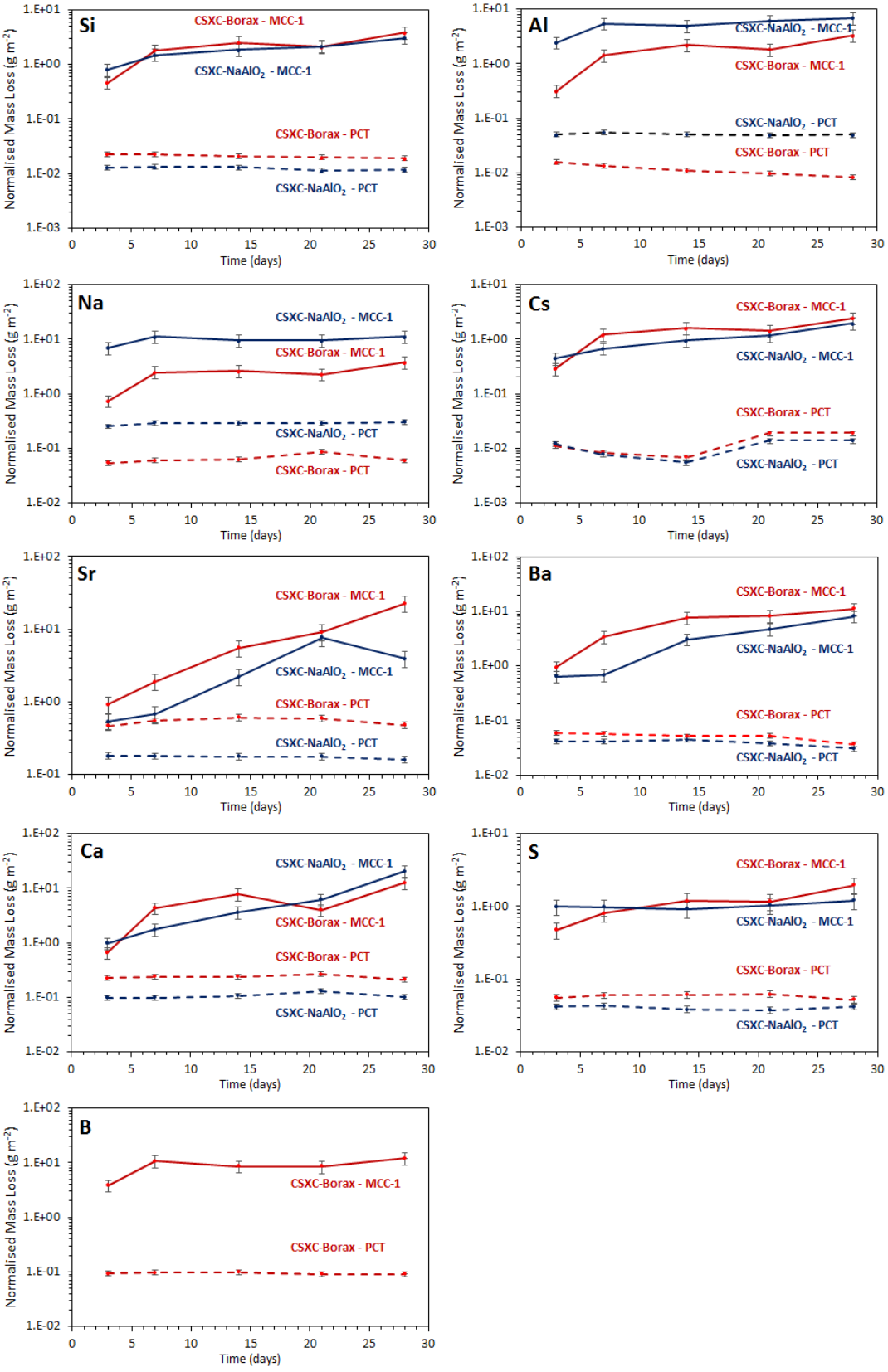

Figure 6.15 - Graphs comparing the normalised elemental mass loss of key elements from MCC-1 and PCT type experiments on CSXC-$NaAlO_2$ and CSXC-BORAX at 90 °C in 18.2 MΩ water.

Element	NL_i (g m^{-2})				NR_i (g m^{-2} day^{-1})			
	PCT		MCC-1		PCT		MCC-1	
	CSXC-$NaAlO_2$	CSXC-BORAX	CSXC-$NaAlO_2$	CSXC-BORAX	CSXC-$NaAlO_2$	CSXC-BORAX	CSXC-$NaAlO_2$	CSXC-BORAX
Si	1.18×10^{-2}	1.90×10^{-2}	3.09×10^{0}	3.86×10^{0}	4.21×10^{-4}	6.80×10^{-4}	1.10×10^{-1}	1.38×10^{-1}
Al	4.96×10^{-2}	8.41×10^{-3}	6.85×10^{0}	3.30×10^{0}	1.77×10^{-3}	3.00×10^{-4}	2.45×10^{-1}	1.18×10^{-1}
Na	3.02×10^{-1}	5.93×10^{-2}	1.11×10^{-1}	3.73×10^{0}	1.08×10^{-2}	2.12×10^{-3}	3.96×10^{-1}	1.33×10^{-1}
Cs	1.38×10^{-2}	1.90×10^{-2}	1.94×10^{0}	2.44×10^{0}	4.91×10^{-4}	6.79×10^{-4}	6.93×10^{-2}	8.71×10^{-2}
Sr	1.61×10^{-1}	4.78×10^{-1}	3.91×10^{0}	2.26×10^{1}	5.75×10^{-3}	1.71×10^{-2}	1.40×10^{-1}	8.05×10^{-1}
Ba	3.04×10^{-2}	3.70×10^{-1}	8.09×10^{0}	1.10×10^{1}	1.08×10^{-3}	1.32×10^{-3}	2.89×10^{-1}	3.94×10^{-1}
Ca	1.00×10^{-1}	2.12×10^{-1}	2.02×10^{1}	1.26×10^{1}	3.57×10^{-3}	7.56×10^{-3}	7.21×10^{-1}	4.49×10^{-1}
S	4.15×10^{-2}	5.23×10^{-2}	1.20×10^{0}	1.95×10^{0}	1.48×10^{-3}	1.87×10^{-3}	4.29×10^{-2}	6.95×10^{-2}
B	N/A	9.15×10^{-2}	N/A	1.20×10^{1}	N/A	3.27×10^{-3}	N/A	4.28×10^{-1}

Table 6.5 – Values of normalised elemental mass loss and normalised elemental loss rates from both 28 days testing of PCT and MCC-1 type experiments of CSXC-$NaAlO_2$ and CSXC-BORAX. Both experiments were performed in 18.2 MΩ H_2O at 90°C with a SA/V of 2000 m^{-1} and 10 m^{-1} respectively. Errors estimated at ± 10% of stated values for PCT and ±25 % for MCC-1.

6.4.2 - Static Aqueous Durability Experiments – Sample Analysis

PCT

Figure 6.16 shows the powders before the PCT experiments. Figure 6.16 a-d show SEM-BSE images of washed CSXC-$NaAlO_2$ powders and Figures 6.16 e-h show SEM-BSE images of washed CSXC-BORAX powders. The particles produced from each composition were broadly comparable and so the following description should be considered representative of both compositions, except where otherwise stated.

The morphologies of the powders show that they are suitable for PCT experiments. Little deviation from the 106 – 180 µm particle size fraction can be seen. The majority of particles have a block like nature with multiple smaller faces and edges covering the main faces of the particles. The edges are sharp and faces smooth, as should be expected from fractured glass particles. However some particles had a more flake like nature than was observed in the general morphology. Where particles were seen to have the rougher 'flaky' surface texture as seen in Figure 6.16 f), SEM-EDX measurements identified these particles as SiO_2 which correlates with the SiO_2 inclusions identified in Section 6.3.

A number of bright spots were identified by SEM-EDX analysis. These were observable on approximately 0.5% of particles and had a globular morphology existing on the edges of particles as can be seen in Figures 6.16 d) and 6. 16 f). These were identified using SEM-EDX as the mixed alkali earth sulphate phase, $Ba_xCa_ySr_zSO_4$, previously discussed in Section 6.3.3.

Figures 6.17 and 6.18 show CSXC-$NaAlO_2$ and CSXC-BORAX powders after PCT experiments. The behaviours of the glass powders after PCT can be considered to be broadly similar. The particle morphologies are as described above. They show no gross alteration of the product illustrating their relative stability in solution. Evidence of sharp edges and multiple faces are seen, although there has potentially been some smoothing of these features. This is, however, difficult to determine with certainty due to the necessity of imaging different particles before and after experiments.

Both compositions show evidence of surface alteration. This is illustrated in Figures 6.17 h) and 6.18 f-h for CSXC-$NaAlO_2$ and CSXC-BORAX respectively. The degree of alteration seems to vary with composition and appears more pronounced in the case of CSXC-BORAX. This is especially true of the area illustrated in Figures 6.18 e-f where evidence of both significant corrosion and the presence of alteration products are observed.

Other differences also exist between the two compositions. Figures 6.17 a-f highlight the behaviour of the mixed alkali-earth sulphate phase for CSXC-$NaAlO_2$. After PCT experiments the presence of mixed alkali sulphate phase was identified in approximately 1:200 particles. However, the morphology of this phase changed significantly during experiments.

Figure 6.17 e) shows that valleys and voids have appeared in the surface of the phase and that it has started to retreat away from the interface it shares with the glass. This indicates the phase has undergone a severe period of corrosion and is retreating at a higher rate than observed for the vitreous materials. Figure 6.17 f) provides further evidence for this using SEM-SE imaging. Here the topography of the mixed alkali sulphate phase sample is clearly recessed which was not the case in the pre-treated particles. This again shows that selective dissolution of the mixed alkali sulphate phase is occurring.

The most significant difference based on composition during PCT experiments was the complete absence of any mixed alkali-earth sulphate phase in CSXC-BORAX sample surfaces when imaged by SEM-BSE. As both the powder sampling methodology and imaging conditions were kept identical, the absence of these bright spots indicates the complete removal of this mixed alkali sulphate phase during these experiments.

This removal is accompanied by a set of new features not previously evident in the pre-treated powders. These features exist with approximately the same frequency of 1:150 particles frequency as the mixed alkali-earth sulphate phase had previously. The most pronounced example of this effect is imaged in Figures 6.18 c-f. The particle here shows severe surface depletion around one edge in comparison to what may be considered the previous reference height of the glass. Severe pitting of the surface correlates with this depression in the surface, which gives this region a sponge like cratered morphology. These craters range in size from a few microns to tens of microns in diameter as shown in Figure 6.18 e). Where the crater meets the ‘sponge’ evidence of severe surface corrosion and alteration products exist.

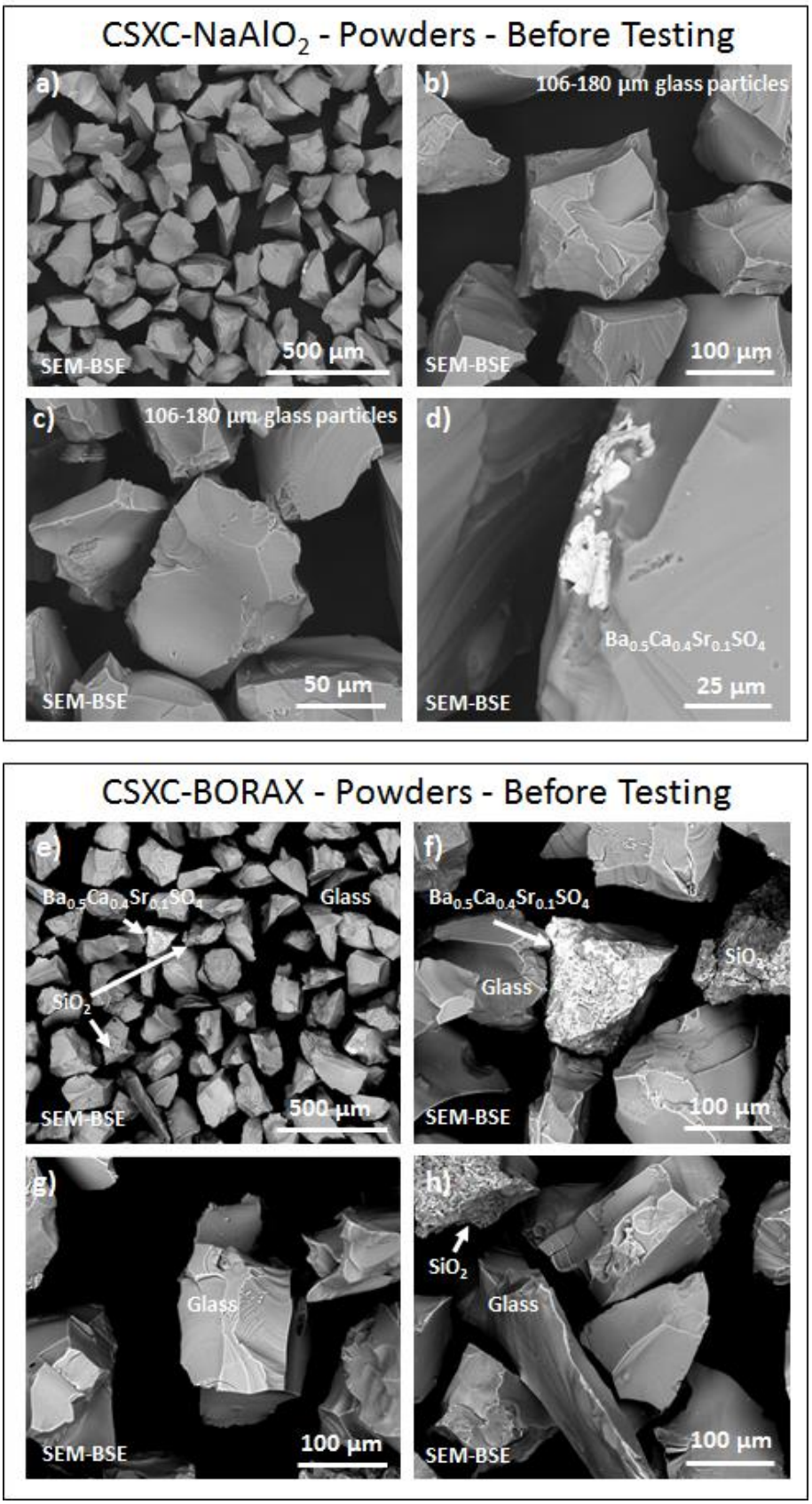

Figure 6.16 – SEM-BSE images of the powders used for PCT and SPFT type experiments of a-d) CSXC-$NaAlO_2$ and e-h) CSXC-BORAX. Powders were imaged after washing prior to dissolution experiments.

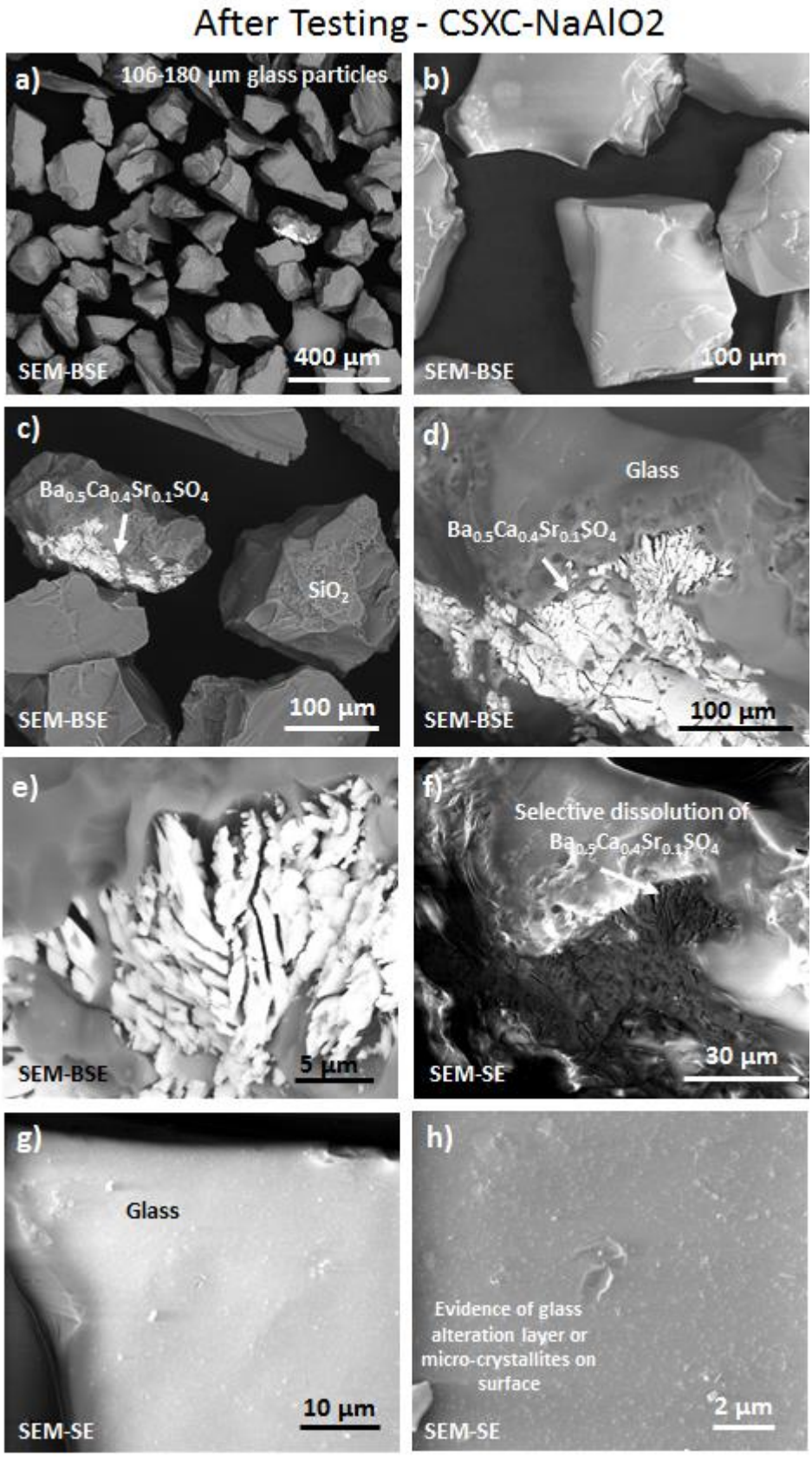

Figure 6.17 – SEM-BSE images of the CSXC-$NaAlO_2$ powders used for PCT type experiments at 90 °C in 18.2 MΩ H_2O after 28 days testing.

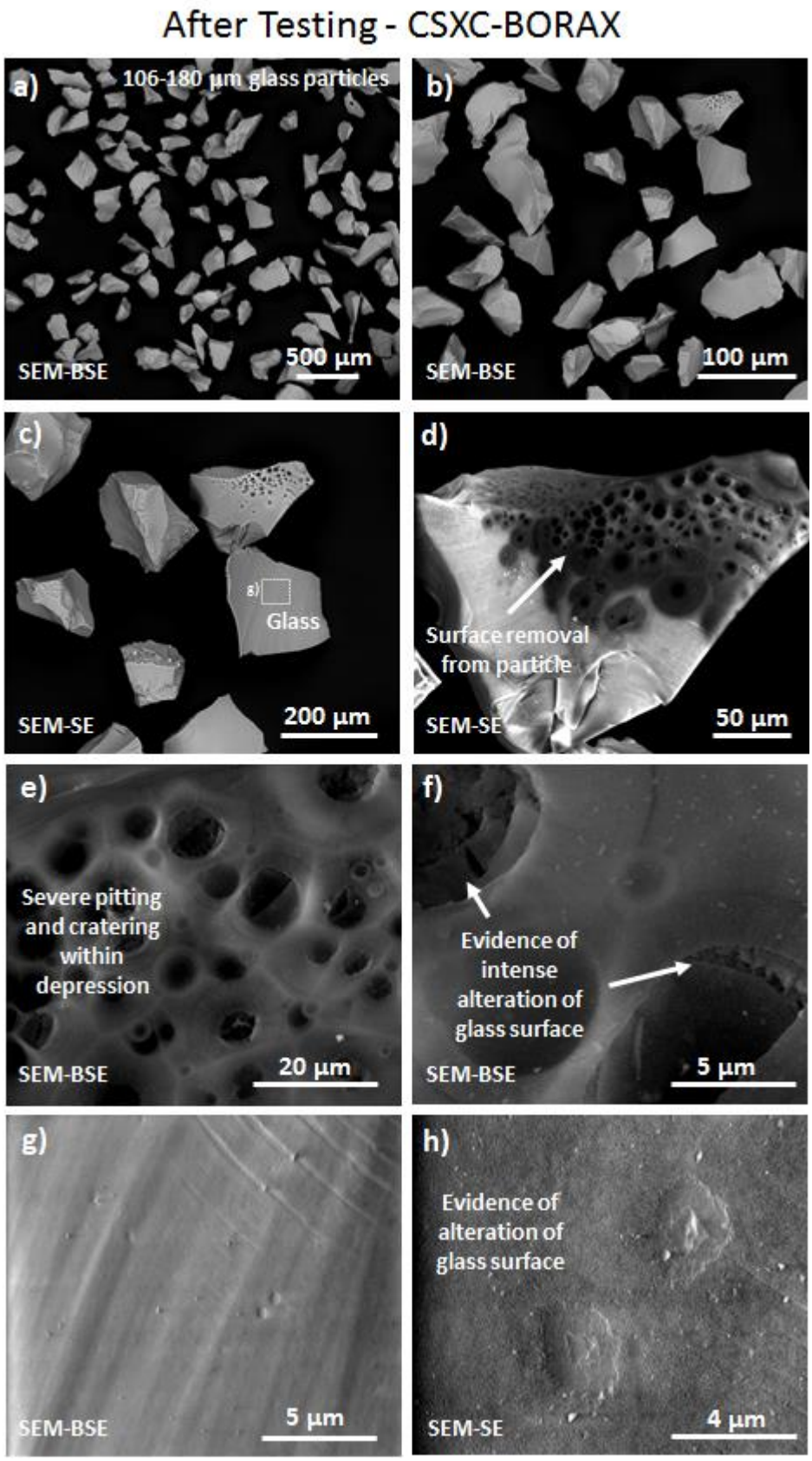

Figure 6.18 – SEM-BSE images of the CSXC-BORAX powders used for PCT type experiments at 90 °C in 18.2 MΩ H_2O after 28 days testing.

MCC-1

MCC-1 samples were examined in cross section after 28 days testing to determine whether alteration products existed. The SEM-BSE images provided in Figures 6.19 and 6.20 display the sample surfaces which were exposed to solution during testing in cross section for CSXC-$NaAlO_2$ and CSXC-BORAX respectively. The behaviour of these samples is practically identical. No evidence of alteration layers, precipitates or crystalline alteration products are observed on the surface of the sample. The effect of corrosion is not the same over the entire sample surface. Some regions show no evidence of corrosion whereas others show significant corrosion based effects in the form of pitting or worming.

Figures 6.19 d) and 6.20 a-b illustrates the effect of corrosion on the sample surface of each wasteform produced. This corrosion is present in the form of pitting and 'wormhole features' on the surface of the sample. These intrusions are sub-micron in width and depth in CSXC-$NaAlO_2$. They are also seen to exist with a similar morphology in CSXC-BORAX where they are more pronounced, penetrating the surface up to a few microns in depth. Not only are these intrusions larger in the CSXC-BORAX sample but also exist over a greater proportion of the sample's surface than observed for the CSXC-$NaAlO_2$ which remained largely unaffected by this process.

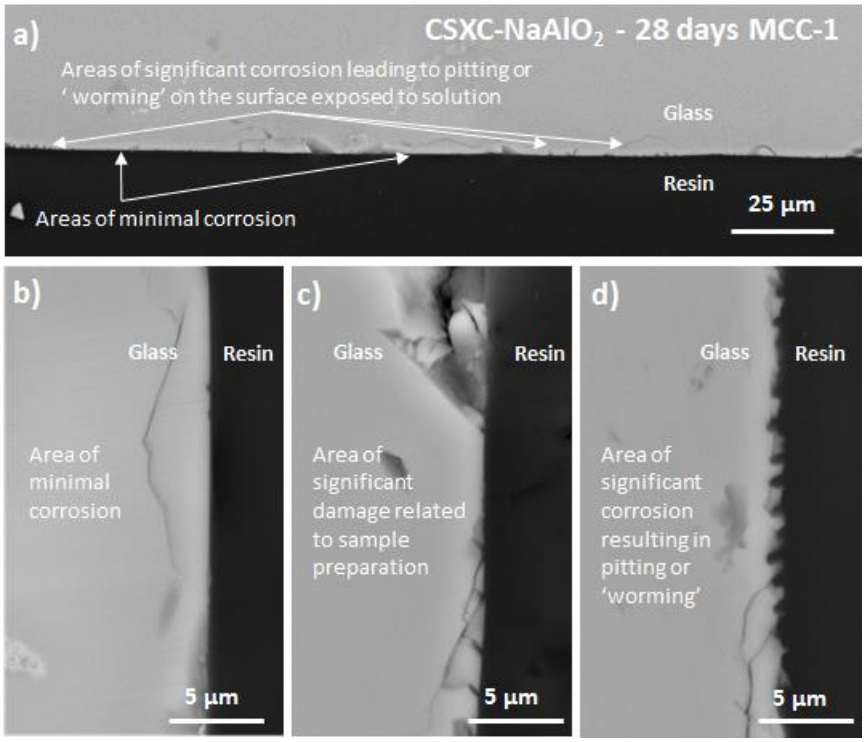

Figure 6.19 – SEM-BSE imaging of the surface corrosion features of CSXC-$NaAlO_2$ after MCC-1 experiments at 90°C in 18.2 MΩ H_2O for 28 days observed in cross section.

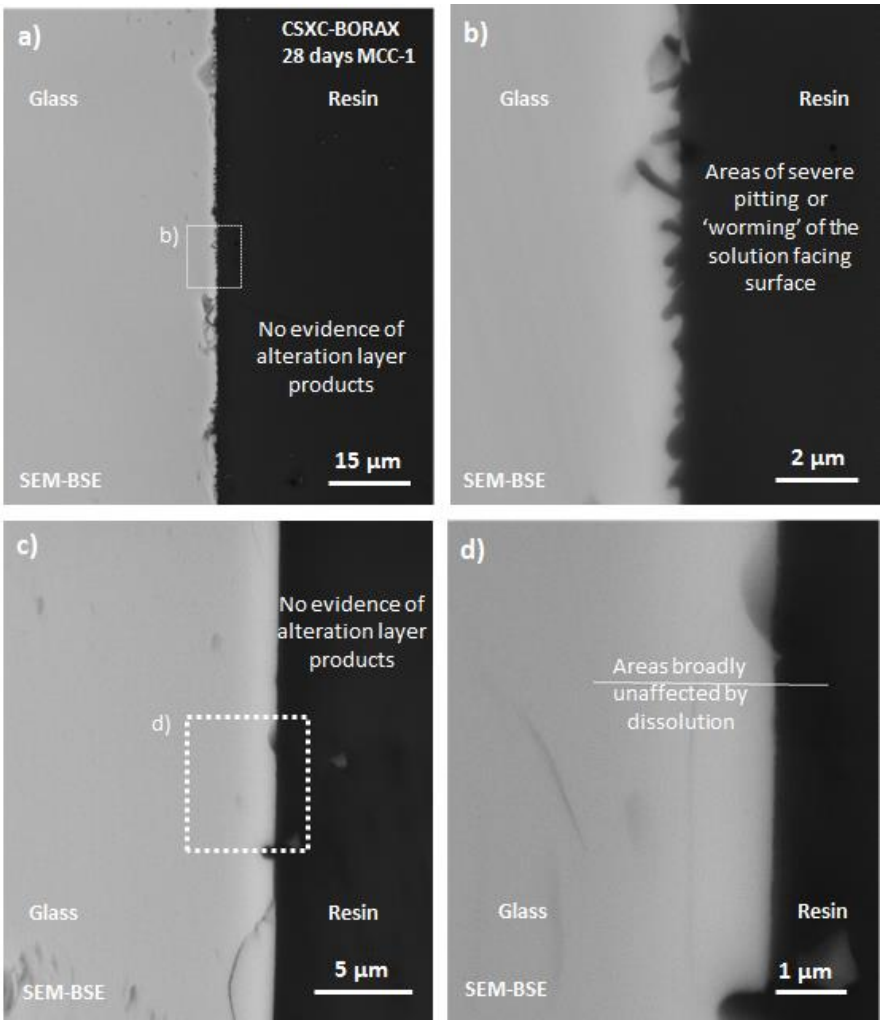

Figure 6.20 – SEM-BSE imaging of the surface corrosion features of CSXC-BORAX after MCC-1 experiments at 90°C in 18.2 MΩ H_2O for 28 days observed in cross section.

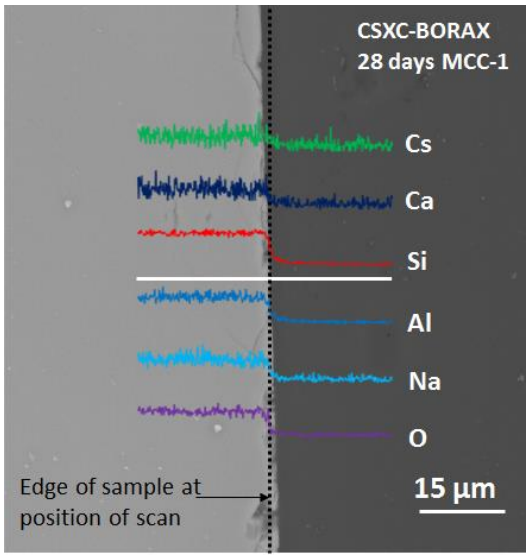

Figure 6.21 – SEM-EDX line scan of key elements from the surface corrosion features of CSXC-BORAX after MCC-1 experiments at 90°C in 18.2 MΩ H_2O for 28 days observed in cross section.

Figure 6.21 shows an SEM-EDX line scan of the CSXC-BORAX MCC-1 sample surface. Here we can see that the concentration of each element is consistent throughout the sample to the edge and no evidence of depletion is observed within the resolution provided by SEM-EDX analysis.

6.4.3 - SPFT Experiments

Experimental Validation

The first experiments performed using SPFT were used to validate the methodology prior to further study. These experiments were used to find the minimum time in which steady elemental release could be achieved, determine the effects of filtration on the measured concentration and to optimise the methodology used in ICP-MS measurement of these samples. This experiment was performed for both CSXC-$NaAlO_2$ and CSXC-BORAX at 90°C with pH 4 solution over the course of 23 days with 10 sampling points. After the collection of eluent, each sample was submitted for ICP-MS analysis in one of four acidified forms; first as an undiluted-unfiltered sample; secondly as a diluted-unfiltered sample; thirdly as an undiluted-filtered sample; and finally as a diluted-filtered sample. The inherent errors involved with this experimental methodology have been previously calculated at ± 30%, this error has been adopted for use in this study [200]. The exception to this is in Figure 6.22 which plots concentration data against time and where the error has been set to ± 10% based on multi-sampling measurements using ICP-MS.

The results of the qualification experiments are shown in Figure 6.22. This figure provides individual elemental plots for the concentration, as measured from the undiluted-filtered and undiluted-unfiltered analysis for both CSXC-$NaAlO_2$ and CSXC-BORAX. Each elemental plot has a secondary plot inlaid to illustrate the point at which concentrations were determined to reach a steady state. Samples prepared using dilutions were disregarded as they were comparable within an error of ± 5% to the concentrations as measured in the undiluted samples in all cases.

Plot Profile: With the exceptions of Ba and the measurements of Si and B (in their unfiltered form) all graphs show that the trend expected for SPFT experiments of vitreous wasteforms. This typical behaviour provides a plot of concentration against time where a large initial release rapidly decreases to provide a steady release of each element to solution. The variations noted above are described further below.

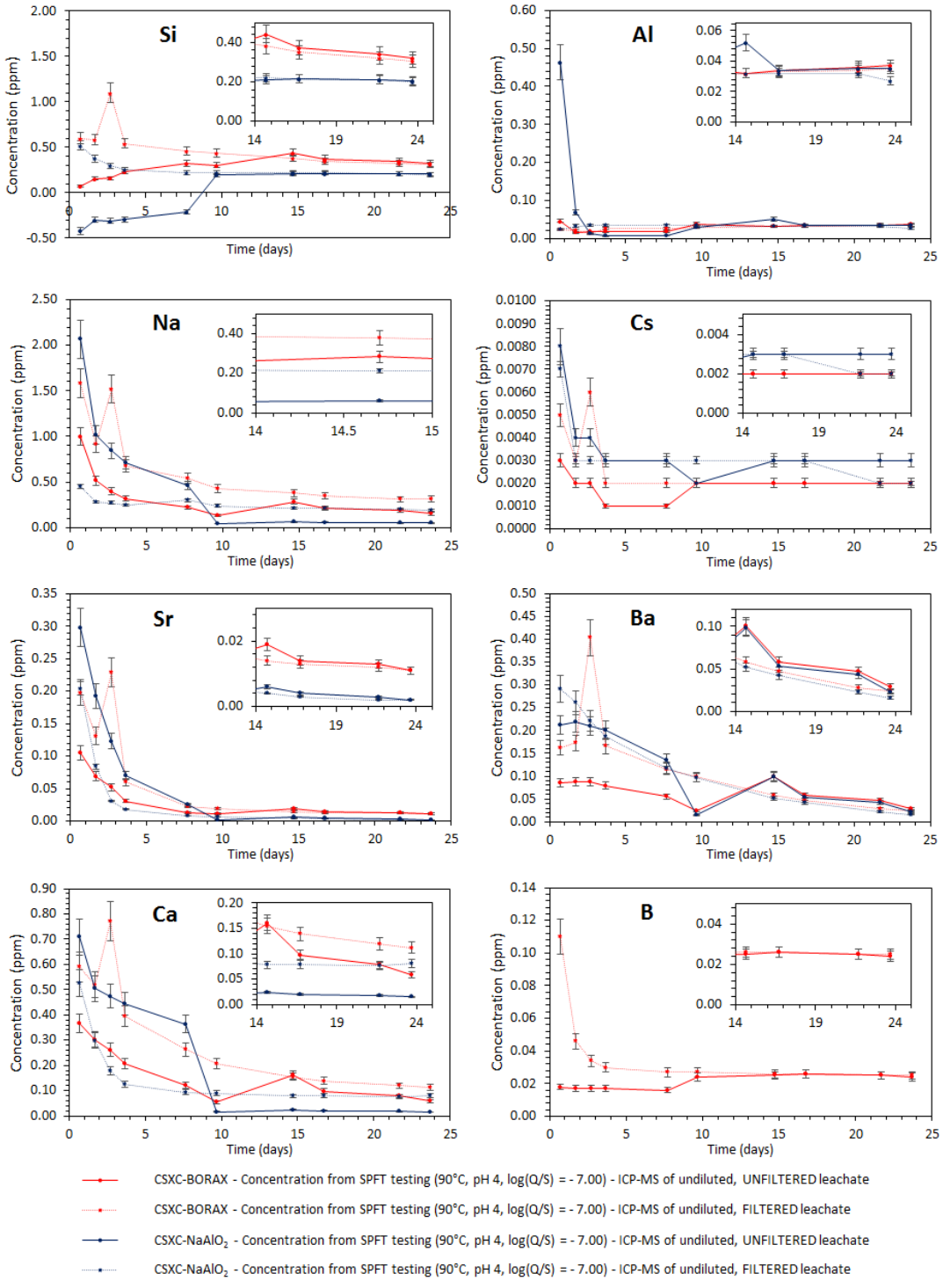

Figure 6.22 – Plots of the measured concentration from SPFT against time for CSXC-$NaAlO_2$ and CSXC-BORAX as measured in filtered and unfiltered samples to qualify the applicability of the experimental methodology. Inlaid are secondary plots of the same parameters highlighting the behaviour of the samples between 14 and 24 days of testing.

The plots of Si and B for the unfiltered solutions in both compositions show a low, and in the case of Si, even negative initial concentration, which then increases to attain a steady state. This does not correlate with the measurement of the filtered samples, which show the

expected trend as described above. This deviation from the expected trend is based on the performance of the ICP-MS. The first 6 sample points for Si in the unfiltered samples were measured separately to those of the last 4 data points and those of the unfiltered samples. The measurement of Si from the first six samplings had not optimised for these samples and therefore these data points must be considered erroneous. As the measurement of the filtered samples matches that those of the unfiltered samples in the second set of measurements, it can be reasonably assumed that the measurements of Si were subsequently validated.

Ba deviates from the expected profile in that it does not reach a point at which a steady state release is obtained within the experimental period. This means forward rates stated for this element in the following section should be treated with caution. There is also some evidence that Ca and Sr should be classified similarly from their residual slope, although this effect is not as pronounced as in the case of Ba.

Filtration: The values obtained from analysis of filtered and unfiltered samples are within the expected error for the majority of elements. This suggests that no precipitates exist in any solutions, at any sampling point. Four examples exist where deviations from this are significant. The first two examples of deviation between the filtered and unfiltered measurements, as discussed previously, are for Si and B. The explanation for this deviation has already been provided above and the difference can be assumed to be due to measurement errors within the ICP-MS methodology.

The deviations between the filtered and unfiltered samples which were considered most significant were those from Ca and Na. In both cases the measurement made for the filtered sample was consistently higher than that observed for the unfiltered sample. This indicates that the filters are contaminating the leachate samples with Na and Ca.

As it was determined that no precipitates were being removed during filtration and that the filters introduced significant contamination into the samples, for the sake of brevity in discussion all future results provided, unless otherwise stated, are from the measurement of the unfiltered, undiluted sampling.

Solution Saturation: As the experimental methodology has been proven, the following data can be considered relevant to the study. In order for SPFT to be valid the solution needs to remain below saturation limit for the formation of alteration phases. Typically alteration layers start to form only when Si in solution surpasses 1 ppm at 90 °C [80]. As Si never surpasses this level during the SPFT experiments, this provides evidence that the selection

of a Log(Q/S) value of -7.0 is appropriate for use in these experiments. However further qualification of this parameter will be described below.

Normalisation of rate data and log(Q/S) Qualification

Description of rate data: Figure 6.23 plots the NR_i from SPFT experiments at pH 4 with a higher log(Q/S) (-7.25) for the key elements of interest. The sampling points indicating the forward rates are plotted as an inlay for each composition. The elemental variation in the forward NR_i for CSXC-$NaAlO_2$ are more diverse than is seen in CSXC-BORAX. This variation is over 3 orders of magnitude in the case of CSXC-$NaAlO_2$ compared with only one of magnitude for CSXC-BORAX. The rates for CsXC-$NaAlO_2$ follow the trend $NL_{Ba} > NL_{Ca} > NL_{Sr} > NL_{Na} > NL_{Si} > NL_{Al} \sim NL_{Cs}$. The rates for CSXC-BORAX follow the trend $NL_{Ba} > NL_{Na} > NL_{B} \sim NL_{Ca} \sim NL_{Sr} \sim NL_{Al} > NL_{Si} \sim NL_{Cs}$. In the case of CSXC-$NaAlO_2$ all elements with the exception of Ba reach the forward rate regime within 14 days. For CSXC-BORAX all elements of interest reach the forward rate regime within 8 days.

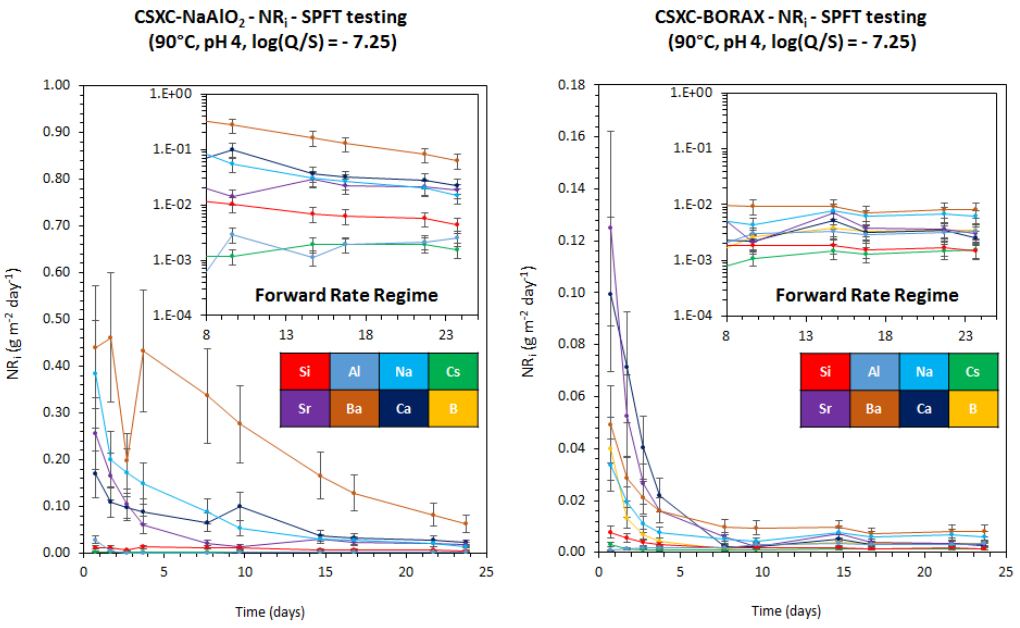

Figure 6.23 – Plots of normalised elemental loss rate against time of CSXC-NaAlO2 and CSXC-BORAX from SPFT experiments at 90 °C at pH 4 and with a loq(Q/S) of -7.25. The forward rate attained is displayed in the inlaid secondary plot for each composition.

The values of NR_i are lower for CSXC-BORAX than for CSXC-$NaAlO_2$, with the exception of NR_{Cs} which is roughly comparable. As steady state releases for the majority of elements were reached within 14 days for both compositions, it was decided that experiments should be

performed for 16 days with 8 sampling points. The average of the data points taken from the 14 and 16 day samplings was used to describe the forward NR_i. Caution should be taken in the cases of Ba, Sr and Ca with the definition of this value as a forward NR_i. As mentioned previously some evidence suggests these elements may exist in a regime where the rate is still decreasing.

log(Q/S) Qualification: To determine whether the experimental set up is within the desired constraints for SPFT experiments, i.e. solution feedback is minimised and the formation of protective alteration layers is excluded from testing, it is customary to compare a number of experiments with variations in the value of log(Q/S). The results of these experiments are provided in Figure 6.24A and 6.24B. These figures contains plots of the NR_i against time for both tested compositions for each element of interest. Each plot shows the behaviour of NR_i with varying log(Q/S) values ranging from -7.25 to -6.4. The behaviour during each experiment is comparable in every case throughout time. This provides further evidence that the experimental set up is valid and that repeatable data can be obtained with small variations in set up.

Importantly, the qualification experiments performed provide data suggesting that the experiments are within the forward rate regime and are likely to be unaffected by solution affinity and/or alteration layer effects. However, in the case of Na, significantly higher NR_{Na} values were obtained in experiments with the highest log(Q/S) values. As this is only the case for Na it is believed this result is an artefact of the measurement via ICP-MS. The NR_{Na} behaviour can be split into two data sets based on values obtained. This makes the data obtained from log(Q/S) = -7.25 and -7.0 roughly comparable and log(Q/S) = -6.7 and -6.4 also comparable. As the ICP-MS was performed separately for these two groupings, it is suggested that this discrepancy in the observed trends is due to variation in the calibration for the ICP-MS measurements of this single element. Figure 6.25 plots the forward NR_i values obtained against log(Q/S) of the experiment.

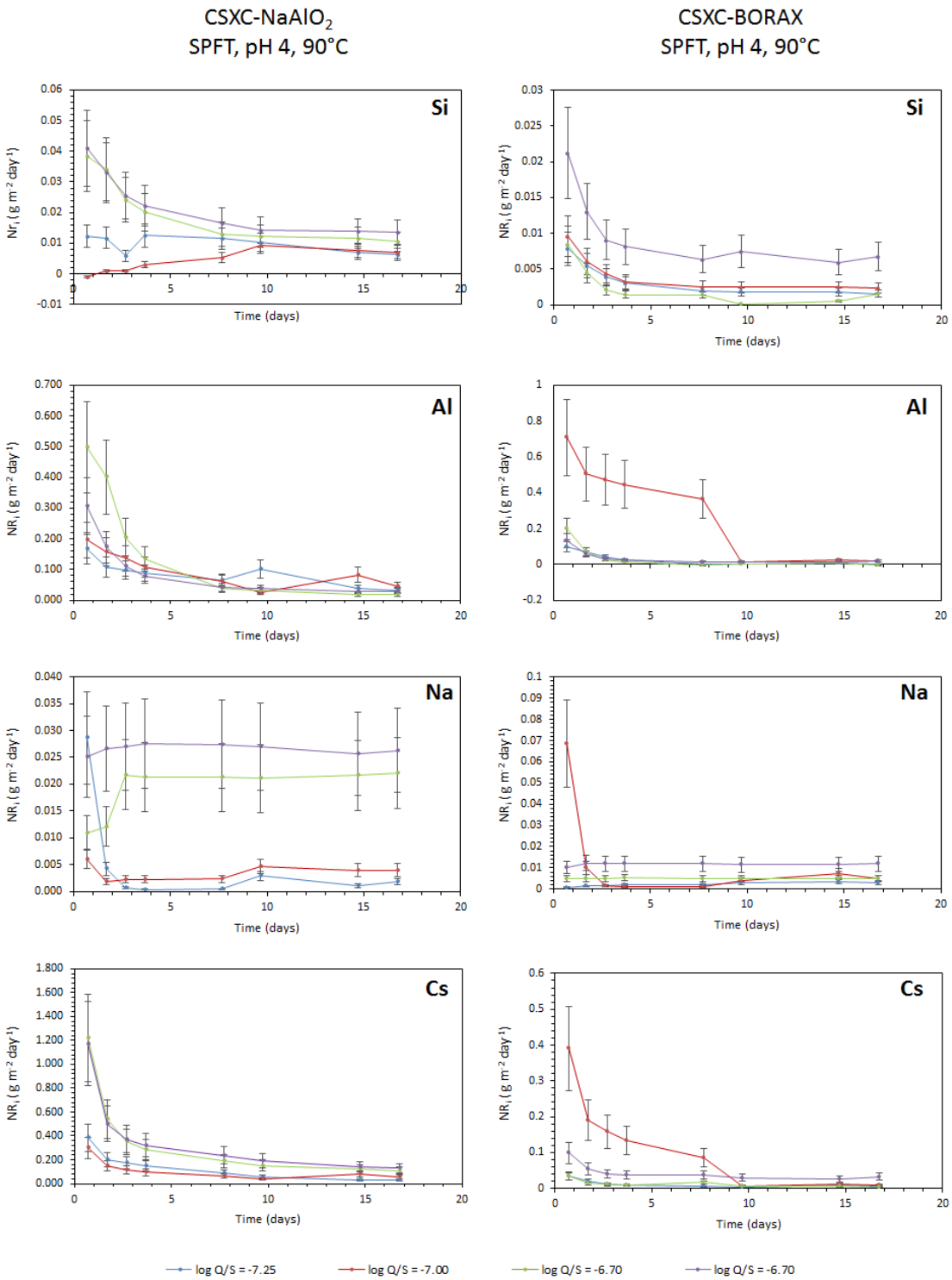

Figure 6.24A - Plots of normalised elemental loss rate for each element of interest with time for CSXC-$NaAlO_2$ and CSXC-BORAX from SPFT experiments at 90°C and pH 4 and with variations in the value of log(Q/S).

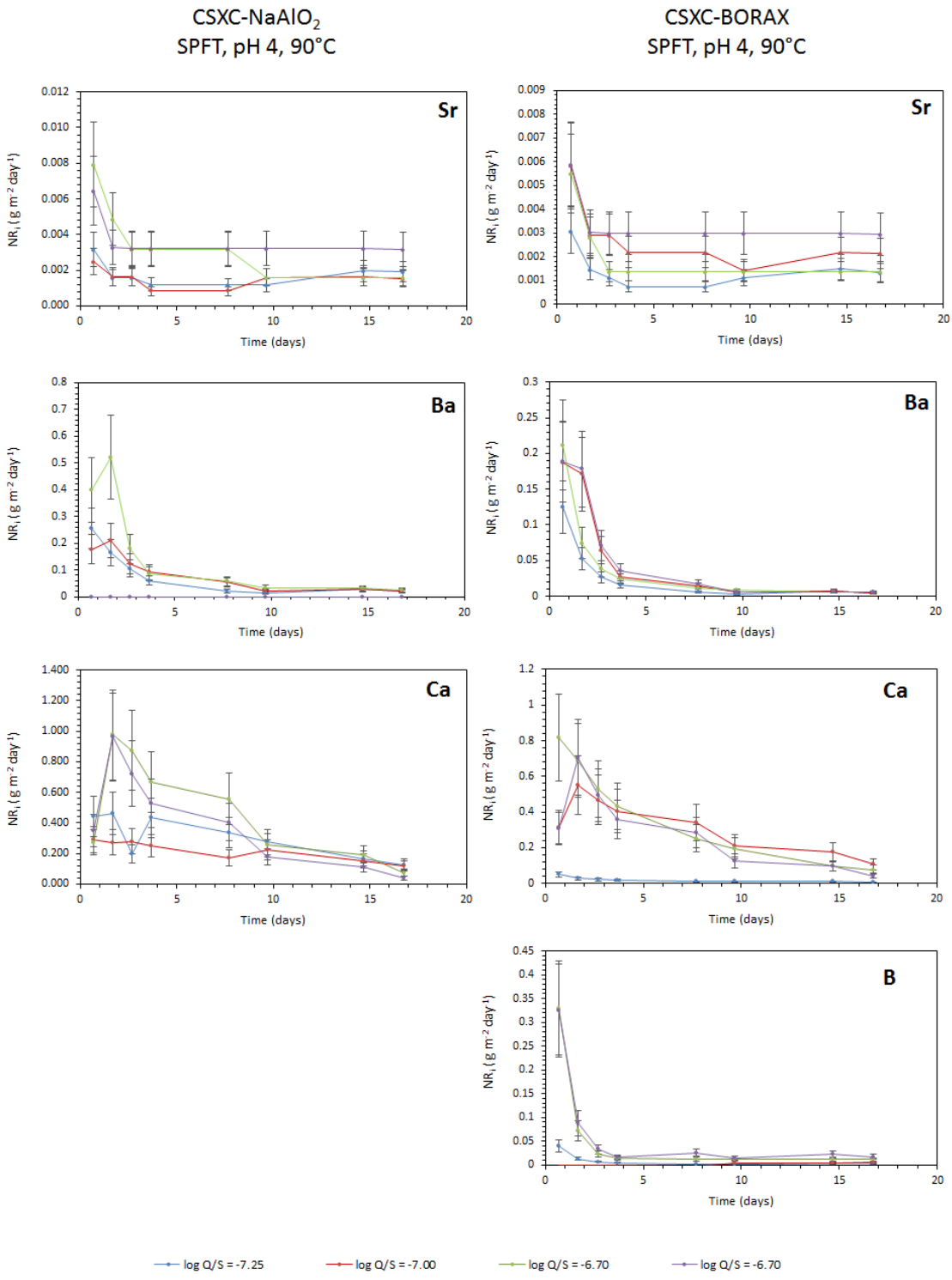

Figure 6.24B- Plots of normalised elemental loss rate for each element of interest with time for CSXC-$NaAlO_2$ and CSXC-BORAX from SPFT experiments at 90°C and pH 4 and with variations in the value of log(Q/S).

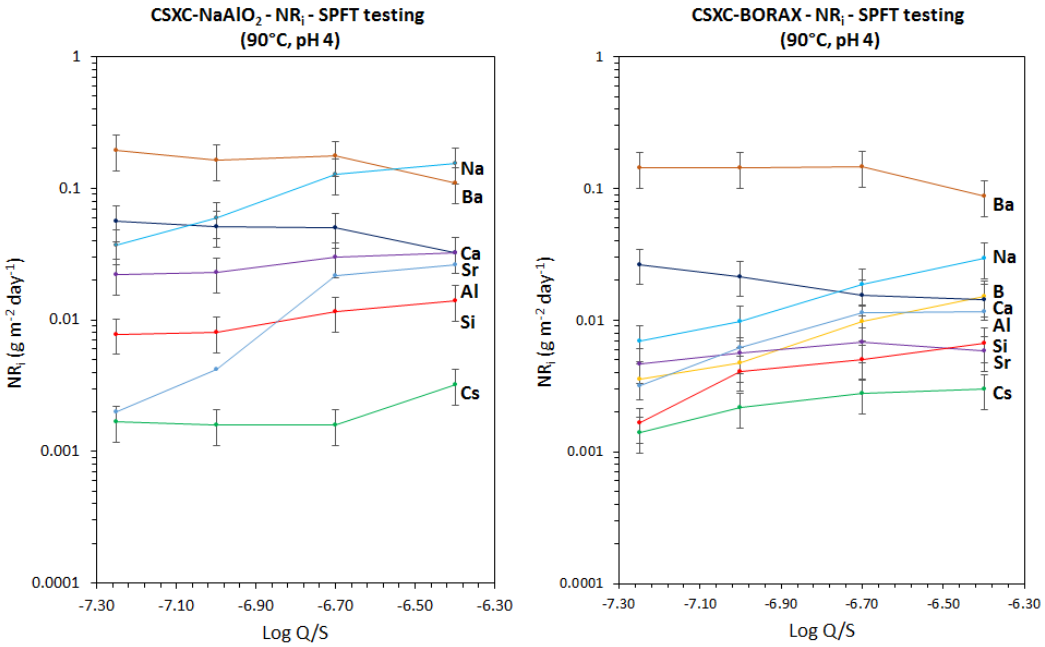

Figure 6.25 - Plots of forward normalised elemental loss rate with variation in the value of log(Q/S)for each element of interest for CSXC-$NaAlO_2$ and CSXC-BORAX from SPFT experiments at 90°C and pH 4.

Based on the low solution concentrations obtained, examination of the available literature and lack of any clearly observable trend suggesting otherwise, it was decided these experiments were likely to be in the forward rate regime. For comparison with previous studies and to allow ready analysis of all elements using ICP-MS, it was determined that the log(Q/S) of -7.0 provided the best overall solution for further testing on the effects of pH and temperature on the dissolution behaviour of these glasses.

Variations to Solution pH and Temperatures

Experiments were performed with alterations made to the pH and temperature of the test solution. These experiments provide an insight into the behaviour of the dissolution mechanism and more information for comparative assessment of the two compositions. It was intended that this selection of data may be used to determine the thermodynamic parameters for the dissolution of the vitreous phases in CSXC-$NaAlO_2$ and CSXC-BORAX, including the activation energy for aqueous dissolution.

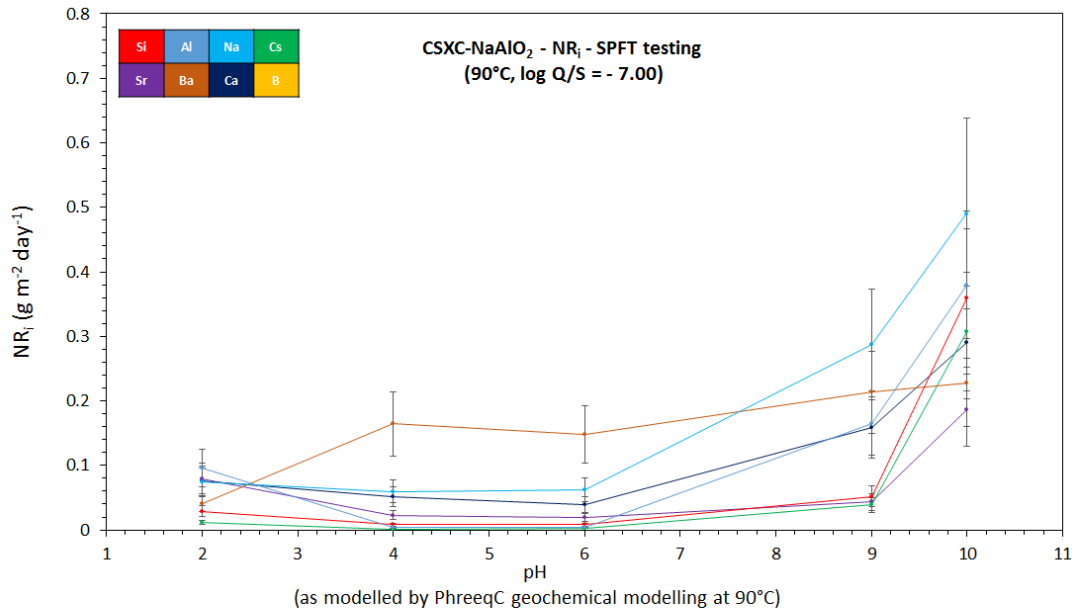

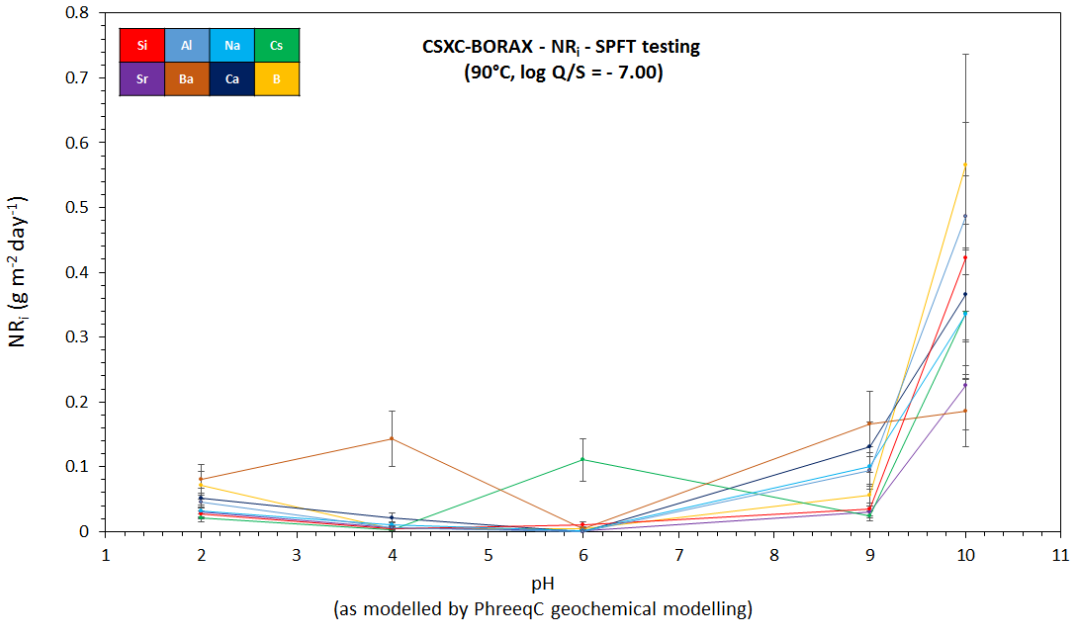

Figure 6.26 - Plots of forward normalised elemental loss rate with variations in solution pH for each element of interest for CSXC-$NaAlO_2$ and CSXC-BORAX from SPFT experiments at 90°C and log(Q/S) = -7.0.

Figure 6.26 contains plots of forward NR_i against pH from SPFT experiments of both CSXC-$NaAlO_2$ and CSXC-BORAX at 90°C where log(Q/S) = -7.0. This figure shows that both compositions have a similar relationship to pH for the release of elements into solution. This involves a minimal release rate near neutral pH. The NR_i is increased by transitions into acidic or alkaline regimes. The greatest NR_i values are apparent when the experiment is performed under highly alkaline conditions. The exception to this is for NR_{Ba} which does not follow this set trend and where behaviour is not comparable between the two tested compositions. In

the case of NR_{Cs} a large spike in seen at pH 6 in the CSXC-BORAX which also does not fit the trend described above. However all other data points for Cs are considered to behave as described above.

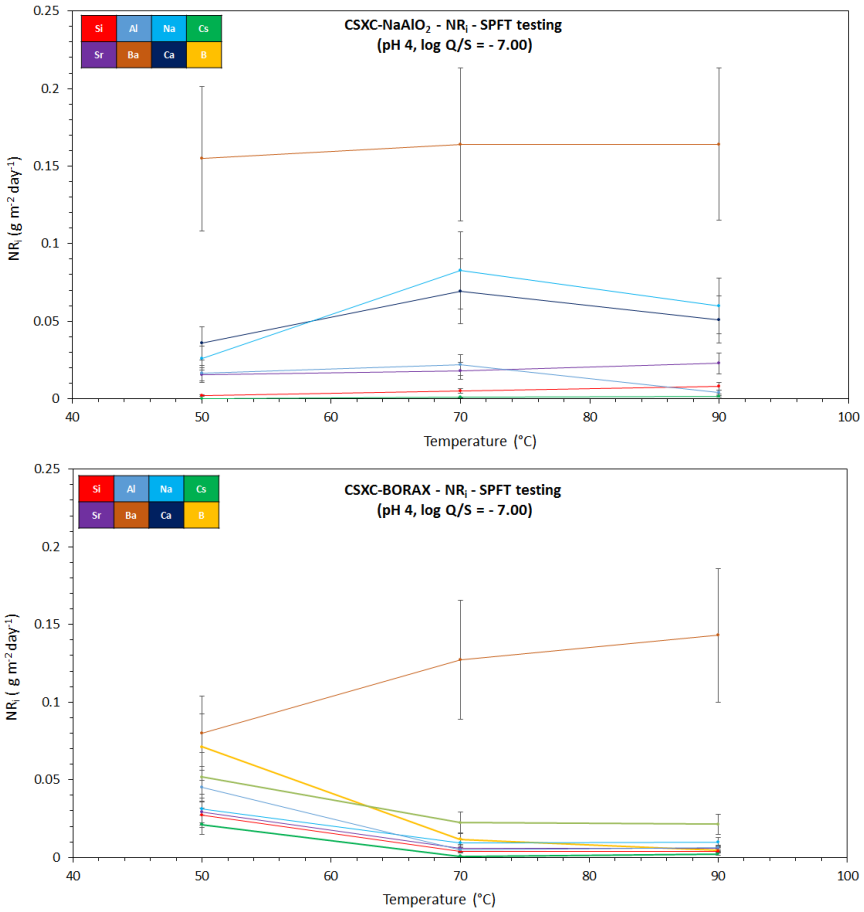

Figure 6.27 - Plots of forward normalised elemental loss rate with variations in temperature for each element of interest for CSXC-$NaAlO_2$ and CSXC-BORAX from SPFT experiments at pH 4 and log(Q/S)= -7.0

Figure 6.27 contains plots of forward NR_i against temperature from SPFT experiments of both CSXC-$NaAlO_2$ and CSXC-BORAX at pH 4 and with a log(Q/S) value of -7.0. The results of this experiment broadly show that no trend is observable in the case of temperature alterations. For CSXC-$NaAlO_2$ the values of forward NR_i increase with increasing temperature. However, this is not true of Na, Ca and Sr which all provided a lower NR_i at 90 °C than was observed at 70 °C. The results for CSXC-BORAX show the highest release is obtained at 50 °C and is approximately an order of magnitude greater than the results obtained at 70 °C and 90 °C. The forward NR_i increases for every element going from 70 °C to 90 °C.

	log(Q/S)	Temperature (°C)	pH	Forward Normalised Elemental Loss Rate (g m^{-2} day^{-1})							
				Si	*Al*	*Na*	*Cs*	*Sr*	*Ba*	*Ca*	*B*
CSXC-$NaAlO_2$	-7.00	90	2.00	2.91×10^{-2}	9.64×10^{-2}	7.40×10^{-2}	1.18×10^{-2}	7.94×10^{-2}	4.12×10^{-2}	7.64×10^{-2}	-
	-7.00	90	4.00	8.04×10^{-3}	4.23×10^{-3}	5.96×10^{-2}	1.59×10^{-3}	2.27×10^{-2}	1.64×10^{-1}	5.10×10^{-2}	-
	-7.00	90	6.00	7.81×10^{-3}	3.51×10^{-3}	6.24×10^{-2}	2.71×10^{-3}	1.94×10^{-2}	1.48×10^{-1}	3.92×10^{-2}	-
	-7.00	90	9.00	5.20×10^{-2}	1.65×10^{-1}	2.88×10^{-1}	3.84×10^{-3}	4.33×10^{-2}	2.13×10^{-1}	1.59×10^{-1}	-
	-7.00	90	10.00	3.59×10^{-1}	3.80×10^{-1}	4.90×10^{-1}	3.07×10^{-1}	1.86×10^{-1}	2.28×10^{-1}	2.91×10^{-1}	-
	-7.25	90	4.00	7.80×10^{-3}	1.98×10^{-3}	3.72×10^{-2}	1.68×10^{-3}	2.20×10^{-2}	1.94×10^{-1}	5.63×10^{-2}	-
	-7.00	90	4.00	8.04×10^{-3}	4.23×10^{-3}	5.96×10^{-2}	1.59×10^{-3}	2.27×10^{-2}	1.64×10^{-1}	5.10×10^{-2}	-
	-6.70	90	4.00	1.15×10^{-2}	2.16×10^{-2}	1.27×10^{-1}	1.59×10^{-3}	2.97×10^{-2}	1.75×10^{-1}	4.97×10^{-2}	-
	-6.40	90	4.00	1.40×10^{-2}	2.63×10^{-2}	1.55×10^{-1}	3.21×10^{-3}	3.23×10^{-2}	1.09×10^{-1}	3.23×10^{-2}	-
	-7.00	50	4.00	1.89×10^{-3}	1.66×10^{-2}	2.60×10^{-2}	0.00E+00	1.52×10^{-2}	1.5×10^{-1}	3.57×10^{-2}	-
	-7.00	70	4.00	5.01×10^{-3}	2.17×10^{-2}	8.29×10^{-2}	7.77×10^{-4}	1.79×10^{-2}	1.64×10^{-1}	6.93×10^{-2}	-
	-7.00	90	4.00	8.04×10^{-3}	4.23×10^{-3}	5.96×10^{-2}	1.59×10^{-3}	2.27×10^{-2}	1.64×10^{-1}	5.10×10^{-2}	-
CSXC-BORAX	-7.00	90	2.00	2.74×10^{-2}	4.52×10^{-2}	3.15×10^{-2}	2.11×10^{-2}	2.95×10^{-2}	8.00×10^{-2}	5.18×10^{-2}	7.11×10^{-2}
	-7.00	90	4.00	4.10×10^{-3}	6.18×10^{-3}	9.87×10^{-3}	2.16×10^{-3}	5.61×10^{-3}	1.43×10^{-1}	2.15×10^{-2}	4.76×10^{-3}
	-7.00	90	6.00	1.10×10^{-2}	-	1.74×10^{-3}	1.10×10^{-1}	1.86×10^{-3}	3.49×10^{-3}	-	4.77×10^{-3}
	-7.00	90	9.00	3.42×10^{-2}	9.36×10^{-2}	1.00×10^{-1}	2.44×10^{-2}	2.99×10^{-2}	1.66×10^{-1}	1.31×10^{-1}	5.60×10^{-2}
	-7.00	90	10.00	4.22×10^{-1}	4.86×10^{-1}	3.35×10^{-1}	3.37×10^{-1}	2.25×10^{-1}	1.86×10^{-1}	3.65×10^{-1}	5.66×10^{-1}
	-7.25	90	4.00	1.65×10^{-3}	3.15×10^{-3}	6.92×10^{-3}	1.40×10^{-3}	4.68×10^{-3}	1.43×10^{-1}	2.65×10^{-2}	3.57×10^{-3}
	-7.00	90	4.00	4.10×10^{-3}	6.18×10^{-3}	9.87×10^{-3}	2.16×10^{-3}	5.61×10^{-3}	1.43×10^{-1}	2.15×10^{-2}	4.76×10^{-3}
	-6.70	90	4.00	4.99×10^{-3}	1.13×10^{-2}	1.86×10^{-2}	2.77×10^{-3}	6.76×10^{-3}	1.46×10^{-1}	1.55×10^{-2}	9.87×10^{-3}
	-6.40	90	4.00	6.73×10^{-3}	1.16×10^{-2}	2.94×10^{-2}	2.98×10^{-3}	5.81×10^{-3}	8.74×10^{-2}	1.43×10^{-2}	1.52×10^{-2}
	-7.00	50	4.00	2.74×10^{-2}	4.52×10^{-2}	3.15×10^{-2}	2.11×10^{-2}	2.95×10^{-2}	8.00×10^{-2}	5.18×10^{-2}	7.11×10^{-2}
	-7.00	70	4.00	3.75×10^{-3}	4.96×10^{-3}	9.15×10^{-3}	7.21×10^{-4}	5.63×10^{-3}	1.27×10^{-1}	2.25×10^{-2}	1.18×10^{-2}
	-7.00	90	4.00	4.10×10^{-3}	6.18×10^{-3}	9.87×10^{-3}	2.16×10^{-4}	5.61×10^{-3}	1.43×10^{-1}	2.15×10^{-2}	4.76×10^{-3}

Table 6.6 - Forward NR_i values obtained from SPFT experiments of CSXC-$NaAlO_2$ and CSXC-BORAX with variations in temperature, log(Q/S) and pH.

The absence of the expected trend in relation to temperature precluded the use of any data for the analysis of thermodynamic properties, as it was clear that either significant other effects are dominating the behaviour. This is likely to occur as a result of the exceptionally low rates of dissolution form found in these wasteforms, which in turn create experimental errors in the low temperature experiments too great to perform any valid analysis.

6.4.4 - VSI Experiments

To determine how the physical retreat of the sample surface can be compared with the solution based experimental data, an experiment was developed utilising the SPFT set up, with monolithic samples and VSI analysis of the surface. It was hoped this novel technique would also help to develop a technique capable of further elucidating solution based dissolution data for phase separated and multicomponent wasteforms using nano-meter resolution measurements.

To perform this experiment a polished, monolithic sample of CSXC-BORAX was characterised using SEM-BSE and SEM-EDX, a gold coat was applied to act as reference for the physical retreat rate of the sample surface and VSI measurements made to provide knowledge of the initial reference heights. After 40 days of dissolution in SPFT conditions, the sample was removed. The SPFT conditions were set to 90°C with pH 4 solution. This dissolution was followed by examination using VSI, optical microscopy and SEM-BSE/EDX analysis to determine where significant changes had occurred and to quantify the physical rate of retreat. It was intended that a study of both compositions was to be performed, however, as a result of difficulties with sample preparation and time constraints, only the CSXC-BORAX could be investigated using this technique.

Figure 6.28 consists of images collected using VSI of the samples surface in the region of the gold coating before and after dissolution. A differential map and a plot illustrating the depth of retreat are provided in Figure 6.28 c). It can be seen from the differential mapping that the retreat observed in this region is in the order of nanometres. No retreat of the glass surface was measured which exceeded 40 nm. The retreat measured was not global and is centred on imperfections, scratches and surface features which previously existed on the sample surface. This provides a maximum physical rate of retreat of approximately 1 nm day^{-1}.

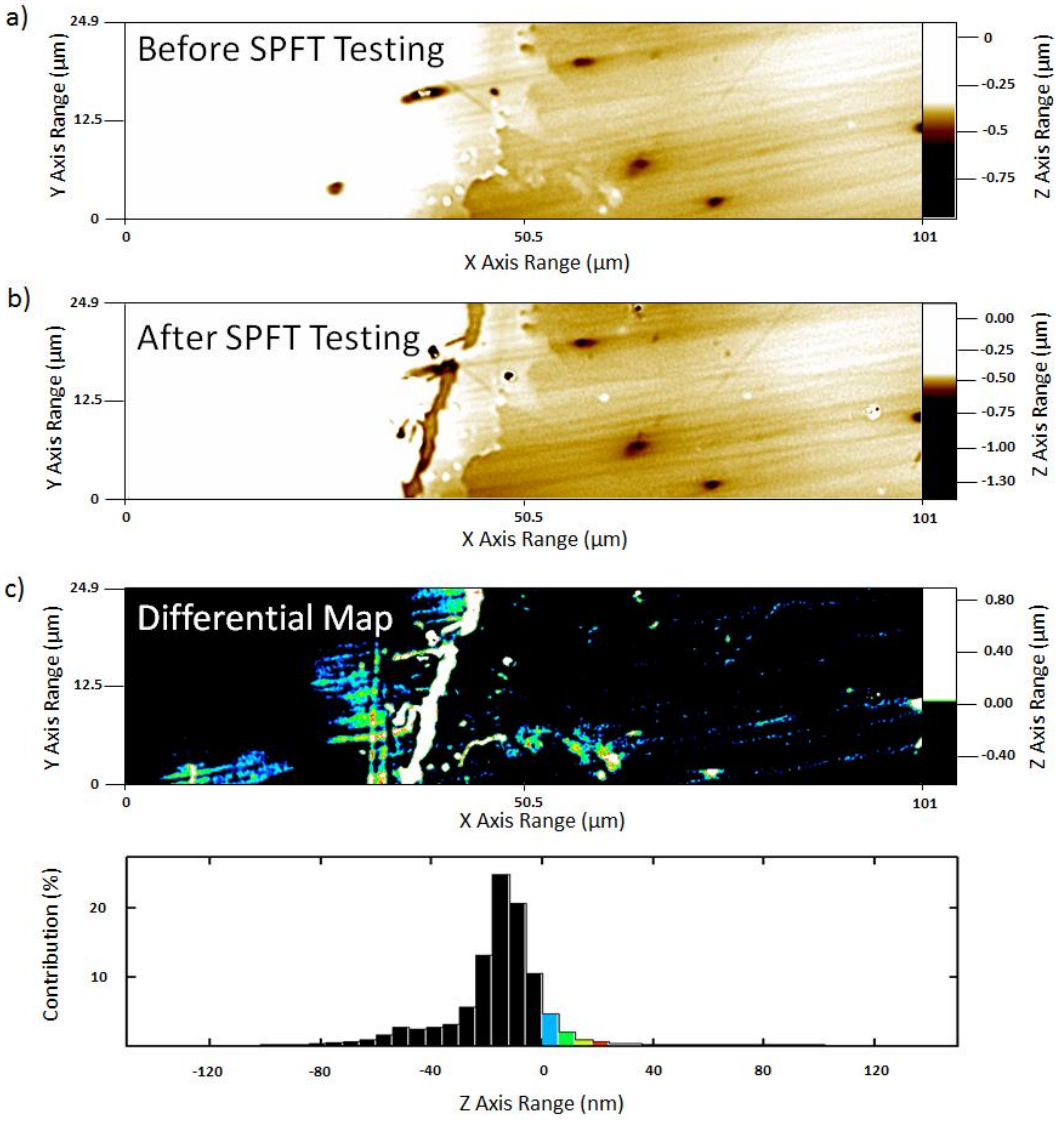

Figure 6.28 – VSI imaging of sample surface in the region of the applied gold mask a) before and b) after dissolution experiments and c) a differential image and graph quantifying the observed retreat in this region.

Figure 6.29 presents a comparison of two regions identified as Region A and Region B imaged using VSI both before and after dissolution. The highlighted areas have been quantified to determine the difference in height which exists between the gold reference coat and the sample surface in the areas outlined in white. This allows for the quantification of the surface retreat as the gold reference should not alter significantly. Region A correlated well with the data presented in Figure 6.28 and had a retreat of 44 nm. Region B however showed a very different behaviour with a surface retreat of 1.22 µm, almost 30 x that measured in Region A. This shows the same sample has very different rates of physical retreat depending upon region of study, despite being subjected to identical conditions during testing.

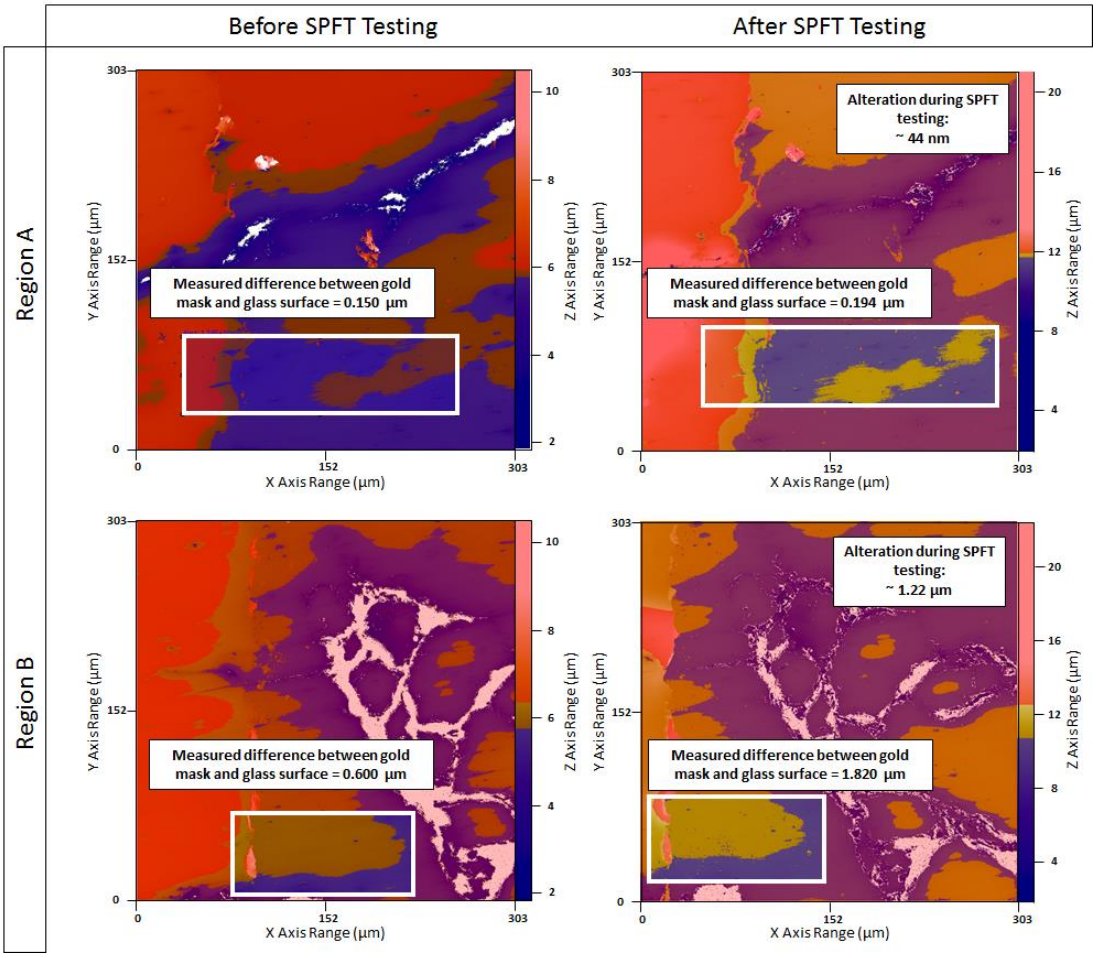

Figure 6.29 – Quantitative VSI analysis of the height variation between two regions of the CSXC-BORAX surface in relation to the gold mask before and after dissolution.

Figure 6.30 illustrates this phenomenon using a region of the sample measured in the absence of the gold coat. As it has been shown the surface retreat is negligible in some areas, yet over 1 µm in other regions, it was decided that a rough approximation could be used where the more stable surface acts as a qualitative reference point for the dissolution of the less stable regions. Figure 6.30 a) highlights a region of variation in the composition of the vitreous matrix previously described in Section 6.3.3 prior to dissolution. Figure 6.31 b) highlights the same region imaged by optical microscopy after dissolution. The differences in the composition of the glass regions have become visible using white light as a result of the dissolution process.

This examination of the sample surface using SEM-BSE shows that the differences between the physical rates of retreat, described in Figure 6.29 are based on the compositional variation in the glass matrix. Figure 6.30 c-f provide a comparative study of a region of Glass A within a region of Glass B. It is immediately clear that the retreat seen in Glass B is

significantly greater than is observed from Glass A. The difference between the physical retreat of Glass A and Glass B is approximately 1 µm. This value correlates well with the data previously presented in Figure 6.29. The line scan across the centre of the depression presented in Figure 6.30 d) also indicates that the depression is greatest in the centre of the region of Glass B and decreases as it gets closer to a region of Glass A.

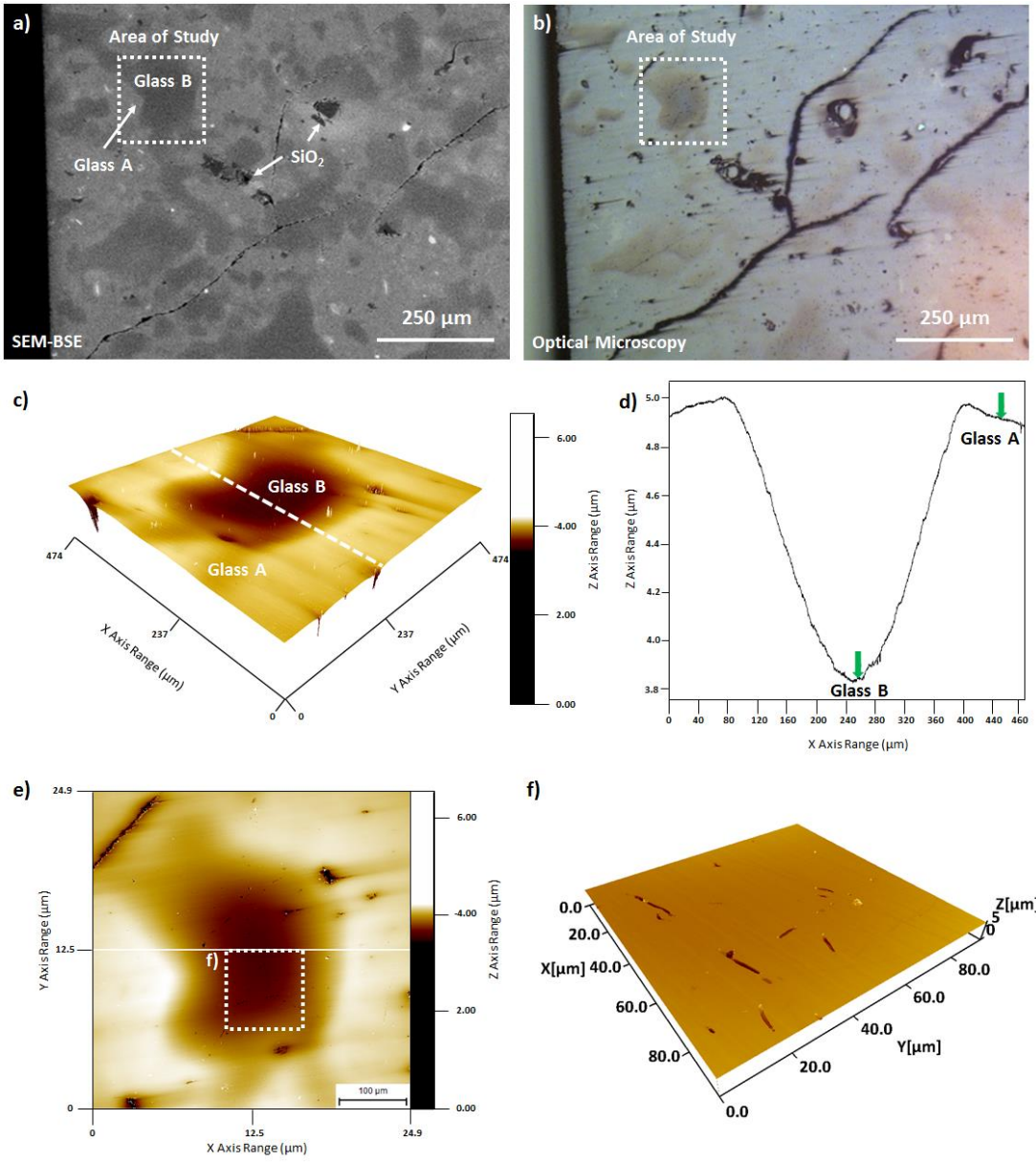

Figure 6.30 – a) SEM-BSE image of CSXC-BORAX surface prior to dissolution identifying a region of compositional variation in the vitreous matrix b) the same region imaged using optical microscopy after dissolution c-f) VSI imaging of the highlighted region providing a comparative assessment of the features of importance in this area.

Figures 6.30 e-f also highlight that a number of features are present in the depressed region of Glass B which are absent in Glass A. These features are up to 20 µm long and between 1-5 µm in width and depth. Two sets of features exist perpendicular to each other.

Figure 6.31 provides images investigating the dissolution behaviour of inclusions embedded within the glass. Figures 6.31 a-b provide a combination of SEM-BSE images, VSI images and a VSI line scan of the area of study before and after dissolution. It can be seen that little change has occurred at POI 1, but POI 2 has shown significant corrosion with selective dissolution of approximately 0.24 µm when compared to the surrounding region of glass. Figure 6.31 c-d provides a comparison of the corrosion features in POI 1 and POI 2 after dissolution. This shows the significance of the increased dissolution in POI 2 when compared with POI 1. Figures 6. 31 e-f illustrate the regions morphology as imaged using SEM-BSE after dissolution and correlates the increased corrosion features in POI 2 with compositional variation provided by high contrast SEM-BSE imaging. Due to the lack of compositional resolution observed via SEM-BSE no EDX measurement was made on POI 2 prior to dissolution.

Figure 6.32 provides SEM-BSE images of the sample surface, both before and after dissolution. This provides a qualitative assessment of significant effects occurring which were not imaged utilising VSI, while providing the ability to qualitatively relate this behaviour to composition. Three regions of interest have been highlighted to illustrate the major effects. In POI 1 large pits are created in the presence of cracks in the sample. These pits are in the order of tens of microns diameter. It is also clear from the compositional variation at the right hand side of POI 1, that the presence of Glass B results in surface features similar to those seen in Figure 6.30 f) and is likely to be a global feature relating to the composition of the Glass B. POI 2 shows complete or partial removal of a number of bright phases inclusions during dissolution. POI 3 highlights the complete or partial removal of several bright phase inclusions and the formation of a large pit within a region of Glass A composition.

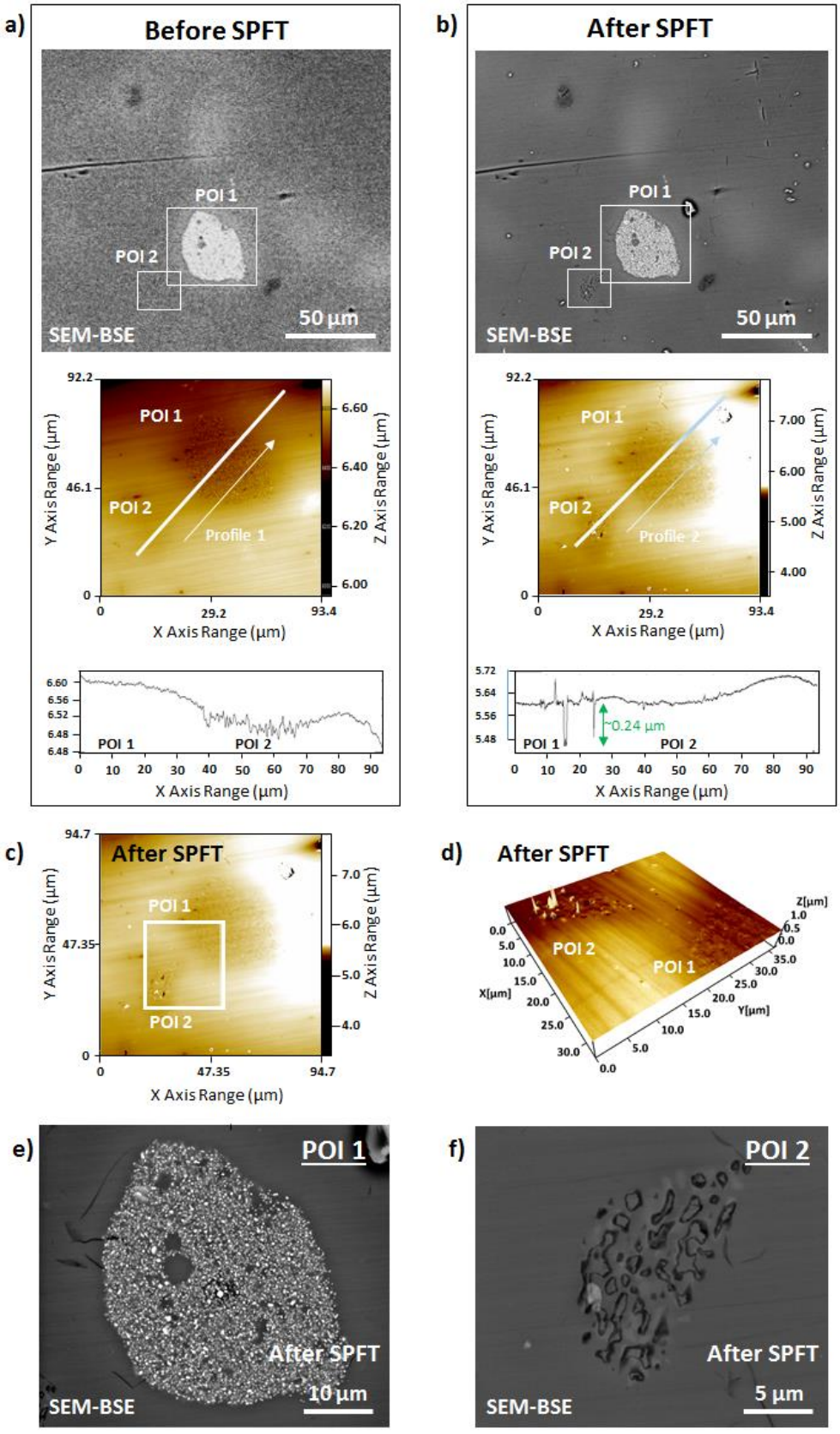

Figure 6.31 – a) SEM-BSE VSI imaging and plot of line scan through POI 1 and POI 2 before and b) after dissolution c-d) VSI imaging of POI 1 and POI 2 interface and SEM-BSE images taken after dissolution of e) POI 1 and f) POI 2.

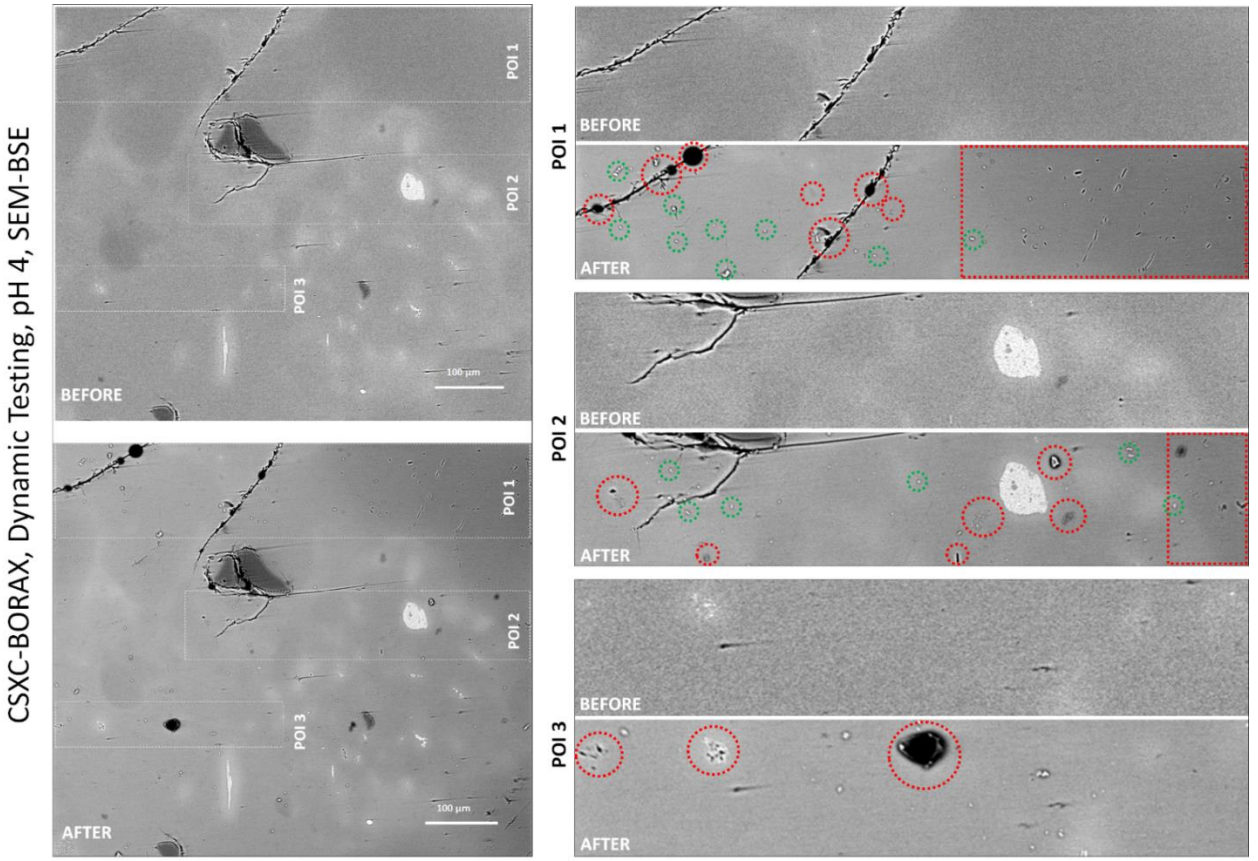

Figure 6.32 – SEM-BSE imaging of CSXC-BORAX before and after dissolution using the SPFT methodology with highlighted regions of interest. Features outlined in red indicate regions where a significant dissolution feature occurs.

6.4.5 - Discussion - Aqueous Durability

A wealth of data is available covering HLW glass wasteform dissolution. As a simplification, these HLW wasteforms can be described as being both homogeneous and well characterised. Thermally treated ILW glasses are likely to differ significantly from this ideal situation. Due to the expectations of high waste loadings, variable or poorly defined waste stream chemistry and less demanding disposal criteria, macroscopically phase separated wasteforms should be expected.

The series of experiments performed in the course of this investigation were designed to serve a dual purpose. Primarily, experiments were performed to determine if the wasteform products were likely to be suitable for disposal based on their aqueous dissolution properties. This can be readily performed using a comparison of the values of NL_i and NR_i, as obtained from PCT and MCC-1 experiments of the wastes, with data from the literature for HLW glass wasteforms and the cemented clinoptilolite materials.

The secondary purpose was to investigate how effective the standardised experiments methodologies are for the study of phase separated vitreous wasteforms. It was hoped to provide some insight into the validity of any such comparisons and of any anomalous results found from the solution based experiments.

Comparison of Wasteform Behaviour with those of Existing Vitreous Waste Materials

Prior to further discussion the nuances involved in this suite of durability experiments, a comparison of the data from these ILW wasteforms should be made with those from existing HLW glasses in order to illustrate the suitability of these materials for geological disposal. This analysis makes it clear that these materials should be considered exceptional matrices for the disposal of radioactive wastes.

The wasteforms produced during the course of this study provided chemical releases into solution which were comparable or significantly lower than those of glasses already in service or under consideration for radioactive waste immobilisation. As the radioactive inventory of these glasses is also significantly reduced they should readily qualify for use as ILW wasteforms on the basis of their aqueous durability.

Glass	PCT		MCC-1	SPFT
	NR_{Si} *18.2 MΩ water* *90 °C* *28 days testing* (g m^{-2} day^{-1})	**Total Cs Loss** *18.2 MΩ water* - - (wt %)	**NR_{Si}** *18.2 MΩ water* *90 °C* *28 days testing* (g m^{-2} day^{-1})	**NR_{Si}** *pH 9* *90 °C* *forward rate* (g m^{-2} day^{-1})
CSXC-$NaAlO_2$	6.8 x 10^{-4}	< 0.015	1.38 x 10^{-1}	3.42 x 10^{-2}
CSXC-BORAX	4.2 x 10^{-4}	< 0.025	1.10 x 10^{-1}	5.20 x 10^{-2}
MW25	2 x10^{-2} [233]	-	-	3.5 x 10^{-1}* [253]
SON68	5.7 x 10^{-3} [232]	-	-	3.0 x 10^{-1} [254]
Cement	-	5 – 65** [47]	-	-

Table 6.7 – Comparison of aqueous dissolution properties for CSXC-$NaAlO_2$ and CSXC-BORAX with HLW glasses and cements from the literature. *measured at 70 °C, **measured after 1 day at 20 °C.

Table 6.7 presents a list of results from aqueous durability testing of the HIPed clinoptilolite wasteforms produced in this study, against those of HLW glasses and cemented clinoptilolite. PCT experiments of the ILW glasses can be compared to the SON68 French base HLW glass composition tested using an identical methodology, the results of which are presented in Section 4. The CSXC-$NaAlO_2$ and CSXC-BORAX ILW wasteforms have an NR_{Si} after 28 days of 4.2 x 10^{-4} - 6.8 x 10^{-4} g m^{-2} day^{-1} respectively. This is approximately an order of magnitude lower than that observed for the SON68 base glass, which has a NR_{Si} at 28 days of 5.7 x 10^{-3} g m^{-2} day^{-1} [232]. The dissolution rate of the clinoptilolite glasses is also over an order of magnitude lower than that of the British MW25 HLW glass which has NR_{Si} at 28 days of ~2 x 10^{-2} g m^{-2} day^{-1} when tested under near identical experimental conditions [233].

These clinoptilolite based wasteforms also outperform HLW borosilicate glasses under non-saturated solution conditions. SPFT experiments on CSXC-$NaAlO_2$ and CSXC-BORAX at 90 °C and pH 9 gave NR_{Si} values of 3.42 x 10^{-2} – 5.20 x 10^{-2} g m^{-2} day^{-1}. This result is roughly comparable in the magnitude of release to that for British HLW magnox waste glasses, when testing is performed at the lower temperature of 70°C. These experiments show that the forward NR_{Si} was three orders of magnitude greater for existing HLW glasses, even when the testing of the clinoptilolite wasteforms was performed at a higher temperature [253]. Further comparison can be made with data presented on SON68 glasses which have a forward NR_{Si} almost an order of magnitude higher when tested under similar conditions, but using a pH 8 solution [254]. The SPFT experiments performed show that the clinoptilolite wasteforms compare favourably with

the high durability LD6-5412 glass, which is under investigation for the disposal of US LLW wastes. The forward NR_{Si} for both glasses as obtained by SPFT experiments at 90 °C and pH 6, was roughly 2 $x10^{-2}$ g m^{-2} day^{-1} [200, 201].

Comparison of the NL_{Cs} with the US reference HLW borosilicate glasses can be made for the MCC-1 experiments performed. The NR_{Cs} values measured for CSXC-$NaAlO_2$ and CSXC-BORAX were 6.93 x 10^{-2} – 6.8.71 x 10^{-2} g m^{-2} day^{-1} after 28 days. This compares very favourably with that obtained by identical testing of the US reference HLW glass which produced a NR_{Cs} of 1.54 g m^{-2} day^{-1} [255]. Cs immobilisation should be considered the most important attribute of any wasteform for clinoptilolite, due to its mobility in ground waters, the presence of the long lived ^{135}Cs isotope and the minimal degree of interaction which occurs between caesium and the potential backfill materials.

The above reported results all illustrate that the wasteforms produced perform exceptionally with respect to their aqueous durability providing levels of elemental retention comparable or superior to that of glasses already utilised for the immobilisation of HLW. A more dramatic analysis can be made by comparison of the releases of Cs from CSXC-$NaAlO_2$ and CSXC-BORAX with those from the baseline cementation methodology.

Static durability experimental data has previously been reported for the immobilisation clinoptilolite within a variety of cement blends [47]. In this work it was reported that 5-65 % of the total Cs inventory is lost to solution after just three days testing at room temperature. It is possible to compare this experimental data with that obtained by PCT experiments of CSXC-$NaAlO_2$ and CSXC-BORAX using Equation 6.1;

$$\text{Total Mass Loss Cs } (\%) = \left(\frac{\bar{X}([Cs]_i \times V_i{}^{H_2O})}{\bar{X}(m_i{}^{WF} \times wt_{Cs}{}^{WF})}\right) \qquad \textbf{Equation 6.1}$$

Where $[Cs]_i$ is the concentration of Cs in sample i at a given time (g l^{-1}), V_i^{H2O} is the volume of leachate in the vessel for sample i at a given time (l), m_i^{WF} is the mass of wasteform used in sample i and wf_{Cs}^{WF} is the weight fraction of Cs in the wasteform.

This calculation shows that < 0.025 % and < 0.015 % of the total Cs inventory had been lost to solution during the PCT type experiments of CSXC-$NaAlO_2$ and CSXC-BORAX respectively. This indicates that HIPing clinoptilolite provides release rates between 200 - 4300 times lower for Cs than cemented wasteforms. As the experiments on the CSXC-$NaAlO_2$ and CSXC-BORAX were performed under significantly more aggressive experimental conditions and for much longer

time frames to simply allow the measurement of loss, this difference should be expected to be increased by further orders of magnitude if comparable experimental methodologies had been utilised.

Sr Release

Although the values relating to Cs loss are extremely favourable for the wasteform produced, Sr has a proportionally higher release, with PCT experiments producing a NL_{Sr} of 0.16 – 0.48 g m^{-2} after 28 days. Although this rate is not considered likely to prohibit disposal of such a waste, Sr exhibits the highest NL_i in the wasteform. This result was predicted in Section 6.3.5 as a result of the presence of Sr in the mixed alkali sulphate phase. This phase has been shown to be preferentially removed from the waste, and as such, would increase the NR_{Sr} values.

The retention of Sr in these wasteform was shown to be effective from the SPFT data, even with the complete removal of the sulphate phase. By multiplying the measured concentration of Sr in solution by the volume of eluent passing through the vessel between sampling points the total mass of Sr realised into solution during the course of testing can be estimated by a summation of this data. It was seen < 0.2% of the samples Sr inventory was released to solution during the experiment in both CSXC-$NaAlO_2$ and CSXC-BORAX.

Comparison of CSXC-$NaAlO_2$ and CSXC-BORAX

Although a small degree of variation was noted during the course of these experiments it was determined that the two wasteforms are of comparable quality. Generally higher release rates were obtained from CSXC-BORAX, with the exception of Na and Al releases, where significantly greater NL_i and NR_i values were obtained from CSXC-$NaAlO_2$. It is hypothesised that this increased release of Na and Al is a result of the presence of residual $NaAlO_2$ in the final waste stream. This could be a result of the incomplete dissolution or precipitation of $NaAlO_2$ in the regions of Glass B during cooling. This would produce a soluble source of both Na and Al which would dramatically skew the NL_i values by comparison with CSXC-BORAX. Some evidence suggesting the presence of $NaAlO_2$ in CSXC-$NaAlO_2$ as discussed in Section 6.3.5. As these regions are well encapsulated within the vitreous waste and as no radionuclide concentration is observed in these regions, increased release, although none ideal, is not deemed to be restrictive in the use of these wasteforms.

Applicability of Experiments and Comparison to Behaviour Expected from Homogeneous Glasses

As most data that exists concerning the aqueous durability of wasteforms is based upon the approximation of a homogeneous glass, some comparison of how these grossly phase separated

materials behave during experiments should be made. This allows us to determine the applicability of the experiments to the comparative analysis given above. The general behaviour of 'standard' vitreous waste materials using these experimental methodologies has been discussed in Chapters 2-6. At a first approximation the behaviour for the release of the elements of interest from CSXC-$NaAlO_2$ and CSXC-BORAX are roughly comparable to those expected from a homogeneous glass. The general trends observed for both wasteforms produced are as follows;

PCT Experiments: The NL_i is initially high, followed by relatively small increases or decreases in the NL_i indicating that a slower rate of release has been obtained, or in some scenarios, that some precipitation is initiated from saturated solution.

***MCC-1 Experiments*:** NL_i values increase at a relatively constant rate throughout the experiments where no evidence of alteration layers has been detected. The NL_i values obtained are significantly higher than those seen using powder dissolution experimental methodologies.

SPFT Experiments: The measured concentrations and the related NR_i are high at the start of experiments which relates to the removal of fines and areas of preferential attack [254]. A forward steady rate was obtained after approximately 10 vessel volumes had passed through the reaction vessel. This forward rate is identified as the forward rate of reaction for the glass and provides the maximum rate at which the glass can be considered to retreat over the course of prolonged periods under given solution conditions.

MCC-1: Although both CSXC-$NaAlO_2$ and CSXC-BORAX generally showed the behaviours described above, several variations from this behaviour were noted. Figure 6.14 shows that although the expected trend is generally observed during MCC-1 experiments, the experiments show a pronounced degree of scatter between sampling points. Although likely to be comparable the results appear to be significantly more prone to error and deviation than is normally evident for this type of experiments. This can be explained by the heterogeneous nature of the systems under investigation and the small SA/V values.

Assuming that different phases have different dissolution rates, as has been shown for the wasteforms studied and is discussed further below, samples with a higher proportion of the lower durability phases will show an increased dissolution. When experiments utilise powdered samples the sample surface tested is more likely to be representative of the overall mixture of phases. In monolithic experiments the surface area being investigated is significantly lower and

the proportional variation in the identity of phases in contact with the solution will have a much larger effect on the observed dissolution. As the MCC-1 experiments compares different monoliths at each sampling, as opposed to the same monolith over a period of time, this variation in solution contacting composition can be expected to be the primary cause of error within monolithic experiments on phase separated wastes.

It can therefore be concluded that any experiments on monolithic, phase separated samples should periodically sample the solution from several individual, well characterised specimens. The SA/V should be corrected appropriately for each sampling and an average of the different specimens collected. This would likely provide more accurate profiles for NL_i against time while also allowing comparison of the variations based on the surface area of each phase in contact with solution.

SPFT: These experiments showed the expected behaviour for most elements tested although it was clear that phase separation had some effect on the results observed. The release of alkali earth elements took longer to reach their forward NR_i than was observed for elements which were primarily associated with the glass matrix. This is clearly displayed in Figure 6.22. It is proposed that this was a result of the presence of the more soluble alkali earth sulphate phase in the wasteform, as is shown in Figure 6.16. The presence of this phase should be expected to vastly increase the NL_i values for the sample. The increased solubility of these phases by comparison to glasses would in turn swamp the releases which relate to the forward NR_i from the glass.

Therefore, to adequately qualify the release from the glass phase where the majority of each element resides, experiments must be run for a sufficient period to completely remove this sulphate phase from the material. This was impractical in this series of experiments due to limitations in the availability of equipment. As a result, all data discussed below concerning alkali earth elements should not be considered to be the true forward NR_i for these elements. However, it is considered that this relates to a maximum possible forward rate, and as such is useful in providing a worst case simplification.

Comparison of Experiments Methodologies

PCT vs SPFT: As discussed above these phase separated materials have been shown to behave similarly to homogeneous glasses, therefore, it can reasonably be assumed that the experimental methodologies are valid. Comparison of these experimental methodologies can provide insight on the dissolution process. The most appropriate comparison possible is to compare results of PCT type experiments and SPFT experiments.

Both the PCT and SPFT experiments show that highest loss rate occurs upon initial contact of the wasteform with solution, this high rate then rapidly drops off as the experiments progresses. The NR_i data as provided in Table 6.5 and 6.6 for PCT and SPFT experiments cannot be directly compared. As discussed in Section 2.2.3, glass dissolution under static conditions passes through a number of rates regimes, these rate regimes are dependent on the solution affinity and presence of alteration layers. Although the initial rate is high in PCT experiments, this rate rapidly drops leaving a low residual rate. The PCT data presented in Table 6.5 provides a cumulative rate over time which is inclusive of this initial period of rapid release. In order to provide a meaningful residual NR_i from PCT data, to compare with the forward rate obtained from SPFT, equation 6.2 should be used. This provides a better estimate of the true residual rate from PCT tests with use of a short 28 day duration, by eliminating the contribution from the initial rapid release.

$$\mathrm{NR_{i(residual-PCT)}} = \frac{\mathrm{NL_{i(28\ days-PCT)}} - \mathrm{NL_{i(3\ days-PCT)}}}{25} \qquad \textbf{Equation 6.2}$$

Where $NR_{i(residual\text{-}PCT)}$ is the residual rate which may be considered roughly comparable to the forward rate obtained for SPFT experiments. A comparison of the $NR_{i(residual\text{-}PCT)}$ against the forward NR_i from SPFT for each glass is provided in Table 6.8. This equation is best applied for Cs as it is present in both glass wasteforms, does not provide a negative $NR_{i(residual\text{-}PCT)}$ (indicating alteration layer formation or precipitation from solution) and is the element of primary interest to qualify these wasteforms for disposal.

$NR_{Cs(residual\text{-}PCT)}$ was calculated to be 8.45 x 10^{-5} and 3.72 x 10^{-4} g m^{-2} day^{-1} for CSXC-$NaAlO_2$ and CSXC-BORAX respectively. The forward NR_{Cs} as obtained by SPFT experiments at pH 9 (comparable with the self-buffered solution pH) was approximately two to three orders of magnitude higher in each experiment at 3.84 x 10^{-2} and 1.01 x 10^{-1} for CSXC-$NaAlO_2$ and CSXC-BORAX respectively. The trend remains the same for other elements where non-negative rates are not observed.

This result provides evidence that both experiments are examining the rate regimes they were intended to and are applicable to the study of phase separated glasses, on the assumption they behave homogeneously. As an approximation this $NR_{i(residual\text{-}PCT)}$ should be considered the lowest possible rate of release in repository conditions at pH 9, whereas this forward NR_i should be considered the highest possible release from these wasteforms at pH 9.

Element	CSXC-$NaAlO_2$		CSXC-BORAX	
	Residual NR_i ($g\ m^{-2}\ day^{-1}$)	Forward NR_i ($g\ m^{-2}\ day^{-1}$)	Residual NR_i ($g\ m^{-2}\ day^{-1}$)	Forward NR_i ($g\ m^{-2}\ day^{-1}$)
Si	-4.81×10^{-5}	5.20×10^{-2}	-1.76×10^{-4}	3.42×10^{-2}
Al	-1.26×10^{-5}	1.65×10^{-1}	-3.46×10^{-4}	9.36×10^{-2}
Na	2.37×10^{-3}	2.88×10^{-1}	2.75×10^{-4}	1.00×10^{-1}
Cs	8.53×10^{-5}	3.84×10^{-2}	3.72×10^{-4}	2.44×10^{-2}
Sr	-9.79×10^{-4}	4.33×10^{-2}	5.28×10^{-4}	2.99×10^{-2}
Ba	-5.32×10^{-4}	2.13×10^{-1}	-1.01×10^{-3}	1.66×10^{-1}
Ca	1.17×10^{-4}	1.59×10^{-1}	-5.9×10^{-4}	1.31×10^{-1}
B	-	-	-5.6×10^{-5}	5.60×10^{-2}

Table 6.8 – Comparison of the residual normalised elemental loss rate as obtained from PCT experiments at 90 °C between samplings at 3 and 28 days in 18.2 MΩ water, which buffered to approximately pH 9, and the forward elemental loss rate, as calculated from the residual rate of SPFT experiments at 90°C with a solution of pH 9 (when modelled at 90°C). Negative values suggests precipitation of an element is occurring. Errors are estimated at 10 % and 30% of stated values for residual NR_i and forward NR_i respectively.

Powder vs monolith experiments: More care should be taken when producing a comparison of the MCC-1 experiments with the powder based experiments due to the inherent errors discussed above and the differences in pH attained during the testing duration. However, some explanation of the much higher NL_i obtained from the monolithic experiments than by SPFT experiments are required. This increased rate would imply that what has been identified as the forward rate from SPFT is not in fact not the highest rate of dissolution attainable for these glass compositions.

As the solution remained unsaturated and no alteration products were formed on the monolithic surface during MCC-1 experiments, it should be assumed that the release values would be higher than for PCT experiments, however, these should not exceed the forward rate obtained as obtained by SPFT. Overly high values of NR_i are a common feature of MCC-1 type experiments and have been attributed to sample surface preparation and the increased rates which are observed with initial contact of a glass surface with aqueous solution. The reasons behind this are qualitatively shown in the enhanced dissolution of surface features, such as those around the cracking imaged in Figure 6.32, labelled as POI 1. Therefore, the high rates obtained via this method should be disregarded in favour of those obtained from SPFT experiments and used primarily as a method for examining surface features.

Variation of SPFT Experimental Parameters

The SPFT suite of experiments was designed to determine whether thermodynamic data could be collected for these heterogeneous wasteforms. It was appreciated from the outset that

determining thermodynamic data, such as pH dependence and activation energy for a multiphase sample, was going to be problematic and that data treatment would require an approximation to a single phase. It was decided that such an analysis of this data suite should not be performed due to a combination of the following factors; 1) the lack of a correlation in the forward NR_i vs temperature plots; 2) the assumptions already required in order to process the data; and 3) the clarity with which the VSI experiments discussed below showed that dissolution was compositionally dependant.

The suite of experiments did however identify the common trend that deviations from neutral pH vastly increase the dissolution rate for these wasteforms. As such, this indicates any use of these materials would ideally be stored without the use of a cementitious backfill material due to the inherently high pH this produces.

Variable surface retreat rates

The existence of variability in surface retreat rates and its dependence on compositional variation has been evident throughout the course of these experiments. Although solution based data appears comparable with that obtained from homogeneous glasses, a fuller picture should be attained where possible by the examination of the surface features after dissolution. This is qualitatively seen in the cross-sectional data for MCC-1 experiments where the presence of wormhole features was noted only in certain regions of the wasteforms surface.

However, the combination of SEM-BSE imaging, SEM-EDX and VSI proved a much more powerful methodology for identification of this type of variation. This allowed for the determination of the rate of surface retreat during these experiments for the two major glass compositions and the features of enhanced corrosion which were correlated with both morphology and composition. It was possible to show; 1) the rate of corrosion of Glass B in the CSXC-BORAX was over thirty times more rapid than seen in Glass A; 2) that significant wormhole features formed only in Glass B; 3) that the complete dissolution of the mixed alkali sulphate phase during dissolution occurred; and 4) that surface features such as cracks are prone to significantly increased localised dissolution.

Wormhole Features in the Glass Surface: Evidence obtained from the sample surfaces of monolithic experiments obtained from both SPFT and MCC-1 experiments indicate that these ‘wormhole’ features may be an artefact of sample preparation. This evidence is best provided in Figure 6.32 at POI 1. Here we observe numerous elongated surface depressions which form after corrosion. These surface features are likely to be of the same origin as those identified as ‘wormhole’ features in cross-sectional imaging of the MCC-1 samples provided in Figures 6.19

b) and 6.20 d). In Figure 6.32 it is clear that the elongated nature of the features are aligned with other features in both parallel and perpendicular orientations.

Preparation of these samples for dissolution was performed by hand using the method of surface removal whereby the all scratches are aligned, until an evenly damaged surface is attained. The sample is then rotated 90 °C for the next grade of abrasive media. This is continued until the desired surface finish is attained. The result of this polishing method is that scratches will only ever exist in two directions perpendicular to each other. As the surface depressions across the imaged sample follow the same pattern it is hypothesised that they exist as a result of the stresses induced during grinding and polishing.

The grinding of brittle materials typically produces a surface layer under compressive stress. Beneath this surface layer, localised regions of tensile surface stress can be formed relating to the maximum penetration depth and fracturing created by the coarse grinding media used for sample removal [256, 257]. Residual tensile stresses are known to increase the aqueous dissolution rate in silicate glass materials [258].

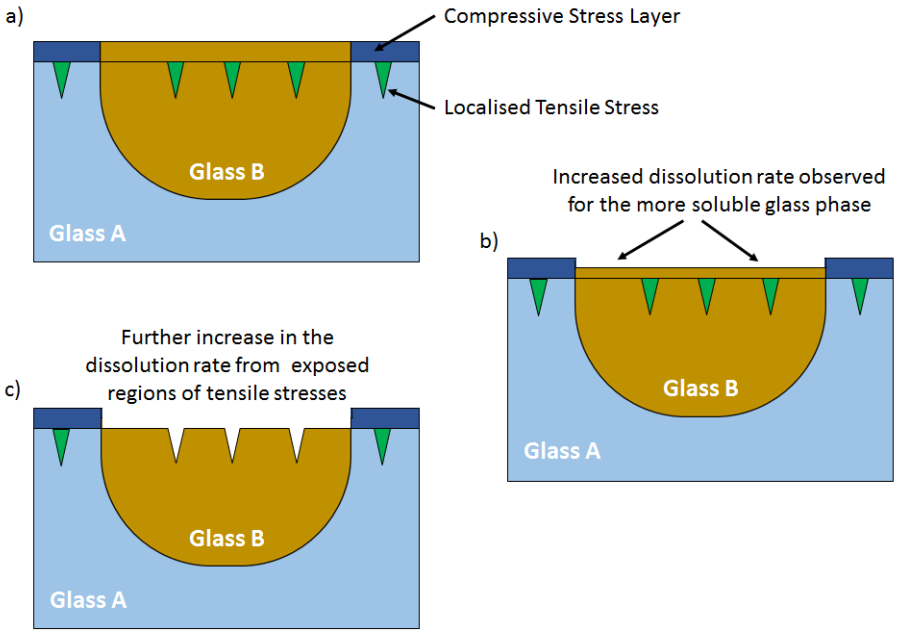

Figure 6.33 – Schematic of proposed mechanisms by which wormhole features form in monolithic samples form as a result of residual stresses from sample preparation. a) proposed stress and compositional distribution, b) preferential dissolution of Glass B and c) increased dissolution rate of tensile stressed region.

It is proposed that the surface features observed are a result the removal of the compressively stressed surface region of glass, which in turn exposes these regions of tensile residual stress. Due to the increased physical retreat rates observed for Glass B, the removal of this compressive region is only observed in these regions of this composition at the point of sampling. This retreat

provides access to the localised regions of tensile stress, which then retreat more rapidly than the surrounding area. It is suggested this is what results in these 'wormhole' features. A schematic illustration of the proposed process is provided in Figure 6.33.

6.5 - Conclusions and Future Work

This scoping study successfully demonstrated the applicability of the proposed thermal treatment methodology to the processing of clinoptilolite. HIPing clinoptilolite at 95% waste loading has been shown to produce a robust glass-ceramic wasteform which should be considered suitable for GDF disposal as ILW. A volume reduction in the order of 50% was obtained.

Phase separation of the material into two vitreous phases was observed, based on the dispersion of flux into the collapsed clinoptilolite structure. The Cs and Sr inventory was found to be well distributed within the vitreous phases of the glass. Numerous inclusions form within the glass-ceramic. Some non-ideal concentration of Sr into a mixed alkali earth sulphate phase increases the release rate of this element. However, most of this element is retained in the glass structure and the true release to solution has been measured to be low and would be expected to be even lower under disposal scenarios.

The aqueous dissolution properties of the wasteform produced are comparable to or improved by comparison with existing HLW glass wasteforms. This highlights the significant improvements in waste from product quality attained by the thermal treatment of clinoptilolite waste over cementation. The solution release data for dissolution experiments of grossly phase segregated wasteforms have been qualified. Alterations from the standard experimental methodologies and use of powdered samples have been suggested to decrease the inherent error seen with these measurements.

A combination of SEM imaging and VSI has been shown to be a powerful tool in determining comparative surface retreat rates in the examination of phase separated materials. It is suggested that further improvements to the wasteform physical and chemical characteristics could be made for clinoptilolite by moving from a fluxing additive to a solubilising additive.

Future work should be performed in the following areas:

- Study of the effect of bake-out and calcination parameters on product. A significant suite of samples should be produced to determine the effect of bake out and calcination on the production of HIPed CLINO wasteforms. Variations in temperature and time

should be applied to determine the lowest time and energy combination capable of successfully HIPing the waste stream. This suite could also be used to determine the envelope limits which prevent successful HIPing by testing partially evacuated samples.

- Full characterisation of the HIPed CLINO at 100 wt% loading. This should be used to differentiate between the effects of differing glass composition and crystallites using VSI investigations.
- The retention of Cs and Sr should be measured accurately via complete sample dissolution.
- Analysis of dissolution samples aged for over one year should be performed to elucidate on any alteration layer products which form on the wasteform surface during dissolution.
- Samples using a combination of glass frit and CSXC-CLINO should be produced and analysed to see if the postulated mechanism of formation from Section 6.3.5 produces a superior waste product. This method could also provide more favourable processing condition, such as lower temperatures and shorter dwells to achieve similar levels of densification.

Chapter 7 - SrTreat®

7.1 - Chapter Summary

This chapter details a scoping study investigating the production of a wasteform by HIPing from a sodium titanate ion exchanger. This ion exchanger is called SrTreat® and is currently employed in the nuclear industry to remove radio Sr from aqueous solutions. More specifically, this chapter aims to investigate the possibility of integrating this waste processing method into in a complete waste management solution. This concept would utilise an ion exchange column which also acts as a HIP canister for the processing and containment of the final disposal package.

This study analysed data from a mixture of techniques including microscopic, XRD and aqueous durability investigations to provide information on the exchange mechanism for Sr, the product formed by the HIPing of SrTreat® powders, the aging of this product in air and its ability to retain Sr in aqueous solution.

Note bene: This work has not been commissioned, funded or sanctioned for release by Fortum Nuclear Ltd. The results presented in the discussion are the authors alone and are should not be considered representative of the views of Fortum Nuclear Ltd.

7.2 - Materials and Experimental

7.2.1 - Materials

SrTreat®

SrTreat® is manufactured by Fortum Nuclear Services, Finland. This study used material identified as lot number (17/08) which was supplied with a grain size of 0.30 – 0.85 mm. The density was measured to be 2.7724 ± 0.0006 g cm^{-3} using helium pycnometry.

Ion exchange

Ion exchange was performed under alkaline conditions to maximise the loading of Sr, as is implemented on an industrial scale [172]. $Sr(NO_3)_2$ (15 g, Sigma-Aldrich, >99 % purity) was added to H_2O (2L, 18.2 MΩ). The preferential exchange for H^+ ions, discussed below, was minimised through the addition of NaOH (0.7g, Sigma Aldrich, >98% purity) to produce a solution of pH

12.15 ± 0.1. The solution was capped to minimise the potential precipitation of $SrCO_3$ from solution and stirred for 24 hours at 25 °C.

The exchanged SrTreat® (XC-SrT) was retrieved by vacuum filtration and the effluent solution pH was measured at pH 12.08 ± 0.1. The XC-SrT was washed with $NaOH_{(aq)}$ (3 x 1 L, 0.0275 M) and then dried for 48 hours at 120 °C. To determine the cause of carbonation after the exchange a 10 g sample of XC-SrT was removed from solution via vacuum filtration, washed three times with NaOH solution to remove un-exchanged $Sr_{(aq)}$ from the surface of the particles then left to dry for five minutes in a vacuum desiccator. Following this the sample was removed and exposed to air while XRD analysis was performed. These scans were performed using a smaller angle range of 24° - 2θ - 27° to allow accurate identification of the $SrCO_3$ peaks, whilst also keeping scan times short enough to allow meaningful analysis of carbonation kinetics.

XRF

The composition of the SrTreat® was measured using XRF before ion exchange (SrTreat®), after ion exchange (XC-SrT) and after HIPing (HIP-SrT). XRF analysis was performed on a Phillips PW2404 XRF Axios at the School of Earth, Atmospheric and Environmental Sciences, The University of Manchester. The compositional results obtained by XRF are displayed in Table 7.1.

Oxide	SrTreat®		SrTreat® - Exchanged (XC- SrT)		SrTreat® - HIPed (HIP- SrT)	
	Wt %	*At %*	*Wt %*	*At %*	*Wt %*	*At %*
TiO_2	92.1	84.9	83.2	85.7	81.8	85.3
Na_2O	7.9	15.1	3.1	6.6	2.6	5.6
SrO	0.0	0.0	13.7	7.7	15.1	8.6
Cr_2O_3	0.0	0.0	0.0	0.0	0.1	0.1
MnO_2	0.0	0.0	0.0	0.0	0.0	0.0
Fe_2O_3	0.0	0.0	0.0	0.0	0.3	0.3
NiO	0.0	0.0	0.0	0.0	0.1	0.0
Sum	100.0	100.0	100.0	100.0	100.0	100.0

Table 7.1 - Oxide compositions of SrTreat® as raw powder, after exchange in aqueous Sr solution and after HIPing at 1100 °C. Error in measurement estimated at ± 2 wt%.

7.2.2 - Synthesis and Characterisation

HIP Sample Preparations

Canning was performed utilising the tube-coin canister design, as outlined in Section 3.3. XC-SrT was preheated to 300 °C and held at temperature for 12 hours to dehydrate the powder. Canisters were packed at 100 % waste loading, without a prior calcination step, utilising a mixture of vibratory packing and uniaxial pressing to minimise the internal void space. The canister lid was then welded on prior to vacuum evacuation. The canister bake-out was performed until a vacuum level of ~3.3 Pa was obtained. The evacuation tube was then crimped and sealed with a weld. Prior to processing the volume of the canister was measured using the Archimedes method.

HIPing

The HIPing of SrTreat® samples was performed using the University of Sheffield HIP facility with an AIP 630-H HIP system. The canisters were processed by HIPing at 1100 °C for 2 hours. The pressure and temperature were ramped simultaneously using a 10 °C min^{-1} temperature ramp rate as the set point. Ramp down was performed at 10 °C min^{-1} with a gradual release of pressure.

Sample retrieval

Powder samples were retrieved by sectioning the welds of the canister lids with an abrasive saw, prior to pressure being applied to the canister walls using a vice. This application of pressure created sufficient fragmentation in the processed wasteform, allowing for collection of fragmented and powdered samples. Further size reduction was performed using a hardened steel percussion mortar, followed by the separation of appropriate size fractions by sieving.

Larger monolithic samples were obtained by sectioning the lids and walls from the canister using an Isomet 5000 linear precision saw fitted with a 0.9 mm diamond blade. The canister was then mounted for sectioning using a combination of hot wax mounting and vice mounting to minimise fracturing effects potentially caused by excessive clamping force. The retrieved monolith was further sectioned to obtain appropriate monoliths using an Isomet low speed saw, fitted with a 0.3 mm diamond wafering blade. Monoliths were prepared for investigation by grinding using P1200 grit SiC papers and polishing with 6, 3, 1 and ¼ µm diamond pastes.

Static Type Aqueous Durability Protocols

PCT type protocols were performed at Forschungszentrum Jülich using a variation of the standard PCT methodology as is described in Section 3.10.1. Samples were produced in duplicate via testing in 60 ml HDPE vessels which were placed in a silicon oil bath at 90 °C. Sampling was performed on each vessel at 3, 7, 14, 21 and 28 days. The mass of the each vessel upon removal from the oven was recorded before and after sampling to allow calculation of how the SA/V ratios altered during the course of these experiments. The SA/V ratio relevant to the sampling point was used for the calculation of NL_i and NR_i according to Equation 3.6 and 3.8 respectively. At each sampling point 2 ml of sample was removed from the test vessel and filtered using 0.2 µm polypropylene filters. This solution was prepared for analysis using ICP-MS by diluting 1 ml of solution with 9 ml of 18.2 MΩ water, followed by the addition of 100 µL of 15.2 M HNO_3.

The solutions used during these experiments were designed to have pH of pH 4, 7 and 9 at 90 °C and their compositions are reported in Table 3.1. For each solution blanks were run in duplicate.

Two monolithic samples were treated under similar conditions. The monoliths were prepared and polished to a 0.25 µm finish before placement in 60 ml PFA containers fitted with a sample basket and filled with 18.2 M Ω water for 28 days at 90°C. These were removed and rinsed with ethanol prior to resin mounting and sample preparation of the monolith as described above.

SPFT protocol

SPFT experiments were performed at Forschungszentrum Jülich according to the methodology outlined in Sections 3.10.3 and 3.10.4. The experiments were performed with a log(Q/S) = -6.95, a particle size of 106 – 180 µm, 90 °C and with solution pH values of 2 and 10, according to the solution compositions listed in Table 3.1. NR_i values were calculated according to Equation 3.9.

7.3 - Results

7.3.1 - Characterisation of Starting Materials and Ion Exchange

TGA

To justify the selection of parameters for canister preparation, TGA analysis was performed on the SrTreat®. The results of this analysis are shown in Figure 7.1. The mass loss from the sample was measured at 17.00 wt % during heating to 1000 °C at 10 °C min^{-1}. Over 86 % of this loss occurred below 400 °C with the remaining 2.35 % of loss occurring up to 785 °C. No sharp peaks are observed, instead the plot shows two regions of volatile loss with varying degrees of mass

loss associated. The first event is more substantial and occurs from ~60 °C to 400 °C and the second mass loss from ~500 °C to 775 °C.

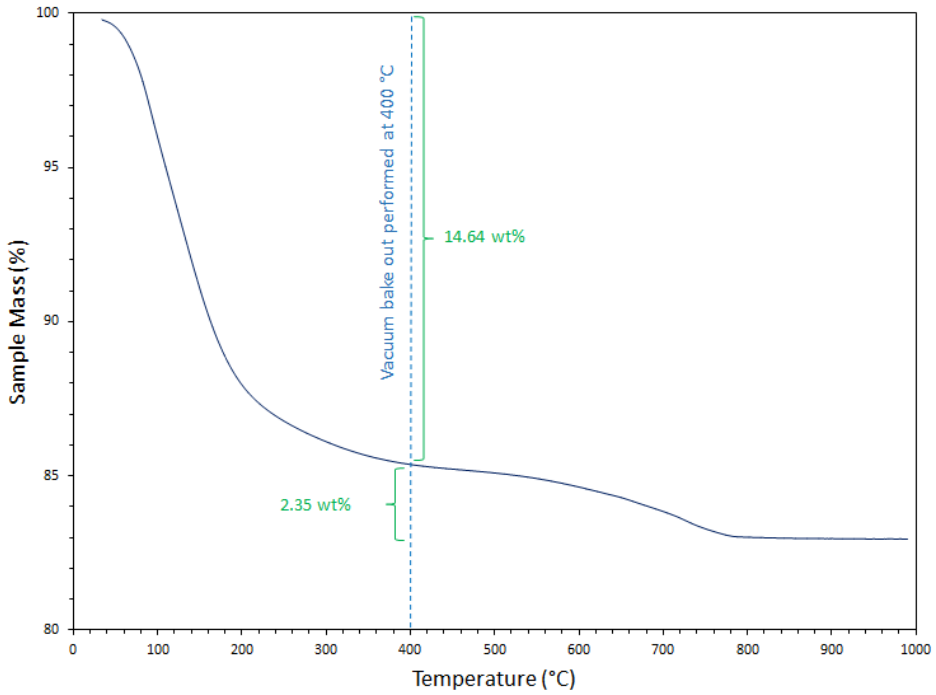

Figure 7.1 – TGA data for XC-SrT when heated from room temperature to 1000 °C at 10 °C min^{-1}. The mass loss before and after the bake out temperature utilised is highlighted.

Composition and exchange

XRF compositional data is provided in Table 7.2 for both pre and post-exchanged SrTreat® powders. XRF measured the Na_2O content in SrTreat® at 15.1 mol % whereas in XC-SrT this decreases to 6.6 mol %. The presence of SrO increased from 0.0 wt% in SrTreat® to 7.7 wt % in XC-SrT. This indicates approximately 50 % of the Na contained in the SrTreat® has been exchanged for Sr during the exchange reaction.

XRD

Figure 7.2 a) shows the XRD patterns for SrTreat® and XC-SrT. The data displayed indicates a disordered, partially amorphous structure exists in both samples. The combination of this data with the XRF data, literature references and XRD patterns identifies this material as a partially amorphous sodium titanate or mixture of such sodium titanate phases [172, 174, 175, 259-262]. Further investigation and discussion regarding the nature of the starting material were not undertaken in an attempt to respect the intellectual property of Fortum Nuclear Ltd.

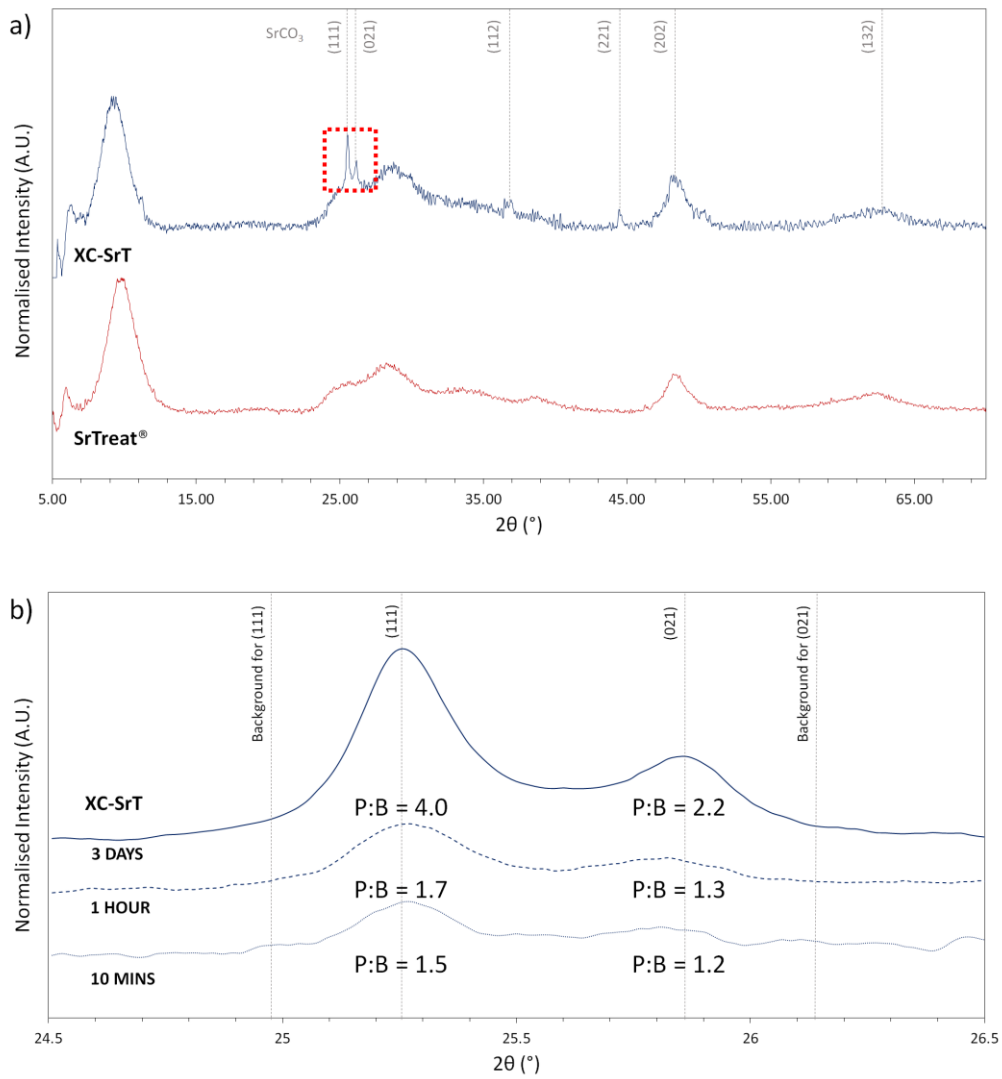

Figure 7.2 - a) Powder XRD patterns for SrTreat® and XC-SrT after storage in air for two weeks and b) the evolution of the (111) and (021) SrCO3 peaks in air from the XC-SrT sample over a period of three days. This data is displayed with the inclusion of peak to background intensity (P:B) data for each time period.

Crystalline peaks which were not previously identified in the un-exchanged SrTreat® were noted in the powder XRD pattern of the XC-SrT. These peaks are indexed in Figure 7.2 a) and have been attributed to the presence of $SrCO_3$ in the XC-SrT.

SEM-EDX Mapping

To determine where the Sr resides in the XC-SrT particles SEM-EDX mapping was performed. The results of this analysis are provided in Figure 7.3. Samples were inserted into epoxy-resin immediately after the exchange was complete to minimise the potential carbonation of the sample surface. Sample polishing was performed immediately before insertion into the SEM for the same reason. No conductive coating was used on the samples to allow for mapping of C. The SEM-BSE image in Figure 7.3 shows the resin mounted XC-SrT particles in cross-section.

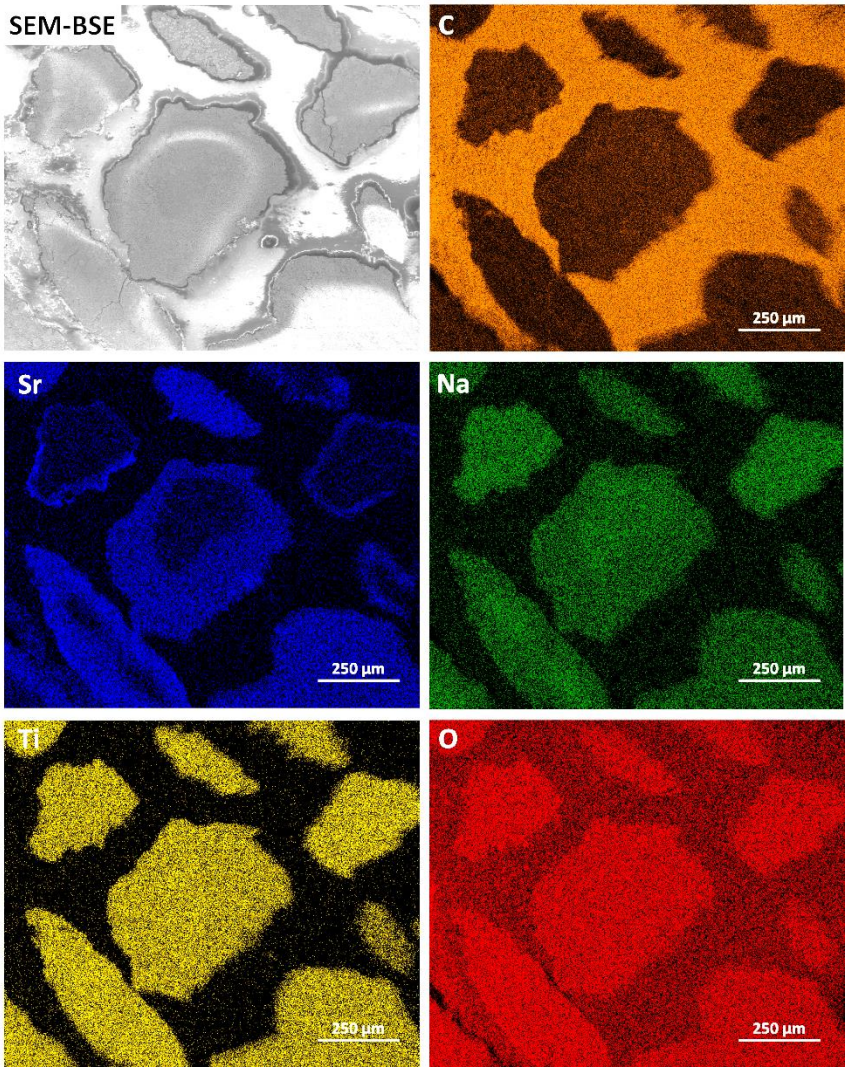

Figure 7.3 - SEM-EDX chemical mapping of sectioned XC-SrT particles illustrating the distribution of main component elements in the structure.

The grey scale variation of the SEM-BSE image are due to the electrical charging of the sample surface occurring due to the lack of conductive coating on the sample surface. The Sr map illustrates effective exchange of Sr has occurred without the precipitation of $SrCO_3$. The Sr map also shows that the individual particles behave differently during the exchange reaction. All particles show increased Sr concentrations at the outer edge exposed to the $Sr_{(aq)}$ solution. Some particles show near homogenous concentrations of Sr throughout the particle, whereas others show a clear concentration gradient from the edges to the centre of the particle. Higher concentrations of Sr correlate with a decreased concentration of Na in the particles. No correlation of Sr or Na exists with respect to C. The concentration of Ti and O are broadly consistent throughout the particles.

7.3.2 - Characterisation of HIP-SrT Wasteform

Pre-Sectioning evaluation of HIP canister

Post-processing, the HIP canister showed effective densification. The HIP canister volumes were measured before and after processing using the principle of volume displacement in water. With this information the waste volume reduction associated with processing were calculated. The total package volume decrease associated with HIP processing of SrTreat® was measured at 49 ± 5% using Equation 3.3. The waste volume reduction was calculated at 73 ± 5% using Equation 3.4. The small error between these sample measurements indicates that both the initial packaging density and the densification on processing behaved in consistent manner in all samples produced.

Visual Inspection of HIPed Product

Figure 7.4 provides an image of the HIP-SrT as a sectioned, polished monolith from the canister's centre. A visual inspection of the HIP-SrT material illustrates a multiphase product has been produced as indicated by the presence of both white and blue regions in HIPed product.

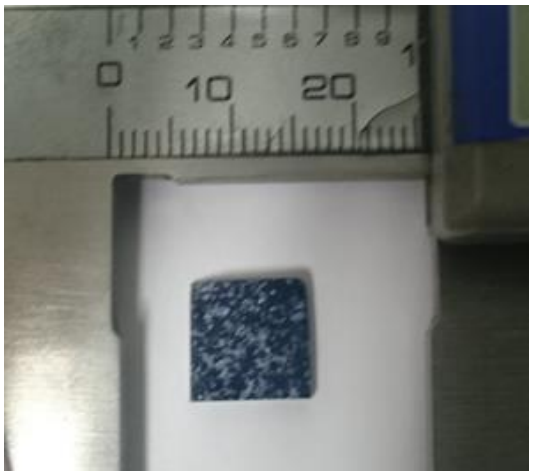

Figure 7.4 - Photograph of polished HIP-SrT monolith illustrating the blue colouration of the previously white powders and the heterogeneous nature of the exchanged wasteform produced.

XRD

The powder XRD pattern obtained from the HIP-SrT wasteform is displayed in Figure 7.5. From this pattern is it possible to identify a mixture of three phases. Indexing of the peaks present indicates the wasteform contains a mixture of $Na_2Ti_6O_{13}$, $Na_2Ti_3O_7$ and $SrTiO_3$. All relevant peak positions are identified and indexed in Figure 7.5. The estimated concentrations of each phase,

as calculated from relative peak intensities using Crystal Dynamics Match! Software, are provided in Figure 7.5.

During HIPing the semi-amorphous structure of the XC-SrT has been destroyed and these three titanate phases have crystallised. The major phase identified in the wasteform is $Na_2Ti_6O_{13}$ at 69.1 wt%, followed by $Na_2Ti_3O_7$ at 23.0 wt % and the lowest measurable phase was $SrTiO_3$ accounting for 7.9 wt % of the phase assemblage.

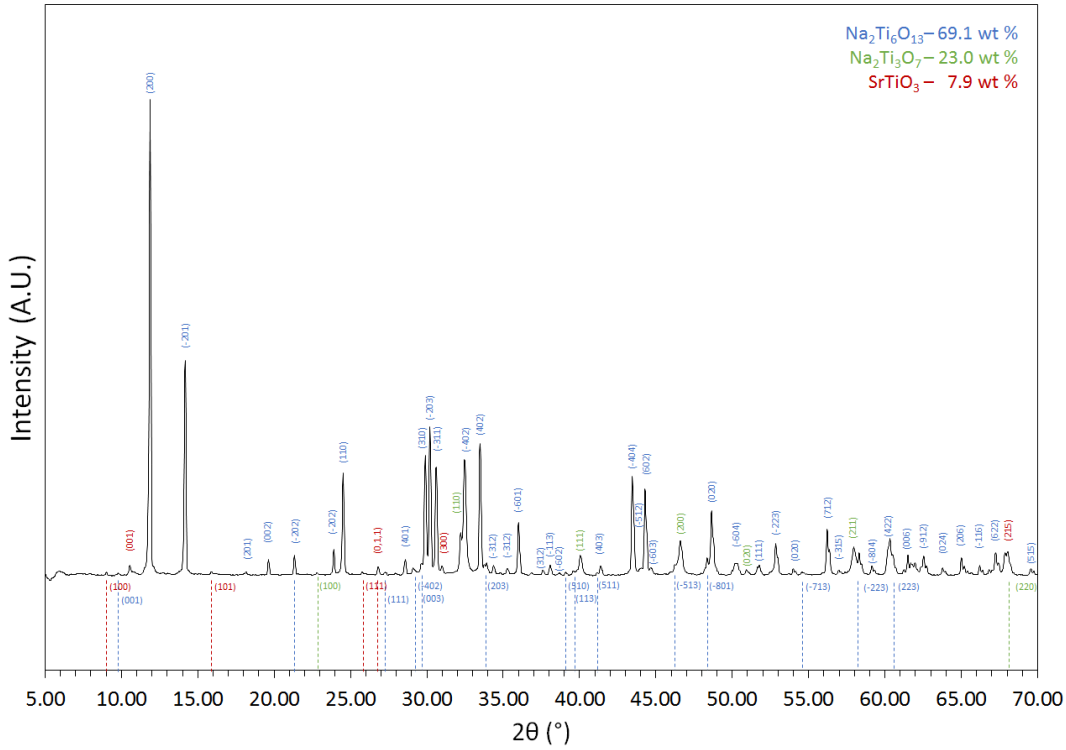

Figure 7.5 - XRD pattern of HIP-SrT with peak positions indexed according to the phases present. Percentage phase abundance as calculated via peak intensity indexing with Match! Software is displayed in the figures legend.

Morphological and Compositional Segregation

Figures 7.6 a–e show SEM-BSE images illustrating the heterogeneous nature of this material. The morphological features present are a similar size and shape to those seen from SEM-EDX mapping of the XC-SrT powders in Figure 7.3. The greyscale variation in the SEM-EDX imaging of HIP-SrT correlates well with the Sr concentration shown in the SEM-EDX mapping of the XC-SrT particles.

Figures 7.6 a) – c) shows that the segregation into morphological regions occurs on both a micro and macroscopic-scale. Figure 7.6 a) provides an overview of the phase assemblages and morphology of these regions on the mm scale. Based on the grayscale values of the SEM-BSE in

image 7.6 a) three distinct regions can be identified based on their composition and morphology. Figure 7.6 b) illustrates these three regions at a higher magnification.

Region A – This was identified as the major phase associated with the wasteform and is imaged at higher magnification in Figure 7.6 c). Needle like crystal structures and small cracks are observable in this region.

Region B – This region is interspersed as islands in Region A. Figures 7.6 d-e illustrate the fine structure of this region. Figure 7.6 e) provides a false colour overlay for the grayscale values identifiable as Region C in this image. There is clearly some overlap which may indicate Region B is a combination of multiple phases.

Region C – This region is observable in at least two morphological forms. The first is as a 'coast line' around the edges of Region B, as seen in Figures 7.6 a) – b) and secondly as 'islands' with a diameter in the range of 5-20 μm, interspersed within Region B as seen in Figures 7.6 b) and 7.6 d). The porous and interconnected nature of this phase is shown in Figures 7.6 b) and d). A third morphological form of Region C may exist as sub-micron crystallites which will be discussed in Section 7.4.2.

Correlation of Elemental Concentrations within Morphological Regions

Further information relating to the identity of these regions can be gathered from the SEM-EDX line scan in Figure 7.7. From XRF analysis over 99.5 wt% of the wasteform was accounted for by Na, Sr, Ti and O, therefore, EDX-line scans were only performed for these elements. As the sample used was cut from the centre of the canister Cr, Mn, Fe and Ni (present from the HIP cans) scans were excluded as it was deemed unlikely they would be present at this depth. This was confirmed by SEM-EDX spot analysis. Figure 7.7 illustrates the variations in chemical compositional responsible for the changes in the SEM-BSE greyscale.

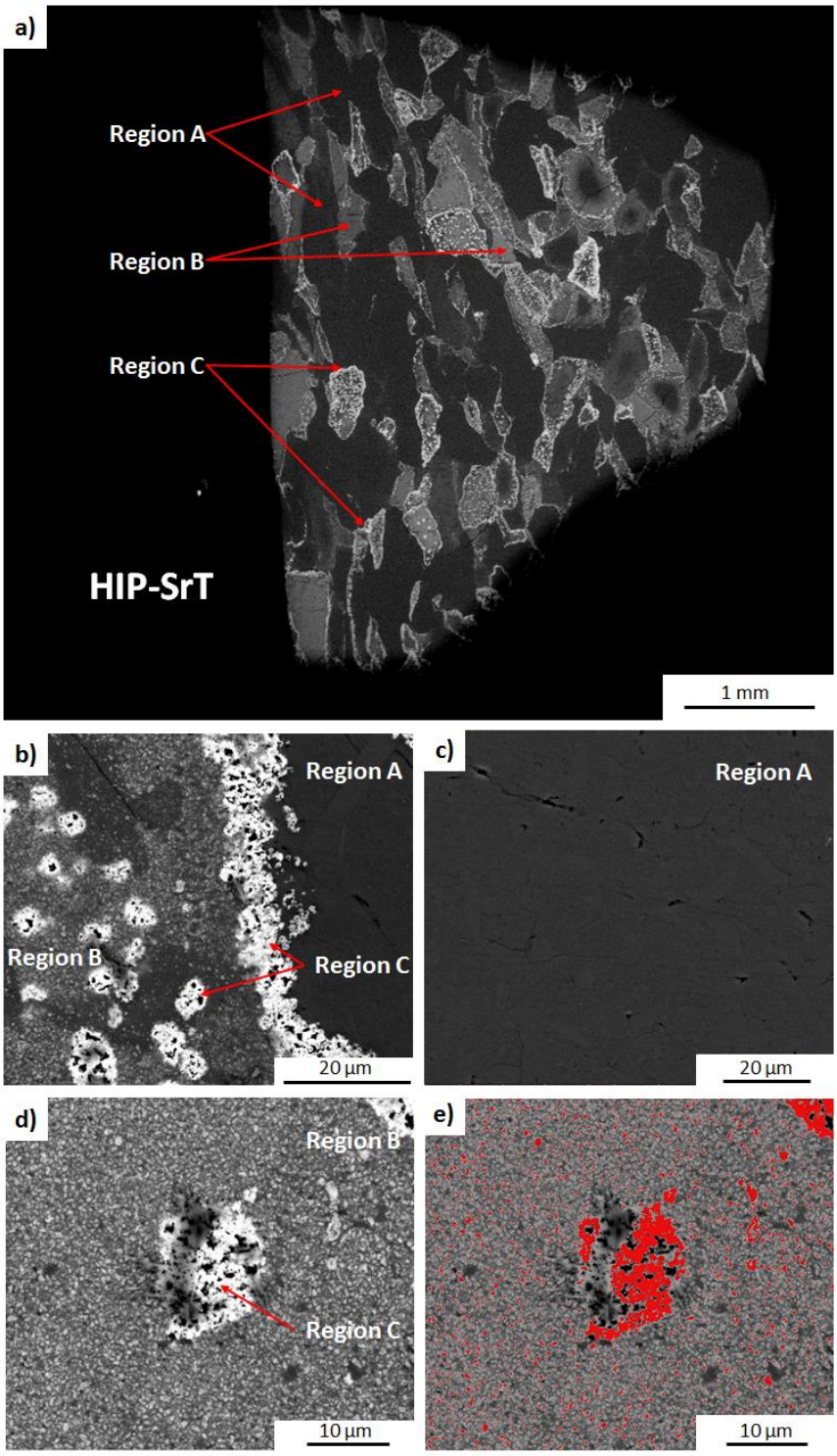

Figure 7.6 - SEM–EDX images illustrating a) an overview of the HIP-SrT wasteform identifying the three morphological regions b) the three identified regions at higher magnification c) Region A at higher magnification d) Regions B and C at higher magnification and e) a false colour overlay of pixel data with greyscale data in the range identified as Region C.

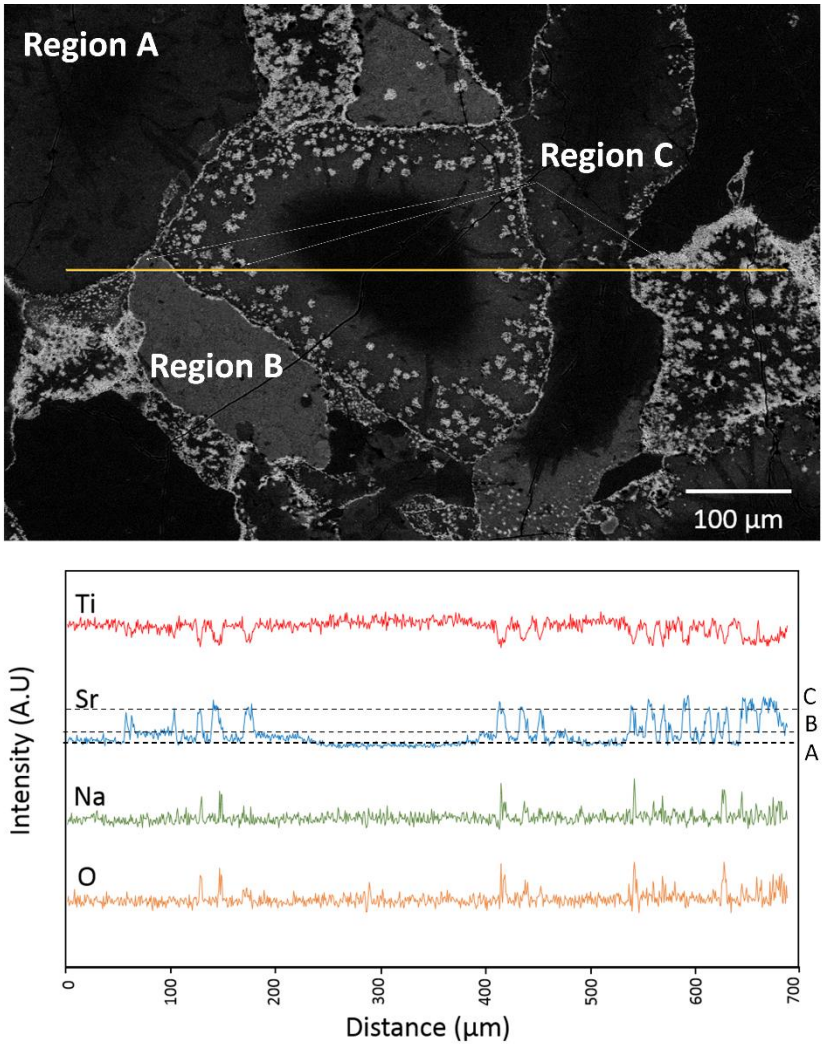

Figure 7.7- SEM-EDX line scan across the different morphological regions illustrating the compositional trends and dependencies on grayscale values in the SEM-EDX imaging. Broken lines displayed on the Sr SEM-EDX line indicate differentiations between morphological regions.

Figure 7.7 shows that a correlation exists between the line scans for Ti and Sr. The Sr concentration increases in the sample as the concentration of titanium decreases. There is also a correlation between Sr concentration and greyscale brightness in the SEM-BSE. This indicates that the major variations in greyscale are dependent on the Sr distribution within the sample. It is also clear that the Sr is not homogeneously dispersed throughout the sample, instead concentrating in Regions B and C.

There is a second correlation which is evident from the line scan data provided in Figure 7.7. When passing through certain areas of Region B and Region C, an increase in the Na and O intensity is observed. This result is discussed further in Section 7.3.3 and 7.4.3.

Mapping of the HIP-SrT was performed to confirm these correlations. The results of these analyses are displayed in Figure 7.8. The Ti and Sr maps in Figure 7.8 each show evidence of the three regions previously been identified as Regions A - C. An inverse correlation exists between Sr and Ti, with increased Sr concentrations responsible for increased brightness in the greyscale of SEM-BSE imaging. The correlation which exists between the maps for Na and O is possibly a result of the needle like structures which will be discussed in more detail in Sections 7.3.3 and 7.4.3.

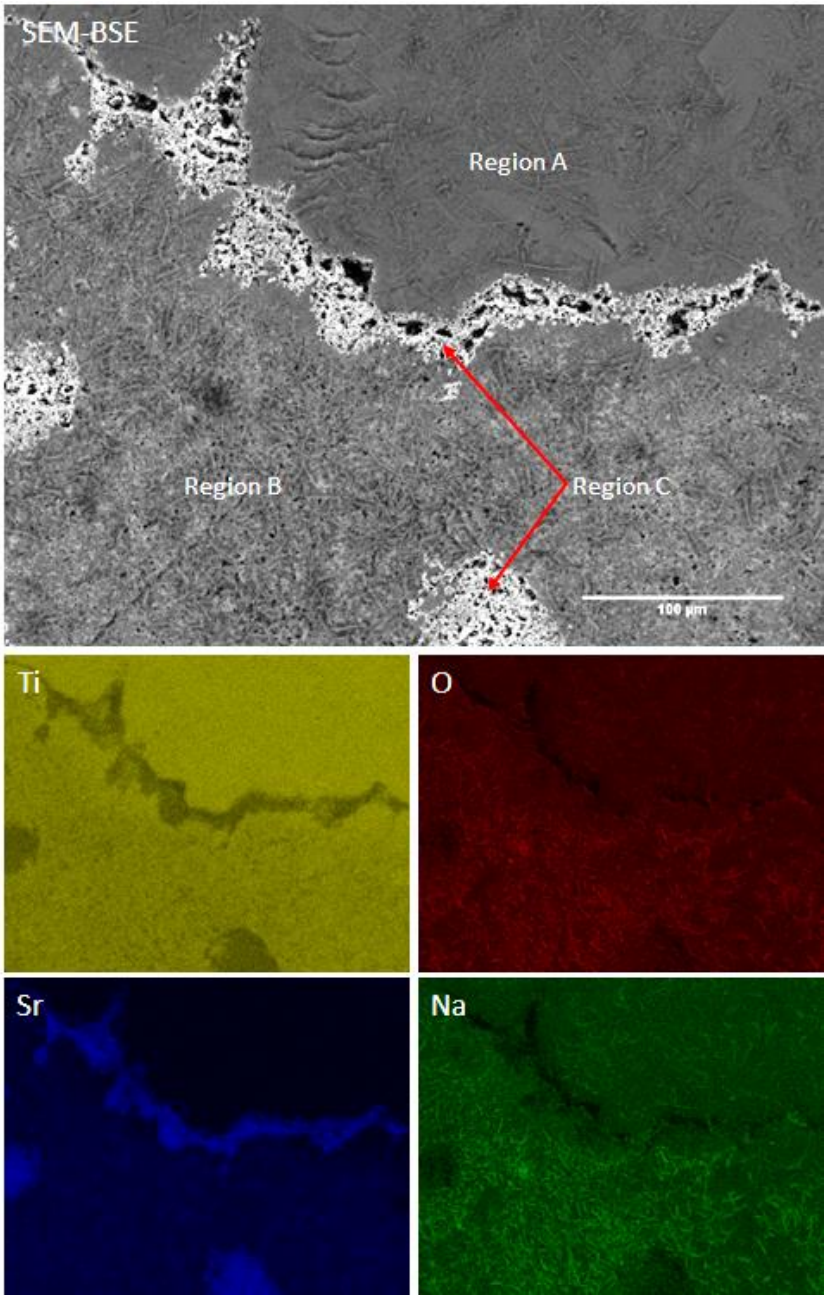

Figure 7.8 - SEM-EDX chemical mapping of a multiphase region of HIP-SrT for the elements Ti, O, Sr and Na performed at 20 kV with a working distance of 10 mm.

Identification of Individual Phases Present

To attribute the identity of each region to the phases identified from XRD analysis of the HIP-SrT a number of semi-quantitative SEM-EDX measurements were performed. This analysis was performed according to the previously identified regions in the HIP-SrT wasteform. Ten measurements were made in the Region A, 104 in the Region B and 16 in Region C. The results of these scans were grouped and averaged. Then the corresponding ratios of each element were calculated and compared to those of the phases as identified from powder XRD. These elemental ratios were calculated according to the following equations.

$$\mathrm{Ti}: (\mathrm{M}^{+} + \mathrm{M}^{2+}) = \frac{\mathrm{Ti}_{\mathrm{at\%}}}{\mathrm{Na}_{\mathrm{at\%}} + (2 \times \mathrm{Sr}_{\mathrm{at\%}})} \qquad \textbf{Equation 7.3}$$

$$\mathrm{Na}: (\mathrm{Na} + \mathrm{Sr}) = \frac{\mathrm{Na}_{\mathrm{at\%}}}{\mathrm{Na}_{\mathrm{at\%}} + \mathrm{Sr}_{\mathrm{at\%}}} \qquad \textbf{Equation 7.4}$$

The results of this analysis are presented in Table 7.2. Table 7.2 also provides an assignment of the chemical compositions which are discussed further in Section 7.3.4.

Quantification of Phase Assemblages within the Wasteform

Semi-quantitative analysis of how these phases contribute to the overall assemblage of the wasteform was performed. To obtain this data 30 SEM-EDX images were collected and combined to produce a single image covering an area of 4.7 mm^2, with a pixel resolution of 0.5 μm^2. This allowed the separation, identification and quantification of phase assemblages, based on the changes in grayscale, with a spatial precision of approximately 1 μm^2 (accuracy stated over a 2 x 2 pixel array) and yet able to cover an area deemed to be representative of the wasteform micro-structure. Both factors are crucial for any adequate characterisation of a material which is both macroscopically and microscopically phase separated.

Figure 7.9 shows both the SEM-EDX image produced via montaging of the SEM-EDX images and also the pixelated data from the separation of grayscale values. This data was correlated with the composition of phase assemblages as measured via SEM-EDX spot analysis. Table 7.3 provides a comparison of the overall contribution from each phase using this analysis with the pure crystal phases as performed by XRD peak intensity analysis.

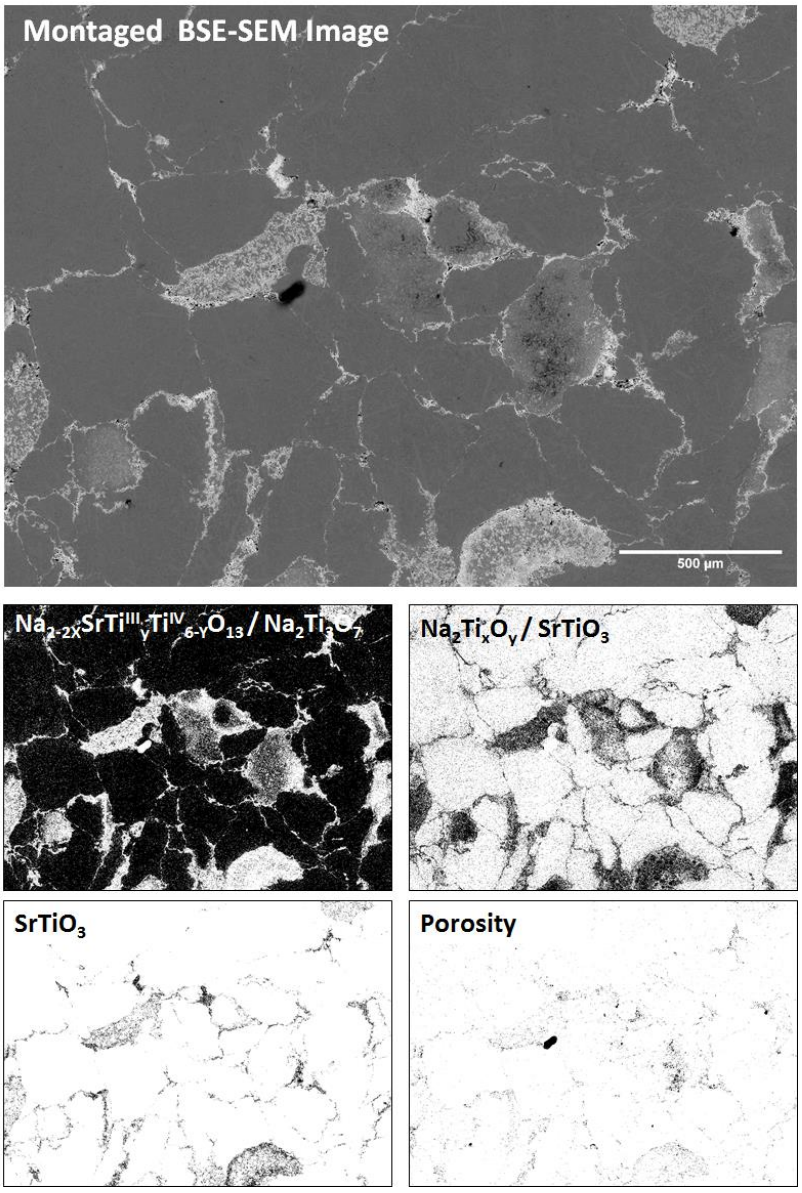

Figure 7.9 - Montaged SEM-EDX images set over pixel data for each identified phase, separated on the basis of image grayscale which was correlated with SEM-EDX measurements.

Region	Element	at%	Ti:(M^{+}+M^{2+})	Na:(Sr+Na)	Assigned Identity
Region A	*Sr*	1.45 ± 0.1	2.3 ± 0.2	0.89 ± 0.01	$Na_{2-2X}Sr_xTi^{III}_yTi^{IV}_{3-Y}O_7$ $Na_{2-2X}Sr_xTi^{III}_yTi^{IV}_{6-Y}O_{13}$
	Na	11.6 ± 0.8			
	O	53.3 ± 0.7			
	Ti	33.5 ± 0.1			
Region B	*Sr*	7 ± 2	1.3 ± 0.2	0.66 ± 0.1	$SrTiO_3$ $Na_{2-2X}Sr_xTi^{III}_yTi^{IV}_{3-Y}O_7$
	Na	11 ± 1			
	O	55 ± 2			
	Ti	29 ± 2			
Region C	*Sr*	14 ± 2	0.6 ± 0.1	0.3 ± 0.1	$SrTiO_3$
	Na	7 ± 2			
	O	55 ± 2			
	Ti	23 ± 2			
$Na_2Ti_6O_{13}$	-	-	3	1	-
$Na_2Ti_3O_7$	-	-	1.5	1	-
Na_2TiO_3	-	-	0.5	1	-

Table 7.2 - Compositions and identifying compositional ratios of each morphological region as obtained from SEM-EDX spot measurement averaged over multiple spots. The table includes comparison of elemental ratios from these measurements with the sodium titanate phases identified via powder XRD indexing. Errors stated are based on the standard deviation across the range of measurements.

Phase contribution – Montaged SEM-BSE from Pixel Grayscale Threshholding Analysis		**Phase contribution – Powder XRD Relative Peak intensity Analysis**	
Identified Region *Composition*	(Area %)	Crystal Composition	(Wt %)
Region A $Na_{2-2X}Sr_xTi^{III}_yTi^{IV}_{6-Y}O_{13}$ / $Na_{2-2X}Sr_xTi^{III}_yTi^{IV}_{3-Y}O_7$	79.1	$Na_2Ti_6O_{13}$	69.1
Region B $Na_{2-2X}Sr_xTi^{III}_yTi^{IV}_{3-Y}O_7$/ $SrTiO_3$	17.0	$Na_2Ti_3O_7$	23.0
Region C $SrTiO_3$	2.7	$SrTiO_3$	7.9
Porosity	1.2	N/A	N/A

Table 7.3 - Comparison of data obtained by both SEM-EDX image analysis and relative peak intensity from powder XRD analysis for the quantification of how each ceramic phase contributes to the overall wasteform structure.

7.3.3 - Carbonation of Aged HIP-SrT

The correlation of Na and O in needle like morphologies on HIP-SrT has been noted above to become more pronounced over time. VSI observations led to a brief investigation into this behaviour. As shown in Figure 7.10 the initial analysis of the sample surface showed a relatively homogeneous surface finish. Some surface imperfections allow for the identification of the three morphological regions previously noted. Most notably this image indicates that no surface features have a needle like morphology.

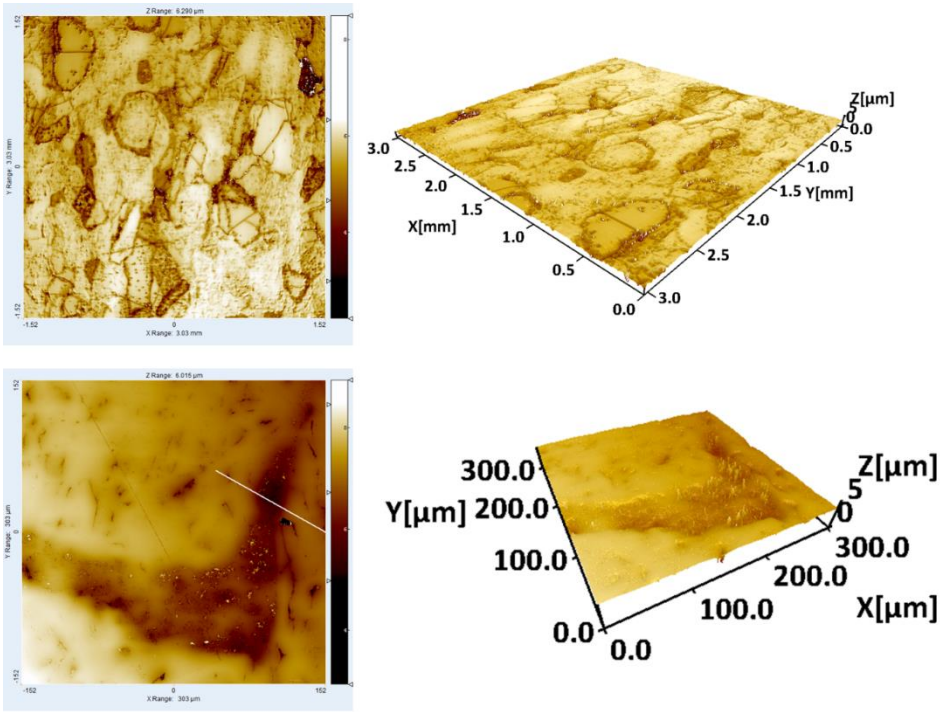

Figure 7.10 – VSI imaging of polished HIP-SrT surfaces prior to the intended dissolution experiment being carried out showing a relatively flat surface with some surface undulation based upon porosity and differential in hardness during the grinding process.

After the initial surface reference mapping was performed, the sample was left for approximately 10 weeks in air. A gold coat was then applied to be used as a reference surface for the dissolution experiments (see Chapter 6 for further information on this technique). Before the SPFT experiment was initiated, characterisation of this reference layer was performed to allow future determination of surface retreat. No reliable data could be obtained from the reference surface due to data drop out from the VSI technique. As both the gold coated reference surface and uncoated material showed these z axis undulations, an investigation into

surface retreat was no longer possible and an investigation into the nature of this change was begun.

SEM-SE imaging shown in Figure 7.11 illustrates why the sample could not be imaged utilising VSI. These SEM-SE images show that the gold coating has been applied over a layer of needle like crystals. These crystal formations are what prevented the effective imaging of the coated surface using VSI. This gold coated region provides a clear illustration of the surface topography and changes which had occurred on the sample surface after storage in air for ten weeks.

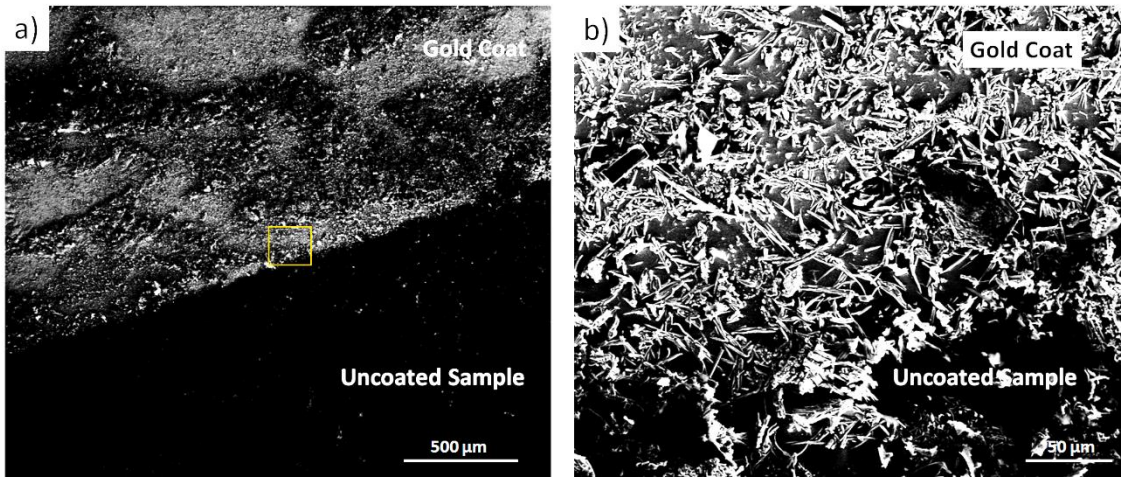

Figure 7.11 - SEM-SE imaging of HIP-SrT prepared for VSI surface retreat experiments a) illustrating the region the where the gold coat was applied and b) an increased magnification of the gold coated region highlighted in a) showing the needle like morphology of the crystal growth.

The HIP-SrT surface is coated with large needle like agglomerations of crystals, tens of microns in length. It is clear from Figure 7.11 a) that the existence of these crystals is not homogeneously distributed over the sample surface. Figure 7.12 displays a combination of SEM-SE and SEM-BSE images of the uncoated region, allowing identification of the phases responsible for crystallite growth. The lower atomic mass region identified in Figure 7.12 a) shows the highest degree of crystal formation. When we compare the SEM-BSE images in Figure 7.12 a) and c) it appears the crystal growth correlates with a similar morphological pattern in Region B and Region C and crystallisation occurs to a lesser degree in Region A.

Comparison of Figure 7.12 a-c illustrates the difference between the aged and unaged samples. The extent of surface crystallisation has eliminated the fine structural detail and phase segregation previously visible using SEM-BSE imaging.

Analysis of the fine structure of the aged HIP-SrT is required to qualify the degree of crystal precipitation and to identify the chemistry responsible for sample degradation. Figure 7.13 illustrates the three main phases identified in the pristine sample. All regions are coated to some degree with crystals which were identified as Na_2CO_3 via SEM-EDX spot analysis of uncoated samples. The crystal morphology is the same in each region, with thin needle like crystallites of the order of tens of microns in length. The crystals are stacked and protrude from the sample surface.

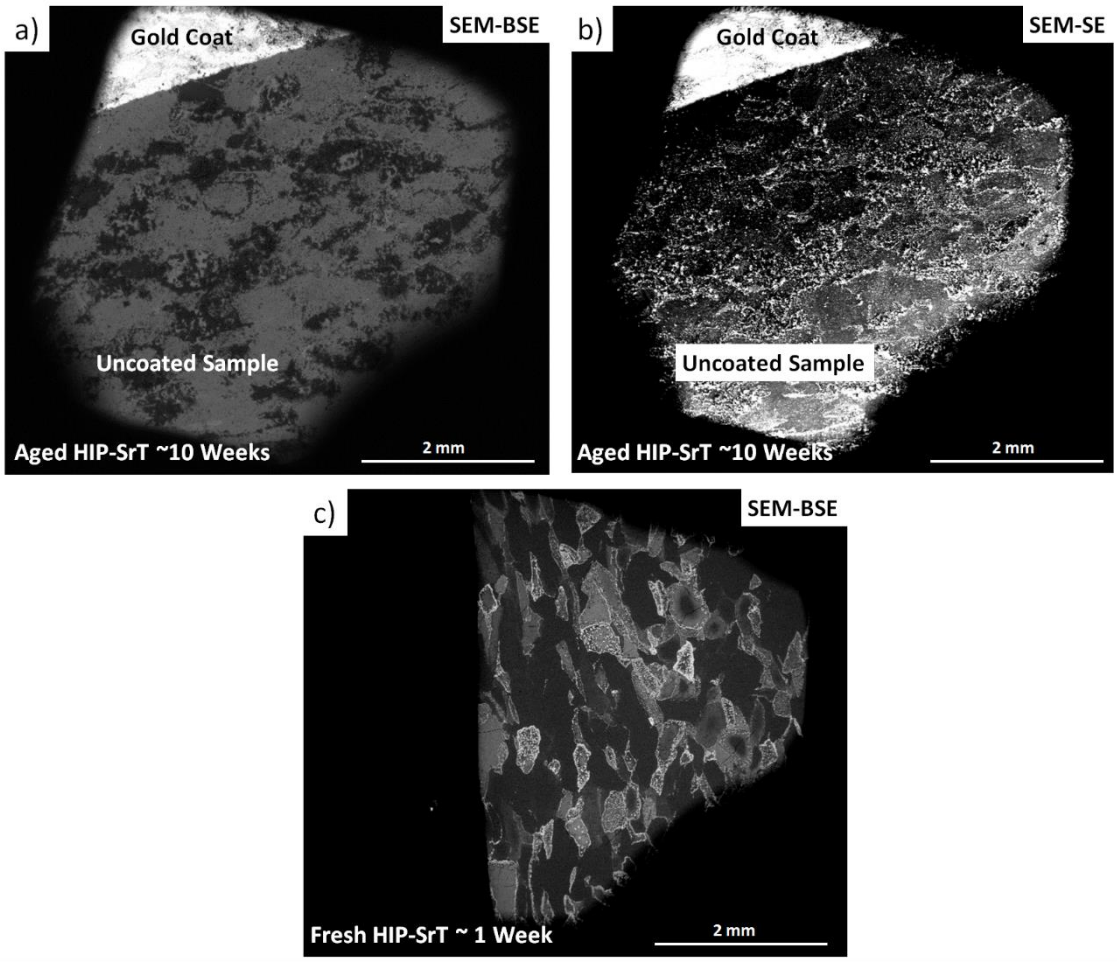

Figure 7.12 - a) SEM-BSE image of 10 week aged HIP-SrT sample surface b) SEM-SE image of 10 week aged HIP-SrT sample surface and c) SEM-BSE image of the same HIP-SrT sample surface after aging for approximately 1 week.

As noted above, the highest degree of crystallisation occurs around Region B as seen in Figure 7.13. In this region the crystals have agglomerated and protrude from the sample surface in large clusters so it is difficult to discern the original surface morphology.

The presence of these Na_2CO_3 crystals on Region A, as illustrated in Figure 7.13 c), appear more dispersed, however, they are still clearly emanating from the sample surface and not from Region B. This indicates that the same phase is present in this region as is seen in Region B, yet to a lesser extent. From the earlier assignment of the crystalline phases it may be expected that a small quantity of $Na_2Ti_3O_7$ would be present in both Region A and Region B. If this is true the effect of carbonation could, as such, be directly related to this phase, therefore, the majority of Region B can be considered to be constituted of $Na_2Ti_3O_7$. Although crystals are present on the sample surface, it is still possible to discern the fine structure of Region C. The crystal growth over this region may be attributed to precipitation from Region A and Region B. Further evidence of this is seen in top right of the SEM-BSE image in Figure 7.13 d-e.

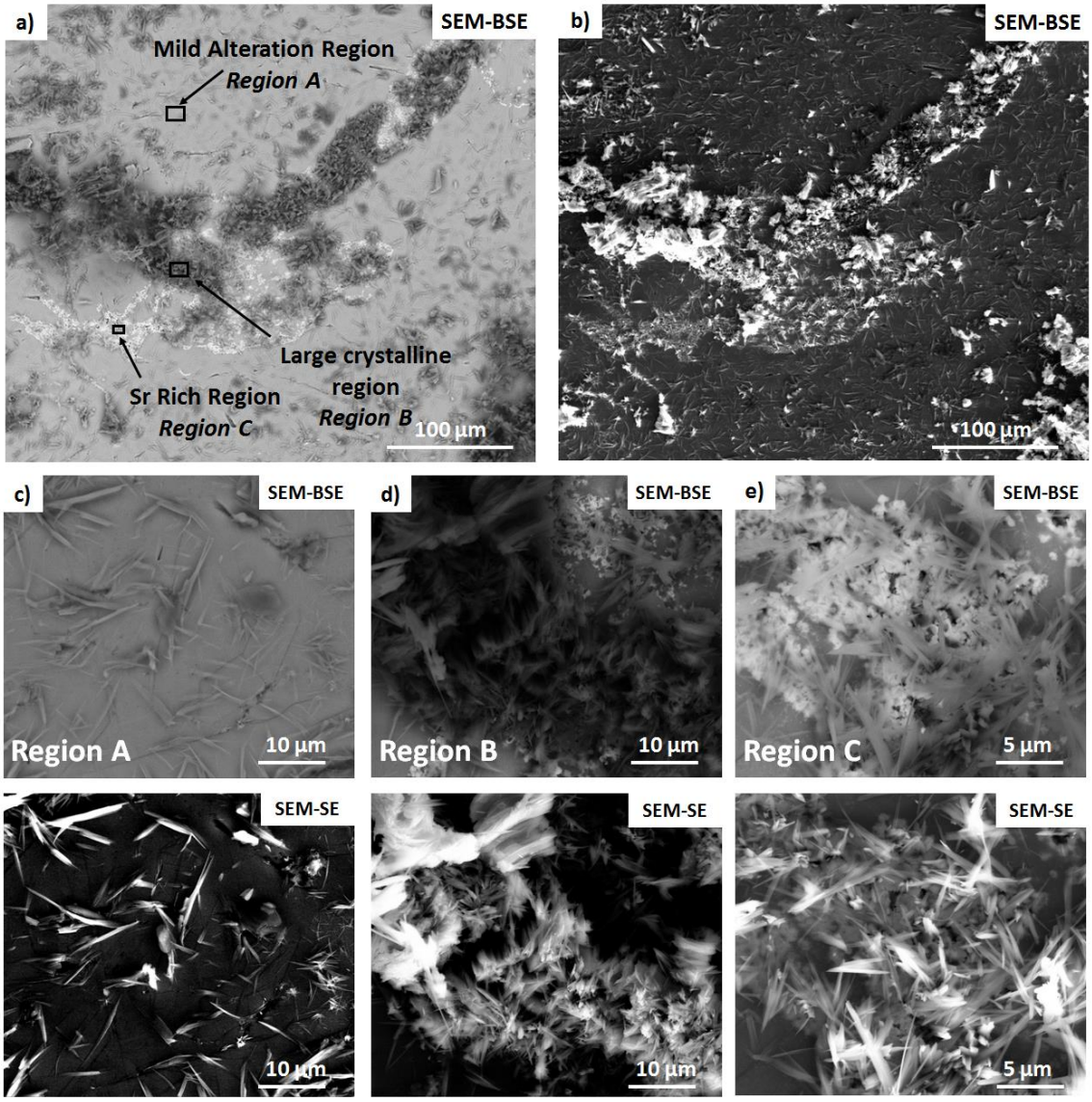

Figure 7.13 - a) SEM-BSE and b) SEM-SE overview of 10 week aged HIP-SrT sample highlighting areas imaged in the SEM-BSE and SEM-SE images in figures c-e illustrating crystal growth on Phases A, B and C respectively.

7.3.4 - Aqueous Dissolution HIP-SrT

As presented in Sections 7.3.2 and 7.4.2, HIP-SrT is a mixture of $SrTiO_3$ and partially exchanged sodium titantes. These sodium titantes are known from the literature to act as ion exchangers. As such, they could determine the ability of the HIP-SrT to retain its Sr inventory upon exposure to aqueous solutions [173, 175]. This is especially true at lower pH values where the H^+ ions are able to form the protonated titanate. A suite of experiments was performed to determine the properties of these wasteforms during aqueous dissolution; using both static (PCT type) and dynamic (SPFT type) experiments with variation in solution pH.

PCT Experiments

PCT type powder experiments were performed as described in Section 7.2.2. The solutions used are outlined in Table 3.1 and provided a starting solution pH values of 4, ~7 and 9 respectively. Figure 7.14 compares NL_i within each experiment over time and Figure 7.15 compares NL_i across the range of tested pH values. The NL_i and NR_i from the end of the experiments are provided in Table 7.4 and Table 7.5 respectively.

Figure 7.14 and Tables 7.4 and 7.5 show that the different elemental NR_i values vary by several orders of magnitude. The final NL_i values after 28 days of testing shows that Na is released in the greatest proportion with a NL_{Na} of 1.8×10^{1} g m^{-2}, followed by Sr with a NL_{Sr} of approximately 3.0×10^{-4} g m^{-2} and finally Ti with a NL_{Ti} varying between 3.0×10^{-5} g m^{-2} and 7.5 g m^{-2}.

In the case of Ti an increased starting pH value lowered the NL_{Ti} observed after 28 days testing. However due to inherent errors in the measurements, this data point is believed to be erroneous. This is because a) NL_{Ti} of the experiment in pH 9 solution data tracks that of the experiments at pH 4 and pH 7 within error up until 28 days and b) the graph of pH alteration over time in Figure 7.15 shows that after 3 days, all three solutions had surpassed their buffering capacity, reaching a new equilibrium value of pH 11.3 ± 1.

Element (i)	NL_i (g m^{-2}) [Data from 28 day sampling point. pH indicates pH of solution at beginning of experiments]		
	pH 4	*pH 7*	*pH 9*
Ti	7.5×10^{-5}	6.23×10^{-5}	3.0×10^{-5}
Na	1.8×10^{1}	1.8×10^{1}	1.8×10^{1}
Sr	3.1×10^{-4}	3.0×10^{-4}	3.0×10^{-4}

Table 7.4 – Tabulated normalised elemental mass losses from PCT type experiments of HIP-SrT after 28 days at 90 °C. Errors estimated at 20 % of stated values.

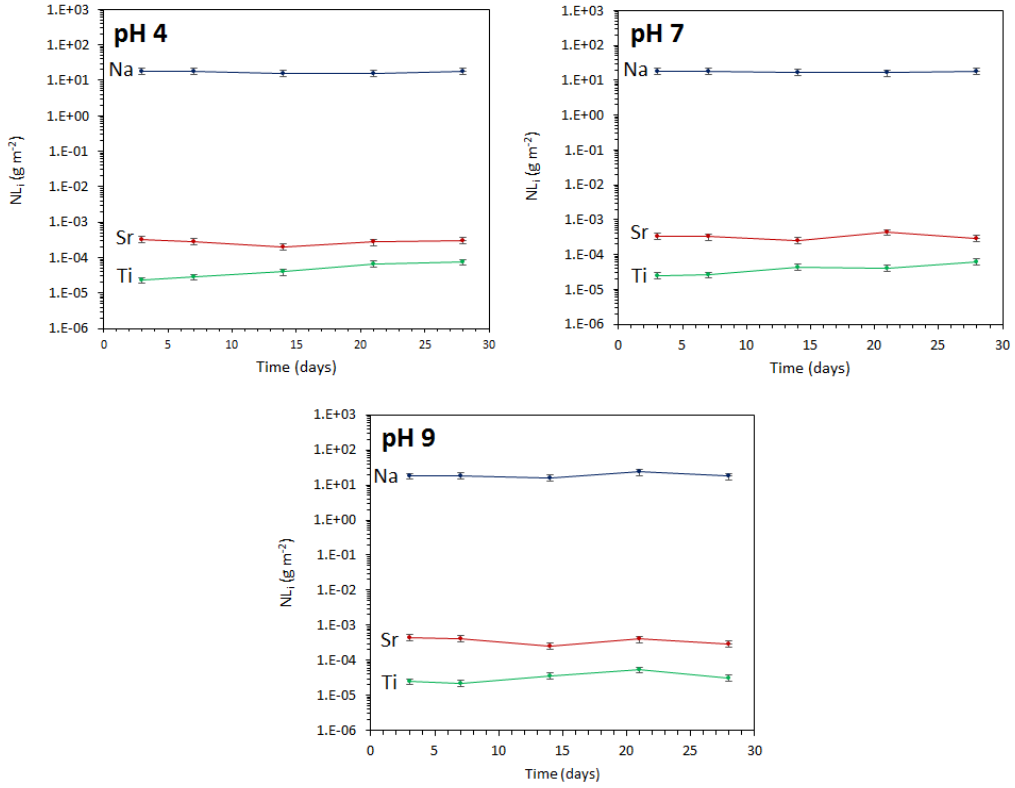

Figure 7.14 – Graphs comparing normalised elemental mass loss over time from PCT experiments of HIP-SrT at 90 °C in a variety of solutions with different starting pH values.

Element (i)	NR_i (g m^{-2} day^{-1}) [Data from 28 day sampling point. pH indicates pH of solution at start of experiment]		
	pH 4	pH 7	pH 9
Ti	2.7×10^{-6}	2.2×10^{-6}	1.1×10^{-6}
Na	6.4×10^{-1}	6.5×10^{-1}	6.3×10^{-1}
Sr	1.1×10^{-5}	1.1×10^{-5}	1.1×10^{-5}

Table 7.5 – Tabulated normalised elemental loss rates from PCT type experiments of HIP-SrT after 28 days at 90 °C. Errors estimated at 20 % of stated values.

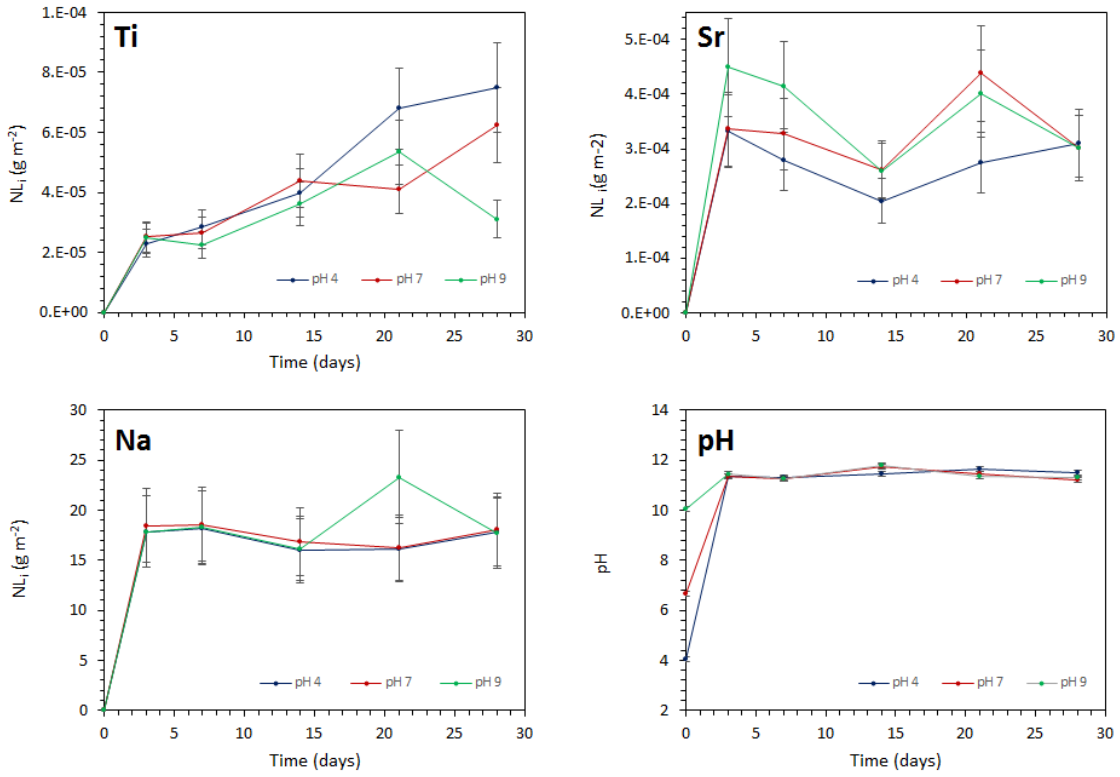

Figure 7.15 – Graphs illustrating the differences in normalised elemental mass loss obtained from PCT experiments on HIP-SrT at 90 °C with changes to initial solution pH values. A plot illustrating the change in pH of solutions with time is also provided.

SPFT Experiments

Two experiments were performed with solution pH values set to pH 2 and pH 10 at 90 °C as outlined in the SPFT solution data provided in Table 3.1. All collected samples were analysed in quadruplicate as a) unfiltered undiluted solution, b) unfiltered diluted (1:10) solution, c) filtered undiluted samples and d) filtered diluted (1:10) samples. As all analysed samples provided results within a 5 % error range, no further discussion of this quadruplicate analysis is provided. No spikes were reported during measurement of the ICP-MS data. The combination of these two observations suggests that no precipitates were present in the collected SPFT effluent, and as such, all data provided is that as measured from the unfiltered, undiluted effluent.

The NR_i data from the SPFT experiments is displayed in Figure 7.16 and the forward NR_i obtained from testing after 9.6 days is provided in Table 7.6. The forward rate was set at 9.6 days as this is the point at which no significant decrease in NR_i occurred for all elements over the period of testing.

Effect of Solution pH on NR_i: The NR_i in each experiment follows the same trend as noted in static experiment, with the highest NR_i for Na then Sr and finally Ti. For all elements the forward NR_i is lower in the basic solution than in the acidic solution. The greatest difference between forward NR_i of these three elements in each solution is seen for Sr, followed by Ti and finally Na. The profiles of the NR_i over time for Na and Ti mirror each in both solutions, however, this is not true in the case of Sr.

Element (i)	Forward NR_i (g m^{-2} day^{-1}) [from SPFT experiments after 9.6 days at 90 °C and log(Q/S) = -6.95]	
	pH 2	pH 10
Ti	$4.4 \times 10^{-6} \pm 1.3 \times 10^{-5}$	$4.5 \times 10^{-7} \pm 1.4 \times 10^{-7}$
Na	$2.2 \times 10^{-3} \pm 6.6 \times 10^{-4}$	$1.24 \times 10^{-3} \pm 3.7 \times 10^{-4}$
Sr	$2.7 \times 10^{-4} \pm 8.1 \times 10^{-5}$	$< 2.3 \times 10^{-6} \pm 6.9 \times 10^{-7}$

Table 7.6 - Forward normalised elemental loss rates for HIP-SrT from SPFT experiments based on the average rate as measured after 9.6 days at 90 °C and log(Q/S) = -6.95.

The shape of the profile can be best described by reference to the point at which the forward NR_i is obtained. After the initial rapid decline in rates, which are typically associated with the removal and dissolution of adhered fines, the forward rates of Ti and Na commence at the same sampling point under both acidic and basic pH conditions. For Ti, this occurs after 2.6 days and

for Na after 9.6 days. This is not true of Sr, where under basic conditions the forward NR_{Sr} is obtained after 2.6 days, yet under acidic solution this does not occur until sampling at 7.6 days.

Plotting the difference between the NR_{Ti} and NR_{Sr} at pH 2 and pH 10, Figure 7.17 helps clarify how the rate profiles of these elements under the two pH regimes are related. Na is not plotted on this graph as the profiles match each other so closely that negative and zero values are also obtained, and as such, cannot be plotted using a log scale.

Figure 7.17 shows that the difference between NR_{Ti} during acidic and basic dissolution is roughly consistent throughout the course of the experiment. However, the difference between NR_{Sr} during acidic and basic testing decreases rapidly over the initial 3.6 days of testing, before settling to a consistent difference after this period.

PHREEQC Modelling of $SrCO_3$ solubility: To qualify how the presence of $SrCO_3$ may have affected NR_{Sr} in each pH condition, PhreeqC geochemical modelling was performed using the data obtained from SPFT experiments. This modelling used the initial release concentrations of elements at both pH 2 and pH 10. This data point was obtained after 15 ml of eluent had passed through the reaction vessel. As such, the data contained the highest concentrations of all elements measured. In a dynamic experiment scenario this should be considered the point where solution saturation of phases can be considered most likely to occur, due to the removal of fines and soluble phases. Figure 7.18 plots the data obtained from geochemical modelling of the solution data, provided in Table 7.7. The model was set to output the saturation index of strontianite ($SrCO_3$) in both experiments. As the amount of dissolved carbon in solution was not measured, a range of data was modelled incorporating aqueous carbon species over a range of seven orders of magnitude. This data is presented in Figure 7.18.

Figure 7.18 shows $SrCO_3$ is more soluble at pH 2 than at pH 10. It also shows that increasing the concentration of $C_{(aq)}$ brings the saturation index of $SrCO_3$ closer to saturation. The most important result is that at all possible concentrations of $C_{(aq)}$, $SrCO_3$ is under saturated in solution.

Elemental Concentration (ppm)	pH 2	pH 10
Na	9.402	10.402
Ti	0.019	0.008
Sr	2.277	0.015
C	0.01 - 10000	

Table 7.7 – Data used in PhreeqC geochemical modelling as obtained from initial data point of SPFT experiments. Modelling was performed conditions set at 90 °C with equilibration of $C_{(aq)}$ speciation enabled.

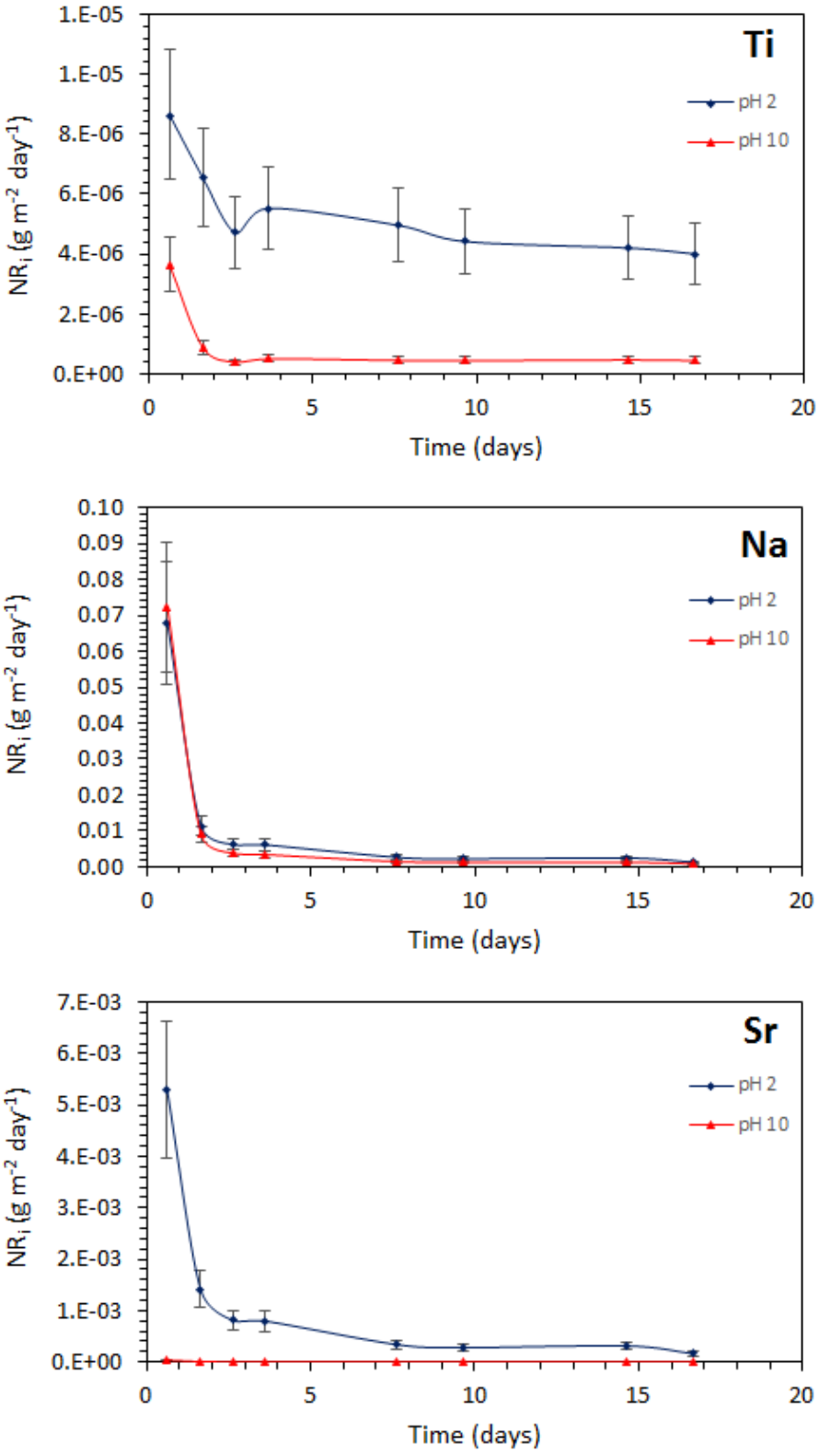

Figure 7.16 – Alteration of normalised loss rate for HIP-SrT for Ti, Na and Sr with time during SPFT experiments at 90 °C in pH 2 and pH 10 solution with a log(Q/S) = -6.95.

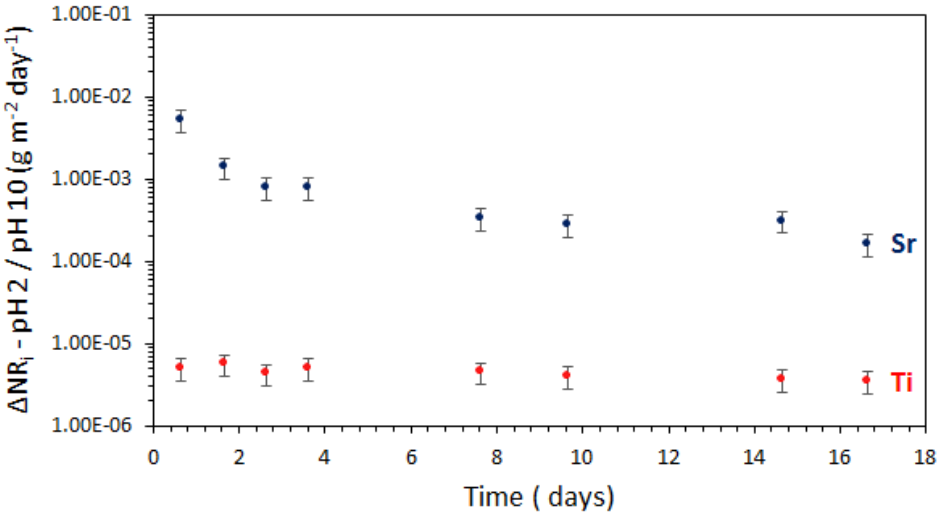

Figure 7.17 – Plot of the difference between normalised loss rate during SPFT experiments of HIP-SrT at pH 2 and pH 10 with time at 90 °C with a log(Q/S)= -6.95.

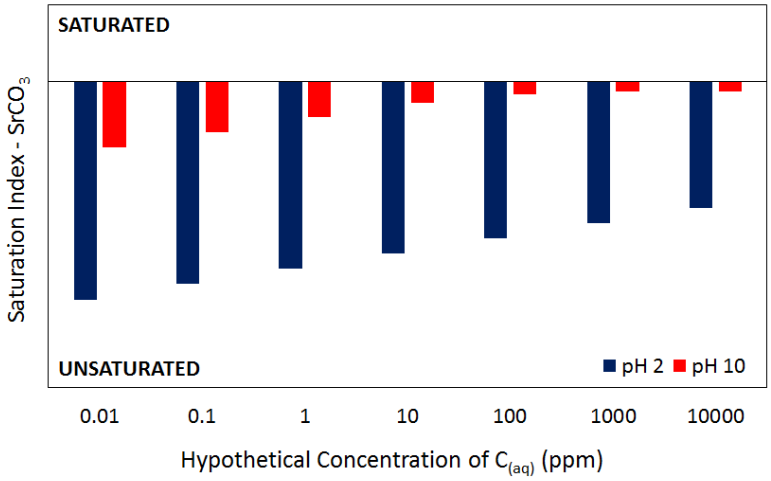

Figure 7.18 – Saturation index of strontianite obtained by PhreeqC geochemical modelling using the LLNL database. Modelling was performed using the highest concentration of elements measured from SPFT experiments at 90°C with variation in the amount of $C_{(aq)}$

Total Loss of Sr from Wasteform: The total loss of Sr from the wasteform during the experiments can be estimated using the volume of fluid which passed through the reactor and from the measured concentrations, according to Equation 7.5.

$$\mathrm{Loss_{Sr}} = \left(\frac{\Sigma \Delta V_{x-y} \times C_{(x)Sr}}{M_{sample} \times f_{Sr}}\right) \times 100 \qquad \textbf{Equation 7.5}$$

Where $\Delta V_{x\text{-}y}$ is the volume of solution which has passed through the reactor between sampling points x and y (L) , $C_{x(Sr)}$ is the concentration of Sr in solution at sampling x (mg L^{-1}), $M_{(sample)}$ is the mass of the sample, f_{Sr} is the elemental weight fraction of Sr in the material and $Loss_{Sr}$ is the total loss of Sr from the wasteform (%).

As this equation assumes the concentration does not drop between sampling points, it provides an estimate with the highest possible percentage loss of the waste element. The first measurement of effluent concentration was taken after less than 25% of the vessel volume had passed through the reactor. This ensures measurement of solution which had first come into contact with the HIP-SrT. The reaction vessel volume was added to the summation of the first volume measurement.

Use of this equation gives an estimated total Sr loss from HIP-SrT at pH 2 of 2.18 % and at pH 10 of 0.025 %. At pH 2 the initial release fraction in the first 62 hours of testing accounts for over 82% of the total loss which occurred. This initial release is even more prevalent at pH 10 with over 90 % of the associated release occurring within 14 hours. Therefore, this release can be attributed to the loss of fines or soluble, accessible materials.

Analysis of Leached Solids: Figure 7.19 provided a combination of SEM-BSE images and SEM-EDX spectra for the leached and un-leached HIP-SrT powders. The images in Figure 7.19 a-f were taken on powders after SPFT experiments at pH 10. These figures show that HIP-SrT has retained its Sr inventory during both leaching.

Figures 7.19 a-g show that little change occurs with the particles during the experiments. The morphological and chemical features observable via SEM-BSE imaging are all retained before and after the experiment. The images provide evidence for Sr retention during sample preparation and SPFT experiments. The greyscale variations in Figures 7.19 b-f are indicative of Sr concentration in the sample, as previously characterised for monolithic samples in Sections 7.3.2 and 7.4.2. The presence of Sr L peaks in the EDX spectra after SPFT experiments indicates

that Sr is still present in the material both before and after dissolution. The two spectra in Figures 7.19 g) and h) are taken from the regions highlighted in Figure 7.19 f).

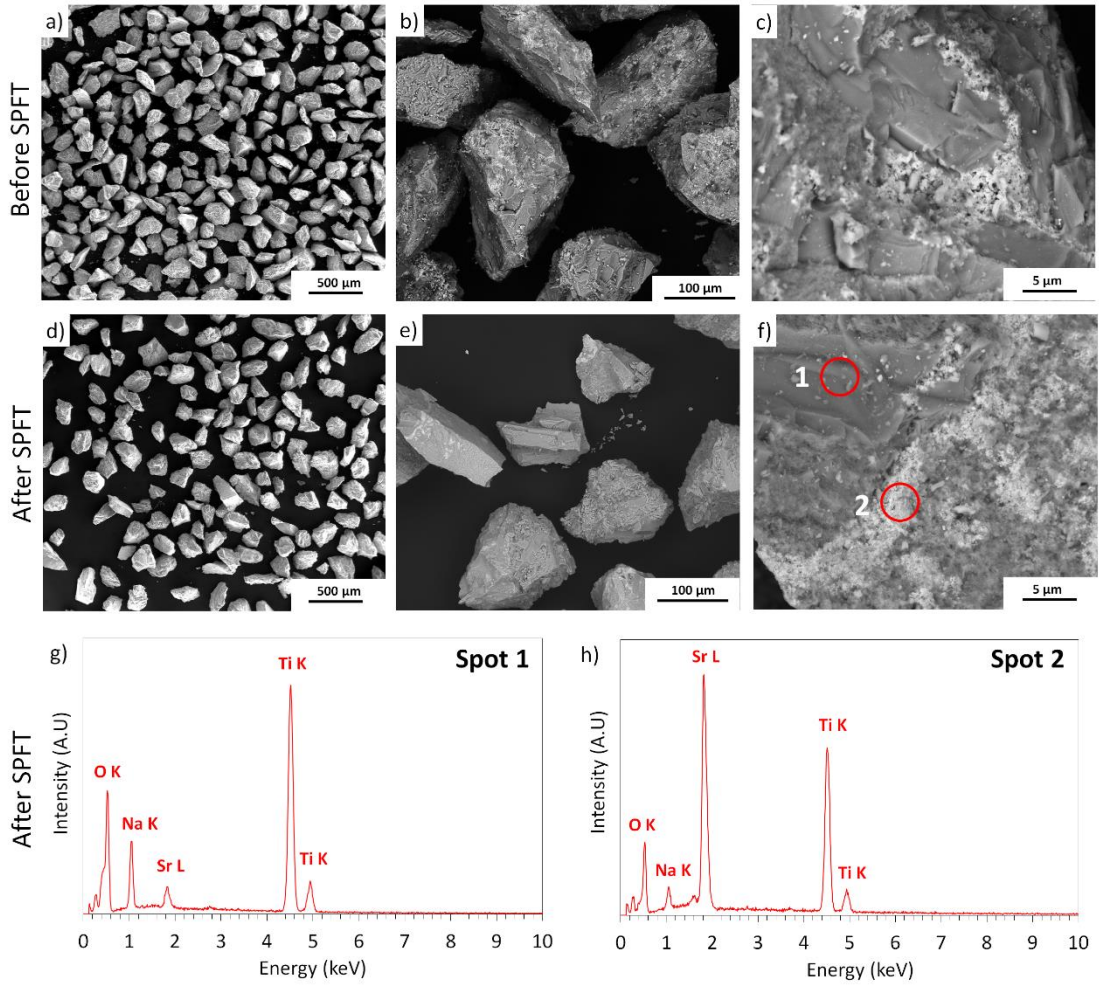

Figure 7.19 - a-c) SEM-BSE images of HIP-SrT powders before SPFT experiments and d-f) after SPFT experiments at pH 10, 90 °C with a log(Q/S) = -6.95 with SEM-EDX spectra g-h obtained after SPFT experiments taken from the spots illustrated in f).

Leaching of Monoliths: The aqueous durability of monolithic HIP-SrT samples were investigated at 90 °C in 18.2 MΩ water, with conditions similar to those stated for the static powder experiments described above. After 28 days of leaching, the monoliths were resin mounted and sectioned in profile for SEM-EDX analysis. SEM-EDX line scans and mapping of these sectioned samples are shown in Figures 7.20 and 7.21. All three morphological regions identified in Section 7.3.2 were included in this analysis for both the mapping and line scan analysis.

The line scan analysis provided in Figure 7.20 shows that the profile of the wasteform is approximately consistent throughout the outer 5 µm and contains all four major elemental components of the wasteform; Ti, Na, O and Sr. This consistent elemental profile is then followed by an abrupt drop in concentration on the edge of the wasteform. No gradual decrease indicative of ion exchange mechanisms, are noted in any of the regions examined.

The mapping is provided in Figure 7.21 a) and indicates the same result. Mapping at a lower magnification is shown in Figure 7.21 b), this illustrates that depletion of the elements has not occurred in the sample at depths up to 75 µm.

Semi-quantitative SEM-EDX data was obtained from the sample surface at the point where the SEM-EDX line scan was performed. This data is provided in Table 7.8. The data shows good correlation with that previously measured for the chemistry of each morphological region as described in Section 7.3.2, which was averaged across multiple spots prior to dissolution.

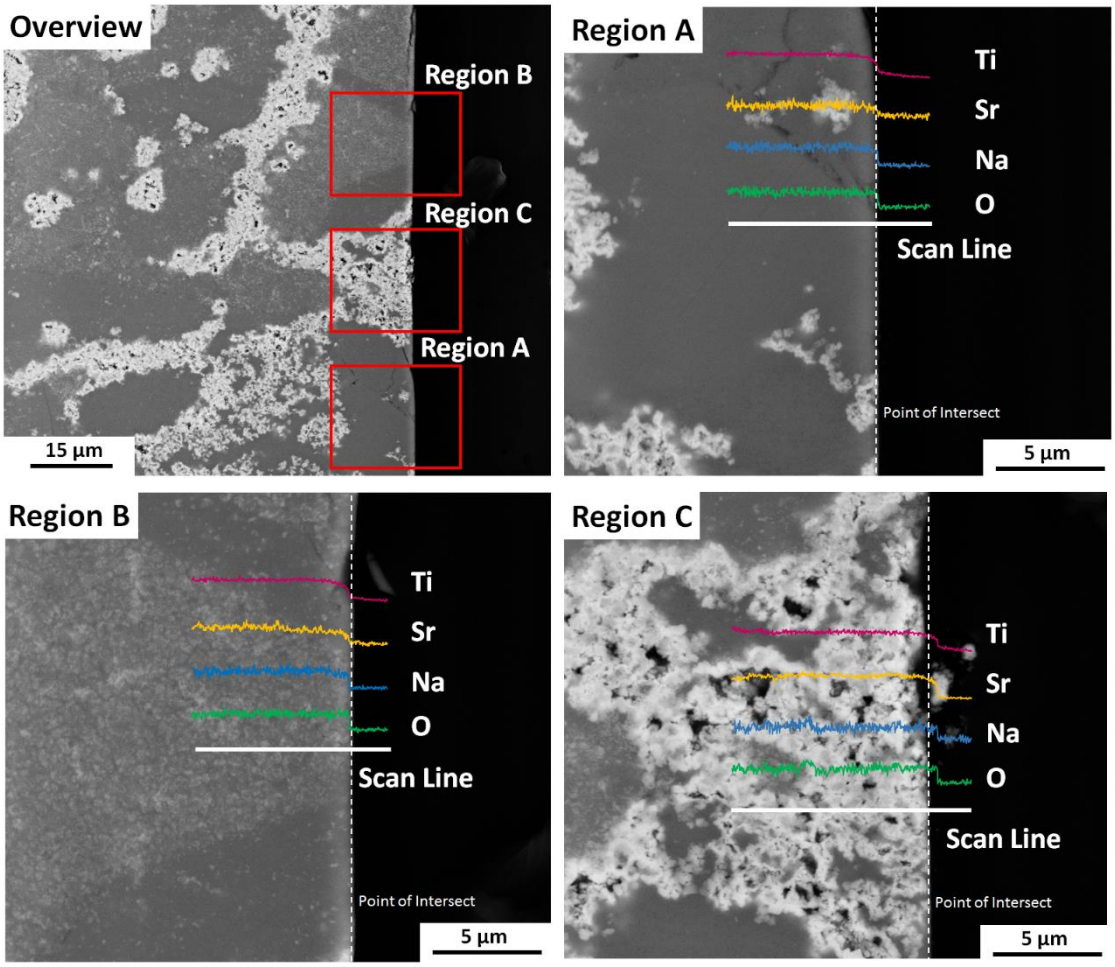

Figure 7.20 – SEM-EDX line scans of HIP-SrT prepared in cross section after static dissolution experiments for 28 days at 90 °C in 18.2 MΩ water.

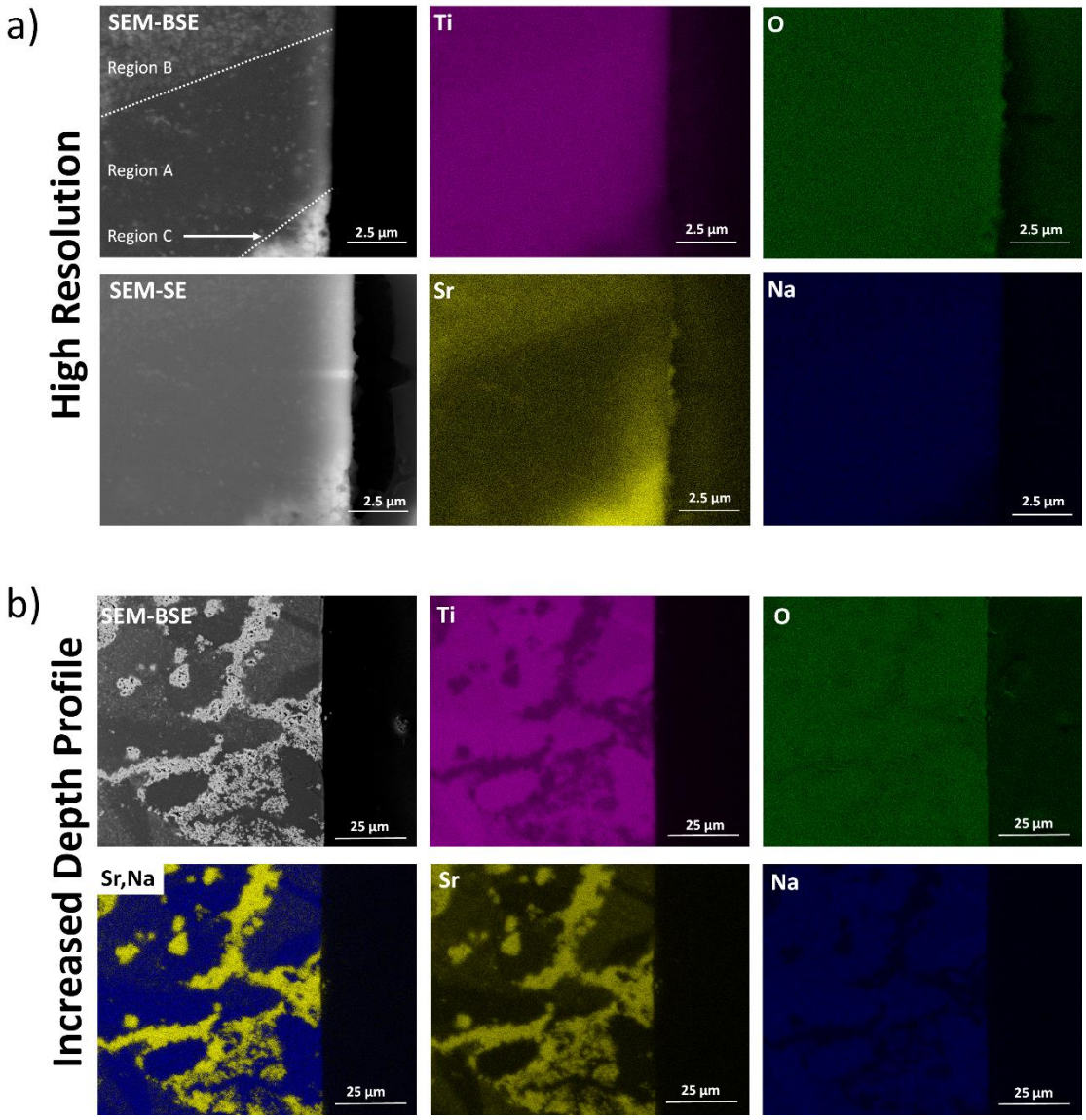

Figure 7.21 – SEM-EDX Mapping for key elements in the area highlighted in Figure 7.20 at a) high resolution and b) an increased depth profile.

Phase	Element	Elemental Contribution from SEM- EDX measurement (at %)	
		No Dissolution	**Post PCT type experiments** (after 28 days)
Phase A	*Sr*	1.45 ± 0.1	1.5 ± 2
	Na	11.6 ± 0.8	10.1 ± 2
	O	53.3 ± 0.7	48.7 ± 2
	Ti	33.5 ± 0.1	34.1 ± 2
Phase B	*Sr*	7 ± 2	4.9 ± 2
	Na	11 ± 2	7.9 ± 2
	O	55 ± 2	54 ± 2
	Ti	29 ± 2	29.0 ± 2
Phase C	*Sr*	14 ± 2	16.0 ± 2
	Na	7 ± 2	3.3 ± 2
	O	55 ± 2	53.1 ± 2
	Ti	23 ± 2	23 ± 2

Table 7.8 – Results of SEM-EDX semi quantitative analysis for each morphological phase of HIP-SrT from monolithic samples, before and after, static dissolution experiments at 90 °C for 28 days.

7.4 - Discussion

7.4.1 - Characterisation of Starting Materials and Ion Exchange

Processability

Consolidation of SrTreat® powder material by HIPing is possible with a high associated volume reduction. This would minimise the footprint on any future GDF disposal. Furthermore, it could be speculated that this may come with numerous associated social and economic benefits for the waste owners. HIPing SrTreat® provides a level of consolidation unlikely to be rivalled using any other technology. 100 % waste loading was achieved with a 49 ± 5 % volume reduction of this packaged material. In scale up, where the contribution of the canning materials is no longer a major contributor, this volume reduction may approach a level closer to that of the direct wasteform contraction (73 ± 5 %).

Figure 7.4 highlights the physically robust nature of the monolith. As abrasive cutting techniques were used to remove the sample from the HIP canister, the ability to readily obtain a monolith proves the physically robust nature of this wasteform. The blue colouration in the Region A is characteristic of the presence of d → d electron transitions from Ti^{III} complexes existing in the wasteform [263]. The presence of reduced titanium could suggest a partial substitution of Na by

Sr. This suggestion would result in Ti^{IV} sites being reduced to Ti^{III} in order to provide the necessary charge compensation, resulting in the observed blue colouration.

TGA analysis indicated that the potential for HIPing these waste streams as desired may however be problematic. To successfully HIP a waste stream the mass loss should be below 0.5 wt% prior to canister closure. As we desired the vacuum bake out to be performed < 400 °C, some issues with the final wasteform were foreseen. As ~2.35 wt% of the material inside the sealed canister is not removed below 400 °C some sublimation and dehydration in the canister is probable during processing, due to the dehydration of loosely and tightly bound water in the strontium titanate structure [264]. The presence of this water does not appear to have been the cause of the residual porosity in the canister and is likely to have been removed by evacuating under vacuum, as evidenced by the lack of porosity within Region A. Instead the residual porosity was determined to be a result of the presence of $SrCO_3$ on the wasteform surface as described below.

Carbonation

Little change was noted in the structure of the SrTreat® after exchange. The presence of $SrCO_3$ noted above in the XC-SrT material requires discussion. This could be explained via one of two mechanisms. The first would be via precipitation of $SrCO_3$ from the high pH solution during the exchange process. This would result in the coating of the grain surfaces with $SrCO_3$. The second mechanism would require $SrCO_3$ to be exolved from XC-SrT through carbonation of the sample surface during storage. The XRD patterns collected over time in Figure 7.2 b) provide evidence that the second mechanism is occurring.

The characteristic (111) and (021) peaks of $SrCO_3$ are indexed in Figure 7.2 b) for the XC-SrT ten minutes after the exchange was performed, after exposure to air for one hour and after exposure to air for three days. These $SrCO_3$ peaks are visible in all scans performed, however the ratio of the peak to background intensity increases with the time the material is exposed to air. As the sample used was identical and remained undisturbed from the sample holder, this data suggests that presence of some $SrCO_3$ is due to reaction of the XC-SrT with air and therefore is potentially unavoidable during the industrial utilisation of SrTreat®.

Although well densified monoliths have been produced by HIPing SrTreat® powders, the presence of $SrCO_3$ in the packaged canister prior to processing is not ideal. The presence of this carbonate species was deemed responsible for the introduction of the porosity noted in the final wasteform. $SrCO_3$ will not start to decompose until approximately 1000 °C. When HIPing at 1100°C this will therefore likely decompose and result in porosity within the final wasteform

(see Section 7.3.1) [265]. However, alterations to processing parameters should be able to negate this issue.

Ion Exchange

The Sr map also shows a gradient within the particles which indicates a diffusive ion exchange process. Compositional analysis and SEM-EDX shown in Table 7.1 and Figure 7.3 provide evidence that a successful exchange of Na for Sr occurred from the balance of cationic species. This mapping provides the best evidence of effective exchange and for a lack of carbonation during this exchange. This suggests that the Sr measured within the particle is part of the structure, as opposed to the alternative of being precipitated or exolved $SrCO_3$.

The Ti and O maps show a homogeneous distribution indicating that the structure of the SrTreat® has not been damaged or altered during this ion exchange reaction. The most convincing evidence of an effective exchange is seen by comparison of the Na and Sr maps, where an inverse correlation of intensity exists. This shows that the presence of Sr is due to a loss of Na which would only occur through an ion exchange mechanism.

The combination of this characterisation shows that the material being investigated has effectively exchanged and is likely to be representative of materials used on an industrial scale.

7.4.2 - Characterisation of Phase Assemblage of HIP-SrT

General Overview of HIP-SrT

HIPing of the XC-SrT particles has resulted in the crystallisation of the wasteform. The crystal phases produced were identified as a mixture of sodium and a strontium titanates phases ($Na_2Ti_6O_{13}$, $Na_2Ti_3O_7$ and $SrTiO_3$) from XRD analysis. The quantity of the each phase decreased according to the following order; $Na_2Ti_6O_{13} > Na_2Ti_3O_7 > SrTiO_3$. It may be assumed that the amount of Sr exchange which occurs in the original wasteform will dramatically affect the phases assemblages formed. This is an area requiring further study where information relating to the industrial loading of SrT would prove helpful.

No phases containing Fe, Mn, Cr or Ni could be identified in the XRD traces, showing the canister has a minimal effect on the overall phase assemblage. However, as a study of the canister interaction has not been undertaken in this scoping study. The existence of other phases in the interaction zone cannot be ruled out and therefore requires further study.

Morphological and Compositional Variations

Overview and porosity: The characterisation of HIP-SrT by SEM supports the assignment of phases made using powder XRD analysis, yet also highlights that the nature of the wasteform is more complex than was suggested from XRD data alone.

For convenience in discussion the wasteform has been presented according to the three morphological regions identified in Section 7.3.2. These phases are closely related to the level of Sr exchange which occurred in the XC-SrT particles prior to HIPing. Evidence from SEM-EDX line scans and SEM-EDX mapping presented in Figures 7.7 and 7.8 shows the SEM-BSE grayscale correlates with Sr concentration. Using this correlation it is possible to compare the Sr map in Figure 7.3 with the SEM-BSE image in Figure 7.6 a). It is clear from this comparison that the nature of the XC-SrT particles is retained in the final wasteform. This indicates that the HIP-SrT wasteform is a formed via direct sintering of XC-SrT particles, with minimal diffusion of the Sr or other elements occurring during processing. With this knowledge, Region C can be identified as the outer edges of the particles prior to processing where the highest Sr concentration tended to result in the formation of $SrTiO_3$. This then allows us to make inferences on the nature and origin of the porosity present.

As discussed in Section 7.4.1 the XC-SrT was observed to exolve $SrCO_3$ after drying. It was further hypothesised that this may decompose upon HIPing, resulting in porosity within the wasteform. As the porosity in the sample is limited to the outer edges of these particles, not within the particles themselves, it may be assumed that the porosity present in Region C is formed as a result of $SrCO_3$ decomposition. Furthermore, it implies that the vacuum bake out at 400 °C was successful in removing the water from the XC-SrT. If the water had not been removed residual porosity within Region A after HIPing should be expected. Further study of the carbonation of the XC-SrT and determination of the mechanism by which this occurs should be performed in an attempt to eliminate the presence of $SrCO_3$, and as such, its impact on this wasteform processing methodology.

Morphological Regions: The identification of the phases present in the sample can be made based on a combination of the evidence provided from SEM and XRD analysis and roughly separated based on the three morphological regions identified.

Region A: This region has been identified as mixture of $Na_2Ti_3O_7$ and $Na_2Ti_6O_{13}$ where the Na has been partially substituted for Sr resulting in the reduction of Ti^{IV} to Ti^{III}. XRD analysis identifies $Na_2Ti_6O_{13}$ as the majority phase, which should correlate with the majority phase as identified on a volume basis in Figure 7.9. This suggests Region A is composed primarily of

$Na_2Ti_6O_{13}$. As this majority phase is also identified as having blue colouration from visual inspection, the presence of Ti^{III} in the phase is probable. Analysis via SEM-EDX using line scans and mapping illustrated the presence of Sr, this further supports the idea of a partial substitution. No evidence of microcrystalline Sr rich phases can be seen Region A so the partial exchange of Na from the titanate structure is the only explanation fitting all the data. Evidence supporting this theory has been presented from semi-quantitative SEM-EDX spot analysis. Here the presence of Sr was identified to correlate with a sodium titanate structure. It should be assumed however that Region A consists of a mixture of both identified sodium titantes, $Na_2Ti_6O_{13}$ and $Na_2Ti_3O_7$. As SEM-EDX lacks the resolution to accurately quantity the identity of each assemblage evidence supporting this hypothesis was found elsewhere. The differences in crystal shape identified in Figure 7.6 c) and the greater percentage of $Na_2Ti_6O_{13}$ measured via XRD (69.1 wt%) than observed via SEM-BSE montaging analysis (79.1 %) support the hypothesis of a mixed phase assemblage in Region A.

Further evidence supporting a combined phase assemblage for Region A was provided by the analysis of the Ti:(M^++M^{2+}) ratio presented in Table 7.2. The ratio obtained is somewhere between those of $Na_2Ti_6O_{13}$ and $Na_2Ti_3O_7$ and does not match any other known sodium titantes. It was therefore concluded that a mixture of the two sodium titanate phases indexed via powder XRD analysis is the most likely explanation of the results.

Region B: Identification of Region B as a single phase is not possible. Region B is a mixture of microcrystalline $SrTiO_3$ contained within a matrix of partially Sr exchanged sodium titantes. Evidence of this is first shown in the SEM-BSE false colour overlay in Figure 7.6 e). Microcrystalline regions exist within Region B whose greyscale values correlate to those assigned to Region C. This indicates that Region B is not heterogeneous in composition.

As we also see increased concentrations of Sr in this region, by comparison with Region A in SEM-EDX mapping and line scans, a combination of the phases present in Regions A and Region C seems the most likely scenario. Further support for this was be gathered from the SEM-EDX maps in Figure 7.8 showing that Region B has a decreased Ti concentration compared to Region A. This decrease in Ti concentration cannot be described by a partial substitution of Sr into the crystal lattice of $Na_2Ti_6O_{13}$ or $Na_2Ti_3O_7$. If this were the case, both Regions A and B would be expected to maintain a similar concentration of Ti in the mapping. The data from Ti mapping therefore supports the hypothesis that Phase B is comprised of a mixture of micron and sub-micron scale crystals of $SrTiO_3$ and a sodium titanate. The increase in the Sr concentrations measured are also suggestive of this.

Semi-quantitative SEM-EDX analysis shows that the average composition of this region fits no known phase composition, however it would provide a good representation of a mixture of sodium titantes and $SrTiO_3$ phases as described above.

Region C: This region has been assigned the identity of $SrTiO_3$. The presence of Na observed, as measured from semi-quantitative SEM-EDX analysis, could suggest that a partially exchanged phase exists in Region C with the composition $Na_xSr_{1-2x}TiO_3$. It is deemed more likely that the measured Na is a result of electron beam interaction with the surrounding phases, or from the inclusion of counts from surface Na_2CO_3, which will be discussed further in Section 7.4.3.

The inclusion of Sr in a titanate ceramic is promising for the ability of HIP-SrT to retain the Sr inventory in aqueous solution and will be further discussed in Sections 7.3.6 and 7.3.7. We can also see that no Sr is lost from the wasteform during processing. Although Sr is not homogeneously distributed throughout the wasteform, its concentration is a result of the partial exchange observed in the XC-SrT particles and reflects the original distribution in the material. As such, the Sr inventory of a full scale wasteform would be well distributed throughout the packaged volume, alleviating worries over the presence of potential radioactive hotspots.

The issue of retained porosity in the Sr rich regions of the wasteform, increases the potential for release of Sr into aqueous solution. Although the phase assemblages and nature of the wasteform produced are promising, further refinement is required for consideration of this methodology as a disposal option.

7.4.3 - Carbonation of HIP-SrT after Aging in Air

Figures 7.7 and 7.8, identified the correlation of increased Na and O in some areas of the HIP-SrT sample. This effect was observed in samples after storage in air. This is assumed to be a result of surface carbonation and results supporting this assignment will be presented and discussed below. As sample preparation took place over a week before investigations were performed, all samples show limited evidence of this effect. Unfortunately as carbon coating was performed prior to sample analysis, this effect was over looked until a point at which repetition of the data presented in Section 7.3.2 was impractical.

The presence of these Na_2CO_3 crystals on Region A, as illustrated in Figure 7.13 c), appear more dispersed, however, they are still clearly emanating from the sample surface and not from Region B. This indicates that the same chemistry is present in this region as seen in Region B, but to a lesser extent. From the earlier assignment of the crystalline phases it may be expected that a small quantity of $Na_2Ti_3O_7$ would be present in both Region A and Region B. If this is true

the effect of carbonation is directly related to the presence of $Na_2Ti_3O_7$. This phase can therefore be assumed to constitute the greater part of Region B. Although Na_2CO_3 crystals are present on the sample surface it is still possible to discern the fine structure of Region C. The crystal growth over this region may be attributed to growth from Region A and Region B. Further evidence of this is seen in top right of the SEM-BSE image in Figure 7.13 d-e.

It is noted from Figures 7.13 c-e that this crystal growth is not accompanied by any pitting or removal of surface material. This supports the earlier suggestion that an ion exchange and precipitation mechanism may be occurring. It is hypothesised that this is due to the presence of water in the air. This water is proposed to interact with the HIP-SrT, resulting in ion exchange mechanism, with preferential removal of Na^+ for H^+. This in turn would create an aqueous surface film with a high pH, rich in OH^- and Na^+. The high pH of the surface film is then likely to result in the uptake of significant CO_2 from the atmosphere resulting in the precipitation of the exchanged Na from the wasteform as Na_2CO_3. This carbonation is expected to be of minimal concern in the final wasteform, as SEM-EDX measurements shows Sr does not appear to co-precipitate in the carbonate form.

The carbonation of this material does however require further study to investigate the rate of crystal growth, possibility of expansive phase's formation and the determination of the responsible mechanism.

7.4.4 - Aqueous Dissolution Properties of HIP-SrT

PCT Experiments

Based on the low NR_i observed for Sr and Ti given in Tables 7.4 and 7.5, HIP-SrT behaves as an excellent matrix for Sr retention in aqueous solution. Although useful for determining comparative product quality, the PCT test is not ideally suited to determining the effects of solution pH on aqueous durability. This is highlighted in Figure 7.15 from the lack of an observable trend in the NL_i data produced. The failure of this experiment can be readily explained using the pH data in the same figure. Here it is shown, that in all three experimental scenarios, the solution pH was altered dramatically before the first sampling point.

An explanation for the behaviour of both the Na release and pH change during these static dissolution experiments can be attributed to the carbonation of the sample surface, as discussed in Section 7.4.1. As noted earlier, HIP-SrT particles are readily carbonated during storage in air. As Na_2CO_3 is highly soluble, this phase would provide an immediate release fraction of Na into solution. This would rapidly increase the solution pH and make the separation of effects based

upon initial solution pH impossible. As a result, no inference of the effect of pH to the aqueous dissolution of HIP-SrT can be attained from this experiment.

Despite the issues associated with the use of PCT experiments to determine the effects of pH on HIP-SrT dissolution, it was deemed that further study of the aqueous dissolution properties were worthwhile, based on the effective retention of Sr within the wasteform.

SPFT Experiments

As static experiments were unable to identify any effect of pH variation on the aqueous dissolution of HIP-SrT, dynamic experiments were performed using the SPFT methodology as described in Sections 3.10.4 and 7.2.2.

The main benefit of using a dynamic experimental methodology is that by refreshing the solution and preventing the initial build-up of Na in solution, the resultant increase in the solution pH is eliminated. This allowed effects of solution pH on dissolution rates to be discerned. These experiments allow for inference on the possible mechanisms responsible for dissolution to be presented. These proposed mechanisms are schematically represented in Figure 7.22.

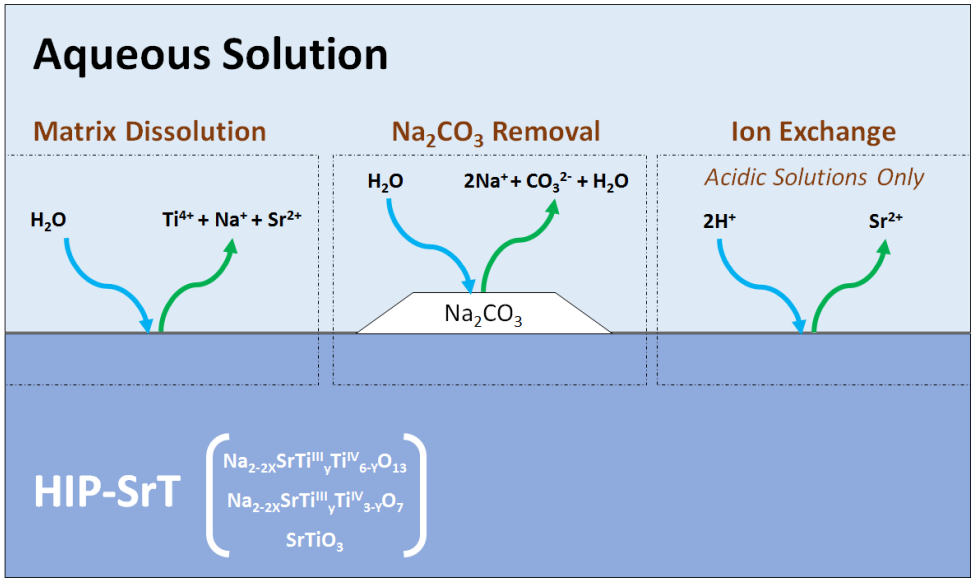

Figure 7.22 – Schematic illustration of the three mechanisms proposed to be prevalent in the aqueous dissolution of HIP-SrT.

Discussion of the data presented in Section 7.3.4 allows us to speculate on what is likely to be happening in the two solutions. Three mechanisms are proposed to contribute to the behaviour seen in these samples. The mechanisms suggested are matrix dissolution, carbonate removal and ion exchange.

Matrix Dissolution: This refers to a process of direct matrix dissolution via hydration. From the low forward NR_{Ti} obtained, this dissolution is proposed to occur slowly. As all elements eventually reach a forward NR_i, and those of Ti and Sr are achieved after approximately the same time in pH 10 solution, it is suggested that the forward NR_i in these cases is result of direct matrix dissolution. The rate of this dissolution is higher under acidic conditions than is observed in basic conditions. This is to be expected from the increased solubility of both Ti and Sr in acidic pH solution [266, 267].

Na_2CO_3 Removal: The high release of Na to solution at the beginning of the experiment is suggestive of the removal of a highly soluble Na rich phase. As was postulated previously for static experiments, the most likely explanation of this involves the removal of Na_2CO_3. After this initial release the subsequent rate then rapidly drops to the forward NR_{Na}, which can be assumed to be correlate with the residual dissolution rate of the matrix material.

Evidence of this effect is provided from investigation of the differences between the initial and forward rates obtained for each element, with varying solution pH. At pH 10 for Ti and Sr an 8-15 fold decrease in NR_i was observed between the initial NR_i and the attainment of the forward NR_i. However, in the case of Na release a 60 fold decrease in rate over the same period was measured. This indicates that this initial massive release Na cannot be put down to removal of fines or to active surface site dissolution as these effects would be expected to affect each NR_i to a similar extent. By combination of this data with that from PCT experiments and of sample carbonation, an assignment can be made with that this initial release of Na results from the removal of the Na_2CO_3 from the sample surface.

Further support for the above assumptions are evident in the profile of NR_{Na} with variation in effluent pH. The release of Na prior to attainment of the forward NR_{Na} is similar under both acidic and basic conditions. This indicates the massive initial release is dominated by an effect which is largely unaltered by solution pH. This would be true of the removal of Na_2CO_3 but not as a result of the removal of fines or matrix dissolution.

Ion Exchange: The difference between the two experiments is steady in the case of Ti, but for Sr it is initially high and levels upon the attainment of forward NR_{Sr}. This shows that in the early stages of dissolution an additional pathway for Sr release is present in acidic solution, which is unavailable at pH 10. This decrease is suggestive of a diffusive ion exchange mechanism at lower temperature, which correlates with what may be expected from the known behaviour of strontium titantes from the literature [173, 175, 260].

It is hypothesised that an ion exchange mechanism exists in the acidic solution whereby $Sr^{2+}_{(s)}$ exchanges for $2H^{+}_{(aq)}$. This is proposed in order to explain the increased initial NR_{Sr} observed under acidic conditions. It is suggested that this mechanism would involve the protonation of the partially exchanged sodium titanate, displacing Sr which is then released to solution. Evidence of this behaviour is highlighted in Figure 7.17, which plots the difference between the NR_i during the pH 2 and pH 10 SPFT experiments. As all other effects can be considered constant in this difference plot, any effects are directly attributable to the effect of solution pH on dissolution.

An alternative argument could be postulated in order to explain the increased initial NR_{Sr} observed under acidic conditions. It could be proposed that the Sr exists as a surface precipitated carbonate phase. This phase could then be subject to a rapid release in the pH 2 experiments. This mechanism has been discounted for two reasons. Firstly as shown in Figure 7.13 there is no evidence in the SEM-BSE images indicating a significant increase in Sr concentration in the surface precipitated carbonate phase.

Further evidence that the increased initial NR_{Sr} found in acidic pH is not due to removal of surface precipitated $SrCO_3$ is provided via the geochemical modelling of the SPFT solution data. As all data points for $SrCO_3$ are below saturation in solution, it can be concluded that solubility limiting effects, based on pH for $SrCO_3$ dissolution, were not responsible for this behaviour. Further evidence that $SrCO_3$ is not affecting the dissolution rates is provided by the lack of precipitates found in the eluents measured. This was shown by comparison of the filtered and unfiltered ICP-MS samples.

General Performance of HIP-SrT in Aqueous Solution: Importantly, HIP-SrT behaves exceptionally as a wasteform for Sr immobilisation, with a maximum residual $NR_{(Sr)}$ measured at $2.7 \times 10^{-4} \pm 8.1 \times 10^{-5}$ g m^{-2} day^{-1}. It should be highlighted that this release rate was obtained using highly aggressive conditions with dynamic experimentation at 90 °C. These experiments provide a much more severe environment that that expected in any repository environment.

Use of Equation 7.5 gives us an estimated total Sr loss from the wasteform of 2.18 % at pH 2 and 0.025 % at pH 10. Although the loss is significantly higher at pH 2 than at pH 10 it should be noted that over 97.72% of the Sr was still retained in the wasteform. The initial release fraction in the first 62 hours of testing accounts for over 82% of the total loss which occurred. This validates the assumption of a low forward NR_{Sr} and an initial release fraction at this level could be readily justified for use in a disposal scenario.

The pH 10 scenario provides even more favourable data supporting the quality of the wasteform. The pH of groundwater in a GDF is more likely to be basic than acidic due to the use of cement in either the structure or backfill of a GDF. Where the ion exchange mechanism is not deemed to be present, over 90% of the total Sr loss is accounted for in the first 14 hours of testing, most likely as a result of the removal of fines from the HIP-SrT powders, followed by a very low residual rate of release.

Concerns may be raised in a cementitious repository due to the release of high proportions of Ca from the cement matrices. As discussed on Section 2.4.3 sodium titantes show a low K_d for Sr in the presence of Ca and therefore it should be assumed that a mechanism similar to the protonation of the wasteform occurring in acidic solution, could develop in the presence of Ca^{2+} in solution. However, from the data presented in Figure 2.12, protonation of the sodium titanates within acidic solution should be considered the most effective promoter of ion exchange with Sr. As the HIP-SrT behaves well at pH 2 it is also assumed it will behave favourably with the presence of Ca^{2+} in solution. However, further work to support this assumption should be performed.

Analysis of Leached Samples: Figures 7.19 a-g show that the little change occurs with the particles during these experiments. The morphological and chemical features observable via SEM-BSE imaging are all retained before and after the experiments. This indicates that the particles are physically stable in solution as should be expected from the low NR_i values obtained during SPFT and PCT experiments on the material. The images also provide evidence for the retention of Sr during sample preparation and SPFT experiments. The greyscale variations in Figures 7.19 b-e and f) are indicative of Sr concentration in the sample, as was characterised for monolithic samples previously discussed in Section 7.3.2 and Section 7.4.2.

Semi-quantitative SEM-EDX data from the sample surface at the point where the SEM-EDX line scan was performed. This data is provided in Table 7.8. The data also shows good correlation with that previously measured for each morphological phase. Furthermore it supports the conclusion made above that Sr is retained in the HIP-SrT wasteform during aggressive aqueous dissolution.

The absence of a concentration gradient at the samples edge for Na and Sr suggests that an ion exchange mechanism is not prevalent at the higher pH values which these static experiments buffer to. The presence of this mechanism cannot, however, be fully discounted as the maximum resolution attainable with SEM-EDX analysis is approximately 0.5 - 5 µm. Further investigation

into the leached layer properties should be performed to confirm the presence of an ion exchange mechanism under acidic experimental conditions.

7.5 - Conclusions and Future Work

The scoping study for this work has successfully processed SrTreat into a solid, durable wasteform. Several properties and behaviours of the wasteform produced are of academic interest and further study should be performed on these materials to qualify their suitability for waste disposal.

The purpose of this work was to study whether an alternative operational route for SrTreat® could be developed, whereby pre-packaged canisters could be used as both the ion exchange column and the waste package container, allow production of a suitable wasteform via direct HIPing. The results of this study are mixed with respect to this proposal.

The HIPing of SrTreat® provides a ceramic wasteform, which results from sintering and crystallisation of the exchanged SrTreat® particles. The phases formed are a mixture of $SrTiO_3$ and partially Sr exchange sodium titantes. This partial exchange of Sr for Na is possibly correlated with a partial reduction of Ti^{IV} to Ti^{III} giving the ceramic its characteristic blue colouration.

It should be noted that a number of properties are highly favourable and suggest this immobilisation methodology, if not the operational modifications suggested, should be investigated further. These include;

1. The production of a solid monolith from a readily dispersible powder.
2. Volume reduction of the packaged waste of at least 50 %.
3. Formation of ceramic phases which retain the entire Sr inventory during processing and also show exceptional aqueous durability properties.

However, there are a number of issues which require addressing with further study. These primarily concern the processing parameters selected and the final wasteform produced.

1. The attempt to eliminate use of a calcination step resulted in significant residual porosity in the sample. This porosity is interconnected throughout the Sr rich region of the wasteform, as such increasing the potential rate of Sr release.
2. There is the issue of the processed samples carbonation. From the data collected it seems likely that this carbonation only results in the removal of Na from the sample. More in-depth analysis should be performed concerning the mechanism by which this

carbonation occurs along with determination of the amount of Sr which co-precipitates with the Na.

Future work should investigate methods to remove $SrCO_3$ prior to HIPing materials and investigate the effect of Ca^{2+} on the dissolution of the wasteforms.

Chapter 8 - Summary

Note to Reader: A more detailed summary of the results and discussion, as relevant to each waste stream, has been provided at the end of each technical chapter. For the sake of brevity these details will not be repeated here.

The overarching aim of this thesis was to investigate the ability to produce ILW wasteforms, for a breadth of waste streams, using thermal treatments. For this reason, the waste streams selected were extremely diverse in their physical, chemical and radiological properties, origin and envisaged disposal volume.

During the course of this thesis methodologies for the immobilisation of four complex and problematic radioactive wasteforms have been presented. Each of these solutions has been shown to meet the primary aim for ILW processing, through the production of a robust, monolithic wasteform. All the processing methods and wasteforms presented have provided improvements in the wasteform quality when compared with the cementitious baseline. Most importantly, all of these wasteforms have been shown to, or should reasonably be expected to, significantly reduce the packaged waste volume and provide an increased retention of radioisotopes upon exposure to aqueous solution.

This thesis has shown that alternatives to cementation can be rapidly developed to thermally process ILW. This is beneficial for the ongoing clean-up operations at the UKs nuclear sites. Although cementation may appear to be the easiest solution in the short term, a multi-mission facility, such as a HIP plant, should be considered beneficial for certain wastes when emphasis is placed on safety during interim storage and long term stability in a GDF. The ability to readily process small volumes of problematic wastes, or to provide huge waste volume reduction for larger waste inventories, provides potential lifetime savings, improved product qualities and social benefits.

Although each waste has been shown to be suitable for disposable it should be noted that each wasteform was compromised in some form. These compromises include composite fracturing, potential volatilisation, chemical segregation, carbonation and residual porosity. Suggestions have been made throughout this thesis for future investigations to optimise these parameters.

The thermal treatment of ILW will inevitably involve the utilisation of processing methodologies similar to those investigated during the course of this thesis. The success of the results presented

here shows the applicability of these techniques, not only the immobilisation of the specific waste streams discussed, but hopefully for a variety of other wastes.

As the plans for a GDF mature, it is expected that the idea of volume reduction in ILWs by thermal treatment will gain wider acceptance. Minimising the total volume of waste will result in a smaller GDF, reduced interim storage capacity, a lower demand for waste packaging containers and fewer waste transports. All of these factors will have significant cost implications on the projected lifetime waste management costs, and as such, are expected to outweigh the cost of constructing a suitable thermal treatment plant. Furthermore, the reduced logistical challenges encountered from a smaller number of waste packages would help expedite the final disposal of UK wastes and closure of a GDF, minimising social disruption. Improved product quality in the processed wasteforms will improve any safety case for GDF disposal, future proof the waste against regulatory changes and potentially provide confidence in the general population for GDF construction. Further research and commercial development into the treatment of ILW is strongly recommended based upon the results of work carried out in this thesis.

Appendix I - Installation of an AIP 630H HIP

During the course of this PhD a significant investment in time was placed into commissioning the University of Sheffield's research scale HIP facility and developing its capability. In order to reflect upon this investment a short appendix is included outlining the commissioning process, operating windows and a basic overview of the American Isostatic Presses AIP 6-30H Research Scale HIP, as is now operational at the University of Sheffield.

The mechanism and process of HIPing has been previously outlined in Section 2.3 and this chapter has the sole aim of highlighting the work performed whilst installing this HIP capability.

AIP 6-30H HIP Specifications

The AIP 6-30H HIP is best described as a research scale HIP rig, having a significantly smaller working dimension than most commercially available HIP rigs. However, the AIP 6-30H offers a wide operating envelope due to its two interchangeable furnace arrays giving a wide range of processing parameters as shown in Table 8.1. This unit also has the capacity to be run as a low temperature vacuum furnace.

Parameter		Operational Range
Temperature	*Molybdenum Furnace*	25 – 1400 °C
	Graphite Furnace	25 – 2200 °C
Pressure		300 Pa – 206 MPa
Vacuum		~ 35 Pa (Temperatures up to 250 °C)

Table AI.1 Operating parameters for the AIP 6-30H HIP installed at the University of Sheffield.

Below is timeline of the installation and operating responsibilities undertaken during the course of this PhD thesis. Figures 8.2 - 8.4 illustrate and label the critical components of this HIP rig.

Timeline of AIP 6-30H HIP Installation

June 2007- AIP 6-30H delivered by American Isostatic Presses to University of Sheffield, Quarrell Laboratory

September 2011- Stage one of Quarrell Lab refurbishment started. Initial HIP risk assessment performed. Working area for HIP site selected.

October 2012- Placement of HIP pressure vessel and control unit in Quarrell lab.

November 2012 - Electrical connections sited for HIP unit and sample preparation station. 4x1 high pressure argon manifold sited.

December 2012 – Off gas plumbing installation completed. Chiller unit installation completed.

January 2013 –Quarrell lab refurbishment completed

February 2013- Final Installation and commissioning by AIP.

March 2013 - Standard operating procedure and functional risk assessment produced.

March 2013- Present – Operations and secondary user training.

May 2014 – Approval granted for processing of sealed radioactive sources in the HIP.

Figure AI.1 Images showing the installation of AIP 6-30H in the Quarrell laboratory, The University of Sheffield

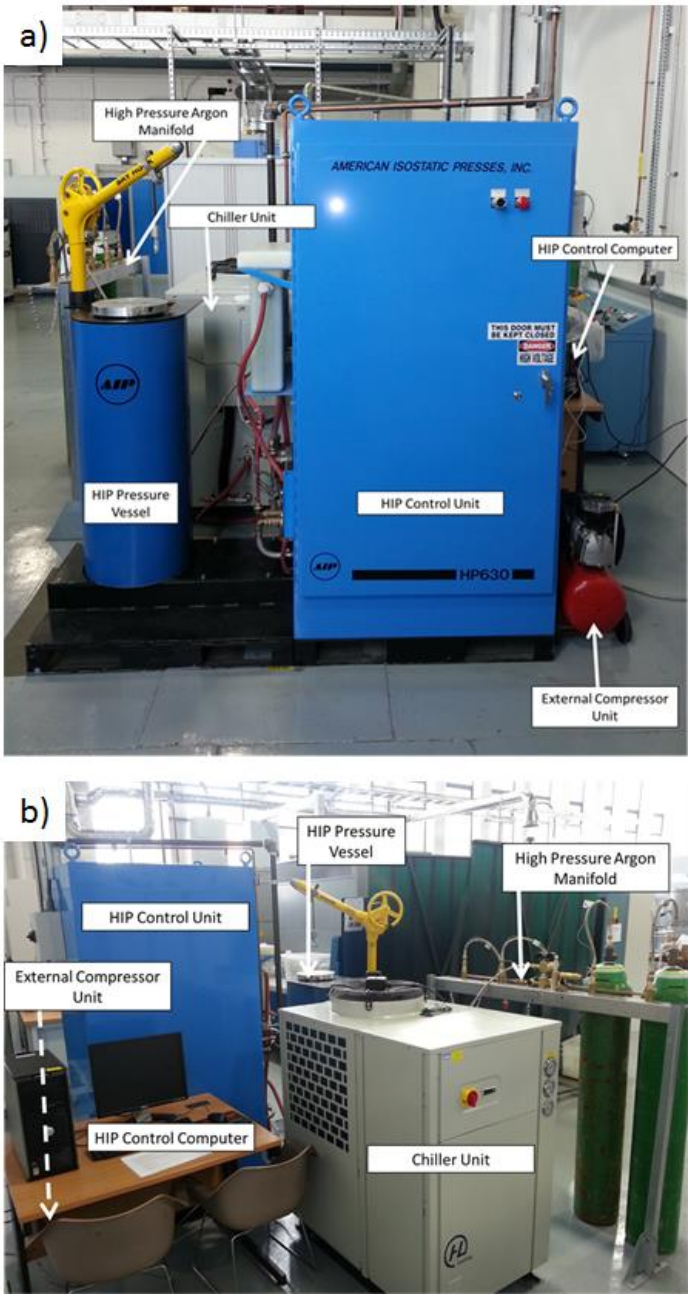

Figure AI.2 a) Front view and b) rear view of main components of the University of Sheffield's AIP 6-30H HI

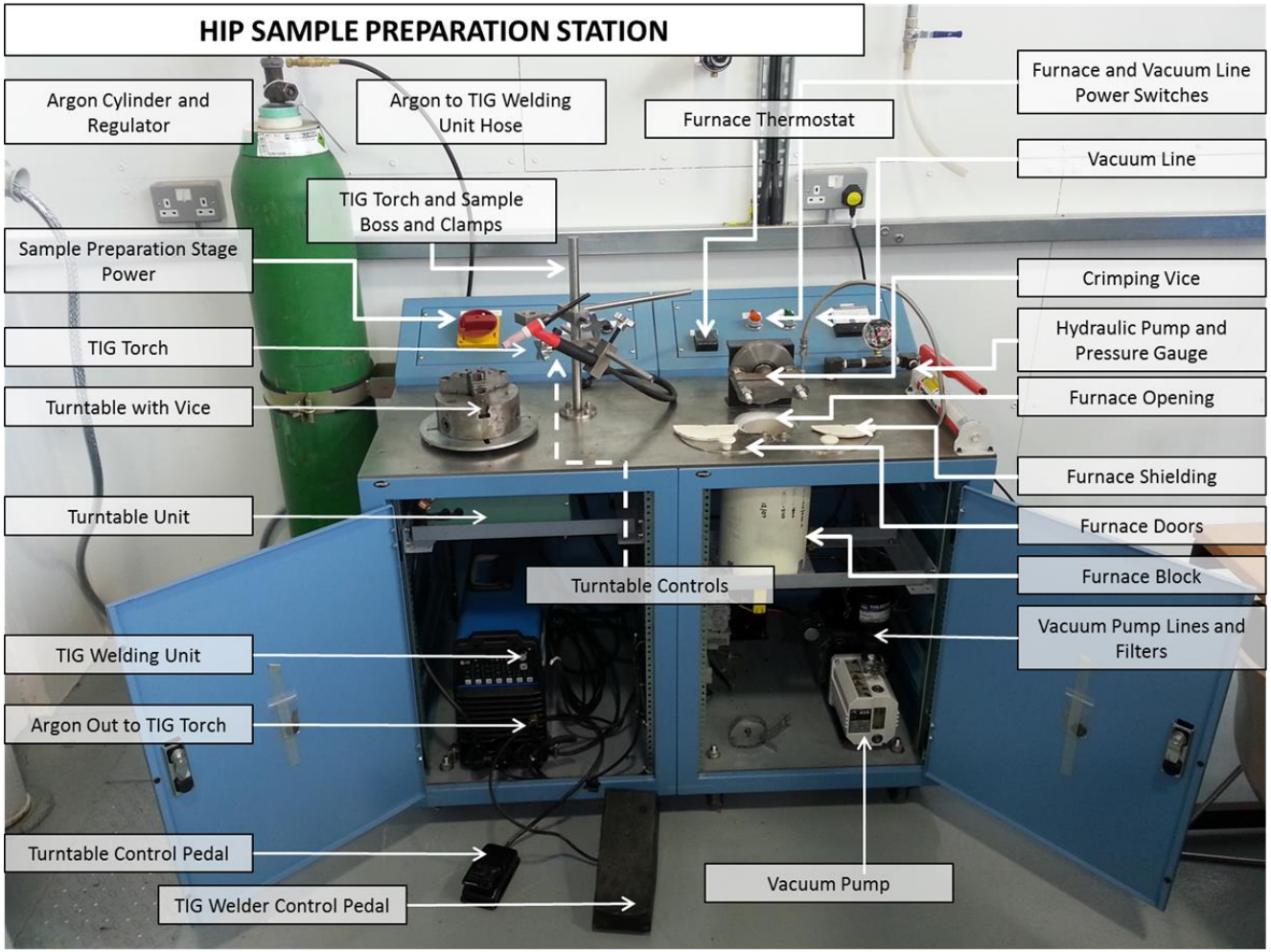

Figure AI.3 Labelled image of sample preparation station for the canning of HIP samples.

Appendix II - List of Figures

Chapter 4

Appendix III - List of Tables

References

[1] I.W. Donald, Waste Immobilisation in Glass and Ceramic Based Hosts: Radioactive, Toxic and Hazardous Wastes, Wiley, London, 2010.

[2] UK Goverment Statisitcs Report, Electricity generation and supply figures for Scotland, Wales, Northern Ireland and England, 2008 to 2011, Available from: https://www.gov.uk/government/uploads/system/uploads/attachment_data/file/65841/7345-elec-gen-2008-2011-et-article.pdf, *Accessed on: 05/12/2013*.

[3] Department of Energy and Climate Change, Historical electricity data: 1920 to 2011, Available from: https://www.gov.uk/government/statistical-data-sets/historical-electricity-data-1920-to-2011, *Accessed on: 24/04/2015*.

[4] M. Ojovan, W. E. Lee, An Introduction to Nuclear Waste Immobilisation, 1st ed., Elsevier B. V., Amsterdam, 2005.

[5] John Liley, Nuclear Physics: Principles and Applications, Wiley & Sons Ltd., London, 2001, p.266.

[6] P. Atkins, J. DePaula, Atkins Physical Chemistry, 8th ed., Oxford University Press, Oxford, 2006, p.8.

[7] Editorial, 'Nuclear' is not the Question, *Nature Materials*, 7 (2008) 9.

[8] P. M. B. Walker, Chambers' Nuclear Energy and Radiation Dictionary, Chambers, Edinburgh, 1992, p. 87-114.

[9] National Research Council, Committee on the Biological Effects of Ionizing Radiation, Health Effects on Populations of Exposure to Low Levels of Ionizing Radiation (BEIR V). National Academy of Sciences, Washington D.C, 1990, Available from: http://www.nap.edu/openbook.php?record_id=1224&page=1, *Accessed on: 05/12/2013*.

[10] John Liley, Nuclear Physics: Principles and Applications, Wiley & Sons Ltd., London, 2001.

[11] D.J. Brenner, R. Doll, D.T. Goodhead, E.J. Hall, C.E. Land, J.B. Little, J.H. Lubin, D.L. Preston, R.J. Preston, J.S. Puskin, E. Ron, R.K. Sachs, J.M. Samet, R.B. Setlow, M. Zaider, Cancer risks attributable to low doses of ionizing radiation: Assessing what we really know, *Proceedings of the National Academy of Sciences*, 100 (2003) 13761-13766.

[12] E.A. Blakely, Biological Effects of Cosmic Radiation: Deterministic and Stochastic, *Health physics*, 79 (2000) 495-506.

[13] A.M. Fred, Medical effects and risks of exposure to ionising radiation, *Journal of Radiological Protection*, 32 (2012) 9.

[14] DEFRA, Managing Radioactive Waste Safely - Proposals for developing a policy for managing solid radioactive waste in the UK, 2001, Available from; http://webarchive.nationalarchives.gov.uk/20031221042814/http:/www.defra.gov.uk/environment/consult/radwaste/pdf/radwaste.pdf *Accessed on 01/04/2014*.

[15] Nuclear Decommisioning Authority, Radioactive Wastes in the UK: A Summary of the 2010 Inventory, Available from: http://www.nda.gov.uk/ukinventory/documents/Reports/upload/2010-UK-Radioactive-Waste-Inventory-Summary-of-the-2010-Inventory.pdf, *Accessed on: 05/12/2013*.

[16] Bureau International Des Poids Et Mesures, Table of Radionuclides, 2008, Available from: http://webarchive.nationalarchives.gov.uk/20130109092117/http:/decc.gov.uk/en/content/cms/statistics/energy_stats/source/electricity/electricity.aspx, *Accessed on: 05/12/2013.*

[17] Nirex, The viability of a phased geological repository concept for the long-term management of the UK's radioactive waste, Nirex Report N/122, (November 2005).

[18] CoRWM, Managing our Radioactive Wastes Safely: CoRWM's Recomendations to Government, July 2006, Available from: http://www.westcumbriamrws.org.uk/documents/700_-_CoRWM_July_2006_Recommendations_to_Government.pdf, *Accessed on: 05/12/2013*.

[19] IAEA, Technical, institutional and economic factors important for developing a multinational radioactive waste repository, IAEA-TECDOC-1021 ISSN 1011-4289, (June 1998).

[20] https://www.nda.gov.uk/ukinventory/waste/ *Accessed on 02/05/2014*.

[21] I.W. Donald, Waste Immobilisation in Glass and Ceramic Based Hosts: Radioactive, Toxic and Hazardous Wastes, Wiley, London, 2010, p.101-121.

[22] M. Ojovan, Handbook of Advanced Radioactive Waste Conditioning Technologies, 2011.

[23] Nuclear Decommisioning Authority, Radioactive Wastes in the UK: Main Report, Available from: http://www.nda.gov.uk/ukinventory/documents/Reports/upload/2010-UK-Radioactive-Waste-Inventory-Main-Report.pdf, *Accessed on: 05/12/2013*.

[24] P.K. Abraitis, G. Davies, Disposability of the UK's Intermediate Level Wastes, *MRS Online Proceedings Library*, 1107 (2008) p. 35.

[25] G.A. Fairhall, The UK National Nuclear Laboratory and Waste Management R&D, *MRS Online Proceedings Library*, 1107 (2008) p.3.

[26] N.W. Brown, A.K. Campen, D.A. Wickenden, E.P.L. Roberts, On-site destruction of radioactive oily wastes using adsorption coupled with electrochemical regeneration, *Chemical Engineering Research and Design*, 91 (2013) 713-721.

[27] S. Doudou, J. McTeer, S. Wickham, R. Thied, R. Woodcock, T. Turner, C. Hamblin, M. Buckley, C. Walsh, Optimised Management of Orphan Wastes in the UK, in: *ASME 2013 15th International Conference on Environmental Remediation and Radioactive Waste Management*, American Society of Mechanical Engineers, 2013.

[28] C. R. Scales, E. R. Maddrell, N. Gawthorpe, B. D. Begg, S. Moricca, R. A. Day and M. A. Stewart, Demonstrating Glass Ceramic route for the Immobilization of Plutonium containing Wastes and Residues on the Sellafield Site, *Waste Management*, Feb. 26th - Mar. 2nd 2006, Tucson Az.

[29] F.P. Glasser, M. Atkins, Cements in Radioactive Waste Disposal, *MRS Bulletin*, 19 (1994) 33-38.

[30] A.E. Osmanlioglu, Progress in cementation of reactor resins, *Progress in Nuclear Energy*, 49 (2007) 20-26.

[31] F.P. Glasser, Fundamental aspects of cement solidification and stabilisation, *Journal of Hazardous Materials*, 52 (1997) 151-170.

[32] D.E. Macphee, F.P. Glasser, Immobilisation Science of Cement Systems, *MRS Bulletin*, 18 (1993) 66-71.

[33] F.P. Glasser, Mineralogical aspects of cement in radioactive waste disposal, *Mineralogical Magazine*, 65 (2001) 621-633.

[34] J. H. Sharp, J. Hill, N. B. Milestone and E. W. Miller, CEMENTITIOUS SYSTEMS FOR ENCAPSULATION OF INTERMEDIATE LEVEL WASTE, *Proceedings of ICEM '03: The 9th International Conference on Radioactive Waste Management and Environmental Remediation*, September 21 - 25, 2003, Examination School, Oxford, England.

[35] R. D. Spence and C. Shi, Stabilisation and Solldification of Hazardours, Radioactive and Mixed Wastes, CRC Press, Boca Raton, 2005.

[36] C. Utton, I. H. Godfrey, Review of stability of cemented grouted ion-exchange materials, sludges and flocs, NNL (09) 10212 Issue 2, (29 January 2010).

[37] M. W. A. Stewart, E.R. Vance, S. A. Moricca, D. R. Brew, C. Cheung, T. Eddowes and W. Bermudez, Immobilisation of Higher Activity Wastes from Nuclear Reactor Production of ^{99}Mo, Science and Technology of Nuclear Installations, Article ID 926026 (2013).

[38] N.B. Milestone, Y. Bai, P.R. Borges, N.C. Collier, J.-P. Gorce, L.E. Gordon, A. Setiadi, C.A. Utton, Q. Zhou, Reactions in cemented nuclear waste forms - The need for a toolbox of different cement types, in: P. VanIseghem (Ed.) *Scientific Basis for Nuclear Waste Management XXIX*, 2006, pp. 673-680.

[39] A. Setiadi, N.B. Milestone, J. Hill, M. Hayes, Corrosion of aluminium and magnesium in BFS composite cements, *Advances in Applied Ceramics*, 105 (2006) 191-196.

[40] M. Hayes and I. H. Godfrey, Development of the Use of Cements for the Treatment of Intermediate Level Waste, *Waste Management,* Feb. 26th - Mar. 2nd 2006, Tucson Az., (March 2007).

[41] A.P. Covill, Novel Encapsulants for Intermediate Level Waste in the UK Nuclear Industry, PhD thesis, Submitted to the Department of Materials Science and Engineering, The University of Sheffield, PhD (2010).

[42] P.J. McGlinn, D.R.M. Brew, L.P. Aldridge, T.E. Payne, K.P. Olufson, K.E. Prince, I.J. Kelly, Durability of a Cementitious Wasteform for Intermediate Level Waste, *MRS Online Proceedings Library*, 1107 (2008) p.101.

[43] N. Milestone, Y. Bai, C.H. Yang, Y.J. Shi, X.C. Li, The Use of Activated Slags as Immobilisation Matrices for ILW, *MRS Online Proceedings Library*, 1107 (2008) p.93.

[44] IAEA, Joint Evaluated Fission and Fusion File, Incident-neutron data, 2 October 2006; Available from http://www-nds.iaea.org/exfor/endf00.htm, *Accessed on 02/05/2014*.

[45] G. Kessler, Sustainable and Safe Nuclear Fission Energy: Technology and Safety of Fast and Thermal Nuclear Reactors, Springer Science & Business Media, 2012.

[46] J. Cronin, N. Collier, Corrosion & Expansion of Grouted Matrix, National Nuclear Laboratory, NNL (11) 11524 Issue 3, (23 November 2011).

[47] L.E. Gordon, N.B. Milestone, M.J. Angus, The immobilisation of clinoptilolite within cementitious systems, *MRS Online Proceedings Library*, 1107 (2008) p.135.

[48] M. Wise, Management of UKAEA graphite liabilities, in: Proceedings of Technical Committee Meeting, Nuclear Graphite Waste Management. Manchester, UK, 1999.

[49] John Rees, Wigner Energy in Irradiated Graphite and Post-Closure Safety, Environment Agency, R&D Technical Report P3—80/TR, 2002.

[50] N.C. Hyatt, M. James, Thermal treatment of ILW, *Nuclear Engineering International*, 58 (2013) 10-13.

[51] J.E. Shelby, An Introdcution to Glass Science and Technology, The Royal Society of Chemistry, 2005.

[52] I.W. Donald, B.L. Metcalfe, R.N.J. Taylor, The immobilization of high level radioactive wastes using ceramics and glasses, *Journal of Materials Science*, 32 (1997) 5851-5887.

[53] R.H. Doremus, Glass Science, 2nd ed., John Wiley and Sons, New York, 1994, p.113-121.

[54] A.C. Wright, R.A. Hulme, D.I. Grimley, R.N. Sinclair, The structure of some simple amorphous network solids revisited, *Journal of Non-Crystalline Solids*, 129 (1991) 213-232.

[55] W.H. Zachariasen, The atomic arrangement in glass, *Journal of the American Chemical Society*, 54 (1932) 3841-3851.

[56] A.C. Wright, G.A.N. Connell, J.W. Allen, Amorphography and the modelling of amorphous solid structures by geometric transformations, *Journal of Non-Crystalline Solids*, 42 (1980) 69-86.

[57] G.N. Greaves, EXAFS and the structure of glass, *Journal of Non-Crystalline Solids*, 71 (1985) 203-217.

[58] G.N. Greaves, A. Fontaine, P. Lagarde, D. Raoux, S.J. Gurman, Local Structure of Silicate Glasses, *Nature*, 293 (1981) 611-616.

[59] B.E. Warren, Summary of Work on Atomic Arrangement in Glass, *Journal of the American Ceramic Society*, 24 (1941) 256-261.

[60] K.H. Sun, Fundamental Condition of Glass Formation, *Journal of the American Ceramic Society*, 30 (1947) 277-281.

[61] J.E. Shelby, An Introdcution to Glass Science and Technology, The Royal Society of Chemistry, 2005, p.94 -112.

[62] J. Krogh-Moe, The structure of vitreous and liquid boron oxide, *Journal of Non-Crystalline Solids*, 1 (1969) 269-284.

[63] D.R. Uhlmann, R.R. Shaw, The thermal expansion of alkali borate glasses and the boric oxide anomaly, *Journal of Non-Crystalline Solids*, 1 (1969) 347-359.

[64] A.C. Wright, G. Dalba, F. Rocca, N.M. Vedishcheva, Borate versus silicate glasses: why are they so different?, *Physics and Chemistry of Glasses-European Journal of Glass Science and Technology Part B*, 51 (2010) 233-265.

[65] H. Doweidar, Consideration of the Boron - Oxide Anomaly, *Journal of Materials Science*, 25 (1990) 253-258.

[66] H. Scholze, Glass - Nature Strucutre and Properties, 1st ed., New York, Berlin, Heidelberg, 1991, p.123 - 136.

[67] H. Scholze, Glass - Nature Strucutre and Properties, 1st ed., New York, Berlin, Heidelberg, 1991, p.54.

[68] *Encyclopedia Britannica II,* 1786, p. 716.

[69] Encyclopedia Britannica Online Article: Glass, Available from http://www.britannica.com/EBchecked/topic/234888/glass *Accessed on 18/02/2014*.

[70] R. Boyle, The Origins of Forms and Qualitites, Oxford, (1666).

[71] L.L. Hench, D.E. Clark, Physical chemistry of glass surfaces, *Journal of Non-Crystalline Solids*, 28 (1978) 83-105.

[72] G.G. Wicks, Nuclear Waste Glasses: Corrosion Behaviour and Field Tests, in: Corrosion of Glass, Ceramics and Ceramic Superconductors, Noyes Publications, New Jersey, 1992, pp. 218-260.

[73] W.E.S. Turner, A Bibliographical Contribution towards the Study of the Durability of Glass, *Journal of the Society of Glass Technology*, 1 (1917) 213-222.

[74] J.R. Beattie, *Journal of the Society of Glass Technology*, 36 (1952) 37-45.

[75] L. Holland, The Properties of Glass Surfaces, Chapman and Hall, London, 1966.

[76] D. E. Clark, C.G Pantano, L. L. Hench, Corrosion of Glass, Books for Industry, New York, 1979.

[77] W. Lutze, R. C. Ewing, Radioactive Waste Forms for the Future, Elsevier Science Publishers (North-Holland), 1988, p.699- 740.

[78] B. Grambow, Geochemical Approach to Glass Dissolution, in Corrosion of Glass, Ceramics and Ceramic Superconductors, Noyes Publications, New Jersey, (1992) 124-148.

[79] C.M. Jantzen, Thermodynamic Approach to Glass Corrosion, in: Corrosion of Glass, Ceramics and Ceramic Superconductors, Noyes Publications, New Jersey, 1992, pp. 152-216.

[80] P. Frugier, S. Gin, Y. Minet, T. Chave, B. Bonin, N. Godon, J.E. Lartigue, P. Jollivet, A. Ayral, L. De Windt, G. Santarini, SON68 nuclear glass dissolution kinetics: Current state of knowledge and basis of the new GRAAL model, *Journal of Nuclear Materials*, 380 (2008) 8-21.

[81] I.W. Donald, Waste Immobilisation in Glass and Ceramic Based Hosts: Radioactive, Toxic and Hazardous Wastes, Wiley, London, 2010, p.275 - 342.

[82] B. Grambow, Corrosion of Glass in: Uhlig's Corrosion Handbook, John Wiley & Sons, 2011, pp. 399-419.

[83] A. V. Elsden, O. Robert, H. S. Jones, The Examination of Optical Glass in Relation to Weathering Properties, *Journal of the Society of Glass Technology*, 3 (1919) 52-69.

[84] S. Gin, C. Guittonneau, N. Godon, D. Neff, D. Rebiscoul, M. Cabie, S. Mostefaoui, Nuclear Glass Durability: New Insight into Alteration Layer Properties, *Journal of Physical Chemistry C*, 115 (2011) 18696 -18706.

[85] T. Geisler, A. Janssen, D. Scheiter, T. Stephan, J. Berndt, A. Putnis, Aqueous corrosion of borosilicate glass under acidic conditions: A new corrosion mechanism, *Journal of Non-Crystalline Solids*, 356 (2010) 1458-1465.

[86] S. Gin, P. Frugier, P. Jollivet, F. Bruguier, E. Curti, New Insight into the Residual Rate of Borosilicate Glasses: Effect of S/V and Glass Composition, *International Journal of Applied Glass Science*, 4 (2013) 371-382.

[87] B. Bunker, Molecular mechanisms for corrosion of silica and silicate glasses, *Journal of Non-Crystalline Solids*, 179 (1994) 300-308.

[88] C. Cailleteau, F. Angeli, F. Devreux, S. Gin, J. Jestin, P. Jollivet, O. Spalla, Insight into silicate-glass corrosion mechanisms, *Nature Materials*, 7 (2008) 978-983.

[89] R.H. Doremus, Y. Mehrotra, W.A. Lanford, C. Burman, Reaction of water with glass - Influence of a transformed surface, *Journal of Materials Science*, 18 (1983) 612-622.

[90] T.A. Wassick, R.H. Doremus, W.A. Lanford, C. Burman, Hydration of soda-lime silciate glass, effect of alumina, Journal of Non-Crystalline Solids, 54 (1983) 139-151.

[91] W.A. Lanford, K. Davis, P. Lamarche, T. Laursen, R. Groleau, R.H. Doremus, Hydration of soda-lime glass, *Journal of Non-Crystalline Solids*, 33 (1979) 249-266.

[92] B.P. McGrail, J.P. Icenhower, D.K. Shuh, P. Liu, J.G. Darab, D.R. Baer, S. Thevuthasen, V. Shutthanandan, M.H. Engelhard, C.H. Booth, P. Nachimuthu, The structure of Na_2O-Al_2O_3-SiO_2 glass: impact on sodium ion exchange in H_2O and D_2O, *Journal of Non-Crystalline Solids*, 296 (2001) 10-26.

[93] M. Tomozawa, D.J. Cherniak, P.J. Lezzi, Hydrogen-to-alkali ratio in hydrated alkali aluminosilicate glass surfaces, *Journal of Non-Crystalline Solids*, 358 (2012) 3546-3550.

[94] D. Gelder, S. Fearn, Anomalous diffusion in the hydration of glass surfaces, *Glass Technology-European Journal of Glass Science and Technology Part A*, 53 (2012) 46-52.

[95] P. Aagaard, H. C. Helgeson, Thermodynamic and kinetic constraints on reaction rates among minerals and aqueous solutions; I, Theoretical considerations, *American Journal of Science*, 282 (1982) 237-285.

[96] R.H. Doremus, Interdiffusion of hydrogen and alkali ions in a glass surface, *Journal of Non-Crystalline Solids*, 19 (1975) 137-144.

[97] G. Geneste, F. Bouyer, S. Gin, Hydrogen–sodium interdiffusion in borosilicate glasses investigated from first principles, *Journal of Non-Crystalline Solids*, 352 (2006) 3147-3152.

[98] F. Delage, F. Larche, E. Vernaz, Dissolution of R7T7 Glass in Static and Flowing Conditions: Influence of Si Diffusion Mechanism in the Leached Layer, *MRS Online Proceedings Library*, 294 (1992) null-null.

[99] D. Rebiscoul, A. Van der Lee, F. Rieutord, F. Ne, O. Spalla, A. El-Mansouri, P. Frugier, A. Ayral, S. Gin, Morphological evolution of alteration layers formed during nuclear glass alteration: new evidence of a gel as a diffusive barrier, *Journal of Nuclear Materials*, 326 (2004) 9-18.

[100] M. Arab, C. Cailleteau, F. Angeli, F. Devreux, Experimental Study and Monte Carlo Modeling of Calcium Borosilicate Glasses Leaching, *MRS Online Proceedings Library*, 985 (2006) null-null.

[101] F. Devreux, A. Ledieu, P. Barboux, Y. Minet, Leaching of borosilicate glasses. II. Model and Monte-Carlo simulations, *Journal of Non-Crystalline Solids*, 343 (2004) 13-25.

[102] P. Frugier, S. Gin, J.E. Lartigue, E. Deloule, SON68 Glass Dissolution Kinetics at High Reaction Progress: Mechanisms Accounting for The Residual Alteration Rate, *MRS Online Proceedings Library*, 932 (2006) null-null.

[103] S. Ribet, S. Gin, Role of neoformed phases on the mechanisms controlling the resumption of SON68 glass alteration in alkaline media, *Journal of Nuclear Materials*, 324 (2004) 152-164.

[104] R.G. Newton, A. Paul, A new approach to predicting the durability of glasses from their chemical compositions, *Glass Technology*, 21 (1980) 307-309.

[105] A. Paul, Chemical durability of glasses- The thermodynamic approach, *Journal of Materials Science*, 12 (1977) 2246-2268.

[106] C.W. Sinton, W.C. LaCourse, Experimental survey of the chemical durability of commercial soda-lime-silicate glasses, *Materials Research Bulletin*, 36 (2001) 2471-2479.

[107] J.E. Shelby, An Introdcution to Glass Science and Technology, The Royal Society of Chemistry, 2005, p.170-199.

[108] K.G. Knauss, W.L. Bourcier, K.D. McKeegan, C.I. Merzbacher, S.N. Nguyen, F.J. Ryerson, D.K. Smith, H.C. Weed, L. Newton, Dissolution Kinetics of a Simple Analogue Nuclear Waste Glass as a Function of Ph, Time and Temperature, *MRS Online Proceedings Library*, 176 (1989) null-null.

[109] X. Feng, I.L. Pegg, A glass dissolution model for the effects of SA/V on leachate pH, *Journal of Non-Crystalline Solids*, 175 (1994) 281-293.

[110] C 1285 - 02 Standard Test Methods for Determining Chemical Durability of Nuclear, Hazardous, and Mixed Waste Glasses and Multiphase Glass Ceramics: The Product Consistency Test (PCT), ASTM International, (2008).

[111] H.V. Atkinson, S. Davies, Fundamental aspects of hot isostatic pressing: An overview, *Metallurgical and Materials Transactions A - Physical Metallurgy and Materials Science*, 31 (2000) 2981-3000.

[112] C.B. Boyer, Historical Review of HIP Equipment, Hot Isostatic Pressing— Theory and Applications, (1992) 465-510.

[113] M. Bocanegra-Bernal, Hot Isostatic Pressing (HIP) technology and its applications to metals and ceramics, *Journal of Materials Science*, 39 (2004) 6399-6420.

[114] S.J. Mashl, Hot Isostatic Pressing of Castings, ASM Handbook, Volume 15: Casting, (2008, p 408-416).

[115] L.H.V. Vlack, Elements of Materials Science and Engineering, 6th ed., Addison-Welsey Publishing Compnay, Massachusetts, 1989, p. 284.

[116] W. D. Callister Jr., Materials Science and Engineering - An Introduction, 7th ed., John Wiley and Sons, 2007, p.482-483.

[117] J.S. Reed, Introduction to the principles of Ceramic Processing, 1st ed., John Wiley and Sons, 1998, p.449-469.

[118] W.D. Kingery, Introduction to Ceramics, Second Edition ed., John Wiley and Sons, 1976.

[119] C. Scales, E. Maddrell, M. Dowson, Developing Ceramic Based Technology for the Immobilisation of Waste on the Sellafield Site, in: *ASME 2009 12th International Conference on Environmental Remediation and Radioactive Waste Management*, American Society of Mechanical Engineers, 2009, pp. 585-592.

[120] M.W.A. Stewart, S.A. Moricca, T. Eddowes, Y.J. Zhang, E.R. Vance, G.R. Lumpkin, The Use of Hot Isostatic Pressing to Process Nuclear Waste forms, *Proceedings of the 12th International Conference on Environmental Remediation and Radioactive Waste Management 2009, Vol 1*, 2010.

[121] E. Maddrell, Hot isostatically pressed wasteforms for future nuclear fuel cycles, *Chemical Engineering Research and Design*, 91 (2013) 735-741.

[122] E.R. Vance, Synroc: A Suitable Waste Form for Actinides, *MRS Bulletin*, 19 (1994) 28-32.

[123] A. E Ringwood, S. E. Kesson, K. D. Reeve, D. M. Levins, and E. J. Ramm, Synroc, in: W. Lutze, R. C. Ewing, Radioactive Wastes for the Future, North-Holland Physics Publishing, Amsterdam, 1988, pp. 233-335.

[124] A.B. Harker, P.E.D. Morgan, J.F. Flintoff, Hot Isostatic Pressing of Nuclear Waste Glasses, *Journal of the American Ceramic Society*, 67 (1984) C-26-C-28.

[125] C.K.W. Cheung, E.R. Vance, M.W.A. Stewart, D.R.M. Brew, W. Bermudez, T. Eddowes, S. Moricca, The Intermediate Level Liquid Molybdenum-99 Waste Treatment Process at the Australian Nuclear Science and Technology Organisation, *Procedia Chemistry*, 7 (2012) 548-553.

[126] US Nuclear Waste Technical Review Board, Calcine Disposition Project, 9th April 2012, Available from www.nwtrb.gov/meetings/2010/june/ramsey.pdfJanuary, *Accessed on: 07/03/204*.

[127] E. Cartlidge, Nuclear's New Generation, *Physics World*, (October 2010).

[128] A.W. Mehner, W. Heit, K. Röllig, H. Ragoss, H. Müller, Spherical fuel elements for advanced HTR manufacture and qualification by irradiation testing, *Journal of Nuclear Materials*, 171 (1990) 9-18.

[129] Z. Zhang, Z. Wu, D. Wang, Y. Xu, Y. Sun, F. Li, Y. Dong, Current status and technical description of Chinese 20 MWth HTR-PM demonstration plant, *Nuclear Engineering and Design*, 239 (2009) 1212-1219.

[130] E. Ziermann, Review of 21 years of power operation at the AVR experimental nuclear power station in Jülich, *Nuclear Engineering and Design*, 121 (1990) 135-142.

[131] R. Simon, P. Capp, Operating experience with the dragon high temperature reactor experiment, *Proceedings on High Temperature Reactors*, (2002) 1-6.

[132] J. R. C. Gough, D. Kern, Studies On The Coating of Fuel Particles for the 'Dragon' Reactor Experiment, *Journal of Nuclear Energy*, 21 (1967) 623 - 642.

[133] W. Schenk, A. Naoumidis, H. Nickel, The behaviour of spherical HTR fuel elements under accident conditions, *Journal of Nuclear Materials*, 124 (1984) 25-32.

[134] B. Liu, T. Liang, C. Tang, A review of TRISO-coated particle nuclear fuel performance models, *Rare Metals*, 25 (2006) 337-342.

[135] G.K. Miller, D.A. Petti, D.J. Varacalle, J.T. Maki, Statistical approach and benchmarking for modeling of multi-dimensional behavior in TRISO-coated fuel particles, *Journal of Nuclear Materials*, 317 (2003) 69-82.

[136] J. Fachinger, K.H. Grosse, M. Hrovat, R. Seemann, Utilization of HTR reflector graphite as embedding matrix for radioactive waste, *Nuclear Engineering and Design*, 251 (2012) 235-238.

[137] J. Fachinger, M. den Exter, B. Grambow, S. Holgersson, C. Landesman, M. Titov, T. Podruhzina, Behaviour of spent HTR fuel elements in aquatic phases of repository host rock formations, *Nuclear Engineering and Design*, 236 (2006) 543-554.

[138] H. Nabielek, G. Kaiser, H. Huschka, H. Ragoss, M. Wimmers, W. Theymann, Fuel for pebble-bed HTRs, *Nuclear Engineering and Design*, 78 (1984) 155-166.

[139] H.N. K. Verfondern, J.M. Kendall, Coated particle fuel for high temperature gas cooled reactors, *Nuclear Engineering Technology*, 39 (2007) 603-616.

[140] A. Abdelouas, S. Noirault, B. Grambow, Immobilization of inert TRISO-coated fuel in glass for geological disposal, *Journal of Nuclear Materials*, 358 (2006) 1-9.

[141] A.A. B. Grambow, D. Grenèche, M.H. Mouliney, J. Fachinger, M. Titov, A. Bukaemsky, S. Neumann, Study of various options for final disposal of HTR coated particles, *3rd International Topical Meeting on High Temperature Reactor Technology*, (October 1-4, 2006).

[142] N.H. Hamodi, T.J. Abram, Microstructure Characterization of Simulated Tri-Isotropic Particles Embedded in Alkaline Borosilicate Glass, *International Journal of Applied Glass Science*, 2 (2011) 334 - 342.

[143] N.H. Hamodi, T.J. Abram, T. Lowe, R.J. Cernik, E. López-Honorato, The chemical durability of glass and graphite–glass composite doped with cesium oxide, *Journal of Nuclear Materials*, 432 (2013) 529-538.

[144] S.E. Jensen, P. L. Olgaard, Description of the Dounreay Fast Reactor, NKS/RAK-2(95)TR-C 1, Rise National Laboratory, Roskilde, Denmark, 1995.

[145] T. B. Cochran, H. A. Feiveson, W. Patterson, G. Pshakin, Fast Breeder Reactor Programs: History and Status, *International Panel on Fissile Materials*, (February 2010).

[146] Nucelar Decomissioning Authority, Waste Stream 5B01 - PFR Raffinate, UK Radioactive Waste Inventory (2007).

[147] K.F. Langley, B.A. Partridge, M. Wise, Immobilisation of Fast Reactor First Cycle Raffinate, Waste Management - Tuscon AZ, (February 2003).

[148] A. L. Nichols, D. L. Aldama, M. Verpelli, *Handbook of Nucelar Data for Safeguards: Database Extensions*, International Nuclear Data Committee, International Atomic Energy Agency, August 2008.

[149] UKAEA, How To Deal with the Management of Prototype Fast Reactor (PFR) Raffinate, 30 September 2004, (2004).

[150] UKAEA, Justification for Classifying PFR Raffinate as ILW, DSRPTC (2003) P11, 2003.

[151] UKAEA, Best Practicable Environmental Option Study For The Management of PFR Raffinate, D3900(04)P027, 2005.

[152] Nucelar Decomissioning Authority, Waste Stream 5B04 - MTR Raffinate, UK Radioactive Waste Inventory (2007).

[153] Nucelar Decomissioning Authority, Waste Stream 5B05 - DFR Raffinate, UK Radioactive Waste Inventory (2007).

[154] O.J. McGann, P.A. Bingham, R.J. Hand, A.S. Gandy, M. Kavčič, M. Žitnik, K. Bučar, R. Edge, N.C. Hyatt, The effects of γ-radiation on model vitreous wasteforms intended for the disposal of intermediate and high level radioactive wastes in the United Kingdom, *Journal of Nuclear Materials*, 429 (2012) 353-367.

[155] P.A. Bingham, N.C. Hyatt, R.J. Hand, C.R. Wilding, Glass Development for Vitrification of Wet Intermediate Level Waste (WILW) from Decommissionning of the Hinkley Point 'A' Site, *MRS Online Proceedings Library*, 1124 (2008) p.1124-Q1103.

[156] G. Plumb, Review of developments in UK commercial reprocessing, *Progress in Nuclear Energy*, 13 (1984) 3-18.

[157] M. Howden, Radioactive Effluent Treatment Plant—Sellafield Reprocessing Factory, *Proceedings of the Institution of Mechanical Engineers, Part A: Journal of Power and Energy*, 201 (1987) 1-15.

[158] H.H. Read, Rutley's Elements of Mineralogy, 25th ed., Thomas Murby & Co, London.

[159] J. Smyth, A. Spaid, D. Bish, Crystal structures of a natural and a Cs-exchanged clinoptilolite, *Cell*, 3 (1990) 2106-2123.

[160] Nucelar Decomissioning Authority, Waste Stream 2D26 - Ion Exchange Material (Clinoptilolite) and Sand, UK Radioactive Waste Inventory (2007).

[161] Nuclear Decomisioning Authority, Geological Disposal - Generic Specification for Waste Packages Containing Low Heat Generating Waste, August 2012, p.27.

[162] C.S. Poon, L. Lam, S.C. Kou, Z.S. Lin, A study on the hydration rate of natural zeolite blended cement pastes, *Construction and Building Materials*, 13 (1999) 427-432.

[163] C.E. McCulloch, M.J. Angus, R.W. Crawford, A.A. Rahman, F.P. Glasser, Cements in Radioactive-Waste Disposal - Some Mineralogical Considerations, *Mineralogical Magazine*, 49 (1985) 211-221.

[164] J. Juoi, M. Ojovan, W. Lee, Microstructure and leaching durability of glass composite wasteforms for spent clinoptilolite immobilisation, *Journal of Nuclear Materials*, 372 (2008) 358-366.

[165] IMPACT Services Inc, GeoMelt Division, Geomelt Trail 2 Feasibility Report, Document 090-002, Rev.0, August 2009.

[166] K. S. Matlack, W. K. Kot, H. Gan, I. L. Pegg, G. A. Diener, B.W. Bowan, Sellafield thermal treatment trials using advanced Joule heated ceramic melter technology, *Proceedings of Waste Management 2010 Conference*, March 7-11 2010, Phoenix, AZ (2010).

[167] D. Deegan, C. Scales, The Role of Tetronics Plasma Vitrification Technology in the Management and Conditioning of Nuclear Waste, *The 11th International Conference on Environmental Remediation and Radioactive Waste Management*, (2007) 1179-1187.

[168] B.G. Parkinson, Influence of Composition on Structure and Caesium Volatilisation from Glasses for HLW Confinement, PhD Thesis, The Univeristy of Warwick, 2007.

[169] M. Asano, T. Kou, Y. Mizutani, Vaporization of alkali borosilicate glasses, *Journal of Non-Crystalline Solids*, 112 (1989) 381-384.

[170] C.R. Gregson, D.T. Goddard, M.J. Sarsfield, R.J. Taylor, Combined electron microscopy and vibrational spectroscopy study of corroded Magnox sludge from a legacy spent nuclear fuel storage pond, *Journal of Nuclear Materials*, 412 (2011) 145-156.

[171] Selion Oy Website, Available from http://www.respons.pp.fi/selion/srframes1.htm *Accessed on 06/08/2014*.

[172] E. Tusa, J. Lehto, Use of Highly Selective Ion Exchanger for Minimisation of Waste Volumes, *Waste Management - Tuscon AZ*, (February 2003).

[173] H. Izawa, S. Kikkawa, M. Koizumi, Ion exchange and dehydration of layered [sodium and potassium] titanates, $Na_2Ti_3O_7$ and $K_2Ti_4O_9$, *The Journal of Physical Chemistry*, 86 (1982) 5023-5026.

[174] B.L. Lehto J, Harjula R,, SrTreat - A Highly Effective Ion Exchanger for the Removal of Radiocative Strontium from nuclear waste solutions, *Radioactive Waste Management and Environmnetal Remediation*, 1997, p. 245 - 247.

[175] J. Lehto, A. Clearfield, The Ion Exchange of Strontium on Sodium Titanate $Na_4Ti_9O_{20}.XH_2O$, *Journal of Radioanalytical and Nuclear Chemistry-Letters*, 118 (1987) 1-13.

[176] R. Koivula, R. Harjula, J. Lehto, Selective removal of radionuclides from nuclear waste effluents using inorganic ion exchangers, in: J.M. Loureiro, M.T. Kartel (Eds.) Combined and Hybrid Adsorbents: Fundamentals and Applications, 2006, pp. 37-47.

[177] R.H. Doremus, Glass Science, 2nd ed., John Wiley and Sons, New York, 1994, p.5.

[178] J.E. Shelby, An Introdcution to Glass Science and Technology, The Royal Society of Chemistry, 2005, p.32.

[179] A.R. West, Basic Solid State Chemistry, 2nd ed., John Wiley & Sons, 2009, p.407.

[180] J.M. Juoi, M.I. Ojovan, The effect of waste loading on the microstructure of glass composite waste forms for the immobilisation of spent clinoptilolite, *Glass Technology-European Journal of Glass Science and Technology Part A*, 48 (2007) 124-129.

[181] O.J. McGann, M.I. Ojovan, The synthesis of graphite–glass composites intended for the immobilisation of waste irradiated graphite, *Journal of Nuclear Materials*, 413 (2011) 47-52.

[182] R. Rottenfusser, E. E. Wilson, M . W. Davidson, Reflected Light Micrscopy, Carl Zeiss Micrsocopy Online Campus, Available from: zeiss-campus.magnet.fsu.edu/print/basics/reflected-print.html *Accessed on 18/10/2013*.

[183] P. J. Goodhew, J. Humphreys, R. Beanland, Electron Microscopy and Analysis, 3rd ed., Taylor and Francis, 2001.

[184] P. J. Goodhew, J. Humphreys, R. Beanland, Electron Microscopy and Analysis, 3rd ed., Taylor and Francis, 2001, p. 126.

[185] L. Reimer, Scanning Electron Microscopy - Physics of Image Formation and Microanlysis, 2nd ed., Springer, 1998, p.8.

[186] R. Tertian, F. Claisse, Principles of Quantitative X-Ray Flourescence Analysis, Heyden & Sons Ltd, London, 1982.

[187] J.C. Russ, Fundamentals of Energy Dispersive X-ray Analysis, 1st ed., Butterworths, 1984, p.6.

[188] P.J. Haines, in: P.J. Haines (Ed.) Principles of Thermal Analysis and Calorimety, The Royal Society of Chemistry, 2002, p.1-8.

[189] P.G. Laye, Differential Thermal Analysis and Differential Scanning Calorimetry, in: P.J. Haines (Ed.) Principles of Thermal Analysis and Calorimety, The Royal Society of Chemistry, 2002, p.55-71.

[190] G.R. Heal, Thermogravimety and Derivative Thermogravimetry, in: P.J. Haines (Ed.) Principles of Thermal Analysis and Calorimety, The Royal Society of Chemistry, 2002, p.10-24.

[191] C.M. Jantzen, N.E. Bibler, The Product Consistency Test (PCT): How and Why it Was Developed, in: Environmental Issues and Waste Management Technologies in the Materials and Nuclear Industries XII, John Wiley & Sons, Inc., 2009, pp. 155-167.

[192] Ahniyaz A., Sakamoto Y., Bergstrom L., Tuning the aspect ratio of ceria nanorods and nanodumbells by a face-specific growth and dissolution process, Crystal Growth and Design, 8 (2008) 1798-1800.

[193] C1220-98 Standard Test Method for Static Leaching of Monolithic Waste Forms for Disposal of Radioactive Waste, ASTM International, (2004).

[194] J.P. Icenhower, B.P. McGrail, W.J. Shaw, E.M. Pierce, P. Nachimuthu, D.K. Shuh, E.A. Rodriguez, J.L. Steele, Experimentally determined dissolution kinetics of Na-rich borosilicate glass at far from equilibrium conditions: Implications for Transition State Theory, *Geochimica Et Cosmochimica Acta*, 72 (2008) 2767-2788.

[195] D.M. Wellman, J.P. Icenhower, W.J. Weber, Elemental dissolution study of Pu-bearing borosilicate glasses, *Journal of Nuclear Materials*, 340 (2005) 149-162.

[196] B.P. McGrail, W.L. Ebert, A.J. Bakel, D.K. Peeler, Measurement of kinetic rate law parameters on a Na-Ca-Al borosilicate glass for low-activity waste, *Journal of Nuclear Materials*, 249 (1997) 175-189.

[197] P.K. Abraitis, B.P. McGrail, D.P. Trivedi, F.R. Livens, D.J. Vaughan, Single-pass flow-through experiments on a simulated waste glass in alkaline media at 40 degrees C. I. Experiments conducted at variable solution flow rate to glass surface area ratio, *Journal of Nuclear Materials*, 280 (2000) 196-205.

[198] P.K. Abraitis, B.P. McGrail, D.P. Trivedi, F.R. Livens, D.J. Vaughan, Single-pass flow-through experiments on a simulated waste glass in alkaline media at 40 degrees C. II. Experiments conducted with buffer solutions containing controlled quantities of Si and Al, *Journal of Nuclear Materials*, 280 (2000) 206-215.

[199] P.K. Abraitis, F.R. Livens, J.E. Monteith, J.S. Small, D.P. Trivedi, D.J. Vaughan, R.A. Wogelius, The kinetics and mechanisms of simulated British Magnox waste glass dissolution as a function of pH, silicic acid activity and time in low temperature aqueous systems, *Applied Geochemistry*, 15 (2000) 1399-1416.

[200] E.M. Pierce, E.A. Rodriguez, L.J. Calligan, W.J. Shaw, B.P. McGrail, An experimental study of the dissolution rates of simulated aluminoborosilicate waste glasses as a function of pH and temperature under dilute conditions, *Applied Geochemistry*, 23 (2008) 2559-2573.

[201] D.K.P. B.P.McGrail, Evaluation of the single-pass flow-through test to support a low-activity waste specification, *PNL Report-10746*, (1995).

[202] C 1285-02 Standard Test Methods for Determining Chemical Durability of Nuclear, Hazardous, and Mixed Waste Glasses and Multiphase Glass Ceramics: The Product Consistency Test (PCT), ASTM International, (2008).

[203] D.C. Harris, Quanitative Chemical Analysis, 8th ed., W. H. Freeman and Company, 2010, p.479 - 502.

[204] T.H. Smith, W.A. Ross, Impact testing of vitreous simulated high-level waste in canisters, Report BNWL-1903, 1975, Available from http://www.osti.gov/bridge//product.biblio.jsp?query_id=2&page=0&osti_id=4225345 Accessed on 18/05/2014.

[205] A.J. Connelly, R.J. Hand, P.A. Bingham, N.C. Hyatt, Mechanical properties of nuclear waste glasses, *Journal of Nuclear Materials*, 408 (2011) 188-193.

[206] T.V. Vorburger, H.G. Rhee, T.B. Renegar, J.F. Song, A. Zheng, Comparison of optical and stylus methods for measurement of surface texture, *International Journal of Advanced Manufacturing Technology*, 33 (2007) 110-118.

[207] US-Patent Nr. 2612074, September 30, 1952, Available from http://patft1.uspto.gov/netacgi/nph-Parser?Sect1=PTO1&Sect2=HITOFF&d=PALL&p=1&u=%2Fnetahtml%2FPTO%2Fsrchnum.htm&r=1&f=G&l=50&s1=2612074.PN.&OS=PN/2612074&RS=PN/2612074 *Accesssed on 05/08/2014*.

[208] R.J. Hocken, N. Chakraborty, C. Brown, Optical Metrology of Surfaces, *CIRP Annals - Manufacturing Technology*, 54 (2005) 169-183.

[209] H. Satoh, Y. Nishimura, K. Tsukamoto, In-situ measurement of dissolution of anorthite in Na-Cl-OH solutions at 22 degrees C using phase-shift interferometry, *American Mineralogist*, 92 (2007) 503-509.

[210] A. Luttge, Crystal dissolution kinetics and Gibbs free energy, *Journal of Electron Spectroscopy and Related Phenomena*, 150 (2006) 248-259.

[211] C.L. Corkhill, Contribution of Energetically Reactive Surface Features to the Dissolution of CeO_2 and ThO_2 Analogues for Spent Nuclear Fuel Microstructures, *ACS Applied Materials Interfaces*, 6.15 (2014) 12279-12289.

[212] Netzsch- Geratebau GmbH, Characterisation of Nucelar Materials - Methods, Instrumentation, Analytical Methods, E.1000.0610.MD.

[213] S.R. Charlton, D.L. Parkhurst, Modules based on the geochemical model PHREEQC for use in scripting and programming languages, *Computers & Geosciences*, 37 (2011) 1653-1663.

[214] N. Rajmohan, P. Frugier, S. Gin, Composition effects on synthetic glass alteration mechanisms: Part 1. Experiments, Chem. Geol., 279 (2010) 106-119.

[215] X. Geng, F. Yang, N. Rohbeck, P. Xiao, An Original Way to Investigate Silver Migration Through Silicon Carbide Coating in TRISO Particles, *Journal of the American Ceramic Society*, 97 (2014) 1979-1986.

[216] M. Barrachin, R. Dubourg, S. de Groot, M.P. Kissane, K. Bakker, Fission-product behaviour in irradiated TRISO-coated particles: Results of the HFR-EU1bis experiment and their interpretation, *Journal of Nuclear Materials*, 415 (2011) 104-116.

[217] P.A. Bingham, R.J. Hand, O.M. Hannant, S.D. Forder, S.H. Kilcoyne, Effects of modifier additions on the thermal properties, chemical durability, oxidation state and structure of iron phosphate glasses, J. Non-Cryst. Solids, 355 (2009) 1526-1538.

[218] R.W. Revie, Uhlig's Corrosion Handbook (2nd Edition), in, John Wiley & Sons, 2000, pp. 411-437.

[219] M. Todorović, L. Radonjić, Study of the mixed alkali effect in glasses and its relation to glass structure and alkali earth ion content, Ceramics International, 15 (1989) 383-388.

[220] C.W. Sinton, W.C. LaCourse, Experimental survey of the chemical durability of commercial soda-lime-silicate glasses, Materials Research Bulletin, 36 (2001) 2471-2479.

[221] R.J.H. P. A. Bingham, N. C. Hyatt, Vitrification of UK intermediate level radioactive wastes arising from site decommissioning: property modelling and selection of candidate host glass compositions, Glass Technol.: Eur. J. Glass Sci. Technol. A, 53 (2012) 83-100.

[222] G.B. Alexander, W.M. Heston, R.K. Iler, The Solubility of Amorphous Silica in Water, The Journal of Physical Chemistry, 58 (1954) 453-455.

[223] C.G. Pantano, G. Chen, D. Qi, Interface reactions and wetting in carbon-fiber-reinforced glass matrix composites, Materials Science and Engineering: A, 126 (1990) 191-201.

[224] S. Gahlert and G. Ondracek, Sintered Glass in W. Lutze, R. C. Ewing, Radioactive Waste Forms for the Future, Elsevier Science Publishers (North-Holland), 1988, p.161 - 193.

[225] C.L. Corkhill, N.J. Cassingham, P. Heath, N.C. Hyatt, Dissolution of UK High-Level Waste Glass Under Simulated Hyperalkaline Conditions of a Colocated Geological Disposal Facility, *International Journal of Applied Glass Science*, 4 (2013) 341-356.

[226] M. Abdullah, J. Ahmad, M. Mehmood, H. Waqas, M. Mujahid, Effect of deflocculants on hardness and densification of YSZ–Al2O3 composites, *Composites Part B: Engineering*, 43 (2012) 1564-1569.

[227] H.G. Richter, F. Kerkhof, Stress Wave Fractography in Fractography of Glasses edited by R. C. Bradt and R. E. Tressler, Plenum Press, (1994).

[228] A. Bukaemskiy, J. Fachinger, D. Bosbach, Physical properties and leaching behaviour of spent fuel BISO coated particles, *Progress in Nuclear Energy*, 57 (2012) 161-164.

[229] P. Hosemann, J.N. Martos, D. Frazer, G. Vasudevamurthy, T.S. Byun, J.D. Hunn, B.C. Jolly, K. Terrani, M. Okuniewski, Mechanical characteristics of SiC coating layer in TRISO fuel particles, *Journal of Nuclear Materials*, 442 (2013) 133-142.

[230] J. Wang, An integrated performance model for high temperature gas cooled reactor coated particle fuel, PhD Thesis submitted to the Department of Nuclear Engineering, Massachusetts Institute of Technology, 2004.

[231] O.O. Gulol, U. Colak, B. Yildirim, Performance analysis of TRISO coated fuel particles with kernel migration, *Journal of Nuclear Materials*, 374 (2008) 168-177.

[232] P.G. Heath, C.L. Corkhill, M.C. Stennett, R.J. Hand, W.C.H.M. Meyer, N.C. Hyatt, Encapsulation of TRISO particle fuel in durable soda-lime-silicate glasses, *Journal of Nuclear Materials*, 436 (2013) 139-149.

[233] H.U. Zwicky, B. Grambow, C. Magrabi, E.T. Aerne, Corrosion Behaviour of British Magnox Waste Glass in Pure Water, *MRS Online Proceedings Library*, 127 (1988) p.129.

[234] G. Roth, S. Weisenburger, Vitrification of High-Level Liquid Waste: Glass Chemistry, Process Chemistry and Process Technology, *Nuclear Engineering and Design*, 202 (2000) 197-207.

[235] M. Atkins, F.P. Glasser, Application of portland cement-based materials to radioactive waste immobilization, *Waste Management*, 12 (1992) 105-131.

[236] Areva Risk Management Consulting, Contents Activity for the Square Corner 3 m^3 Box Waste Package Transported in an SWTC-285 Transport Container, *R07-023(C) J6214.23*, NDA, RWMD, 2009.

[237] Department of Energy & Climate Change, Waste Transfer Pricing Methodology for Disposal of Higher Activity Waste from Nuclear Power Stations, URN 11D/923, (2011).

[238] P. E. Vickery, Clean out of storage ponds and silos at Sellafield, *Proceedings of the Waste Management Symposium*, 1998, Available from: http://www.wmsym.org/archives/1998/html/sess56/56-03/56-03.htm, Accessed on: 04/06/2015.

[239] M.B. Crawford, S.M. Wickham, CoRWM Criteria Discussion Paper: Cost, Report no: 0516-3. v.2, November 2005.

[240] Goverment tender document- A-2000319528-10000192 - Sellafield Box Procurement Project., Available from; http://england.unitedkingdom-tenders.co.uk/41744_A-2000319528-10000192_-_Sellafield_Box_Procurement_Project_2013_Warrington Accessed on 03/06/2015.

[241] Nuclear Decomissioning Authority, Geological disposal- Review of baseline assumptions regarding dispsoal of core graphite in a geological disposal facility, NDA Technical Note no: 16495644, May 2012.

[242] Toxicological Review of Barium and Compounds, US Environmental Protection Agency, EPA/635/R-05/001, March 1998.

[243] E. Yorukogullari, G. Yilmaz, S. Dikmen, Thermal treatment of zeolitic tuff, *Journal of Thermal Analysis and Calorimetry*, 100 (2010) 925-928.

[244] G.D. Knowlton, T.R. White, H.L. McKague, Thermal studies of types of water associated with clinoptilolite, *Clays and Clay Minerals*, 29 (1981) 403-411.

[245] British Stainless Steel Assocaition, Melting temperature ranges for stainless steels, Available from http://www.bssa.org.uk/topics.php?article=103 *Accessed on 30/01/2015*.

[246] R. Short, N. Gribble, N. Solutions, A. Riley, Widening the envelope of UK HLW vitrification–Experimental studies with high waste loadings and new product formulations on a full scale non-active vitrification plant–8348, *Proceedings of the Waste Management Conference,* Phoenix AZ, 2008.

[247] S.J. Chipera, D.L. Bish, Rehydration kinetics of a natural analcime, *European Journal of Mineralogy*, 22 (2010) 787-795.

[248] F.M. Wahl, R.E. Grim, R.B. Graf, Phase transformations in silcia as examined by continuous X-ray diffrraction, *American Mineralogist*, 46 (1961) 196-208.

[249] F.A. Gilabert, M.D. Bó, V. Cantavella, E. Sánchez, Fracture patterns of quartz particles in glass feldspar matrix, *Materials Letters*, 72 (2012) 148-152.

[250] C. Zong, From deep holes to free planes, *Bulletin of the American Mathematical Society*, 39 (2002) 533-555.

[251] J.H. Jean, Y.C. Fang, S.X. Dai, D.L. Wilcox, Devitrification kinetics and mechanism of K_2O-CaO-SrO-BaO-B_2O_3-SiO_2 glass-ceramic, *Journal of the American Ceramic Society*, 84 (2001) 1354-1360.

[252] C.M. Jantzen, M.E. Smith, D.K. Peeler, Dependency of Sulfate Solubility on Melt Composition and Melt Polymerization, in: Environmental Issues and Waste Management Technologies in the Ceramic and Nuclear Industries X, John Wiley & Sons, Inc., 2006, pp. 141-152.

[253] N.J. Cassingham, Structure and Durability of Simulated UK High Level Nuclear Waste Glasses, PhD Thesis; submitted to the Department of Materials Science and Engineering, The University of Sheffied, (2013).

[254] J.P. Icenhower, C.I. Steefel, Experimentally determined dissolution kinetics of SON68 glass at 90°C over a silica saturation interval: Evidence against a linear rate law, *Journal of Nuclear Materials*, 439 (2013) 137-147.

[255] J.A. Stone, Comparative leach testing of high-level waste forms, DP-MS-81-109, *84th Annual Meeting of the American Ceramic Society*, May 2-5, (1982).

[256] D. Marshall, A. Evans, B.K. Yakub, J. Tien, G. Kino, The nature of machining damage in brittle materials, *Proceedings of the Royal Society of London. A. Mathematical and Physical Sciences*, 385 (1983) 461-475.

[257] D. Johnson-Walls, A.G. Evans, D.B. Marshall, M.R. James, Residual Stresses in Machined Ceramic Surfaces, *Journal of the American Ceramic Society*, 69 (1986) 44-47.

[258] M. Tomozawa, Stress corrosion reaction of silica glass and water, *Physics and Chemistry of Glasses-European Journal of Glass Science and Technology Part B*, 39 (1998) 65-69.

[259] J. Lehto, L. Brodkin, R. Harjula, E. Tusa, Separation of radioactive strontium from alkaline nuclear waste solutions with the highly effective ion exchanger SrTreat, *Nuclear Technology*, 127 (1999) 81-87.

[260] J. Lehto, R. Harjula, A.M. Girard, The equilibrium of strontium ion exchange on sodium titanate, $Na_4Ti_9O_{20}.xH_2O$, *Journal of the Chemical Society, Dalton Transactions*, (1989) 101-103.

[261] J. Lehto, H. Leinonen, R. Harjula, Sodium titanate ion exchanger for radionuclide removal, e.g. strontium|comprises granules with specified particle size and sodium-to-titanium molar ratio, for e.g. industrial scale removal of strontium from waste, in, Ivo Int Oy; Ivo Power Eng Oy; Fortum Nuclear Services Oy; Ivo Int Ltd.

[262] T. Moller, R. Harjula, J. Lehto, Ion exchange of Sr-85, Cs-134 and Co-57 in sodium titanosilicate and the effect of crystallinity on selectivity, *Separation and Purification Technology*, 28 (2002) 13-23.

[263] P. Atkins, J. DePaula, Atkins Physical Chemistry, 8th ed., Oxford University Press, Oxford, 2006.

[264] H. Izawa, S. Kikkawa, M. Koizumi, Ion exchange and dehydration of layered titanates, $Na_2Ti_3O_7$ and $K_2Ti_4O_9$ *Journal of Physical Chemistry*, 86 (1982) 5023-5026.

[265] I. Arvanitidis, S. Seetharaman, X. Xiao, Effect of heat and mass transfer on the thermal decomposition of SrCO3 compacts, *Metallurgical and Materials Transactions B*, 30 (1999) 901-908.

[266] W.M. Haynes, CRC Handbook of Chemistry and Physics, 93rd Edition, Taylor & Francis, 2012.

[267] J.D. Hem, G. Survey, Study and Interpretation of the Chemical Characteristics of Natural Water, Department of the Interior, U.S. Geological Survey, 1985.

Notes